A Precision Measurement of the Z^0 Lineshape Parameters for the Process $Z^0 \rightarrow \tau^+\tau^-$

by

Robert Lahmann

Dissertation submitted to the Faculty of the Graduate School of the
University of Maryland at College Park in partial fulfillment
of the requirements for the degree of
Doctor of Philosophy
1996

Advisory Committee:

Andris Skuja, Professor of Physics, Chairman/Advisor
Associate Professor Abolhassan Jawahery
Associate Professor Nicholas Hadley
Professor Dieter Brill
Research Professor Michael Coplan

Abstract

Title of Dissertation: A Precision Measurement of the Z^0 Lineshape Parameters for the Process $Z^0 \rightarrow \tau^+\tau^-$

Robert Lahmann, Doctor of Philosophy, 1996

Dissertation directed by: Andris Skuja, Professor of Physics
Department of Physics

In this dissertation, a measurement of the partial decay width of the process $Z^0 \rightarrow \tau^+\tau^-$ using data collected during 1993 and 1994 at the OPAL detector at CERN is described. The cross sections of this process at three center-of-mass energies near the Z^0 resonance were determined, and from a fit to those cross sections, the mass of the Z^0, its total decay width and its partial decay width into $\tau^+\tau^-$ final states were determined as $M_Z = 91.183 \pm 0.020$ GeV, $\Gamma_{tot} = 2.514 \pm 0.018$ GeV and $\Gamma_{\tau\tau} = 84.54 \pm 0.59$ MeV. Using published results for M_Z, and Γ_{tot} with higher accuracy, a value for the partial decay width of $\Gamma_{\tau\tau} = 84.02 \pm 0.20$ MeV was obtained. Further using published results for the decay width of the Z^0 into quark pair final states, the invisible decay width of the Z^0 was determined as $\Gamma_{inv} = 496.9 \pm 4.1$ MeV, and the number of neutrino generations was determined as $N_\nu = 2.974 \pm 0.025(\text{exp}) \pm 0.007(m_{top}, M_{Higgs})$. All results were found to be in good agreement with the Standard Model predictions and were consistent with the assumption of lepton universality within the Standard Model framework.

Dedication

To my parents Jutta Lahmann, née Neukirch, and Erdwin Lahmann

Acknowledgements

Unfortunately it is impossible to thank everybody who has directly or indirectly contributed to the work presented in this thesis. I thank my colleagues who made the OPAL experiment a great place to work and live. I am also grateful to the members of the High Energy Group at Maryland for making this part of the physics department an enjoyable place to work. Special thanks to Sally Megonigal who provided much needed assistance in various bureaucratic battles across the Atlantic.

First, I would especially like to thank two people who have provided help and support during all of the way. My advisor, Dr. Andris Skuja, provided the guidance which was necessary to complete this thesis. Wayne Springer introduced me to the Wonderful World of Hardware in Particle Physics and provided invaluable help and support while I was working at OPAL. Wayne also helped to make my stay at CERN more enjoyable by suggesting projects from white water rafting to biking across the Alps.

In what seems a lifetime ago, Alfred Lee IV and John Lorah, as well as Adriaan Buijs and Keith Riles, helped me with my first steps at CERN and were extremely helpful and patient in introducing me to all aspects of the OPAL working environment. Austin Ball introduced me to the Hadron Calorimeter and was always a great source of support.

Dick Kellogg showed unparalleled enthusiasm in the frantic effort to build the Silicon Tungsten Calorimeter and to measure the luminosity on a more than tight time scale. Starting from scratch, the hard work of the members of the Silicon Tungsten Group made it possible to obtain a measurement with unprecedented precision. Maurice (Moe) Foucher was not only a crucial member of the Silicon Tungsten Group, but also provided help and support while I was trying to finish

up my thesis.

It was a pleasure to work with Julie Kirk on the tau pair analysis, and Tim Smith provided help and guidance with many aspects of the analysis. Most of the code that was used for my analysis is based on the code originally written by Toshio Tsukamoto and Rob Akers. Without their work and willingness to answer my questions, the analysis presented in this dissertation would hardly have been possible.

Last but not least, I would like to thank my parents, Erdwin and Jutta, as well as my sister Sabine and my brother Peter for providing the support which allowed me to pursue my academic ambitions. I would also like to thank Mary Amann who has been a friend in good times and in bad.

Table of Contents

List of Tables

List of Figures

Chapter 1

Introduction

The present theoretical description of electroweak interaction is based on the Glashow Weinberg Salam model [1], which unifies the electromagnetic and weak force in a local gauge theory with an underlying SU(2) $\times$ U(1) symmetry. The theory predicts the existence of two charged and one neutral massive gauge boson, $W^{\pm}$ and Z^0. The discovery of the neutral current in neutrino experiments marked the first experimental success of the model [2]. Since then, progress in both theoretical and experimental understanding have extended the theory and established the Standard Model of electroweak interactions in considerable detail. The Standard Model and the theoretical framework of this dissertation will be discussed in chapter 2.

The Large Electron Positron collider (LEP) at CERN allows the investigation of the Z^0 lineshape by colliding e^+ and e^- beams with precisely measured center-of-mass energies around the Z^0-peak and therefore provides a unique opportunity to probe the properties of the Z^0 to the level of quantum corrections. The precision electroweak measurements performed with the OPAL experiment at LEP combine the luminosity measurement of a small angle luminometer with an event rate measurement of the Z^0 decay into the multihadronic and the three leptonic decay

channels, yielding a cross section measurement at three well defined energy points around the Z^0 peak. Data were collected during 1993 at 3 center-of-mass energies, namely at the nominal Z^0 peak and at about ± 2 GeV from the peak. In 1994, data were taken exclusively at the peak energy. The LEP collider and the measurement of the beam energy will be discussed in chapter 3. The hardware and software components of the OPAL experiment will be described in chapter 4.

In this dissertation, a measurement of the decay width of the Z^0 into $\tau^+\tau^-$ final states will be presented. This measurement, combined with the lineshape analysis for multihadronic and the remaining leptonic final states performed by the OPAL collaboration, measures the free parameters of the Standard Model and tests the consistency of its predictions. The measurement of the partial decay width for the process $Z^0 \rightarrow \tau^+\tau^-$ provides a test of lepton universality and contributes to the measurement of the number of neutrino generations and the invisible decay width of the Z^0. The cross section for $\tau^+\tau^-$ final states for a given energy is calculated by

$$\sigma_{\tau\tau} = \frac{f_{\tau\tau} \cdot N_{\tau\tau}}{\mathcal{L}} ,$$

where $\mathcal{L}$ is the integrated luminosity, $N_{\tau\tau}$ is the number of events that pass the tau pair selection criteria, and $f_{\tau\tau}$ accounts for inefficiencies and backgrounds of the selected sample of tau pair events. Care has to be taken that the events contributing to the measurement of $\mathcal{L}$ and $N_{\tau\tau}$ are collected over the same time period without biasing either distribution.

The integrated luminosity during a given time interval is measured by counting events of the dominant process at small angles, the t-channel photon exchange process of bhabha scattering, within a well defined geometric and kinematic acceptance. Theoretical calculations of the cross section for the process are used to set the absolute scale of the luminosity measurement. In early 1993, the Sil-

icon Tungsten Calorimeter was installed in the OPAL detector to determine the luminosity with a precision of better than 1/1000. This upgrade was done since the increasing statistics of recorded Z^0 decays reduced the statistical error of the recorded multihadronic and leptonic event samples, while the luminosity measurement of the original luminometer was limited by its systematic error. In chapter 5, we will discuss the Silicon Tungsten Calorimeter. The luminosity measurement will be presented in chapter 6.

For the selection of $\tau^+\tau^-$ final states, events that pass various geometric and topological cuts consistent with a Z^0 decaying into a $\tau^+\tau^-$ final state are accepted. The resulting sample of events is studied to assess the level of background contamination an its agreement with $\tau^+\tau^-$ Monte Carlo, which is used to correct for the inefficiencies of the selection cuts. Since the τ lepton decays after about 300×10^{-15} s, or after 2.2 mm in the rest frame of the OPAL detector, the tau pair selection cuts have to be sensitive to the whole range of leptonic and hadronic decay channels of the tau. The selection criteria and the analysis of $\tau^+\tau^-$ final states are presented in chapter 7.

The ZFITTER [3] software package uses a semi-analytical approach to calculate fermion pair production in e^+e^- collisions and provides the theoretical parametrization of the Z^0 lineshape. In chapter 8, the mass of the Z^0, M_Z, its total decay width Γ_Z, and the peak cross section for the process $Z^0 \rightarrow \tau^+\tau^-$, $\sigma^0_{\tau\tau}$ are determined with ZFITTER. Using further theoretical assumptions and experimental data, the partial decay width of the Z^0 into $\tau^+\tau^-$ final states, $\Gamma_{\tau\tau}$, and the number of neutrino generations is deduced from the data. The study is concluded in chapter 9.

Chapter 2

Theoretical Framework

2.1 Introduction to the Standard Model

In the Standard Model, all known elementary particles are grouped into leptons and quarks, which are spin-$\frac{1}{2}$ particles, and mediators of the interactions with integer spin. For each particle an antiparticle exists, and each quark has an additional color charge of red, blue or green. Spin-$\frac{1}{2}$ particles can be represented by 4-component Dirac spinors, describing right- and left-handed particles and antiparticles, where left-handed (right-handed) is equivalent to helicity -1 $(+1)$ in the limit of vanishing rest mass of the particle. The wave function of a free fermion can be written as $\Psi = u(p)e^{-ipx}$ for particles and $\Psi = v(p)e^{+ipx}$ for antiparticles, where the spinors $u(p)$ and $v(p)$ satisfy the momentum space Dirac equations [4],

$$\begin{aligned} (\gamma^\mu p_\mu - m)u(p) &= 0 \\ (\gamma^\mu p_\mu + m)v(p) &= 0\,. \end{aligned} \tag{2.1}$$

In the above equation and for the remainder of this chapter, p_μ denotes the four-momentum of the particle, m its mass, and the definition of the γ-matrices can be found in [5] or any other book on quantum field theory. In the following discussion,

only particles will be considered, where the results for antiparticles are obtained by applying the charge conjugation operator.

The spinor corresponding to a fermion can be decomposed into its orthogonal left and right-handed components using the projection operators P_l and P_r,

$$u = u_r + u_l = P_l u + P_r u = \frac{1}{2}(1-\gamma^5)u + \frac{1}{2}(1+\gamma^5)u \; . \tag{2.2}$$

In the Glashow Weinberg Salam (GWS) model, electroweak interactions are represented by a $SU(2)$ group of "weak isospin" (I) and a $U(1)$ group of weak hypercharge (Y). The weak hypercharge is given by the Gell-Mann-Nishijima formula

$$Q = I^3 + \frac{1}{2}Y, \tag{2.3}$$

where Q is the electric charge in units of $|e|$ and I^3 the third component of the weak isospin. The left-handed and right-handed components, u_l and u_r, of the fermions are grouped into iso-spin doublets χ_l and iso-spin singlets ψ_r as shown in table 2.1. The corresponding quantum numbers are also shown in the table. The electron, muon, and tau lepton together with their corresponding neutrino form three lepton generations. The weak eigenstates of the quarks are not identical to the strong eigenstates, so that the components d', s', b' are obtained from the strong eigenstates d, s, b of the down, strange and bottom quark by multiplying by the Kobayashi-Maskawa matrix. The rotated eigenstates form three quark generations with the up, charm, and top quark, respectively.

Together with the $SU(3)$ color group representing the strong interaction in Quantum Chromodynamics (QCD), electroweak and strong interactions are combined into a local gauge theory based on the group $SU(3)_c \times SU(2)_I \times U(1)_Y$, called the Standard Model.

FERMIONS							
				I	I^3	Y	Q
χ_l	$\begin{pmatrix} \nu_e \\ e^- \end{pmatrix}_l$	$\begin{pmatrix} \nu_\mu \\ \mu^- \end{pmatrix}_l$	$\begin{pmatrix} \nu_\tau \\ \tau^- \end{pmatrix}_l$	$\frac{1}{2}$	$+\frac{1}{2}$	-1	0
					$-\frac{1}{2}$	-1	-1
	$\begin{pmatrix} u \\ d' \end{pmatrix}_l$	$\begin{pmatrix} c \\ s' \end{pmatrix}_l$	$\begin{pmatrix} t \\ b' \end{pmatrix}_l$		$+\frac{1}{2}$	$+\frac{1}{3}$	$+\frac{2}{3}$
					$-\frac{1}{2}$	$+\frac{1}{3}$	$-\frac{1}{3}$
ψ_r	e_r^-	μ_r^-	τ_r^-	0	0	-2	-1
	u_r	c_r	t_r			$+\frac{4}{3}$	$+\frac{2}{3}$
	d_r'	s_r'	b_r'			$-\frac{2}{3}$	$-\frac{1}{3}$
BOSONS							
γ	$W^\pm$	Z^0	Higgs			gluons	

Table 2.1: Particles in the Standard Model. For the fermions, the quantum numbers used in the GWS model are shown.

The Standard Model is constructed on the notion that the underlying fields be locally gauge invariant. In analogy to the Yukawa theory of strong interactions, and only writing terms involving fermions (i.e. writing the free part $\mathcal{L}_{free}$ and the interaction part of the fermion with the electroweak field, $\mathcal{L}_{EW}$) a Lagrangian fulfilling this requirement can be written as:

$$\mathcal{L}_{ferm} \equiv \mathcal{L}_{free} + \mathcal{L}_{EW} = \sum_f \overline{f} i\gamma^\mu \mathcal{D}_\mu f, \tag{2.4}$$

where the covariant derivative $\mathcal{D}_\mu$ contains a term for each of the three gauge symmetries of the theory:

$$\mathcal{D}_\mu = \partial_\mu + ig_1 \frac{Y}{2} B_\mu + ig_2 \frac{\tau_i}{2} W_\mu^i + ig_3 \frac{\lambda_a}{2} G_\mu^a. \tag{2.5}$$

The 2nd, 3rd, and 4th term on the right side of equation 2.5 represent the $U(1)_Y$,

$SU(2)_I$, and $SU(3)_c$ symmetry of the theory, respectively. The Y, τ_i, and λ_a are the generators of the respective groups *, where Y is a scalar, while the indices i and a run from 1 to 3 and 1 to 8, respectively, according to the general rule that the (complex) $n \times n$ matrix representing a $SU(n)$ group has $n^2 - 1$ independent parameters. Finally, each term contains a coupling strength g_i and a vector boson corresponding to a spin-1 field, namely B_μ, W^i_μ, and G^a_μ. The fields were introduced into the Lagrangian as shown in equations 2.4 and 2.5 to satisfy the requirement that the Lagrangian of the theory be locally gauge invariant. So far, both the fermions and the vector fields have been assumed to be massless, since any naively introduced mass-terms would spoil the local gauge symmetry of the Lagrangian in equation 2.4.

For completeness,the $SU(3)$ part of the theory representing the QCD sector of the Standard Model so far has been included. At this point, the $SU(3)_c$ symmetry will be dropped and the emphasis put on the electroweak sector, since this dissertation is not concerned with strong interactions.

The fermion states f from equation 2.4 correspond to the SU(2) doublets χ_I and singlets ψ_r from table 2.1. Using the notation from the table, the electroweak interaction part of equation 2.4 can be written in a more explicit form as

$$\mathcal{L}_{EW} = -\frac{g_1}{2}(Y_I \overline{\chi}_I \gamma^\mu \chi_I + Y_r \overline{\psi}_r \gamma^\mu \psi_r) B_\mu - \frac{g_2}{2} \overline{\chi}_I \gamma^\mu \begin{pmatrix} W^3_\mu & W^1_\mu - iW^2_\mu \\ W^1_\mu + iW^2_\mu & -W^3_\mu \end{pmatrix} \chi_I \,, \tag{2.6}$$

where the Pauli matrices have been substituted for the τ^i from equation 2.4 to form the product $\tau^i W^i_\mu$. It is convenient to make the following definitions and

* The factor 1/2 is purely conventional for spin-$\frac{1}{2}$ particles. Strictly speaking, the generators are $\frac{Y}{2}$, $\frac{\tau_i}{2}$, and $\frac{\lambda_a}{2}$.

replace the corresponding expressions in equation 2.6 :

$$\begin{aligned} W_\mu^\pm &= \frac{W_\mu^1 \mp iW_\mu^2}{\sqrt{2}} \\ W_\mu^0 &= W_\mu^3 \,. \end{aligned} \tag{2.7}$$

In the electroweak sector of the Standard Model it is assumed that the three lepton and quark families can be treated independently in exactly the same manner (lepton universality). Without loss of generality, the calculation can therefore be continued by appropriately substituting the electron and its neutrino for ψ_r and χ_l in formula 2.6. The Lagrangian then reads:

$$\begin{aligned} \mathcal{L}_{EW} &= \frac{g_1}{2}[Y_l(\bar{e}_l\gamma^\mu e_l + \bar{\nu}_l\gamma^\mu\nu_l) + Y_r\bar{e}_r\gamma^\mu e_r]B_\mu \\ &- \frac{g_2}{2}[(\bar{\nu}_l\gamma^\mu\nu_l - \bar{e}_l\gamma^\mu e_l)W_\mu^0 + \bar{\nu}_l\gamma^\mu e_l\sqrt{2}W_\mu^+ + \bar{e}_l\gamma^\mu\nu_l\sqrt{2}W_\mu^-] \,. \end{aligned} \tag{2.8}$$

The Lagrangian in equation 2.8 consists of a charged current part ($\mathcal{L}_{CC}$) and a neutral current part ($\mathcal{L}_{NC}$). The terms involving the charged weak isospin currents $j_+^\mu = \bar{\nu}_l\gamma^\mu e_l$ and $j_-^\mu = \bar{e}_l\gamma^\mu\nu_l$ are interpreted as corresponding to the weak processes $\nu_e \rightarrow e^- + W^+$ and $e^- \rightarrow \nu_e + W^-$. $W^\pm$ are the charged vector bosons of the weak force. The charged part of the lagrangian from equation 2.8 can then be written

$$\mathcal{L}_{CC} = -\frac{g_2}{\sqrt{2}}(j_+^\mu W_\mu^+ + j_-^\mu W_\mu^-) \,. \tag{2.9}$$

The neutral part $\mathcal{L}_{NC}$ involves the neutral weak isospin current $j_0^\mu = \frac{1}{2}(\bar{\nu}_l\gamma^\mu\nu_l - \bar{e}_l\gamma^\mu e_l)$ and the weak hypercharge current, $j_Y^\mu = Y_l(\bar{e}_l\gamma^\mu e_l + \bar{\nu}_l\gamma^\mu\nu_l) + Y_r\bar{e}_r\gamma^\mu e_r$. With the values for Y_l and Y_r fixed as shown in table 2.1, it is easily verified that corresponding to the relation from equation 2.3 the hypercharge current can be expressed as

$$j_\mu^Y = 2j_\mu^{em} - 2j_\mu^0, \tag{2.10}$$

where $j_\mu^{em} = Q(\bar{e}_l\gamma^\mu e_l + \bar{e}_r\gamma^\mu e_r)$ is the electromagnetic current.

The neutral term as it stands in equation 2.8 is interpreted as a mixture of the interaction of the particles with the 'ordinary' electromagnetic field A_μ and the neutral part of the weak force, Z_μ. We assume the fields to be orthogonal and write

$$\begin{aligned} A_\mu &= +B_\mu \cos\theta_w + W^0_\mu \sin\theta_w \\ Z_\mu &= -B_\mu \sin\theta_w + W^0_\mu \cos\theta_w \ , \end{aligned} \tag{2.11}$$

where a new parameter, the weak mixing angle (or Weinberg angle) θ_w has been introduced. The part of the Lagrangian in equation 2.8 which describes the neutral current can now be rewrite it in terms of the fields Z_μ and A_μ:

$$\begin{aligned} \mathcal{L}_{NC} &= -\frac{g_1}{2} j^\mu_Y B_\mu - g_2 j^\mu_0 W^0_\mu \\ &= -(\frac{g_1}{2} j^\mu_Y \cos\theta_w + g_2 j^\mu_0 \sin\theta_w) A_\mu - (-\frac{g_1}{2} j^\mu_Y \sin\theta_w + g_2 j^\mu_0 \cos\theta_w) Z_\mu \end{aligned} \tag{2.12}$$

In order to retrieve the QED Lagrangian for particles interacting with an electromagnetic field, we arrive at the condition

$$e j^{em\,\mu} = \frac{g_1}{2} j^{Y\,\mu} \cos\theta_w - g_2 j^{0\,\mu} \sin\theta_w, \tag{2.13}$$

and comparing this equation to equation 2.10, we get the correlation

$$g_1 \cos\theta_w = g_2 \sin\theta_w = e. \tag{2.14}$$

From the coefficient of the field Z_μ in equation 2.12 we can derive the neutral weak current, and, using equations 2.10 and 2.14, decompose it into an electromagnetic and a weak current:

$$\begin{aligned} g_z j^{Z\,\mu} &= -\frac{g_1}{2} j^\mu_Y \sin\theta_w + g_2 j^\mu_0 \cos\theta_w \\ &= \frac{e}{\cos\theta_w \sin\theta_w} (j^\mu_0 - \sin^2\theta_w j^\mu_{em}) \ . \end{aligned} \tag{2.15}$$

We can therefore write the coupling constants g_w and g_z for the $W^{\pm}$ and the Z^0 boson, respectively, in terms of the electromagnetic coupling constant e and the Weinberg angle θ_w:

$$g_w \equiv g_2 = \frac{e}{\sin\theta_w} \tag{2.16}$$

$$g_z = \frac{e}{\cos\theta_w \sin\theta_w}. \tag{2.17}$$

In order to endow the the gauge bosons and the fermions with mass, the GWS theory invokes the process of "spontaneous symmetry breaking". In this process, a symmetry which is valid for a Lagrangian is spontaneously broken by selecting a specific ground state of the system out of the set of all possible ground states. For any specific choice, the underlying symmetry is not valid, but since it is valid for the corresponding Lagrangian, the symmetry is said to be "hidden". In the Standard Model, the Higgs mechanism [6] is employed for the spontaneous symmetry breaking. In this model, a Higgs field is introduced which is assumed to be a SU(2) doublet, where the vacuum state is chosen as

$$\Phi_0 = \frac{1}{\sqrt{2}} \begin{pmatrix} 0 \\ v \end{pmatrix} , \tag{2.18}$$

and v is a scalar. While the value of v is not determined by the theory, it is related to the masses of the vector bosons as

$$M_{\mathrm{W}} = \frac{1}{2} v g_w \tag{2.19}$$

$$M_{\mathrm{Z}} = \frac{1}{2} v g_z \, . \tag{2.20}$$

The prediction of the existence of the heavy vector bosons $W^{\pm}$ and Z^0 and of their mass ratio (taking only into account first order Feynman diagrams with two

vertices, called tree level)

$$M_{\mathrm{W}}/M_{\mathrm{Z}} = g_w/g_z = \cos\theta_w \tag{2.21}$$

was a major accomplishment of the GWS theory. The Higgs boson, however, which arises in the theory as the quantum of the Higgs field, remains yet to be detected.

Masses for the fermions are introduced into the Lagrangian of the theory through additional gauge invariant terms, where each fermion term contributes a new coupling constant. However, the Standard Model makes no predictions about the absolute or relative size of the fermion masses, and the coupling constants merely introduce one more free parameter for each fermion into the theory.

2.2 Electroweak Interactions

Particle scattering amplitudes are most conveniently calculated in the Feynman calculus. Some Feynman rules on tree level for vertices between a vector boson and a fermion pair are shown in figure 2.1. In the Standard Model, the vertex factors are obtained by returning from the left- and right-handed fermion states as shown in table 2.1 to the physical states u of the fermions from equation 2.2. Starting with the Lagrangian for the fermion boson coupling $f + \overline{f} \rightarrow \mathrm{Z}^0$ (or $f \rightarrow f + \mathrm{Z}^0$) and using equations 2.15 and 2.2 as well as some algebra of the γ-matrices, we get:

$$\begin{aligned}
\mathcal{L} &= -ig_z j^{Z\,\mu} Z_\mu \\
&= -ig_z[\frac{1}{2}(\overline{\nu}_l\gamma^\mu\nu_l - \overline{e}_l\gamma^\mu e_l) - \sin^2\theta_W(\overline{e}_l\gamma^\mu e_l + \overline{e}_r\gamma^\mu e_r)]Z_\mu \\
&= -ig_z[\frac{1}{4}(\overline{\nu}\gamma^\mu(1-\gamma^5)\nu - \overline{e}\gamma^\mu e) - \sin^2\theta_W Q(\overline{e}\gamma^\mu e)]Z_\mu \\
&= -i\frac{1}{2}g_z\overline{e}\gamma^\mu[(-\frac{1}{2} - 2Q\sin^2\theta_W) + \frac{1}{2}\gamma^5]e - i\frac{1}{2}g_z\overline{\nu}\gamma^\mu(\frac{1}{2} - \frac{1}{2}\gamma^5)\nu \ . \qquad (2.22)
\end{aligned}$$

	c_v	c_a
ν_e, ν_μ, ν_τ	$\frac{1}{2}$	$\frac{1}{2}$
e^-, μ^-, τ^-	$-\frac{1}{2}+2\sin^2\theta_W$	$-\frac{1}{2}$
u, c, t	$\frac{1}{2}-\frac{4}{3}\sin^2\theta_W$	$\frac{1}{2}$
d', s', b'	$-\frac{1}{2}+\frac{2}{3}\sin^2\theta_W$	$-\frac{1}{2}$

Table 2.2: The vector and axial vector couplings for the Z^0 vertex.

For a given particle $u = e$ or ν, this can be written as

$$\mathcal{L} = \overline{u}[-i\frac{gz}{2}\gamma^\mu(c_v - c_a\gamma^5)]u, \tag{2.23}$$

where the expression in square brackets is interpreted as vertex factor for the reaction $u \rightarrow Z^0 + u$ or $u + \overline{u} \rightarrow Z^0$. The coefficients c_v and c_a for vector and axial vector coupling are given by the relations

$$c_v = I_l^3 - 2Q\sin^2\theta_w \tag{2.24}$$

$$c_a = I_l^3 \tag{2.25}$$

for any lepton from table 2.1, where I_l^3 denotes the third isospin component of the left-handed component for the charged fermions. The remaining vertices in figure 2.1 can be worked out in the same fashion. The coupling of a fermion pair to a Higgs particle is proportional to the ratio $m_f/v = g_z m_f/M_Z$ and can therefore be neglected in first order for final states other than the top quark.

The numerical values of the couplings are shown in table 2.2. Together with the propagators for spin-1 particles with momentum q,

$$\text{massless} \quad : \quad \frac{-ig_{\mu\nu}}{q^2} \tag{2.26}$$

$$\text{massive} \quad : \quad \frac{-i[g_{\mu\nu} - q_\mu q_\nu/m^2]}{q^2 - m^2} \tag{2.27}$$

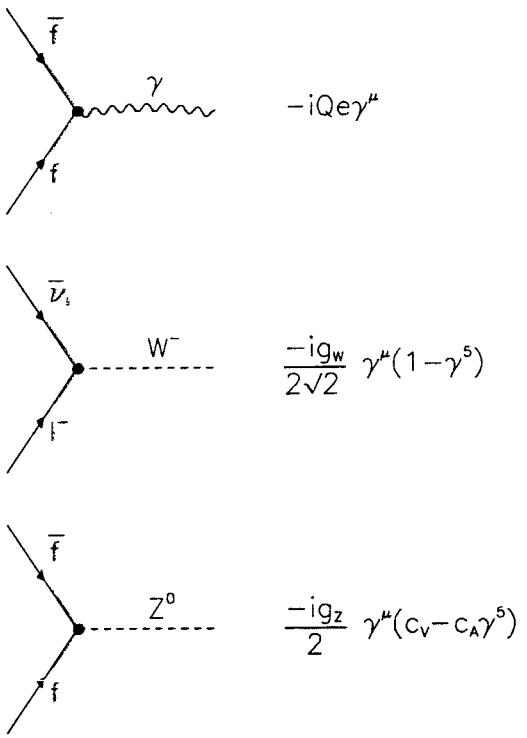

Figure 2.1: The vertex factors for the processes $f + \overline{f} \rightarrow \gamma$, $l^- + \overline{\nu_l} \rightarrow W^-$, and $f + \overline{f} \rightarrow \mathrm{Z}^0$, respectively, where f stands for any fermion and l for any lepton. The process to create a W^+, $l^+ + \nu_l \rightarrow W^+$, has the same vertex factor as the corresponding process creating a W^-.

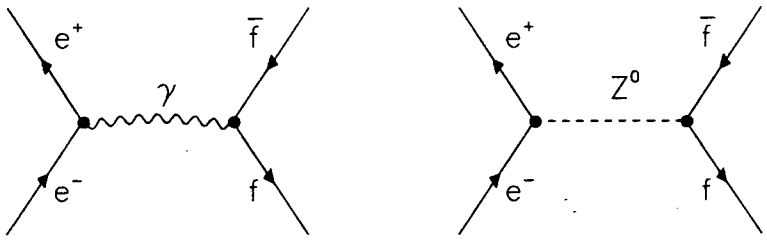

Figure 2.2: Tree level Feynman diagrams for the s-channel of the process $e^+e^- \rightarrow f\bar{f}$.

the cross-sections for matrix elements corresponding to the Feynman diagrams of interest can be calculated.

2.3 Cross Sections for e^+e^- Scattering

For a two-body scattering process, $p_1 + p_2 \rightarrow p_3 + p_4$, the differential cross section in the center-of-mass frame can be calculated according to the rule

$$\frac{d\sigma}{d\Omega} = \frac{1}{64\pi^2 s}|\mathcal{M}|^2 \,, \tag{2.28}$$

where $\mathcal{M}$ is the matrix element for the given process and s denotes the square of the center of mass energy. The calculation rule for the matrix element can be symbolically written as

$$\mathcal{M} = i\bar{v}(\text{vertex})u(\text{propagator})\bar{u}(\text{vertex})v \,, \tag{2.29}$$

where the particle and antiparticle spinors u and v satisfy the momentum space Dirac equations 2.1. At tree level, the diagrams shown in figure 2.2 contribute to

the process $e^+e^- \rightarrow f\bar{f}$. Using the vertex factors and propagators introduced in the previous subsection, the matrix elements for these processes can be calculated according to equation 2.29, and the differential cross section of the process can be computed according to equation 2.28. At tree level, and assuming negligible fermion masses, the cross section corresponding to the s-channel processes shown in figure 2.2 in the vicinity of the Z^0 resonance is given by

$$\sigma(s) = \sigma^0_{f\bar{f}} \frac{s\Gamma_Z^2}{(s - M_Z^2)^2 + M_Z^2\Gamma_Z^2} + \{\gamma Z^0\} + \{\gamma\} \; . \tag{2.30}$$

Here $\{\gamma Z^0\}$ and $\{\gamma\}$ represent small $\mathcal{O}(1\%)$ corrections to the cross section from the photon Z^0 interference and from the pure photon interaction term [7]. If the final state is an electron pair, t-channel processes have to be taken into account as well. This will be discussed in the next subsection. The Standard Model predictions for the partial decay widths of the Z^0 into fermion pair final states are given at tree level by

$$\Gamma_{f\bar{f}} = \frac{G_F M_Z^3}{6\pi\sqrt{2}} [(c_a^f)^2 + (c_v^f)^2] \; , \tag{2.31}$$

where the couplings c_a and c_v are those from table 2.2. The pole cross section $\sigma^0_{f\bar{f}}$ can be written in terms of the Z^0 total decay width and the partial decay width of the initial state electron pair and the final state fermion pair,

$$\sigma^0_{f\bar{f}} = \frac{12\pi}{M_Z^2} \frac{\Gamma_{ee}\Gamma_{f\bar{f}}}{\Gamma_Z^2} \; . \tag{2.32}$$

Equation 2.30 contains three free parameters that need to be determined from experiment, M_Z, G_F, and Γ_Z. The choice of these input values is not unique, but can be chosen such that they are experimentally convenient to access. The free parameters were introduced into the theory through the three parameters g_1, g_2 and v from the previous subsection. An experimentally convenient choice is G_F, α, and M_Z, where those three parameters are related to the Weinberg angle through

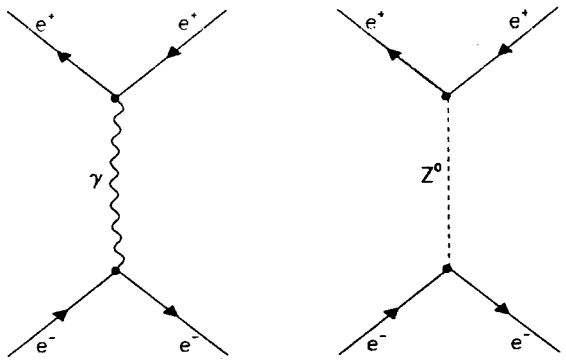

Figure 2.3: Tree level Feynman diagrams for the t-channel of the process $e^+e^- \rightarrow e^+e^-$.

the relation

$$\sin^2\theta_w \cos^2\theta_w = \frac{\pi\alpha}{\sqrt{2}G_F}\frac{1}{M_Z^2} \; . \tag{2.33}$$

The fine structure constant α and the Fermi constant G_F have been measured with high accuracy [8]. The determination of the mass of the Z^0 is the task of the LEP experiments.

The tree level predictions, equations 2.30 to 2.33 disagree with experimental results, which indicates that higher order diagrams have to be taken into account. This will be discussed below.

2.4 Cross Section for Bhabha Scattering

For Bhabha scattering $e^+e^- \rightarrow e^+e^-$, the contribution from photon and Z^0 exchange diagrams as shown in figure 2.3 has to be included in the calculation of the cross section. For both of those diagrams, a matrix element of the form

$$\mathcal{M} = i\overline{u}(\text{vertex})u(\text{propagator})\overline{v}(\text{vertex})v \tag{2.34}$$

has to be added, yielding a total of four spin averaged matrix element at tree level. At small angles, the dominant process for e^+e^- production is the t-channel photon exchange term. Small angles here mean small scattering angles from the incident electron and positron direction, which corresponds to a θ angle near 0 deg or 180 deg of the scattered particle in the OPAL reference frame. The contribution from the photon exchange diagram to the differential cross section in the ultrarelativistic case is calculated as

$$\frac{d\sigma}{d\Omega} = \frac{\alpha^2}{8s} \frac{1+\cos^4(\theta/2)}{\sin^4(\theta/2)} \,. \tag{2.35}$$

Making the small angle approximation $\sin\theta \approx \theta$, one arrives at the dependence

$$\frac{d\sigma}{d\theta} \approx \frac{1}{\theta^3} \,. \tag{2.36}$$

Small angle Bhabha events are used to measure the beam luminosity by e^+e^- collider experiments. For this measurement, Bhabha events are counted in a well defined geometric acceptance. The resulting number has to be divided by the theoretically calculated cross section for the process to yield the integrated luminosity over the time the detector was active. In the approximation from equations 2.36, the cross section of accepted luminosity Bhabha events within an inner and outer cut θ_{min} and θ_{max} can be calculated as

$$\int_{\theta_{min}}^{\theta_{max}} \frac{d\sigma}{d\theta} d\theta = \frac{4\pi\alpha^2}{s} \left(\frac{1}{\theta_{min}^2} - \frac{1}{\theta_{max}^2}\right) \,. \tag{2.37}$$

Calculations of the Bhabha cross section beyond tree level and including contributions from the diagrams other than the photon exchange can be found in [9]. Due to the complicated experimental acceptance, Monte Carlo programs provide the cross section calculations needed for the luminosity analysis. With the recent improvements of the luminosity measurement by OPAL and the other LEP experiments, providing Monte Carlo programs for Bhabha events with a precision of $\sim 1/1000$ for the cross section calculation has been a major challenge for theorists.

2.5 Radiative Corrections

Feynman diagrams beyond tree level, i.e. diagrams with internal loops or vertex corrections, are referred to as radiative corrections. The order of radiative corrections is usually expressed in terms of α, where a correction of the order α^n denotes processes with $2n$ additional vertices beyond the tree level vertices. The calculation of the matrix elements corresponding to Feynman diagrams for radiative corrections in QED yields results that are characterized by divergent integrals. To get finite results for calculations of cross sections or other physical quantities at a given order, *all* Feynman diagrams with the same final states have to be included, independent of the intermediate states. Applying the process of renormalization, the integrals can then usually be separated into a finite part and a divergent part, where the divergent parts cancel each other when all diagrams of a given order are combined. This procedure introduces dependences of formerly constant parameters on the center of mass energy, such that these parameters have to be defined at a particular center-of-mass energy and their values have to be determined experimentally. The most common renormalization scheme applied in the Standard Model is the "on-shell" renormalization scheme [10], where the electromagnetic fine structure constant α is defined at zero energy, and the masses of the gauge bosons $W^{\pm}$ and Z^0 are defined on their respective mass shell with $q^2 = M_W^2$ and $q^2 = M_Z^2$, respectively.

In figure 2.4 some first order radiative corrections for the process $e^+e^- \rightarrow f\bar{f}$ are shown. It is convenient to separate radiative corrections into three classes [7] as shown in the figure. The first class are "photonic corrections", which are characterized by additional photons in the tree level Feynman diagrams. While events with initial or final state radiation have an additional real photon in the final state,

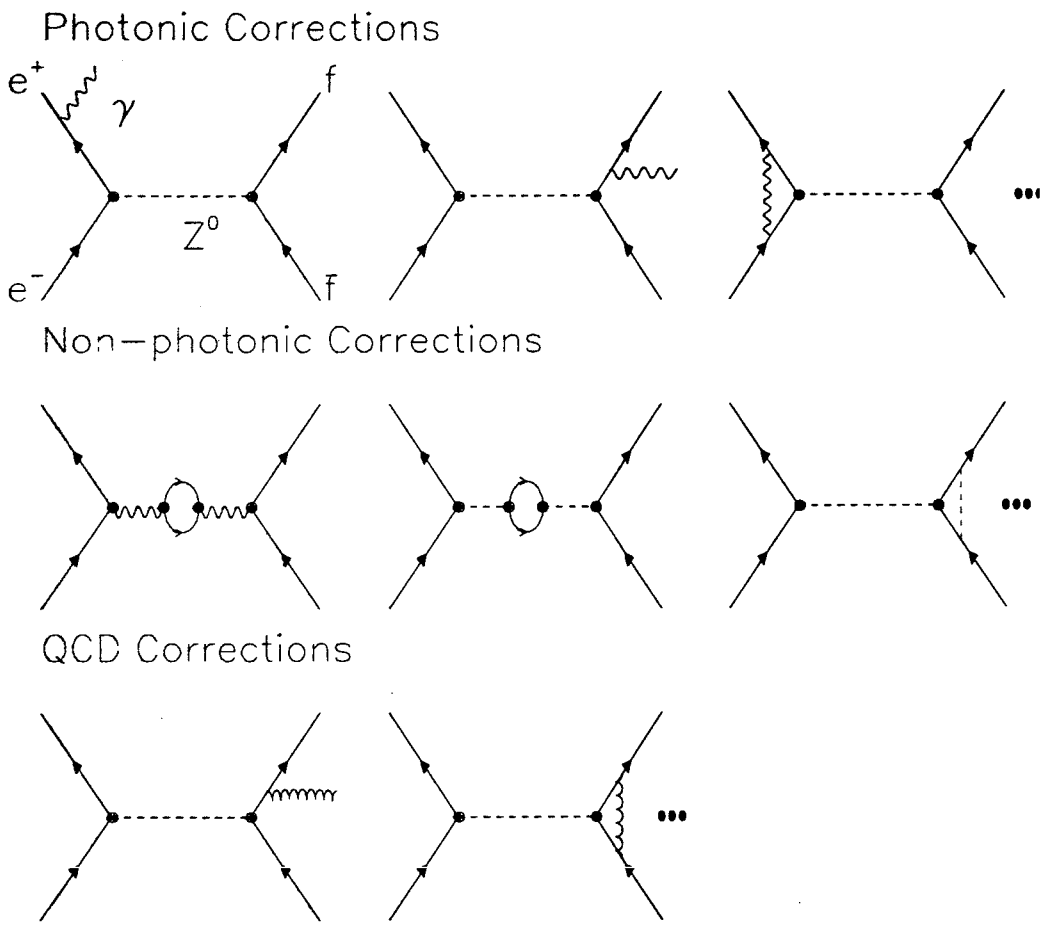

Figure 2.4: Some first order radiative corrections. The photonic corrections which are shown are (from left to right) initial state radiation, final state radiation, and the photonic vertex correction. The non-photonic corrections shown are the vacuum polarization diagrams for a photon and a Z^0, and a non-photonic vertex correction. First order QCD corrections arise from gluon radiation and are only relevant for quark pair final states.

due to the finite resolution of the experimental apparatus and the experimental cuts that are applied is this photon not always detected. Diagrams containing both virtual and real photons therefore have to be considered. Photonic corrections are large, depending on the experimental conditions up to $\mathcal{O}(30\%)$ at the Z^0 peak, and are dominated by effects from initial state radiation. Initial state radiation reduces the center-of-mass energy of the e^+e^- pair and therefore substantially affects the cross section near the Z^0 peak. These effects are well understood and are treated by convoluting the cross section for the hard scattering process by a radiator function which can be calculated within QED. For small angle Bhabha scattering, the theoretical precision of the cross section calculation required to match the experimental precision of the luminosity measurement necessitates the inclusion of corrections beyond the first order. Details of the treatment of radiation corrections for Bhabha scattering can be found in [9].

Non-photonic corrections denote diagrams in which additional fermions or gauge bosons are added to the tree level diagrams. These corrections modify the Born description of the Z^0 lineshape given in equation 2.30 by introducing a s dependence of both the electromagnetic coupling constant α and the total decay width of Γ_Z.

Photonic and non-photonic corrections together form the electroweak corrections. While the separation into photonic and non-photonic corrections is only meaning full in $\mathcal{O}(\alpha)$, it is justified by the smallness of higher order corrections. The third class of radiative corrections are QCD corrections and account for radiation of gluons from real and virtual quarks. These correction apply (at least in the first order) only in the case that the final state is a quark pair and will not be discussed here.

2.6 Parametrization of the Lineshape

The program ZFITTER [3] allows for several different parametrizations of the Z^0 lineshape for leptonic final states of which two were used in the analysis presented in this dissertation. The first parametrization calculates all matrix elements in the Standard Model framework. The program has to be provided with values for the the top mass, the Higgs mass and the mass of the Z^0 in order to calculate the cross section for a given energy.

The second approach is referred to as the 'improved Born approximation' [11]. This approach assumes that the Z^0 boson interacts with fermions through real constant vector and axial vector couplings, but makes no specific assumptions about the size of these couplings. In practice, this approach is realized by substituting the Standard Model values for the vector and axial vector coupling described in section 2.3, c_a and c_v, by "effective couplings" $\hat{c}_a$ and $\hat{c}_v$. Furthermore, non-photonic radiative corrections lead to a modification of the hard scattering process. The electromagnetic coupling constant has to be replaced by a "running" constant which is a function of the squared center-of-mass energy: $\alpha \to \alpha(s) = \frac{\alpha}{1-\Delta\alpha(s)}$. The total decay width of the Z^0 also assumes a s dependence which is well approximated by replacing $\Gamma_Z \to \Gamma_Z(s) = s/M_Z^2 \cdot \Gamma_Z(s = M_Z^2)$. In the following, the definition $\Gamma_Z \equiv \Gamma_Z(s = M_Z^2)$ will be used. Neglecting small $\mathcal{O}(0.1\%)$ effects of fermion masses for demonstrational purposes, the total cross section is then parametrized by [7]

$$\sigma(s)(e^+e^- \to \ell^+\ell^-) = \frac{4\pi\alpha^2}{3s}\left|\frac{1}{1-\Delta\alpha}\right|^2 + 4\frac{4\pi\alpha^2}{3s}\Re\left\{\frac{2}{1-\Delta\alpha}\chi(s)\hat{c}_v^e\hat{c}_v^l\right\}$$
$$+ 16\frac{4\pi\alpha^2}{3s}|\chi(s)|^2(\hat{c}_a^{e\,2} + \hat{c}_v^{e\,2})(\hat{c}_a^{l\,2} + \hat{c}_v^{l\,2})\,, \qquad (2.38)$$

where

$$\chi(s) = \frac{G_F M_Z^2}{8\pi\alpha\sqrt{2}} \frac{s}{s - M_Z^2 + is\Gamma_Z/M_Z} \,. \tag{2.39}$$

The first term in equation 2.38 is the pure photon contribution, the second is the $\gamma - Z^0$ interference and the third term is the s channel Z^0 cross section. The third term is equivalent to the Z^0 cross section given in equation 2.30 with the couplings c_a and c_v replaced by the effective couplings $\hat{c}_a$ and $\hat{c}_v$ and the total decay width replaced by an s dependent decay width $\Gamma_Z(s)$ as described above[†]. The effective couplings, together with the mass of the Z^0 and its total decay width, are then treated as free parameters by ZFITTER. This calculation is completely Standard Model independent except for small imaginary contributions to the coupling constants [3].

The invisible width of the Z^0 decay is obtained by subtracting the three leptonic decay widths and the decay width for multihadronic final states from the total decay width Γ_Z. Deviding this decay width by the Standard Model prediction for the decay width of the Z^0 into neutrino pair final states, one obtains the number of neutrino generations N_μ within the Standard Model framework.

[†] Note that in equation 2.30 only the Γ_Z^2 in the denominator has to be replaced—the Γ_Z^2 in the numerator cancels with the Γ_Z^2 in the definition of $\sigma_{\bar{f}f}^0$.

Chapter 3

The LEP Collider

3.1 LEP Operation

The Large Electron Positron (LEP) Collider at CERN has a circumference of 26.66 km and is located 50 m to 170 m underneath the surface in the border area between Switzerland and France. In LEP, e^+ and e^- beams are rotating in opposite directions, synchronized to collide at designated interaction regions, where for n equally spaced bunches of electrons and positrons per beam, the two beams interact at $2n$ points. Four e^+e^- interaction regions are instrumented with particle detectors, called L3, ALEPH, OPAL, and DELPHI. LEP I, the first phase of LEP, operated from 1989 through 1995 and was designed for center of mass energies around the Z^0 peak at $E_{cm} \approx 92$ GeV with a maximum center of mass energy of 110 GeV. The previously existing CERN accelerators, the Proton Synchroton (PS) and the Super Proton Synchrotron (SPS) were modified to serve as injectors for LEP. Full technical details of the LEP collider can be found in [13].

For a "LEP fill", the beams are injected into the LEP ring with an energy of 20 GeV each and are accelerated to reach the desired energy. Once the beams have been stabilized to the satisfaction of the LEP control room, the detectors

start data taking. The "physics run" is ended when the beam luminosities are reduced to a certain level or if the stable beam orbits are lost due to unfavorable circumstances.

Initially, the number of electron and positron bunches in LEP was four, with bunch crossings occurring once every 22.2 μs at the interaction regions ("4 on 4 operation"). After successful testing in 1992, the number of bunches was doubled ("8 on 8 operation") for operation from 1993 onwards, reducing the time between bunch crossings to 11.1 μs. This upgrade doubled the luminosity of the LEP collider, but forced changes to the trigger systems of the LEP experiments to handle the increased beam crossing frequency without introducing unacceptable deadtimes. The trigger of the OPAL detector, and the changes necessitated by the increased beam crossing frequency, will be discussed in section 4.2.

In 1993, about 60% of the luminosity was delivered in at two "off-peak" points, roughly 1.8 GeV above and below the Z^0 mass, while the remaining luminosity was delivered within 200 MeV of the Z^0 mass [14]. These three energy points will be referred to as "peak−2", "peak", and "peak+2" (or p−2, p, p+2 for short). During 1994, the LEP beam was operated exclusively at the peak point, increasing the statistics of the 1993 peak data by a factor of about five.

3.2 Collider Optics and Beam Dynamics

The main components of a circular accelerator like LEP are bending magnets, quadrupole focussing magnets and radio frequency (RF) cavities. The bending magnets force the particle beams on a circular path, where the amount of energy lost per turn through synchrotron radiation by a particle of charge q and velocity

$\beta = v/c$ in the bending field is (in SI units) [15]

$$U_s = \frac{4\pi}{3\varepsilon_0}\frac{q^2\beta^3\gamma^4}{\rho} \ . \tag{3.1}$$

Here ρ is the bending radius and $\gamma = (1-\beta^2)^{-1/2}$. The steep rise of the energy loss with increasing particle momentum as γ^4 results in a sharp limit of the maximum beam energy for a collider with given radius. The energy lost to synchrotron radiation is fed back into the circulating beams in the RF cavities. The RF power limits the energy of the beam, since synchrotron radiation loss must be compensated by the energy provided by the RF cavities. The RF cavities in LEP are positioned symmetrically at the respective sides of the OPAL and L3 detectors. Altogether, LEP contains more than 1300 focussing magnets and 3400 bending magnets. The quadrupole magnets positioned closest to the OPAL detector are located at about ± 7 m from the OPAL interaction point, and can deflect off-momentum particles into the acceptance of the Silicon Tungsten Calorimeter. This machine dependent background will be discussed in chapter 6.

The beam lifetime τ_b is limited by the decrease of particles in the beam according to the relation

$$N(t) = N_0 e^{-\frac{t}{\tau_b}} \ . \tag{3.2}$$

The beam lifetime in LEP is fundamentally limited by beam-beam bremsstrahlung and, to a smaller degree, through beam-gas interactions. The design lifetime for beams in the LEP machine was about 6 hours. During 1993 and 1994 operation, lifetimes well over 10 hours have been achieved.

3.3 Collider Luminosity

In any collider, the production rate for a process with cross section σ is given by

$$\frac{dN}{dt} = \sigma \mathcal{L}_c \,, \tag{3.3}$$

where the luminosity $\mathcal{L}_c$ is determined by the collider properties. For the case of colliding e^+ and e^- beams of relativistic particles, the luminosity delivered by the collider is given by

$$\mathcal{L}_c = fn\frac{N_+ N_-}{A} \,, \tag{3.4}$$

where N_+ and N_- are the number of particles in each bunch of the positron and electron beams, respectively, n is the number of bunches per beam and A is the interaction cross section of the beams. The revolution frequency of the beams is given by f. Assuming the particle density in each beam to have a Gaussian distribution perpendicular to the beam direction, the interaction cross section can be calculated from the R.M.S. deviations of the two beams in x and y direction by means of a folding integral as $A = 4\pi\sigma_x\sigma_y$ [16]. Introducing the total circulating currents $i^{\pm} = nN^{\pm}ef$, the collider luminosity can then be written

$$\mathcal{L}_c = \frac{i_+ i_-}{4\pi n f e^2 \sigma_x \sigma_y} \,. \tag{3.5}$$

The maximum average luminosity achieved for a LEP fill in 1993 was $12.8 \cdot 10^{30}\mathrm{cm}^{-2}\mathrm{s}^{-1}$, in 1994 it was $19.2 \cdot 10^{30}\mathrm{cm}^{-2}\mathrm{s}^{-1}$.

The integrated luminosity received by OPAL (or any of the other three detectors at LEP) is then given by

$$\mathcal{L}_{int} = \int_{t_{start}}^{t_{end}} \mathcal{L}_c \varepsilon(t) dt \,, \tag{3.6}$$

where $\varepsilon(t)$ is the detector efficiency. Since for the lineshape measurement exclusively integrated luminosities are measured, the symbol $\mathcal{L}$ will be used to refer to the integrated luminosity.

3.4 The Energy Measurement

A precise measurement of the center of mass energies is, besides the luminosity measurement and the event selection for the process of interest, the third crucial component of the lineshape measurement. Since 1991, the LEP beam energy has been calibrated with the method of resonant depolarization [19]. This method exploits the fact that under favorable conditions, the beams in an e^+e^- storage ring build up a transverse polarization, a phenomenon referred to as the Sokolev-Ternov effect [18]. In an ideal storage ring, which is a storage ring without any magnetic field components parallel to the particle direction, the spin tune ν_s for the electron or positron ensemble in a bunch is directly proportional to the beam energy,

$$\nu_s = \left(\frac{g-2}{2}\right)\frac{E_{beam}}{m_e c^2} = \frac{E_{beam}}{440.6486(1)\mathrm{MeV}} \,. \tag{3.7}$$

Here g is the electron gyromagnetic constant and m_e the electron mass. The spin tune is defined as the ratio of the spin precession frequency and the revolution frequency f of the beams in the ring. Resonant depolarization is produced by exciting the beam with an oscillating radial magnetic field, where the oscillation frequency is slowly varied. A field oscillating with a frequency f_{osc} is at resonance with the spin precession if it is related to the revolution frequency f by [20]

$$f_{osc} = (k \pm [\nu_s])f \,, \tag{3.8}$$

where k is an integer and $[\nu_s]$ indicates the non-integer part of ν_s. For the resonance frequency of the magnetic field, the induced spin rotations about the radial direction add up coherently with each successive revolution of the beam. For the LEP frequency of $f = 11.25$ kHz, the polarization vector of the beam is turned into the horizontal plane after about 10^4 turns ($\approx$ 1 second) and is flipped after twice that time. To determine the resonance frequency f_{osc}, the polarization of

the beams is measured using the effect that circular polarized laser light shows spin dependent Compton scattering. The oscillation frequency f_{osc} is chosen such that only the resonance conditions $f_{osc} = (0 + [\nu_s])f$ and $f_{osc} = (1 - [\nu_s])f$ are possible. The sign ambiguity is then resolved by varying the beam energy and observing if the $[\nu_s]$ for which resonance is observed moves to smaller or greater values. To determine the integer n of the spin tune $\nu_s = n + [\nu_s]$, measurements of the magnetic fields of the LEP dipole magnets and an identical reference magnet are performed [19]. The beam energy is then easily calculated according to relation 3.7.

Depolarization measurements were performed at the end of physics runs roughly twice per week, where each measurement was performed over a time of about 4 hours. Since the RMS variations of the center of mass energies during a LEP fill are as large as 15 MeV, a model has been developed to extrapolate the energy over the duration of a physics run, where the required input measurements for the model were logged during the fill [17]. These measurements include the dipole field strength, ring temperatures, and beam orbit positions as well as tidal effects. Most recently it has been discovered that electrically powered trains departing from the Geneva train station affect the LEP beam energy through ground loops.

While the intrinsic precision of the depolarization measurement is of the order of 1 MeV, the error of the beam energy measurement for a complete fill is dominated by uncertainties in the extrapolation model.

The errors on the mean energies of the three energy points and their correlations for 1993 are given in form of a covariance matrix in [17]. The errors for M_Z and Γ_Z can be derived from this matrix using the formulas

$$\Delta M_Z \approx 0.5\Delta(E_{p+2} + E_{p-2}) \tag{3.9}$$

$$\Delta\Gamma_Z \approx \frac{\Gamma_Z}{E_{p+2}-E_{p-2}}\Delta(E_{p+2}-E_{p-2}) = 0.71\Delta(E_{p+2}-E_{p-2}) , \quad (3.10)$$

which yield the results $\Delta M_Z = 1.5$ MeV and $\Delta\Gamma_Z = 1.4$ MeV at the peak energy. The error for the 1993 peak energy is $\Delta E_p = 5.4$ MeV. For the 1994 energy, no final energy calibration is available yet. Following [14], an error of $\Delta E_p = 4$ MeV has been assigned, uncorrelated with the 1993 energy measurements.

The energy of the particles in the beams is distributed over an energy spectrum around the mean that is large compared to the error on the mean beam energy. The measured cross section for a given mean energy is therefore the convolution of the energy spectrum with the "true" cross sections σ for the energies of the spectrum [21]. In second order approximation, and assuming a Gaussian distribution of the particle energies around the mean with RMS Δ_E, the measured cross section σ_{meas} is related to the "true" cross section at the mean energy $\overline{E}$ through the relation

$$\sigma_{meas} = \sigma(\overline{E}) + \frac{\Delta_E^2}{2}\frac{d^2\sigma(E)}{dE^2}\bigg|_{\overline{E}} . \quad (3.11)$$

This correction will be applied in the lineshape fitting procedure in chapter 8. The beam spread has been determined to be $\sigma_E = (55 \pm 5)$ MeV for 1993 [17], the preliminary result used for 1994 is $\sigma_E = (54 \pm 5)$ MeV, in accordance with [14].

Chapter 4

The OPAL Experiment

4.1 The OPAL Detector

OPAL, the Omni Purpose Apparatus for LEP [22], is located in a huge experimental area roughly 100 m underground. The detector is a multipurpose device to detect all interactions occurring in e^+e^- collisions and has an acceptance for Z^0 decays over a solid angle of almost 4π. The detector itself has a cylindrical shape with a diameter of about 11 m and is roughly 12 m long. A general layout of the detector is shown in figure 4.1, a cross section of a quadrant in the $x-y$ and $y-z$ plane is shown in figure 4.2. Points in the detector are referenced in a standard coordinate system, which is chosen such that the z axis coincides with the direction of the LEP e^- beam. The y axis points upwards, and the x axis towards the center of the LEP ring. The origin of the coordinate system is at the nominal interaction point of the e^+ and e^- beams in the center of the detector. The polar angle θ is measured from the z axis and the azimuthal angle ϕ from the x axis in the $x-y$ plane. In reference to the elevator shaft leading to the experimental area, the side with $z < 0$ is referred to as the left side, and the side with $z > 0$ as the right side; the side with $x < 0$ is called the near side and the

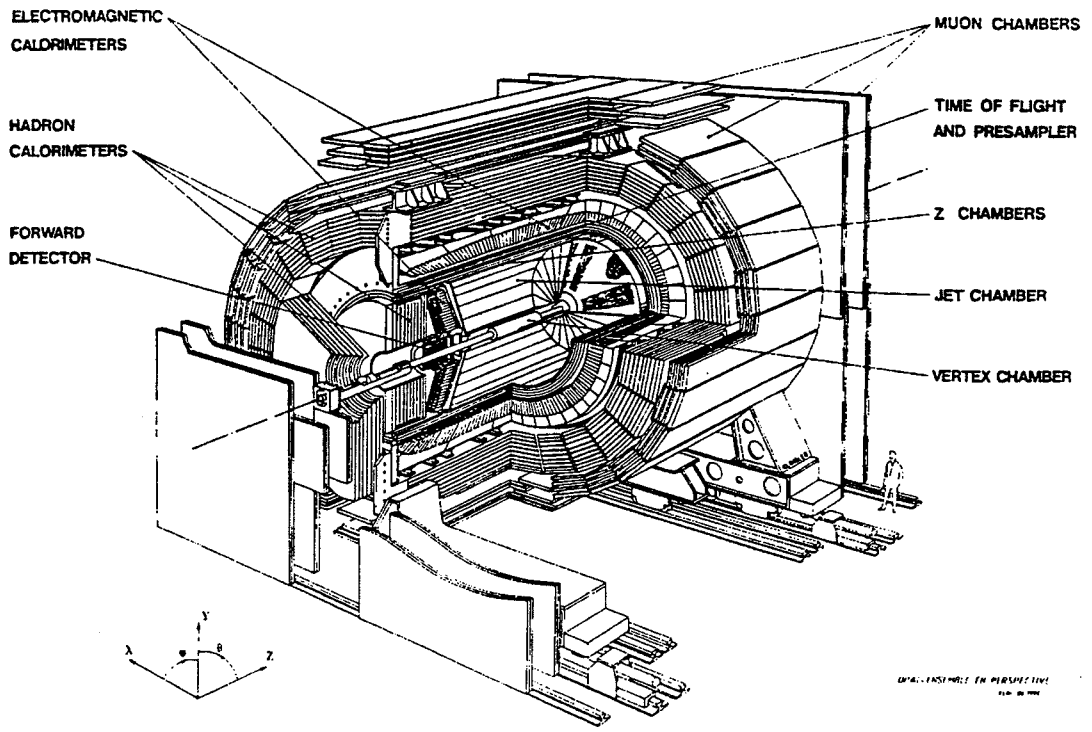

Figure 4.1: General layout of the OPAL detector. Shown is the design of the original detector for the startup in 1989.

side $x > 0$ the far side.

From the beam line in the radial direction outwards, OPAL consists of a central tracking system, a solenoid coil, a time-of-flight counter and various calorimeters. Altogether, OPAL contains 16 subdetectors, which are arranged into a barrel region covering the range $|\cos\theta| \lesssim 0.8$, an endcap and poletip region with $0.8 \lesssim |\cos\theta| \lesssim 0.95$, and a forward region covering the region close to the beam line.

OPAL started data taking in 1989 and has been constantly upgraded to improve the detector performance as the volume of recorded data has increased. Major upgrades have been the installation of a silicon microvertex detector inside the vertex detector in 1991 and of the silicon tungsten luminometer in 1993.

At the near and far side of the detector, several barracks are stacked which

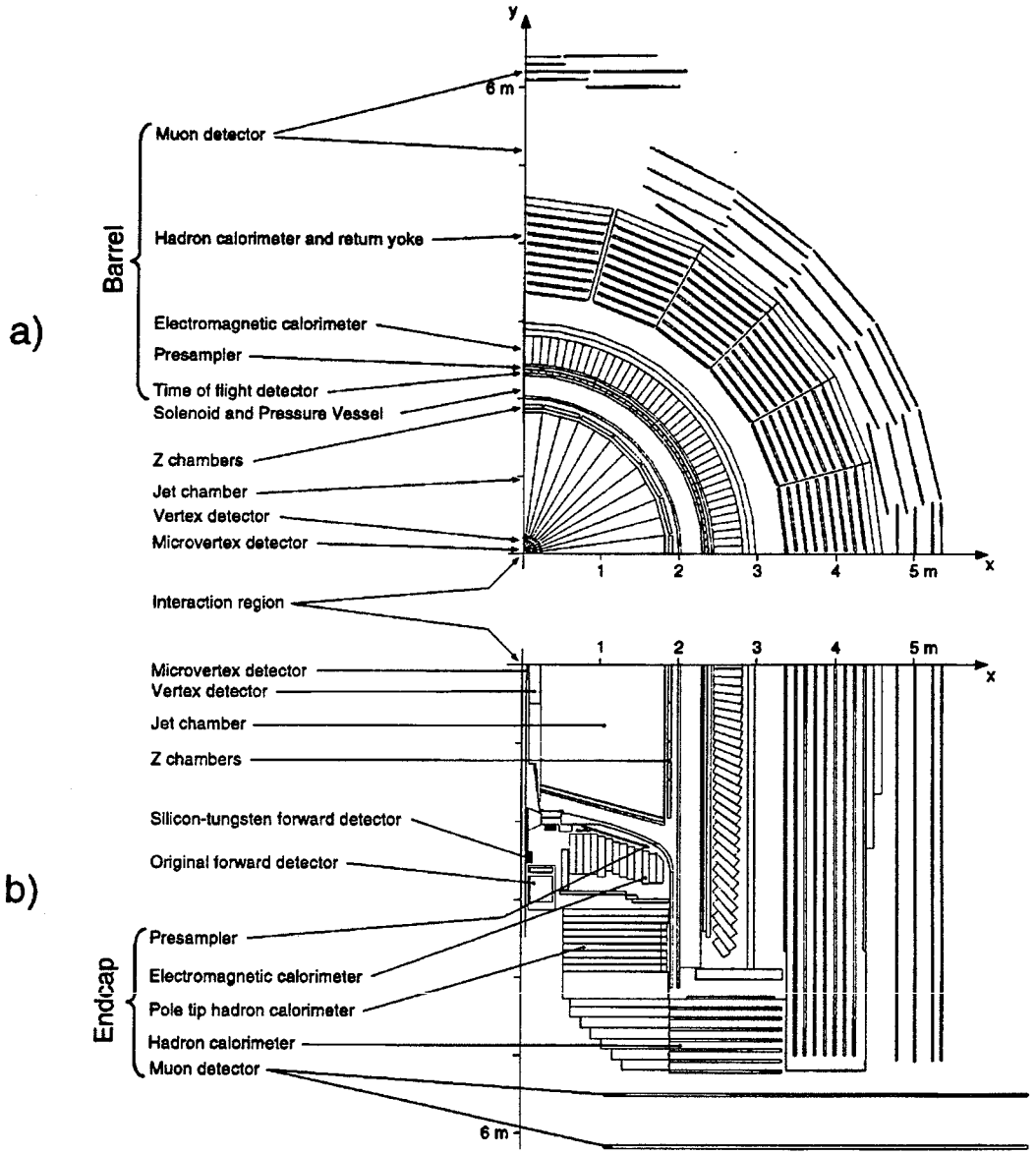

Figure 4.2: Cross section view of a quadrant of OPAL. Shown is the detector as it was implemented for the 1993/94 data taking periods, including the Silicon Microvertex detector and the Silicon Tungsten Calorimeter.

hold the digitization and control electronics for the detector as well as the OPAL control room. 4 'gondolas' are suspended from the ceiling of the experimental area which hold some more subdetector electronics, mainly for the endcap detectors.

In the following subsections we will briefly describe the subdetectors with emphasis on their properties which are relevant for our analysis. Full details can be found in [22] and references therein.

4.1.1 Magnet and Beampipe

The magnet, consisting of a solenoidal coil and an iron yoke, allows momentum and charge determination by the central tracking system. The solenoid is located outside the central detector and was designed to be as 'transparent' as possible for showering particles. The return yoke consists of a barrel, endcap and poletip region and is instrumented as a hadron calorimeter, which will be discussed below. The axial magnetic field produced in the cylindrical volume containing the central tracking system has a strength of 0.435 T and was measured to be uniform within $\pm 0.5\%$.

The original beampipe has a radius of 78 mm and consists of 1.3 mm thick carbon fiber with a 100 μm aluminum inner lining, holding a vacuum and providing a conducting surface for the operation of the LEP beams. The carbon fiber beampipe supports the pressure of 4 bar in the pressure vessel inside which the central tracking system is operated. In 1991, a 1.1 mm thick beryllium beam pipe with a radius of 53.5 mm was added to the OPAL detector. Beryllium has the advantage of reduced multiple scattering over the material of the original beam pipe. With the installation of a silicon microvertex detector between the old and new beampipe, the reconstruction of decay vertices of short-lived particles could be greatly improved.

4.1.2 Central Tracking System

The central tracking system is composed of the silicon microvertex detector and three drift chamber devices: the vertex detector, the jet chamber, and the z-chambers. The three tracking devices are located inside the pressure vessel with a radius of about 2 m. The central tracking system measures momenta of charged particles and provides particle identification by multiple sampling of the energy loss of charged particles traversing the gas.

The silicon microvertex detector (SI) has been upgraded several times after its first phase started data taking in June 1991. The phase II detector, which was in operation during the 1993 and 1994 data taking, consisted of two cylindrical layers of "ladders". Each ladder consists of 3 wafers with silicon strips for z and ϕ determination. The inner layer contains 11 ladders, the outer 14 with an active length of 180 mm with no azimuthal overlap. The inner and outer layers have radii of approximately 61 mm and 75 mm. SI is mainly used to improve the precision of track reconstruction for (charged) decay products from short lived particles. The detector is not used for the analysis presented in this dissertation.

The vertex detector (CV) is a 1 m long, 470 mm diameter, high precision cylindrical drift chamber surrounding the carbon fiber beam pipe. The detector consists of two layers comprising 36 azimuthal sectors each. In the inner layer, each sector contains 12 anode wires running parallel to the beam line and arranged in a plane parallel to the beam line, spanning radii from 103 mm to 162 mm. The cells in the second layer are inclined at a stereo angle of about 4 deg, each cell containing 6 anode wires that lie between radii of 188 mm and 213 mm. Each anode wire is read out at both ends, the ϕ coordinate is determined from the drift time and a coarse measurement of the z-position is obtained from the time difference between

the signals from the two ends of the wires. While this measurement is fast and is used as input for the track trigger as well as for off-line track-finding, a more precise z-measurement is done by combining axial and stereo cell information. The range $|\cos\theta| < 0.92$ is covered by both axial and stereo wires, while the acceptance of the axial wires extends to $|\cos\theta| < 0.95$.

Surrounding the beam pipe and vertex detector is the jet chamber (CJ) with a cylindrical volume of 4 m length, inner and outer radius of 250 mm and 1850 mm, respectively. CJ is divided into 24 azimuthal sectors, each one containing a plane of 159 sense wires strung in parallel to the beam line. The wires are equally spaced 10 mm apart between radii of 255 mm and 1835 mm and are stretched between two conical endplates. Within the range $|\cos\theta| < 0.73$, measurements from all 159 wires can be obtained for a track originating from the interaction point and within the range $|\cos\theta| < 0.98$, at least 8 wires provide information. At each end of the sense wires, the signal is amplified and its time evolution recorded by high speed flash analog-to-digital converters. The ϕ coordinate is then obtained from the drift time, and the z coordinate by measuring the charge division of the signals at the two ends of the wires. By summing the charges received at both ends of the wires and fitting the development in radial direction, the energy loss of a particle, dE/dx, is calculated.

The z-chamber (CZ) is arranged in a cylindrical shape between CJ and the pressure vessel and covers the region $|\cos\theta| < 0.72$ and 94% of the azimuthal angle. It provides a precise measurement of the z coordinate of charged particles as they leave CJ. The detector consists of 24 drift chambers with 4 m length and 50 cm $\times$ 5.9 cm cross section. Each chamber is divided in the z direction into 8 cells, with 6 sense wires being strung in the middle of each cell in a plane perpendicular to the z direction. The wires have a spacing of 4 mm in the radial direction. Each

4.1.4 Electromagnetic Calorimeter

The electromagnetic calorimeter consists of a presampler and as the main part a lead glass calorimeter. The presampler system consists of a barrel part (PB) covering the polar angle range $|\cos\theta| < 0.81$ and an endcap part (PE), covering $0.83 < |\cos\theta| < 0.95$. The presampler measures the position and samples the energy of showers before entering the lead glass calorimeter, since due to about 2 radiation lengths (X_0) of material in front of the lead glass calorimeter most electromagnetic showers are initiated before entering the lead glass. PB consists of 16 chambers with two layers of limited streamer tubes each, covering the surface of a cylinder with 2388 mm radius and 6623 mm length between the time-of-flight counter and the lead glass calorimeter. The anode wires run parallel to the z axis and are read out through two sets of 1 cm wide cathode strips per layer of streamer tubes, forming an angle of $\pm 45^o$ with the anode wires. The hit multiplicity in the streamer tubes is approximately proportional to the energy lost by an electron initially showering before reaching PB.

PE is located between the pressure bell and the endcap lead glass calorimeter. It consists of 32 chambers of multiwire proportional counters, arranged in the shape of an umbrella in front of the endcap part of the lead glass calorimeter.

Detection and measurement of energy and position of electrons and photons is done with the lead glass calorimeter, which is divided into a barrel part (EB) covering the region $|\cos\theta| < 0.81$, and an endcap part (EE), covering $0.81 < |\cos\theta| < 0.98$.

EB is constructed from 9440 SF57 lead glass blocks, arranged into a cylindrical array with inner radius of 2455 mm. Each lead glass block has a cross

wire is read out at both ends, allowing the determination of the z coordinate from the drift time and the determination of the ϕ coordinate by charge division.

Two important parameters derived from the reconstructed tracks are the impact parameters of tracks in z direction and in the $r-\phi$ plane, z_0 and d_0, respectively. These are used to reject cosmic ray events outside the acceptance of the time-of-flight counter. In [22], the d_0 and z_0 resolutions from the three drift chamber devices combined were measured to be $\sigma = 75\mu$m and $\sigma = 2$ mm, respectively, for dimuon events.

4.1.3 Time-of-Flight Counters

A main use of the TOF counters (TB) is to reject cosmic ray background by identifying the events as being out of time with the expected time of arrival of particles from e^+e^- collisions. TB furthermore provides a fast trigger and allows particle identification for low momentum particles in the range $0.6 \sim 2.5$ GeV/c. The TOF system consists of 160 scintillation counters, each one 6840 mm long, arranged as a barrel with a mean radius of 2.36 m. The system therefore covers the polar angle range $|\cos\theta| < 0.82$. The light is collected at both ends of each scintillation counter via plexiglas lightguides which are glued to phototubes. Each signal is split into three outputs which are sent to a charge integrating ADC, a 50 ps/count TDC and a mean timer. The signals from the mean timers are used for the trigger generation. It was determined for dimuon events that the OPAL TOF counters have a resolution of about 7.5 cm for measuring the z position of a track and a time resolution of roughly 460 ps [22].

section of approximately 10 cm $\times$ 10 cm and a depth of 37 cm, corresponding to 24.6 radiation lengths. The lead glass blocks are arranged to point towards the interaction region but are slightly tilted from a perfect pointing geometry. This design ensures that electron showers are contained within one or two lead glass blocks, and prevents particles from escaping detection through gaps between the lead glass blocks. Cherenkov light produced by relativistic charged particles in the lead glass is detected by phototubes at the bases of each block. Mechanically, EB is divided into a near and far part along the $y-z$ plane, and each of those halves is divided into 5 segments in θ. This design results in gaps between the 10 half-ring structures which in turn results in a decreased showering energy which is recorded for particles traversing the gaps.

Each of the two endcaps of the lead glass calorimeter consists of 1132 CEREN-25 lead glass blocks of varying length between 380 and 520 mm, arranged in a dome shape to fit between the pressure bell and the hadron poletip calorimeter. Typically, the lead glass blocks provide 22 X_0 of material with a minimum of 20.5 X_0. Unlike EB, the EE lead glass blocks are mounted coaxially with the beam line and do not point to the interaction point. The EE blocks are read out by specially developed vacuum photo triodes to allow operation in the full axial field of the magnet.

In a recent measurement [24], the energy resolution for electrons and photons in the OPAL lead glass calorimeter has been determined as $\sigma(E_\gamma)/E_\gamma \approx 20\%/\sqrt{E_\gamma}$ in EB and $\sigma(E_\gamma)/E_\gamma \approx 22\%/\sqrt{E_\gamma}$ in EE.

4.1.5 Hadron Calorimeter

The hadron calorimeter consists of a barrel part (HB), covering the region $|\cos\theta| < 0.81$, an endcap part (HE), covering $0.81 < |\cos\theta| < 0.94$, and a pole tip (HP) with

geometric acceptance $0.91 < |\cos\theta| < 0.99$. The hadron calorimeter, offering 4 interaction lengths of iron absorber, has about ~ 2.2 interaction lengths of material in front of it, resulting in most hadronic showers being initiated before reaching the hadron calorimeter. In order to determine the total energy of a hadronic shower, one therefore has to combine the signals from the electromagnetic calorimeter and the hadron calorimeter. In the analysis presented in this dissertation however, the detector has been mainly used to veto events containing muons as decay products.

Both HB and HE are mechanically divided into 24 wedges in the ϕ direction. Each wedge in HB consists of 9 layers of plastic streamer tubes as active elements, alternating with 8 layers of 10 cm slabs of iron. The iron layers in the barrel lie in a plane parallel to the beam line, spanning radii from 3.4 m to 4.4 m. The limited streamer tubes between the iron layers run (depending on the layer) the whole or half the length of the calorimeter, their length ranging from 3.0 m to 7.3 m. HE is donut-shaped with inner and outer radii of 1910 mm and 3305 mm. It consists of 8 layers of plastic streamer tubes, alternating with 7 layers of 10 cm thick iron, where each layer lies in a plane orthogonal to the beam line. The limited streamer tubes are arranged in 4 quadrants and are aligned in the x direction, their lengths varying between 0.5 m and 2.2 m.

In both HB and HE, the induced signals are read out through 4 mm wide aluminum strips running the full chamber length above the streamer tubes, and through large pads of typical size 0.5 m $\times$ 0.5 m below the tubes. The strips allow the determination of the ϕ position of a shower and layer-by-layer sampling of the energy, while the pads form towers of all 9 layers in the case of HB or 8 layers in case of HE. These towers point roughly at the interaction point and divide HB and HE into 48 half-wedges in ϕ, HB into 17 towers in θ, and each of the two endcaps into 2 towers in θ.

The data acquisition is combined for the barrel and endcap region, but is done independently for the towers and strips. Therefore, the hadron calorimeter (excluding the pole tip region) is divided into the strip part (HS) and the tower part (HT) for online purposes, while for the offline analysis it is divided into HB and HE.

In order to improve the energy resolution in the forward region, HP has a sampling frequency of 10 iron layers, each 8 cm in thickness. Between the iron, thin multiwire chambers are placed as active material. Just as in the case of HB and HE, the readout is done through both strips and pads.

4.1.6 Muon Detector

The outermost subdetector of OPAL is designed to identify muons. Over almost its complete acceptance the amount of material in front of the muon detector corresponds to at least 1.3 m of iron equivalent. The probability for any detectable particle other than a muon to reach the muon detector from the interaction point is therefore extremely small. The muon detector is divided into a barrel part (MB) and endcap part (ME). MB consists of 110 large area drift chambers with cross section 120 cm $\times$ 9 cm and ranging in length from 6.0 m to 10.4 m. 44 chambers are mounted at the near and far side each, furthermore 12 in the top module and 10 in the bottom module, as can be seen in figure 4.1. MB covers the region $|\cos\theta| < 0.68$ with 4 layers and $|\cos\theta| < 0.72$ with at least one layer of drift chambers. Each of the 110 chambers is divided into two adjoining cells. At the center of each cell is mounted an anode wire running the whole length of the chamber, parallel to the beam line. The ϕ coordinate is determined by the electron drift time to an accuracy of better than 1.5 mm. The z coordinate is determined in three processes, coarse, medium, and fine, to an accuracy of 2

mm. The coarse z coordinate is determined from the difference in time and pulse heights of the signals arriving at the two ends of the anode. The medium and fine determination is done with the induced signals on two diamond shaped cathode patterns, repeating every 1710 mm and 171 mm, respectively.

ME covers the region $0.67 \lesssim |\cos\theta| \lesssim 0.985$, where the geometric acceptance averaged over ϕ varies between $\sim$ 50% and 100%, gaps in the acceptance resulting from the beam line, support structures and cables leading to subdetectors inside of the muon detector. Each side of ME consists of 2 layers of 4 quadrant chambers, each one 6 m $\times$ 6 m in size, and 2 patch chambers with an area of 3.0 m $\times$ 2.5 m each. The arrangement of the chambers can be seen in figure 4.1. Each chamber contains two layers of limited streamer tubes which are arranged in a plane perpendicular to the z direction. The anode wires are spaced 10 mm apart and run parallel to the x and y axis in the respective layers. The streamer tubes are read out through two sets of 8 mm wide strips on the respective sides of each layer, one set running perpendicular to the anode wire, the other parallel.

4.1.7 Forward Detectors

The primary objective of the forward detectors is to measure the luminosity of the LEP machine by detecting small angle bhabha scattering. The original forward detector (FD) was composed of two identical elements at the left and right end, each one consisting of a number of tracking and calorimetry devices. With the installation of the silicon tungsten detector (SW) in 1993, FD had to be displaced about 15 cm axially, away from the interaction point. Part of its original acceptance is now shadowed by SW. SW is a calorimetric device of 22 radiation lengths of Tungsten, interspaced with 19 layers of Silicon detectors and readout electronics. Since this dissertation describes an analysis with a luminosity mea-

surement based exclusively on SW, the detector will be discussed in more detail in chapter 5. At this point, only the most important components of the original forward detector will be discussed. Full details can be found in [22] and references therein.

The main part of FD is a lead-scintillator sandwich of 24 X_0 depth, read out through wavelength shifters from 35 sampling layers. The calorimeter has a cylindrical shape with inner and outer radius of 106.8 mm and 403.4 mm, respectively. The front face of the left and right calorimeter are located at about $z = \pm 2.5$ m [25]. Each layer is divided into 16 azimuthal segments which are read out individually. After the first 4 X_0 of the calorimeter, three layers of proportional tubes rotated by 45° with respect to each other form the tube chamber. The position of the tubes has been surveyed with a precision of 0.5 mm [23], allowing an absolute internal calibration on that level of the shower coordinate reconstructed with the calorimeter. The uncertainty of the inner edge of the bhabha acceptance for the luminosity measurement with FD is the dominant systematic error of that measurement. Furthermore FD is installed fairly far away from the beam line so that the statistics of Bhabha events inside its fiducial acceptance are smaller by about a factor of 2.5 than the statistics of multihadronic Z^0 decays. These fundamental limitations of FD prevented the determination of the luminosity with an accuracy matching the increasing statistics of recorded Z^0 decays and motivated the installation of SW.

4.2 Trigger and Pretrigger

Crossings of the e^+ and e^- beams for 8-on-8 LEP operation occur at the OPAL interaction point every 11.1 μs, or at a frequency of roughly 90 kHz. The function

of the trigger system is to decide whether for a given beam crossing the data recorded by the subdetector front end electronics should be digitized and read out or if the data should be abandoned and the electronics reset for the next beam crossing. The trigger system is a part of the online system, but since it is rather complex, it is discussed separately in this section. The remaining steps of the online system, after the trigger indicates that a given event should be read out, will be discussed in the following section.

Readout and digitization of an event introduces a deadtime of about 5 ms, equivalent to the time it takes the slowest subdetector to read out and digitize the data, resulting in roughly 450 missed beam crossings. This makes a trigger system crucial, which is sensitive to all known Z^0 decays as well as possible new physics, while rejecting background events such as cosmic rays and beam-gas collisions. At the same time, the system should provide a sufficient degree of redundancy in order to be able to cross check trigger efficiencies and to be less dependent on the performance of individual subdetectors.

The OPAL hardware trigger is a two-stage system consisting of a pretrigger and a trigger. The original trigger logic was designed for 4-on-4 LEP operation with beam crossings occurring every 22.2 μs. The original trigger needed about 14.5 μs to form the trigger decision and in the case of a negative decision, roughly an additional 5 μs were needed to reset the front end electronics of the subdetectors [28], [29]. In case of a negative trigger decision, the detector was therefore completely reset and operational for the following beam crossing. With the introduction of 8-on-8 operation during 1992, the time between beam crossings was reduced to 11.1 μs, which would have introduced an unacceptable deadtime without modifications to the trigger system. Since the trigger decision time could not be reduced to make the decision available before the next beam crossing, a pre-

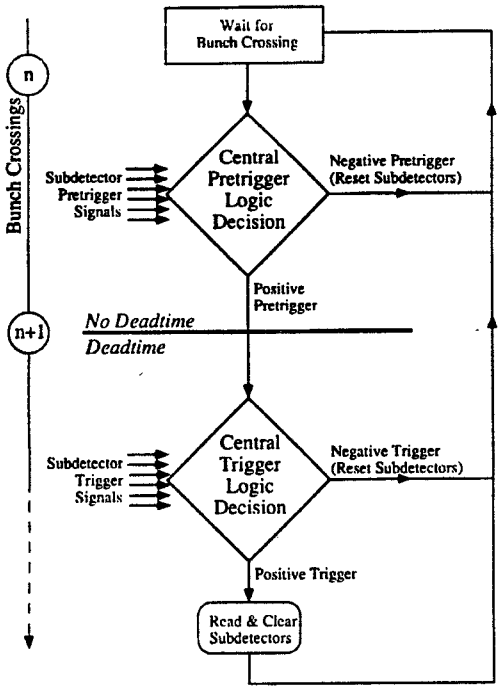

Figure 4.3: Overview of two-stage OPAL event trigger system.

trigger was added to form a two-stage trigger system [28]. The pretrigger takes the fastest available trigger signals from the subdetectors and forms a pretrigger decision before the next beam crossing. Only in case of a positive pretrigger decision is the outcome of the trigger decision waited upon. One beam crossing is lost in the case of a positive pretrigger and negative trigger decision. Both the trigger and pretrigger rate decrease with time as the currents in the LEP ring decrease. For 1994, a typical run started off with a pretrigger rate of about 700 Hz and a trigger rate of roughly 7 Hz. The average pretrigger and trigger rate for a physics run lasting 5 to 10 hours were $\sim$ 400 Hz and $\sim$ 5 Hz, respectively. A schematic overview of the two-stage event triggering is given in figure 4.3. In the following subsections, first an overview of the operation of the complete trigger system will be given. Then the trigger generation by the subdetectors and the trigger decision formed by the central trigger logic will be discussed in more detail.

4.2.1 Operation of the Trigger System

The trigger signals from the subdetectors are provided by dedicated trigger electronics which are part of the respective subdetector electronics and are transmitted to the central trigger logic (CTL). The trigger signals divide into two complementary parts: Elements of the "θ-ϕ matrix" and direct input signals [28]. Trigger signals for the θ-ϕ matrix (TPM) are provided by 5 different subdetectors of OPAL, from the central detector (which provides the inputs for the track trigger), the TOF, the electromagnetic calorimeter, the hadron calorimeter and the muon chambers. The hadron trigger is currently not implemented. These five parts of the detector can be regarded as layers from the interaction point outward, each layer being sensitive to various types of particles. In order to establish geometric coincidences between the subdetectors, each of the 5 layers is divided into 7 bins in θ and 24 bins in ϕ, the exact boundaries of the bins being determined by the geometry of the contributing subdetectors. For the θ-bins, the first and last bin correspond to the endcap region and the 5 central bins to the barrel region. To form the actual bins of the θ-ϕ matrix, adjacent bins in θ and ϕ are combined to form 24 overlapping bins in ϕ and 6 bins in θ, with the bins in the barrel region overlapping. Thus each layer comprises up to 144 matrix elements, the exact number of bins depending on the respective subdetector geometry. The trigger generation by the θ-ϕ matrix is demonstrated in figure 4.4.

Besides the θ-ϕ matrix, up to 64 direct trigger signals can be processed by a so-called Single Input Module (SIM) in the central trigger logic. These direct signals are usually fired if the energy (or number of tracks found in case of the central detector) deposited in a subdetector or parts of it exceeds a predetermined threshold. Besides the detectors that contribute to the θ-ϕ matrix, the Forward

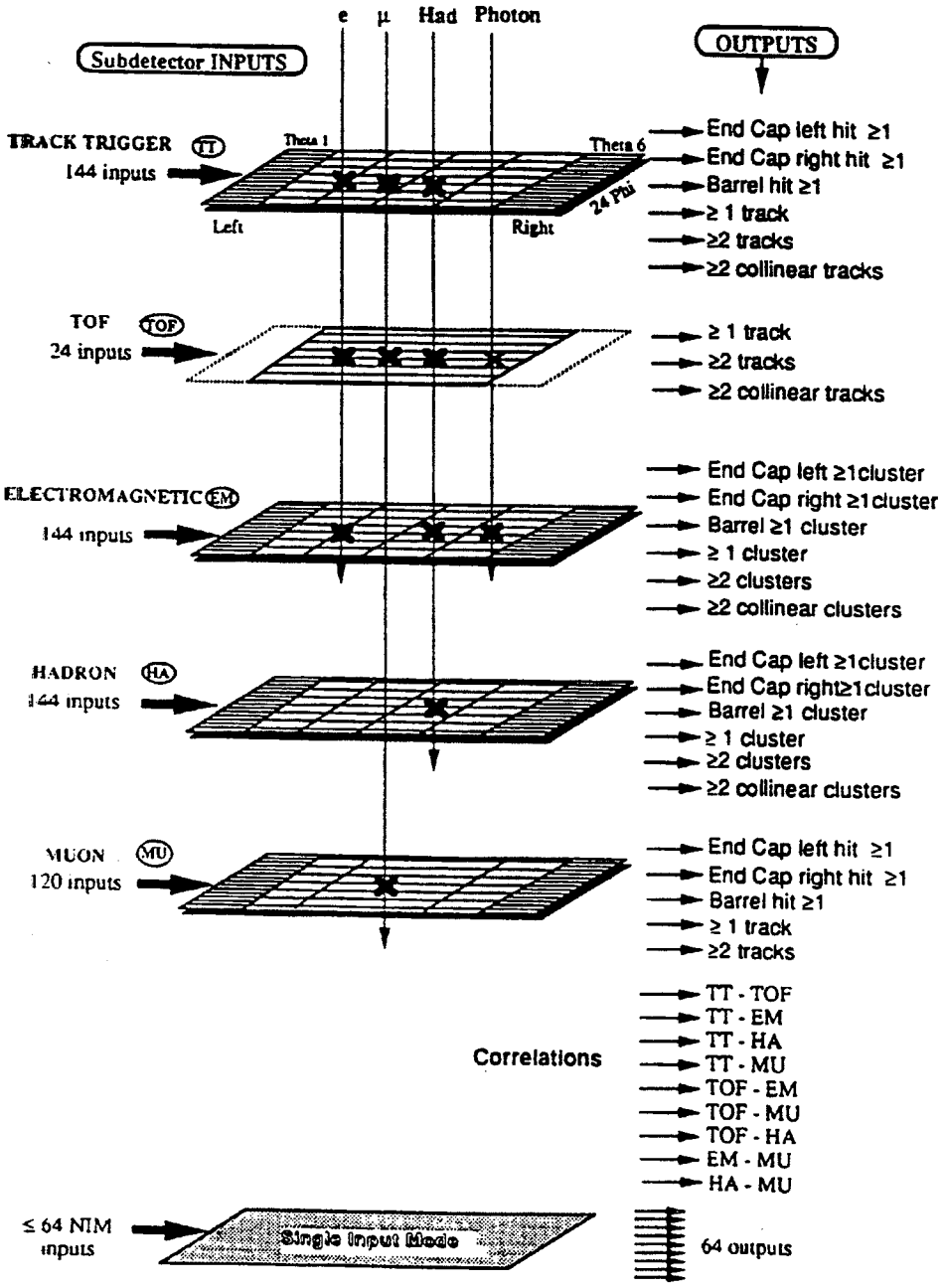

Figure 4.4: Overview of trigger generation by the θ-ϕ matrix.

Detector and the Silicon Tungsten Calorimeter provide trigger signals to the SIM. The latter triggers are crucial to trigger on small angle Bhabha events for the luminosity analysis and will be discussed in detail in chapter 5.

The pretrigger system aims at being 100% efficient for single particles. Its fundamental design is similar to that of the trigger and is discussed in detail elsewhere [29]. Corresponding to the trigger θ-ϕ matrix of the trigger is a ϕ-matrix of the pretrigger. The ϕ-matrix divides the detector into 12 bins in ϕ, each one running the whole length of the detector in θ. Depending on the subdetector, the bins are 40 deg to 60 deg wide, resulting in an overlap of 10 deg to 30 deg. Direct input signals from the subdetectors are provided to the PSIM of the central pretrigger logic, which corresponds to the SIM of the central trigger logic.

In the case of a negative pretrigger decision, the pretrigger logic sends a RESET signal to the Global Trigger Unit (GTU) in the CTL, which aborts the formation of the trigger signal. If the pretrigger logic sends a PRETRIGGER signal, the GTU will not send a RESET to the subdetectors – the next beam crossing is missed while the GTU awaits the trigger decision from the PAM. If the trigger decision is negative, the GTU will then send a RESET to the subdetectors. If the trigger decision is positive, the GTU sends a TRIGGER signal to the subdetectors. The GTU communicates over a dedicated trigger bus with a so-called local trigger unit (LTU) in each subdetector crate. The principal process of forming the trigger decision is shown in figure 4.5.

The GTU receives a synchronization signal from LEP, called BX signal, 800 ns before the actual beam crossing at the OPAL interaction point. If the GTU is ready for triggering, it broadcasts a RESET signal to the LTUs of the subdetectors

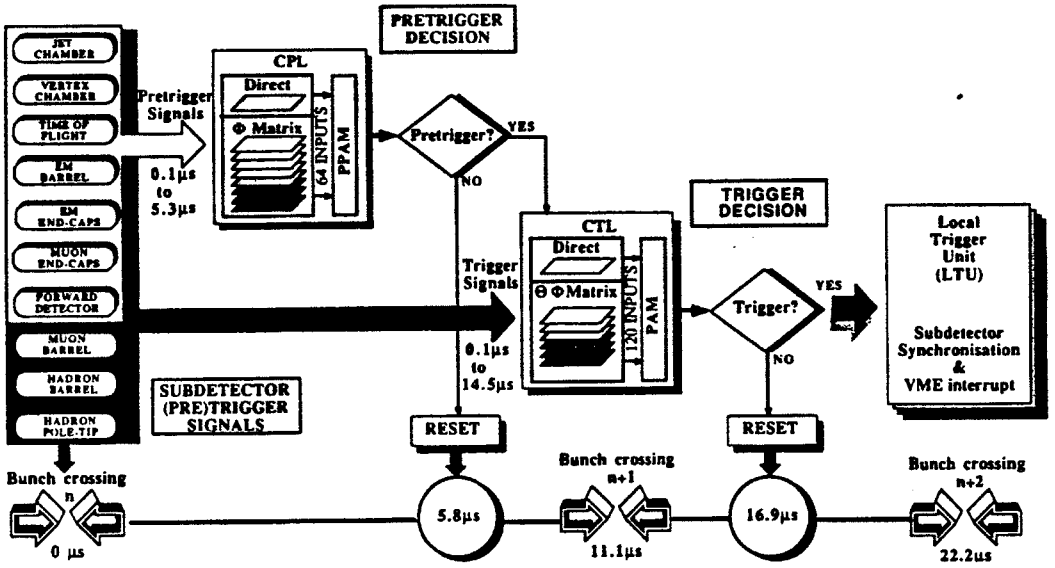

Figure 4.5: Overview of event triggering. The diagram does not include the SW detector, which also provides trigger and pretrigger signals.

4.5 μs before a BX signal. While the subdetectors are busy with the readout after receiving a TRIGGER signal from the GTU, they send a BUSY signal to the GTU, which will not send another RESET as long as any of the subdetectors asserts the BUSY line. When the last subdetector has cleared the BUSY line, the GTU is ready to send a RESET in synchronization with the next BX-signal and the trigger cycle will start over again.

4.2.2 The Subdetector Trigger Systems

An overview of the subdetectors providing trigger and pretrigger signals is shown in table 4.1. The track trigger (TT) combines signals from the 12 axial wires in each sector of CV and from 3 groups of 12 adjacent wires in each sector of CJ, forming 4 concentric rings at different radii. The CJ wire groups cover the regions $|\cos\theta| < 0.97$, $|\cos\theta| < 0.93$, and $|\cos\theta| < 0.82$. The segmentation

subdetector	pretrigger		trigger	
	ϕ-matrix	PSIM	θ-ϕ matrix	SIM
SI				
CV	•		provides TT-input	
CJ	•		provides TT-input	
CZ				
TT			TT	•
TB	•		TOF	•
PE				
EE	•		EM	•
HP				
ME	•		MU	•
FD		•		•
SW		•		•
PB				
EB	•	•	EM	•
HS				
HT				
MB			MU	•

Table 4.1: Overview of the subdetectors contributing to the the trigger and pretrigger systems as implemented during the 93 and 94 data taking. The subdetector abbreviations correspond to those introduced in section 4.1, the notation for the θ-ϕ matrix corresponds to the layers shown in figure 4.4.

in ϕ coincides with the 24 sectors of CJ. Charged tracks traversing the central detector with transverse momenta of interest are essentially straight lines in the $r - z$ plane, the axial magnetic field providing for only a small distortion. For a particle originating from the interaction point, a constant value of θ is expected along its path. With the r position of a wire being determined by the geometry of the detector, the ratio z/r for a measured z position of a track is done in CV and CJ using look up memory. The track trigger crates contain one module per ϕ bin for histogramming of the ratio $z/r \equiv \cot\theta$. Tracks that should be triggered on are characterized by sharp peaks of the z/r measurements. The measurements are combined to coincided with the standard 6×24 overlapping bins of the θ-ϕ matrix. An element of the θ-ϕ matrix fires if the number of entries in a bin of the corresponding histograms exceed a predetermined threshold.

Besides the inputs for the θ-ϕ matrix, a "multiplicity crate" in the track trigger electronics determines the track multiplicity as $\geq 1, \geq 2, \geq 3$ in both the full θ range and in the barrel region only as inputs for the SIM. The barrel region for the track trigger is defined as $|\cos\theta| < 0.81$, which is the region covered by the outermost jet chamber ring.

The time-of-flight trigger uses signals from the mean timers at the two ends of each scintillation counter and requires the coincidence of the two signals within 50 ns of each other and within 50 ns of the expected arrival time for a relativistic particle originating from the interaction point. The 160 signals thus obtained are used to produce the 24 overlapping ϕ bins for the θ-ϕ matrix. The signals are not segmented in θ and cover the barrel region, corresponding to θ bins 2 to 5 of the θ-ϕ matrix.

The time-of-flight trigger also produces direct signals, based on hit multiplic-

ities. These signals however have only been used in the early operation of OPAL or provide complementary signals for single photons.

The original trigger electronics of the electromagnetic calorimeter were too slow to be used for the pretrigger. Furthermore, low level noise in the readout electronics was enhanced by forming analog sums to obtain the signal for the original trigger, such that the thresholds could not be lowered far enough to trigger on single particles.

Therefore, the trigger electronics was upgraded with the installation of the pretrigger system [29]. For the electromagnetic calorimeter trigger, analog sums of 12 adjacent lead glass blocks are formed, which are digitized, noise suppressed and combined to form sums of 48 adjacent blocks. From the total of 200 of these units in EB and 24 in each endcap, the 144 signals for the θ-ϕ matrix are formed, and the total energies in the barrel region, and the left and right endcap are derived. The energy signals in the barrel and the left and right endcap are each discriminated by both high and low thresholds which are currently set to 5 GeV and 1.8 GeV in the barrel and 2.4 GeV and 1.6 GeV in each endcap. These thresholds are to be compared with a minimum ionizing particle (e.g. a muon) that deposits about 0.5 GeV in the lead glass calorimeter.

The muon detector provides 120 signals for the θ-ϕ matrix and 4 direct signals to the SIM in the central trigger logic. The 220 cells in MB provide one discriminated signal each, which go to four custom designed "layer" boards, one board for each layer of barrel chambers. The boards provide as output the 24 ϕ sector signals for each layer, where each sector covers θ bins 2 to 4 without segmentation in θ. The signal for each ϕ sector is formed from an OR of the signals from up

to 4 cells, where the chambers on the edge of each sector are included in the OR of the adjacent, in order to provide some overlap of the bins. A ϕ bin fires, if in at least 3 out of the 4 layers a signal was detected. As direct input signal, MB provided the logical OR of the 24 signals.

ME provides information from two layers of chambers with altogether 4 layers of strips in both x and y direction in each endcap. The trigger signals are provided by the analog sum of 64, 96, or 128 adjacent strips in both the x and y direction. From the 4 layers of x and y strips in each of the two endcaps, a total of 480 raw trigger signals are formed by discriminating the analog sums of the strips by a software adjustable threshold. Track elements are searched along 120 predefined x and y roads, loosely pointing to the vertex. A segment fires if in at least 2 of the 4 layers a hit was registered, with some additional requirements imposed in the case that only two layers fired. The 120 segments in the $x-y$ plane are correlated through look up memory to 96 bins of the θ-ϕ matrix, 24 ϕ bins for each of the 1st, 2nd, 5th, and 6th θ bin. As direct input signals, ME provides the logical OR from the 48 $\theta - \phi$ signals in each of the left and right endcaps. A third direct signal is fired if a hit in both the left and right endcap with a loose collinearity requirement is found.

The pretrigger signals for the ϕ-matrix are basically derived in a straight forward manner by reformatting the θ-ϕ matrix input signals from the subdetectors to comply with the segmentation and overlap requirements of the ϕ-matrix [29]. However, CV, CJ, and the lead glass calorimeter required some modifications in order to provide pretrigger signals. The CV pretrigger signals are derived from the number of axial wires with signals above a predetermined threshold. Each of the 36 sectors of CV can be individually programmed to fire if 4, 6, 8, or 10 out of

its 12 axial wires show a hit. The resulting 36 signals are combined to form the 12 overlapping bins of the ϕ-matrix. In a simular manner are the CJ ϕ-matrix-input signals based on the number of wires that fired within three groups of 12 adjacent wires per sector. These groups are identical to those which were used to derive the track trigger decision. The signals from adjacent groups in ϕ and from the groups within a sector are combined to form the input of the ϕ-matrix.

For the lead glass calorimeter, the signal sums from two units of 48 lead glass blocks each are added and compared to a threshold. The resulting 100 signals for EB and 12 signals for each endcap are combined to form the inputs for the ϕ-matrix. The logical OR of the 100 EB signals forms a stand alone single particle trigger with a nominal threshold of 320 MeV.

Under normal circumstances, the only subdetectors providing signals for the PSIM are FD, SW, and EB. However, any subdetector can force a pretrigger for test or calibration purposes.

4.2.3 The Central Trigger Logic

The final trigger decision is formed by the Pattern Match Module (PAM) in the central trigger logic by combining the signals from the SIM and TPM. The combination of those signals by logical ANDs and ORs is done flexibly in programmable array logic. Table 4.2 shows the main triggers for the Z^0 decay channels which are relevant for the lineshape analysis as they were implemented for the 1993 and 1994 data taking periods.

The PPAM is the part of the central pretrigger logic which, corresponding to the PAM of the central trigger logic, combines signals from the PPAM and the PSIM to form the pretrigger decision. Table 4.3 shows the pretriggers that were implemented for the 1993 and 1994 data taking periods.

Trigger condition	Sensitivity			
	$q\bar{q}$	e^+e^-	$\mu^+\mu^-$	$\tau^+\tau^-$
total acceptance:				
≥ 1 pair of collinear TT tracks	•	•	•	•
≥ 1 correlated θ-ϕ bin in TT and EM	•	•		•
≥ 1 correlated θ-ϕ bin in TT and MU			•	(•)
≥ 1 pair of collinear hits in EM	•	•		•
barrel only:				
≥ 1 correlated θ-ϕ bin in TOF and MU barrel			•	(•)
total energy in EB ≥ 5 GeV	•	•		•
total energy in EB ≥ 1.8 GeV and ≥ 1 TOF ϕ bin	•	•		•
total energy in EB ≥ 1.8 GeV and ≥ 1 TT track	•	•		•
endcap only:				
total energy in left or right EE ≥ 2.4 GeV	•	•		•
correlated hits in ME left and right side			•	(•)
ME left or right hit and ≥ 1 TT track			•	(•)

Table 4.2: Some of the main second level triggers and their sensitivities to various Z^0 decay channels. A •-sign indicates a high efficiency for the given Z^0 decay channel, a (•)-sign for $\tau^+\tau^-$ final states indicates that the trigger is only efficient if one or both of the taus decay to muons. The acronyms used in the table correspond to those from figure 4.4 and to the subdetector acronyms introduced in section 4.1. Luminosity triggers are not included.

Pretrigger condition	Acceptance	Efficiencies			
	$\lvert\cos\theta\rvert$	$q\bar{q}$	e^+e^-	$\mu^+\mu^-$	$\tau^+\tau^-$
≥ 1 CJ ϕ-bin	< 0.97	100%	100%	100%	100%
≥ 1 TB ϕ-bin	< 0.82	100%	100%	$\sim 100\%$	$\sim 100\%$
≥ 1 EE ϕ-bin	$0.81 - 0.98$	100%	100%	$\sim 70\%$	$\sim 100\%$
≥ 1 ME ϕ-bin	$\sim 0.67 - \sim 0.98$	$\sim 10\%$	0%	$\sim 90\%$	$\sim 30\%$
≥ 2 CV ϕ-bin	< 0.97	100%	100%	100%	$\sim 100\%$
≥ 2 EB ϕ-bin	< 0.82	100%	100%	$\sim 100\%$	$\sim 100\%$
≥ 320 MeV in EB	< 0.82	100%	100%	$\sim 100\%$	$\sim 100\%$

Table 4.3: Acceptances and efficiencies for different Z^0 decay processes for the stand alone pretriggers. For EE and ME, one ϕ-bin is required in either the left or the right side, and the two ϕ bins for the CV and EB pretrigger are required to be non-adjacent. All pretrigger efficiencies are calculated within the respective acceptances. Luminosity triggers are not included.

Besides the physics triggers, random beam crossing triggers (BXRs) are generated by the pretrigger at a rate of 4 Hz. In the second level trigger, the coincidence with another random beam crossing trigger, BXRSA, is formed such that the resulting signal forms a "stand-alone random trigger" which fires at a rate of 0.1 Hz. Furthermore, coincidences between the BXR signal and loose trigger signals from various subdetectors are formed. The coincidences with the BXR signal are used by the subdetectors for calibration purposes, efficiency studies and to detect potential problems with the essential physics triggers.

4.3 The OPAL Online System

The primary functions of the OPAL online system comprise the data acquisition (DAQ) and data selection in the individual subdetectors, as well as the collecting, processing and storing of the merged raw data [26]. In order to be flexible and able to adjust to the specific requirements of the subdetectors, the data acquisition systems for the subdetectors are implemented locally. They are capable of operating both in autonomous mode and as part of common data taking mode. Most of the subdetector data acquisition systems are implemented in VME standard. The DAQ systems for each subdetector are quite different and are discussed in [26]. Each subdetector has at least one "local system crate" (LSC) which contains a standard hardware and software interface to the "event builder" VME crate (EVB). Furthermore, each subdetector has at least one local trigger unit (LTU) which usually (but not necessarily) is located in the LSC.

If an event was flagged by the trigger for readout, the EVB merges the input from the individual subdetectors and sends them to the filter which acts as a third-level software trigger. In the last step of the online event processing, the data from

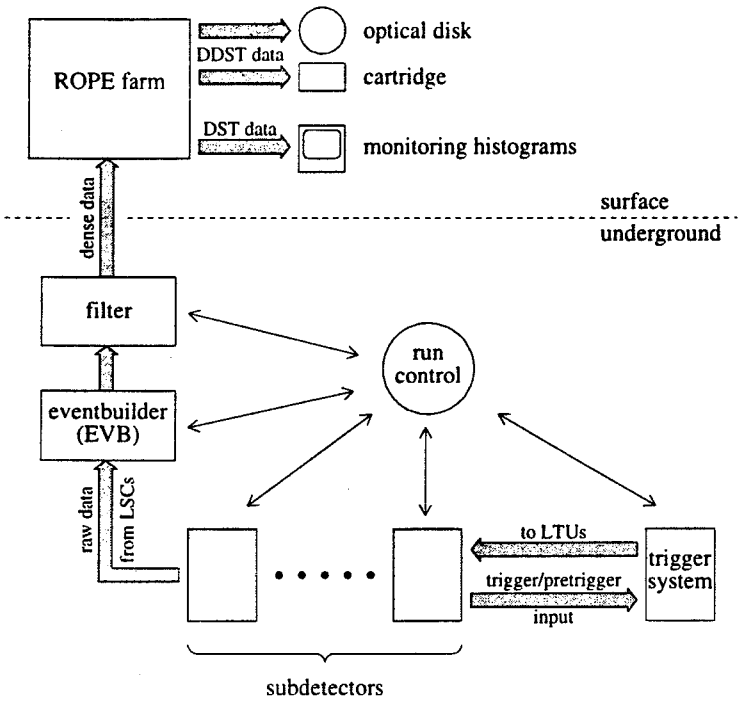

Figure 4.6: Overview of the OPAL data acquisition system.

the filter are processed on a computer farm called the "ROPE-farm". ROPE, the program for Reconstruction of OPAL Events, reconstructs actual physical quantities that are needed for the physics analysis from the raw data recorded by the subdetectors. Finally, the data are stored and monitoring histograms using the reconstructed physics quantities are created. An overview of the OPAL DAQ system is shown in figure 4.6. In the following subsections, each of the steps in the acquisition, processing and storing of the data will be discussed in more detail.

4.3.1 Eventbuilder and Filter

Once an event has been triggered and the data in the subdetectors have been digitized, the results are transmitted from the LSCs to the event builder (EVB) through VIC links. There the data are merged and written to the filter event buffer disk. The filter serves as a third level software trigger and is implemented on an

Apollo workstation. Depending on the background and trigger conditions, the filter discards roughly a third of the events, such as beam-gas events and cosmic rays, as uninteresting. Furthermore, the filter compresses the raw data from the subdetectors into the dense data format [27]. This format reduces storage and bandwidth requirements for the data by almost a factor of 5, at the cost of a 14% increase in CPU time for the unpacking prior to event reconstruction. The dense data are stored in files of approximately 20 MByte size on the filter disk, which are copied to the front end buffer disk of the ROPE farm. The filter also provides detailed monitoring of data quality and of the detector status, and sends events to the online event display.

4.3.2 The ROPE Farm

The OPAL event reconstruction program ROPE will be discussed in section 4.4. An online version of ROPE processes data on the ROPE farm, consisting of at least 9 HP workstations. Roughly 30 minutes after ROPE has copied a dense data file from the filter disk, the reconstructed data are available, which for historical reasons is called DST (Data Summary Tape) data. The DST data contains the first reconstruction of the physical quantities, such as track momenta and energy, and is used to produce online monitoring histograms. The combined dense data and DST data (DDST data) are written to optical disk and at the same time backed up on cartridge. When both operations are completed successfully, the corresponding file is deleted from the filter disk.

4.3.3 Run Control

During physics data taking, an e^+e^- expert and a data acquisition expert (DAQ expert) are present in the OPAL control room. The e^+e^- expert communicates with the LEP control room and responds to potential problems with the beams, such as excessive background. The e^+e^- expert also monitors the quality of the data using the DST and online histograms. The DAQ expert, through a run control program running on a local workstation, performs all operations on the subdetectors, as well as on the trigger system and event builder, which are normally required during a physics run. These operations include rebooting of subdetectors in case of crashes and adding or removing subdetectors from a global run. It is the responsibility of the DAQ expert to start and end physics or monitor runs depending on the status of the LEP machine.

4.3.4 Slow Control System

The OPAL slow control system [30] operates independently of the data aquisition system and monitors a wide range of parameters, such gas flow, high voltage, power supply status, and temperature for the individual subdetectors. The system is continuously operational and is implemented on seven dedicated VME stations in different electronics huts, and a supervising station in the control room. The system provides warning and alarm messages, or takes automatic corrective action, in case parameters are found to be outside a predefined range. Since various safety related parameters are monitored, the local operation of each station was made as independent as possible of external services like power supply or the computer network. At the OPAL experimental area, at least one SLIMOS (Shift Leader In Matters Of Safety) is constantly present to respond to potential safety hazards.

4.4 Software and Offline Analysis

The OPAL offline software environment is coded in FORTRAN using the CERN utility programs PATCHY [31] as a tool for source code maintenance and ZEBRA [32] as memory management system. ZEBRA supports dynamic memory management in the FORTRAN environment and is used in OPAL to create and manipulate data structures in both the online and offline code.

The framework used for the reconstruction of events from the dense data recorded by the experiment and their analysis is a collection of modules called ROPE (Reconstruction of OPAL Events). The Monte Carlo program used by OPAL to simulate the OPAL detector is called GOPAL [33]. It creates data from the simulated detector response to a given physics process in the same format as the dense data produced by the detector. The reconstruction and analysis of Monte Carlo events is then performed in the same manner as for data.

The data reconstruction in the ROPE environment and the GOPAL program will be discussed in the following subsections.

4.4.1 Event Reconstruction

ROPE has two main functions: First, the creation of the DST data from the dense data which is recorded by the OPAL detector, and second to provide a framework for the analysis of the DST data. ROPE contains processors for each subdetector, processors for merging of clusters and association of tracks between different subdetectors, as well as utility routines and libraries for physics analysis.

The creation of DST data from the dense data is done in consecutive passes, the first pass being the DST data created online on the ROPE farm as described in section 4.3.2. This first pass is mainly used for offline quality control and

calibration. In intervals of several month, a new pass of DST data with updated calibrations and tuning is produced. Typically, for the data of a given year, 4 to 5 passes are produced. ROPE accesses the OPAL data base system OPCAL [34], to store and retrieve calibration data for the experiment.

ROPE also provides the necessary tools and auxiliary programs to access the DST data and perform the physics analysis. Besides the physics quantities, the DST data contains general information about the status of the subdetectors for each event as well as book keeping entries and information about the LEP beam, such as the beam energy and position of the beam spot. The status of each subdetector and the status of its trigger electronics are originally determined during data taking and recorded as a number from 0 and 3. Status 0 indicates that the detector status is unknown, while status 3 indicates that the subdetector is fully operational without apparent problems. The detector status is set to 1 if the subdetector was not switched on and set to 2 if the detector was operating with some problems such as low voltage or hardware problems. The detector performance is checked offline and if necessary, the detector status bits are modified for the next pass of DST data.

4.4.2 Monte Carlo

GOPAL, the OPAL Monte Carlo program, simulates the OPAL detector using the CERN GEANT3 [35] package. GEANT provides tools for the user to define the shape and material of the detector and to simulate the tracking of particles through the detector, including the necessary physics processes such as scattering, decay and interactions. GOPAL is divided into a set of routines for each subdetector. The code for each subdetector defines its shape and structure using the GEANT routines, stores the resulting hit parameters for a particle traversing the detector

and then simulates the response of the detector readout and digitization system to these hits. The results are stored in ZEBRA structures identical to those for the data from the detector, and can be processed and analyzed using ROPE in the same fashion as the data. As input, GEANT uses four-vectors from Monte Carlo generators such as JETSET [36] for multihadronic decays of the Z^0, or KoralZ [37] for leptonic reactions $Z^0 \rightarrow \ell^+\ell^-$. GOPAL also provides an interface to user-defined generators, generating the four-vectors during the execution of GOPAL rather than reading them from a file.

Chapter 5

The Silicon Tungsten Luminometer

5.1 Motivation

The Silicon Tungsten Luminometer (SW) was installed in the OPAL detector at the beginning of 1993 with the aim of reducing the systematic error of the luminosity measurement to a level of less than 1/1000. This precision is necessary to make efficient use of the $\sim 5 \times 10^6$ Z^0 decays that were recorded by OPAL during LEP I operation for lineshape measurements [38]. Since the partial decay width of the Z^0 into multihadronic final states is about a factor of 21 bigger than for each leptonic final state, the precision of the luminosity measurement is however much more crucial for the lineshape measurements involving multihadronic final states.

The most crucial parameter for the luminosity measurement is the determination of the *inner* edge of the Bhabha acceptance; due to the $1/\theta^3$ dependence of the differential Bhabha cross section is a precise knowledge of the outer edge much less critical. For a fiducial acceptance ranging from 30 mrad to 55 mrad, a systematic uncertainty of 10 μrad on the inner acceptance angle results in a luminosity systematic uncertainty of about 1/1000. At a distance of 2.5 m from the OPAL interaction point, this systematic uncertainty expressed in the radial dimen-

sion is 25 μm. Determining the radial coordinate of showering electrons within the luminometer with a systematic error of only a few microns requires both a high geometric precision of the luminometer and an excellent capability for the reconstruction of particle trajectories. To meet these requirements, a calorimetric luminometer was built, based on dense tungsten absorber plates interspaced with silicon pads to sample the ionization created by the electromagnetic showers of incident electrons. A calorimeter is preferable to a tracking device for reconstructing the trajectories of Bhabha events, since it is much less sensitive to effects from preshowering in upstream material and final state radiation. The longitudinal and lateral spreads of electron showers depend on the material, giving the mechanism of shower development fundamental importance for the detector design. Tungsten was chosen as absorber because it allows a compact design of the calorimeter, complying with the rather stringent constraints on the size of the luminometer due to the existing OPAL hardware. Silicon allows a very precise definition of the detector geometry, where the size of the readout pads must be chosen to match the lateral shower spread in the luminometer. The characteristics of electromagnetic shower development and their influence on the detector design will be discussed in more detail in the next section.

The SW detector was installed close enough to the beam line to have a fiducial cross section of about 80 nb, compared to the multihadronic cross section of about 30 nb at the Z^0 peak, providing enough statistics for a precision luminosity measurement and for the analysis of the systematic errors of the luminometer.

5.2 Electromagnetic Shower Development

Electrons with an energy of $\sim$ 45 GeV passing through matter loose basically all their energy by radiation. The critical energy E_c, at which the radiation loss equals the ionization loss is approximately given by $E_c = 550$ MeV$/Z$ [40], where Z is the atomic number of the absorber. For tungsten with $Z = 74$, one gets $E_c \approx 7.5$ MeV, corresponding to 0.02% of the energy of the incident electron. The longitudinal and transverse development of electromagnetic showers in a medium sets the scale for the required size of a calorimetric luminometer. The scale for the longitudinal size of electromagnetic showers is the radiation length (X_0). An estimate of a radiation length for a material with atomic number Z and atomic weight A is obtained from the approximation [40]

$$X_0 \simeq 180 \frac{A}{Z^2} \frac{\mathrm{g}}{\mathrm{cm}^2}$$

with an accuracy of better than 20% for materials with $13 \leq Z \leq 92$. For tungsten, the radiation length is about 3.5 mm. A calorimeter using lead with $X_0 = 5.6$ mm as absorber would require 1.6 times the depth of a tungsten based calorimeter in order to achieve the same longitudinal containment of electromagnetic showers.

The mean longitudinal profile of the energy deposited by a showering electron is reasonably well described by a "differential gamma function" [40], [41]

$$\frac{dE}{dt} = E_0 b \frac{(bt)^{a-1} e^{-bt}}{\Gamma(a)} , \tag{5.1}$$

where t is the depth of the absorber in units of X_0, a and b are energy dependent parameters of the material and $\Gamma(a)$ normalizes the total shower energy to E_0. This distribution shows a sharp rise to a maximum value at

$$t_{max} = (a-1)/b \approx \ln(\frac{E}{E_c} - 0.5) \tag{5.2}$$

and for $t > t_{max}$ a slow exponential decay. From equation 5.2 we find that an electron with an initial energy of 45 GeV has its maximum energy loss after about $8X_0$. Using equations 5.1, 5.2, and the approximation $b \approx 0.5$ [41], we estimate that 98% of the energy of a 45 GeV showering electron is contained within a calorimeter depth of about 22 X_0, or 80 mm of Tungsten.

Electromagnetic showers spread out laterally, mainly due to multiple scattering of electrons with an energy that is below the critical energy, but high enough for the electrons to travel far away from the incident particle direction [40]. The size of the spread is determined by the angular deflection of such electrons per radiation length, and in all materials, the spread is of the order of a Molière unit,

$$R_m = E_s \frac{X_0}{E_c} \approx 7 \frac{A}{Z} \frac{\mathrm{g}}{\mathrm{cm}^2} ,$$

where the scale energy E_s is given by $E_s = \sqrt{4\pi/\alpha}\, m_e c^2 \approx 21$ MeV, m_e being the electron rest mass. A Molière unit for tungsten is about 9 mm [42]. The actual lateral energy distribution of a shower depends strongly on the depth of a layer within the detector: with increasing depth, the lateral shower spread becomes wider and less peaky.

The radial position of a shower centroid is determined by charge division between Silicon readout pads from the first few layers of the detector, so that the lateral shower spread determines the required size of the readout pads. The $r - \phi$ geometry of the detector results in the pads having curved boundaries and their sizes increasing with increasing radial distance from the beam line. These properties in turn result in biases of the reconstructed radial shower position, which will be discussed in chapter 6. The smaller the lateral shower spread is in a medium, the smaller are these biases. In this respect tungsten again is preferable to lead, since the value of R_m is about 1.6 times as big for lead than it is for tungsten.

A good energy resolution of the luminometer is important to separate the mainly machine dependent background from the Bhabha events. The machine dependent background was already mentioned in section 3.2 and its effect on the luminosity analysis will be discussed in detail in chapter 6. Roughly, the energy resolution in a silicon tungsten sandwich calorimeter is expected to behave like $\sigma(E)/E = 18\%\sqrt{t/E}$ for a fully contained shower, where t is the number of radiation lengths of passive material interspaced between two sampling layers of silicon [39]. Longitudinal and lateral confinement of the electron shower is important for an optimal energy resolution [40]. With a relatively small lateral shower spread of electron showers in tungsten, fiducial acceptance cuts roughly ~ 1 cm away from the edges of the geometric acceptance effectively avoid lateral energy leakage.

5.3 Design and Construction

The Silicon Tungsten Luminometer consists of two identical, cylindrical calorimeters, mounted around the beam pipe at about ± 2.5 m from the interaction point [44]. Each of the two calorimeters is composed of two interlocking C-shaped modules, as shown in figure 5.1. Each module consists of 19 half-layers, which by convention will be numbered from 0 to 18, where the zero-th layer is the layer closest to the interaction point. Each half-layer comprises a tungsten half disk, glued to the inner radius of a 2 mm thick aluminum support plate.

Upstream of the tungsten, on the aluminum support plate of each half-layer, are mounted eight silicon detector wedges and a semi circular printed circuit board providing control functions, called the mother-board. The 18th layer, in absence of any downstream silicon detectors, contains no tungsten plate but rather a con-

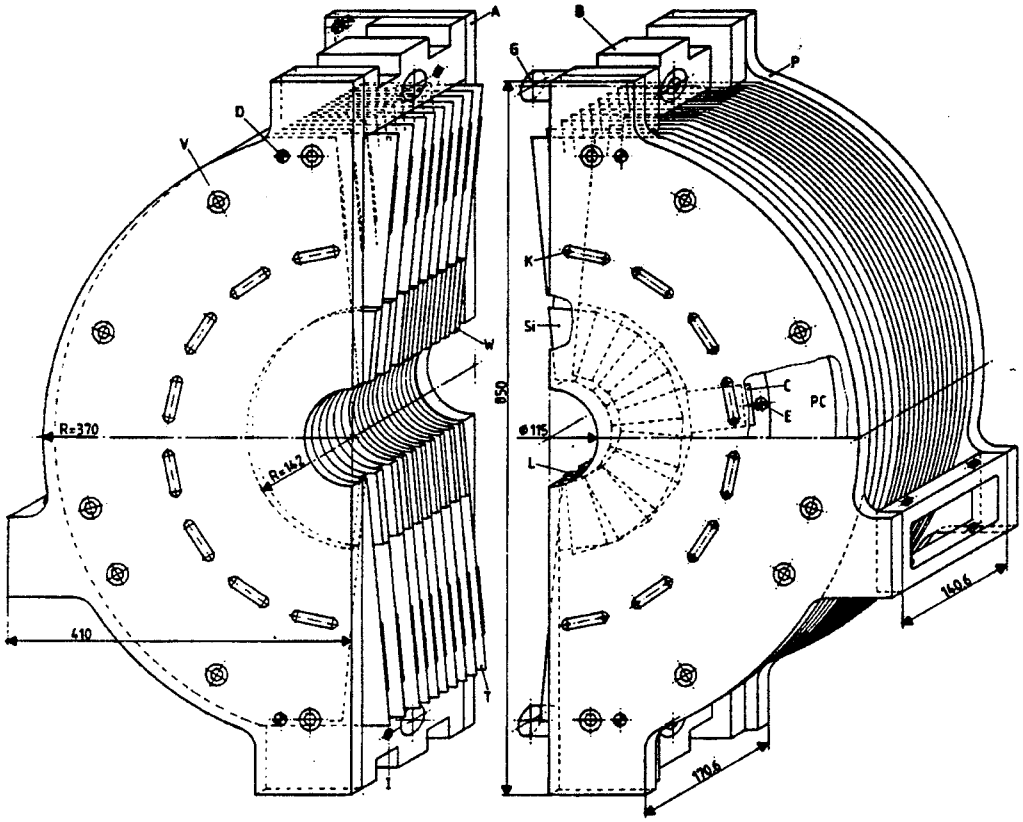

Figure 5.1: Isometeric view of one Silicon Tungsten Calorimeter, consisting of two interlocking C-shaped modules. Indicated are the ceramics (C) and the silicon wedges (Si) glued to them, the mother-board (PC), the Tungsten plates (W), the precision dowels (D) and the cooling pipes (K). All dimensions are in mm.

tinuous aluminum plate. A half-layer is shown schematically in figure 5.2. In total, the 18 layers of tungsten represent 22 radiation lengths of material. The first 14 tungsten plates are each one radiation length thick, the remaining 4 plates two radiation length.

Altogether, the two calorimeters comprise 608 silicon detectors, each a (310.8 ± 1.5) μm thick low conductivity n^+ silicon wafer in the shape of a trapezoid [44]. The front side of the silicon is implanted with a p^+ diode pattern shown in figure 5.3. The wafer is thus divided into two 11.25° wide azimuthal columns and 32 radial rows of 2.5 mm width, forming 64 pads. The sensitive region of the silicon detectors is 80 mm in the radial direction with its inner edge mounted 62 mm from the beam line. During data taking, a bias voltage of 80 V is applied to the silicon detectors.

The precise fabrication of the pads is crucial to avoid systematic errors in the reconstruction of the r coordinate of a showering electron, and therefore is essential for the luminosity measurement. Using photolithographic techniques, the diode patterns are implanted on the silicon with a precision at the micron level and the electromagnetic field in the 50 μm gap between adjacent pads defines a sharp division between the sensitive areas. Each pad implant is covered by a layer of aluminum, giving a visible reference point for the detector metrology. During the metrology it was found that the edges of the aluminization show some systematic deviations from their nominal value at the 5 μm level.

A simplified diagram of a detector assembly is shown in figure 5.4. The implanted side of the silicon wafer is glued to the wedge-shaped part of a ceramic substrate which holds the electronics necessary to measure, store, and multiplex the charges from each of the 64 pads onto one output line per detector. An aluminum support plate, which serves to mount the detector assembly on the half-layer, is

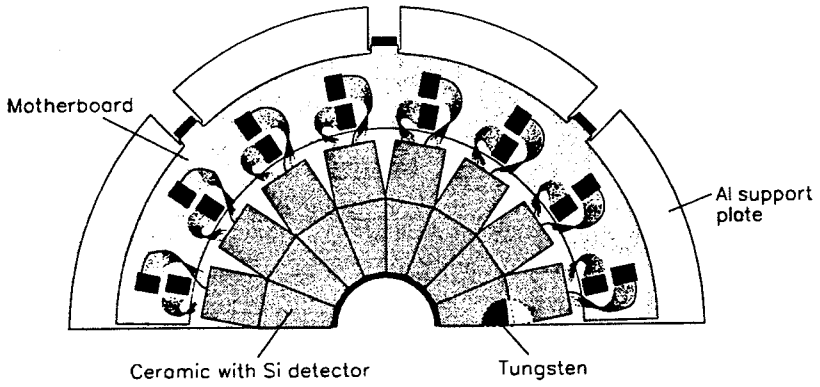

Figure 5.2: Schematic drawing of a half-layer.

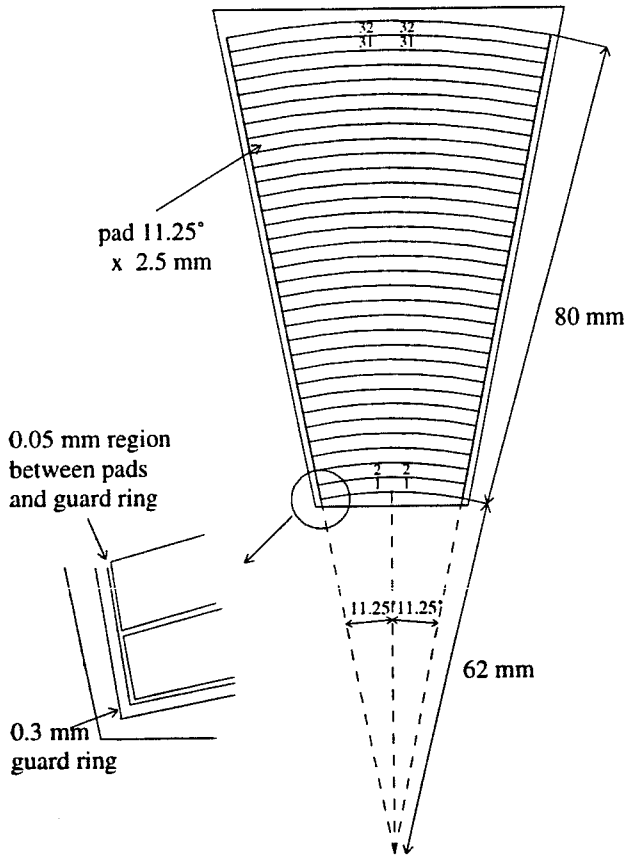

Figure 5.3: The geometry of the diode implanted side of the silicon wafer.

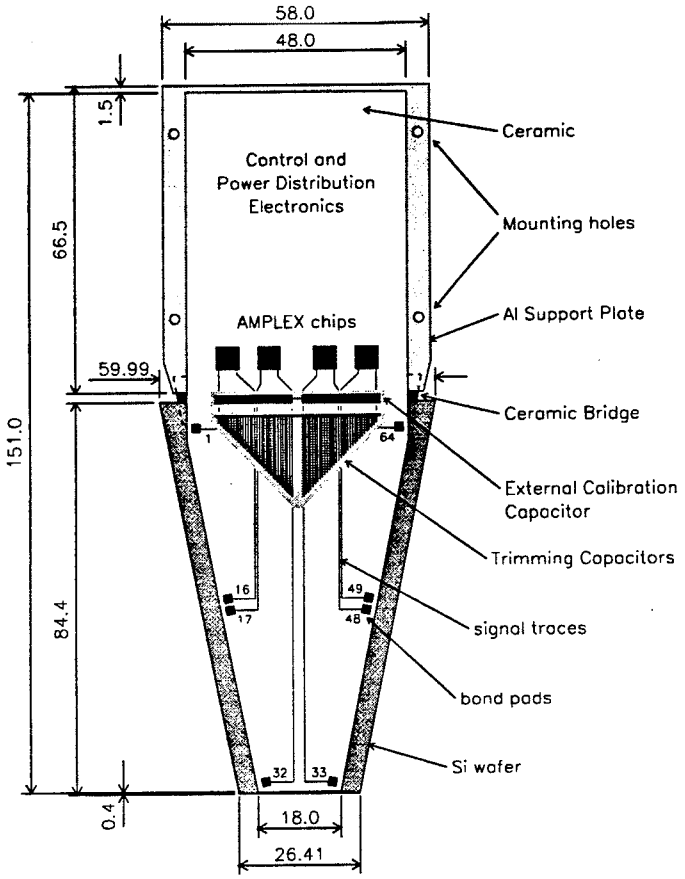

Figure 5.4: A simplified diagram of a silicon-ceramics detector assembly. Of the 64 bond pads and signal traces, only the first and last for each AMPLEX chip are shown. All dimensions are in mm.

glued to the rectangular part of the ceramic. Each pad of the silicon wafer is bonded to bond pads on the ceramic from where signal traces carry the deposited charge to one of the 4 AMPLEX chips per detector. An integrated trimming capacitor array ensures that each AMPLEX input sees a uniform total capacitance despite the changing area of the annular Silicon pads. The OPAL AMPLEX chip is a slightly upgraded version of the ALEPH SiCal AMPLEX chip [47]. Each OPAL AMPLEX chip reads 16 input channels and individually amplifies, shapes, and holds the charge from each channel. The single output buffer amplifier of

the AMPLEX averages the signals of the channels selected by the 16 bits of an output shift register. Each channel contains a TRACK/HOLD switch in front of the output buffer, which is closed in tracking mode, allowing signals to be passed to the buffer, while it is opened when the stored charge in the buffer should be held while awaiting readout.

Even though SW does not trigger on muons in the OPAL environment, the ability of the electronics to be sensitive to minimum ionizing particles is essential for test beam studies of systematic biases of the shower reconstruction for electrons. Therefore, the electronics must have a wide enough dynamic range to detect muons, which deposit a few MeV per layer, while being far away from saturation for 45 GeV electrons, which deposit about 5 Gev in the layer with the maximum energy deposition. The calorimeter electronics meet these requirements with a dynamic range of over 5000 and a noise level equivalent to 1/10th of a minimum ionizing particle per channel [44].

Within a half-layer, the ceramic part of the detectors are alternately glued to a high (1.6 mm) and low (0.8 mm) aluminum support, allowing the silicon wedges to overlap in order to avoid energy leakage through gaps between detectors. In order to further reduce the effect of potential detector gaps, the half-layers in alternating layers are rotated by 11.25° with respect to each other, thereby aligning the edge of a silicon wafer with the centers of the wafer in the layers above and below.

The mother-board has two connectors for each detector to distribute the control commands and operating power and to receive the multiplexed analog voltage from the detector. The mother-board of each half-layer is connected through three connectors to custom made multiwire cables, each roughly 7 m long, which join 20m standard twisted cables at a patchpanel attached to the outside of the OPAL

magnetic return yoke endcap. These cables convey the signals to racks in the electronics hut. One cable transmits the bias voltage for the silicon, the second the digital control signals, and the third contains 8 cables carrying the analog readout from the 8 detectors per half-layer.

Removing the heat generated by the electronics on the ceramics is essential to keeping thermal expansion under control. For this purpose, 16 water cooling pipes penetrate the detector at a radius of 220 mm, as close as possible to the AMPLEX chips which constitute the major heat source. During operation, 3 liters per minute of 16 °C cooling water keep the average temperature of the calorimeter at a constant value. The temperature is monitored with one thermistor per half-layer. Thermistors in even layers are placed on the aluminum support plate close to the AMPLEX chips, while thermistors in odd layers are mounted on the aluminum plate well outside the ring of cooling pipes. Therefore, the temperatures of the hottest and coldest spots in each half-layer are monitored, yielding a measurement for the average temperature of the calorimeter during operation of (21.5 ± 0.2) °C, with a 2 °C maximum temperature gradient across a half-layer [45].

At the front and rear, 15 mm thick aluminum face plates ensure the mechanical integrity of the luminometer stacks. The rear plate can be seen in figure 5.1. At two points per module, 15 mm precision dowels run through the whole depth of the calorimeter, keeping the aluminum support plates of each layer in place. The mounting of the silicon ceramic hybrids in a half-layer and the stacking of the half-layers were done on two designated, precise jig tables, referred to as the "mounting table" and the "stacking table". Both tables were equipped with a set of two microscopes having ocular graticules for a position measurement of reference points on the Silicon detectors during assembly with an accuracy of 2 μm.

The two modules forming one calorimeter slide together on two massive brass dowels, allowing the detector to be mounted around the beam pipe. The calorimeters are mounted to the jet-chamber pressure bell which expands and contracts as a function of its temperature and pressure, requiring the use of position monitors to track the distance between the two calorimeters during operation. The mechanical stability of the detector and the knowledge of its absolute coordinates within OPAL contribute directly to the overall luminosity errors. This will be discussed in section 6.4.

5.4 The SW Data Aquisition System

The SW data aquisition system is implemented in VME architecture and is located in 5 racks inside one of the OPAL electronics huts. An overview of the system is given in figure 5.5. The SW hardware comprises the local system crate, the trigger electronics, all necessary power supplies, fanouts for the control signals and the analog signals from the detector, the hardward and software to digitize and process the raw data and a dedicated VME crate as well as electronics for monitoring the performance of the detector [48]. Two basically identical VME crates house the front end electronics to power and control the two calorimeters, the LTU and custom designed digitizers, and a sequencer to readout and digitize the data from the detectors. These two front end crates, called SWFE1 and SWFE2 for the right and left calorimeter, respectively, are connected via VIC links to the SW local system crate (SWLSC), which in turn is connected to the event builder and transfers the digitized and zero-suppressed data to be merged with the data from the remaining subdetectors.

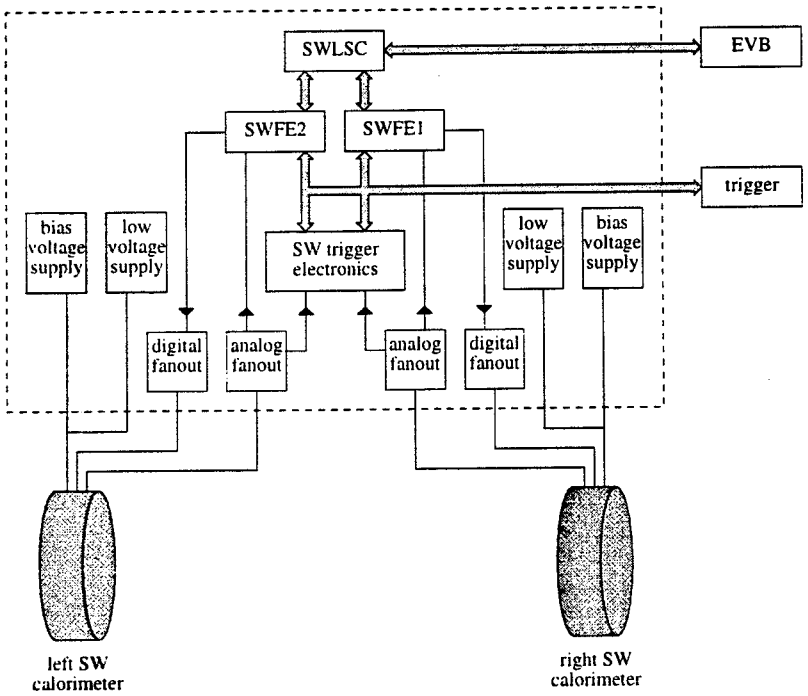

Figure 5.5: Overview of the Silicon Tungsten data acquisition system.

The analog signals from the detector are routed to a passive fanout module in the electronics hut, which splits the signals and sends them to the SW trigger and the digitizers in the front end crates. Each digitizer can handle the analog input from two layers. Therefore, 10 digitizers are needed for the 19 layers of each side, with one digitizer input remaining unconnected. Each digitizer contains one 14-bit sampling ADC, so that the $2 \times 16 \times 64 = 2048$ pads from two layers (or 1024 pads from one layer for the case of the 10th digitizer) are processed sequentially. The detector provides pairs of differential inputs which the digitizers convert to digital signals which takes less than 2 μs per channel [49]. The digitized results are mapped to the VME backplane bus where they are available for the CPU of the crate for further processing.

The energy from each pad is digitized in steps of about 1 MeV, such that a 14-bit digitization is sensitive to minimum ionizing particles while the maximum recordable energy of more than 15 GeV is well above the maximum deposited energy per layer. The resulting data size of one 14-bit word from each of the 38912 readout channels proved too large to be completely stored for each event without exceeding the OPAL budget for storage media. Therefore, a zero-suppression scheme was used to retain the information from enough pads to fully reconstruct electromagnetic showers, while discarding information from pads without significant energy deposition.

The digitizers also attempt to keep each channel at a predetermined value of 1024 digitizer counts when there is no signal present. This is called the pedestal value. For each channel, the digitizer stores a digital value which is transferred to an analog voltage by a digital-to-analog converter (DAC). This analog value is subtracted from the signal in each channel before digitization. The appropriate digital inputs for the DACs are calculated during normal operation of the detector

by looking at random beam crossing events which show no significant activity in the SW calorimeter. If the average of a number of such "pedestal events" yields an ADC output significantly different from the target value of 1024 for a given channel, the input for the DAC is modified accordingly.

Each of the two front end crates contains a sequencer which provides the digitization cycle for the digitizers and the control signals for multiplexing of the signals stored in the AMPLEX chips. During normal operation, the sequencer provides the TRACK and HOLD signal for the AMPLEX chips in synchronization with the BX and RESET signals provided by the LTU. Upon receipt of a trigger signal from the LTU, the sequencer initiates the readout of an event. One AMPLEX Control Unit (ACU) per front end crate provides an interface between the VME crate and the mother-boards in the detector and sets appropriate registers to route the signals to the proper half-layer. A control fanout is located in a separate crate and houses 19 modules per side, each module routing the digital control lines to the two mother-boards of a layer. One control unit per fanout is connected over twisted flat cables to the sequencer and the ACU in the corresponding front end crate.

Details of the operation and the data readout with the Silicon Tungsten detector are given in appendix A.

5.5 The SW Trigger

An obvious requirement for a luminosity measurement with a precision of the order 1/1000 is a trigger efficiency of much better than 99.9% for Bhabha events. Trigger redundancy is essential to monitor the trigger performance and get quantitative estimates of the trigger efficiency. With no other OPAL subdetector pro-

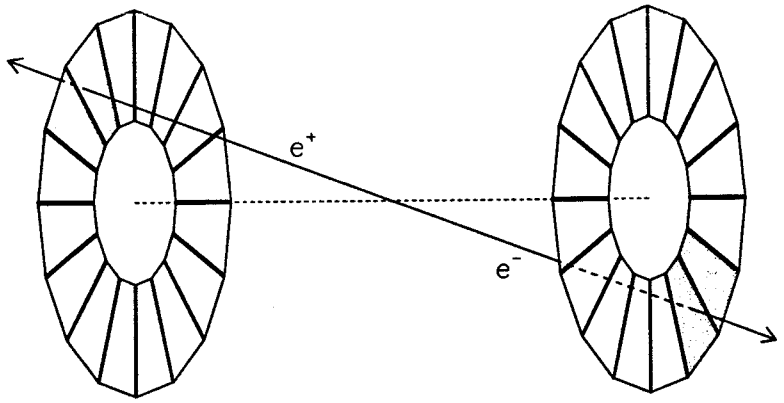

Figure 5.6: The principal SW trigger, SWSEG, fires if back-to-back segments in opposite sides are above a threshold. In this figure, the segments in two corresponding layers in the left and right calorimeter are shown. The actual threshold is applied on towers of segments from 18 layers on each side as described in the text.

viding independent triggers over the major part of the SW acceptance, SW relies on the deposited electron energies themselves for triggering. Trigger redundancy can therefore only be obtained by independently triggering on different parts of the detector. The SW trigger decision is based on an analog sum of pad energies from layers 1 to 18. For the trigger readout, all the channels for a silicon detector are averaged, yielding a signal corresponding to the energy sum being sampled by the 64 pads of a detector. After receiving the analog inputs from the detector through the fanout, the SW trigger electronics forms various triggers by creating analog sums, applying appropriate thresholds and forming coincidences. The SW trigger decisions are then communicated to the GTU in the central trigger unit which forms the global trigger decision as described in section 4.2.

The main process used for the luminosity measurement is t-channel Bhabha scattering, as described in section 2.4. These events show a strong back-to-back event kinematics. Initial state radiation results in a portion of the events being acollinear, whereas the energy from most final state photon radiation is detected

in the SW calorimeter. Consequently, a high shower energy is observed for all Bhabha events except for those radiating highly energetic photons which are not within the SW acceptance. The principal SW trigger therefore is the SWSEG trigger, which fires if the signal in diametrically opposite towers of segments in the left and right calorimeter show a signal consistent with a showering particle. A segment is defined as two adjacent silicon wedges in a layer. By summing the analog signals, 16 half-towers of such segments are individually formed for even and odd layers in each side. 16 full towers are formed by summing the signals from corresponding odd and even half-towers. The staggering of the silicon wedges by 11.25 deg in alternate layers results in an identical staggering of the odd and even half-towers with respect to each other. Consequently, for the full towers, a central region of $3 \times 11.25°$ in azimuth is sensitive in all 18 layers, while the two 11.25° regions at the respective sides are instrumented with silicon pads from the 9 odd or even layers only. The half-towers are discriminated at a nominal threshold of 8 GeV, the full towers at a nominal threshold of 16 GeV. For both detector sides, the logical ORs are formed from corresponding odd half-towers, even half-towers and full towers, yielding 16 signals per side. If such signals are detected back-to-back in the left and right side of the calorimeter, the SWSEG trigger fires. Using sums of two adjacent silicon wedges assures that for a shower with its center near the edge of a wedge, its full energy is used to form the trigger decision. Back-to-back half-towers contributing to the SWSEG trigger accept Bhabha events with an acoplanarity of about ± 22.5 deg, nearly independent of the shower position within a wedge. Back-to-back full towers have an acoplanarity acceptance ranging from about ± 17 deg to ± 28 deg, depending on the position of the shower centers within the towers [50].

A second principal trigger with essentially 100% efficiency provides redundancy

for the SWSEG trigger. This trigger is formed by the coincidence SWHIOR AND SWSUM. The SWSUM trigger fires if the total deposited energy is above a low threshold of about 5 GeV in both calorimeters, and the SWHIOR trigger fires if the energy in either detector is above a high threshold of about 35 GeV. The combined trigger, called SWHILO then fires if the energy in one calorimeter is above the low threshold and the energy in the other calorimeter above the high threshold.

Besides the two main triggers, other triggers are formed by coincidences with the forward detector, the electromagnetic calorimeter or elements of the trigger θ-ϕ matrix. These triggers are mainly intended for cross-checks or to catch extremely radiative events for special studies.

In addition to generating these logical trigger outputs, the trigger system also digitizes each of the basic half-tower sums as well as the total trigger energy seen in the detector. This is done for every beam crossing, independent of the global trigger decision. This digitized trigger information is stored in a circular buffer with a depth of 40 bunch crossings, which is itself read out on each triggered event. The information from the current, seventh and eighth previous crossing is written to the data stream.

An important tool for background studies is the so-called accidental or delayed coincidence trigger SWSEGA. For this trigger, coincidences between the segments in one side are formed with the segments of the other side from 8 bunch crossings earlier. The SWSEGA trigger is formed by combining segments from "out-of-time" hits in the same manner as the SWSEG trigger is formed for "in-time" hits in the left and right side of the calorimeter. To keep the accidental trigger rate within reasonable limits, a prescale factor of 1/16 was applied during 93 and a prescale factor of 1/4 during the 94 data taking. The prescaled accidental rate

was about 0.4 Hz in 1994.

The pretrigger signal provided by SW is the combination SWSEG OR SWSEGA OR SWSUM.

Chapter 6

Luminosity

6.1 The Analysis Strategy

To determine the beam luminosity from the data recorded by the SW calorimeter, events have to counted inside a well defined fiducial acceptance, corresponding to a Bhabha cross section which is to be calculated using the BHLUMI [52] small angle Bhabha Monte Carlo program. Using the theoretically calculated Bhabha cross section σ_{ee}^{theo}, corresponding to the fiducial acceptance of Bhabha events in the SW detector, the integrated luminosity can be calculated according to the relation

$$\mathcal{L}_{int} = \frac{1}{\sigma_{ee}^{theo} \cdot f_{\rm sim}} \sum_{i=1}^{N_{ee}} \frac{1}{f_{\rm LEP}^{i}} , \tag{6.1}$$

where it is summed over the Bhabha events passing the fiducial acceptance cuts of the SW detector, up to the total number of N_{ee} events. The correction factor has been split into two parts: The factor $f_{\rm sim}$ accounts for differences between the cross section as calculated by Monte Carlo (MC) and the effective experimental cross section for a set of standard conditions. The factor $f_{\rm LEP}$ accounts for divergences of the experimental conditions from the standard conditions assumed in the Monte Carlo during the LEP operation and is not constant throughout the year

and

$$\frac{\Delta\mathcal{L}}{\mathcal{L}} \approx -\frac{\Delta R_{out}}{110\ \mu\mathrm{m}} \cdot 10^{-3}\ .$$

The dependence of the luminosity on the reconstructed half-distance between the two calorimeters can be readily calculated as

$$\frac{\Delta\mathcal{L}}{\mathcal{L}} \approx -\frac{\Delta z}{1.23\ \mathrm{mm}} \cdot 10^{-3}$$

and is much less crucial for the luminosity measurement.

No attempt was made to use Monte Carlo simulations for the modeling of the detector response to showering particles. Instead, four-vectors were created with the program BHLUMI covering the acceptance of the SW calorimeter. These four-vectors were then convoluted with a detailed parametrization of the SW detector response [45]. This procedure will be discussed in section 6.4.5.

6.4.1 Measurement of the Detector Acceptance

A limiting factor on the precision of the luminosity measurement is the knowledge of the detector acceptance within the OPAL coordinate system. It was therefore essential to accurately survey the detector geometry prior to installation and to keep the detector mechanically stable during operation. It will now be discussed how the position of the inner radius of the geometric detector acceptance was determined. First the position of the inner acceptance under standard metrology conditions will be derived and then it will be estimated how this measurement will get distorted under OPAL operating conditions. Finally, the results of the metrology will be presented, which was performed when the luminometer was removed from the OPAL detector during the LEP shutdowns between 1993 and 1994, and between 1994 and 1995.

The stacking of the two C-shaped modules constituting each of the two Silicon Tungsten Calorimeters on the stacking table was described in chapter 5.3. The two microscopes used for the survey of the silicon sensitive region were mounted on a metrology arm which could be freely rotated at any fixed height around a steel pillar in the bore of the calorimeter. The inner and outer microscope were located at radii close to the inner and outer edge of the nominal acceptance of the Silicon wafers at 62 mm and 142 mm, respectively. The outer microscope was used for the metrology and its radial position was continuously monitored using a calibration plate which was equipped with 30 reference marks at a radius of 142 mm, equally spaced in ϕ over a half-circle. This calibration plate was positioned on top of the stacked half-layers for the calibration measurements. The plate itself was independently calibrated by the CERN metrology laboratory and by using a laser interferometer [57]. The resulting measurement for the radius of the microscope was

$$R_{micr} = 142.028 \pm 0.001 \pm 0.003 \text{ mm} ,$$

where the first error is statistical and the second one systematic. This microscope was then used to measure two reference points on each Si wafer, after a given half-layer had been assembled and stacked on top of the previously assembled half-layers on the stacking table. The two reference points were chosen in close proximity to the left and right outer edge of the Silicon geometric acceptance, with a well known offset with respect to the exact position of the geometric acceptance. Altogether, 32 measurements were obtained per layer, to which three fits with MINUIT [58] were performed: One fit each to the two half-circles formed by the 16 points of each half-layer separately, and one fit to the circle formed by all 32 measurements. If the χ^2 of the fit to either half-layer was not consistent with

unity, assuming a 2 μm error on each of the 16 measurements, the mechanical alignment of the silicon detectors in the half-layer was redone.

The radius of the fit to a complete layer is not equal to the radii obtained from the half-layers due to small misalignments on the ~ 20 μm level between the two halves of a calorimeter. These misalignments result in a systematic displacement of the measured positions of the reference points on the silicon wafer with respect to the radius of the circle fitted to the 32 measurements. The radius obtained from the fit to the complete layer is the parameter entering the calculation of the final acceptance. Since the luminosity measurement is done over the full range of ϕ, biases due to the displacement of the two detector halves with respect to each other cancel almost completely and were found to be negligible [57]. Each of the 19 results for the fits to the layers was corrected for offsets with respect to the outer radius of the Silicon acceptance and the nominal length of the silicon wedge (80 mm) was subtracted to obtain results for the inner edge of the acceptance. Figure 6.5 shows the distribution of those results from the 19 layers in each calorimeter. The distributions for the two calorimeters are approximately gaussian and centered around the same radius. The mean of a gaussian fit to the combined results from the two calorimeters was used as the estimated mean radius of the inner acceptance. The result for the inner radius of the Silicon acceptance under standard metrology conditions was then determined as

$$R_{std} = 62.0039 \pm 0.0006 \pm 0.0049 \text{ mm} ,$$

where the first error is statistical and the second systematic. The statistical error was derived from the R.M.S. of the gaussian fit, taking into account that only about half of the layers are used for the measurement of the radial coordinate. The systematic error is dominated by the 3.2 μm error on the radius of the microscope

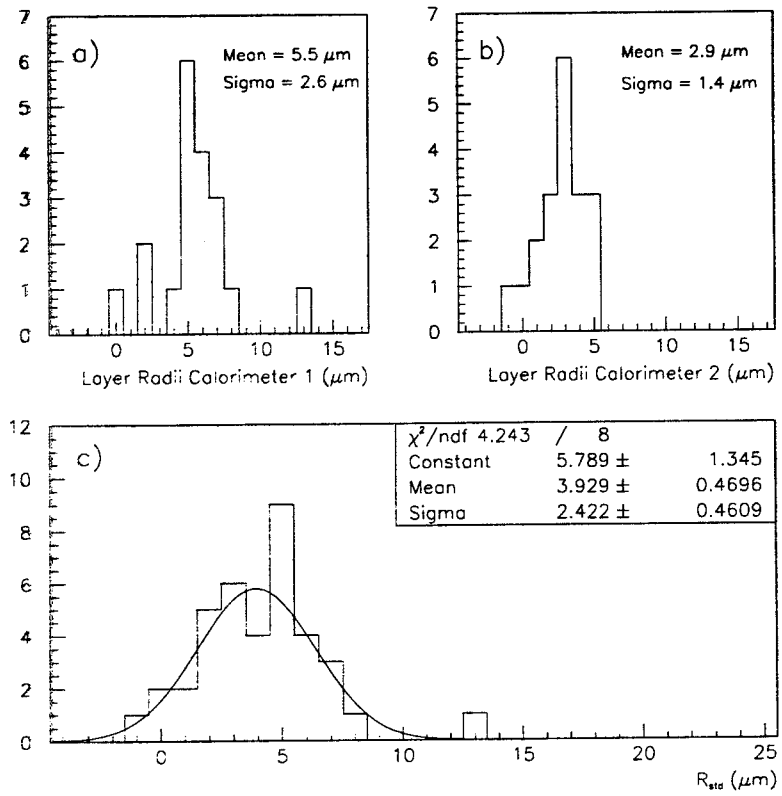

Figure 6.5: **Fit** radii of the fit to the full circle for each layer in (a) the right calorimeter, **(b)** the left calorimeter and (c) for both calorimeters together. Radii given on the x axis are in μm above the nominal inner radius of 62 mm of the calorimeter **sensitive** region. The gaussian fit shown in plot (c) is used to derive the inner **radius** of both calorimeters under standard metrology conditions (R_{std}).

R_{micr}. Remaining contributions are due to temperature gradients in the aluminum support plate of each half-layer when operating the AMPLEX chips, the opening and closing of the calorimeter which was necessary whenever a new layer was stacked, and a 5 μm offset that had to be subtracted from the measured position of each Silicon detector with a low aluminum support plate [57]. The additional correction for the low detectors was necessary since for those the actual edge of the sensitive silicon region was hidden under the high detectors, such that the position of the edge of the aluminization was measured (cf. section 5.3).

In a second set of metrology measurements, the conditions under which the calorimeter would be operated in the OPAL environment were simulated. Holes were drilled into the front aluminium face plate of the calorimeter, allowing the measurement of the positions of the reference points of the zero-th layer (which was stacked last) after the calorimeters had been completely assembled. Furthermore, reference marks were attached to the inner tungsten radius, allowing the measurement of the relative distance of the two calorimeter halves in each layer. To simulate operating conditions, each calorimeter was flipped from the horizontal into the vertical position, and the AMPLEX chips and cooling system were operated under OPAL conditions (cf. chapter 5.3).

Measurements were compared on the stacking table, before and after mounting the aluminum face plate, before and after flipping each detector into the vertical position and then in the vertical position, with and without operating the AMPLEX chips and cooling system. As mentioned in chapter 5.3, the average temperature of the detector was kept constant during operation to 0.2 °C. The temperature dependence of the half-ring diameters was experimentally determined as 2.5 ± 0.4 μm/°C at the nominal inner radius of 62 mm. While this means that effects due to changes of the *average* temperature are quite small, the temperature

gradients of about 2 °C within the support plates reduce the average radius of the geometric acceptance by a few μm. The measurement of the combined effects of the temperature and mechanical distortions yielded a change of -5 ± 1 μm for the radius of the right calorimeter, and -11 ± 1 μm for the radius of the left calorimeter with respect to the result under standard metrology conditions. In average, this is a change of -8 ± 3 μm, which has been added to the result for the inner radius under standard metrology conditions, R_{std}, to yield the inner acceptance under operating conditions of

$$R_{in} = 61.996 \pm 0.005 \text{ mm}$$

where the errors on R_{std} and on the correction to R_{std} have been added in quadrature.

After the 1993 data taking period, the SW detector was removed from OPAL during the LEP shutdown and the detector was partially disassembled for repair work. The top five layers of the right calorimeter and the top ten layers of the left calorimeter were unstacked and restacked, and the metrology measurements for those layers were repeated during both the unstacking and the restacking procedure. Neither the comparison of the fits to the half circles for the half layers, nor the fits to the complete circle showed any significant deviation from the original measurements.

During the 1994-1995 LEP shutdown, the top 14 layers in each calorimeter were disassembled to modify the Silicon detectors for the changes in the LEP operation for the 1995 running. Again, the metrology was repeated for those layers during the unstacking and restacking. The average inner radius was found to have increased by 3 μm. This was attributed to a 1 °C increase in the average detector temperature during that year, resulting from the gradual obstruction of

a filter in in the cooling system [57]. The radius for the inner acceptance therefore was determined at 61.995 ± 0.005 mm for 1993 and 61.998 ± 0.005 mm for 1994. The error of 5 μm on the radial coordinate contributes an error of $2 \cdot 10^{-4}$ to the luminosity measurement.

6.4.2 z - Reconstruction

The measurement of the z position of a given layer in the SW Calorimeter can be divided into two parts: First, the determination of the half-distance between the rear surfaces of the two calorimeters under operating conditions of LEP and second, the determination of the internal positions of the individual Silicon layers with respect to the rear end of the calorimeters. Given a half-distance of about 2.5 m between the rear ends of the two calorimeters, the first measurement is more crucial. The half-distance between the two calorimeter rear surfaces has to be measured with an accuracy of about a millimeter for a luminosity measurement on the 0.1% level. In the remainder of this subsection, first the internal metrology of the SW calorimeter will be discussed, then the determination of the length of the beam pipe, and finally the tracking of the distance between the SW calorimeter and the beam pipe during LEP operation.

The internal geometry of the silicon wedges for layers 0 to 13 was established in the 1994-1995 LEP shutdown when the two SW calorimeters were removed from OPAL, and layers 0 to 13 were unstacked and restacked [55]. The relative z position of the four corners of each silicon wedge within a given layer was determined by focussing the microscopes on the stacking table to the four edges of the wedge. Two comparators, resting on an aluminum lip glued to the inner edge of the tungsten plate in each half-layer, indicated the vertical position of the focal planes.

To establish the absolute distance between the focal plane of a given microscope position and the aluminum lip, the microscope was removed from the stacking table and focussed on a gauge block which was large enough for both comparators to rest on it at the same time. Finally, a stand with a mounted comparator with known zero-position was used to determine the distance of the lip in each half layer with respect to the rear end of the calorimeter. Combining these measurements, the distance of the middle of the 310 μm thick Silicon wedge in layer 7 with respect to the rear end of the calorimeter was determined as 105.941 ± 0.022 mm for the left calorimeter and 105.913 ± 0.022 mm for the right one.

Before the Beryllium beam pipe was installed in OPAL in 1993, two independent measurements of its length were performed [55]. The two measurements differed by only $45 \pm 85\mu$m after extrapolating the results to the average OPAL temperature of 22.5 °C. As the final result, a half-length of the beam pipe of 2369.929 mm with an error of 31 μm was obtained.

The pressure bell on which the SW calorimeters are mounted expands by about 10 mm after it has been pressurized to its operating pressure of 4 bar, which for safety reasons is done only after access to the vicinity of the central detector parts has been closed. During OPAL operation, it expands and contracts as a function of pressure and temperature. To cope with this continuous movement, a set of optical grating position sensors were mounted on pneumatically driven chariots to measure the distance between the beam pipe flange and the rear face of the nearby SW calorimeter. At each calorimeter, two sensors measured the position of the rear face of the SW detector at a radius of 65 mm at a common detector diameter, ensuring that the average measurement is insensitive to any potential inclination of the calorimeter with respect to the $x-y$ plane of the OPAL reference frame. A measurement was performed under computer control every three hours and from

calibrating the position sensors at the beginning and end of each year of data taking, a 30 μm calibration error was attributed to all position monitor measurements.

Combining all measurements, the half-distance between the two reference layers (7th layer of Silicon in the left and right calorimeter) was determined to be approximately 2640 mm, where the exact distance changes during LEP operation and is known at any point in time with a systematic error of 43 μm for both 1993 and 1994 operation. The main components of this error are the contribution of 22 μm from the measurement of the position of the reference layer with respect to the rear end of the calorimeter, and the error of 31 μm from the determination of the half length of the beam pipe. Uncertainties in the temperature during OPAL operation and during the measurement of the length of the beam pipe of 0.5 °C in both cases contribute two additional errors of 15 μm each. The total error contributes less than $0.4 \cdot 10^{-4}$ to the error of the luminosity measurement and can be neglected compared to the error of determining the inner edge of the detector acceptance that was discussed in the previous subsection. Errors due to the expansion and contraction of the pressure bell during data taking will be discussed in section 6.4.4 where errors due to potential detector instabilities will be estimated.

6.4.3 Radial Coordinate Reconstruction

In section 6.3.2 the measurement of the systematic shift of the reconstructed radial coordinate within a layer with respect to the true radial position of a pad boundary of

$$\text{Pad Boundary Bias} = 8 \pm 6 \ \mu\text{m}$$

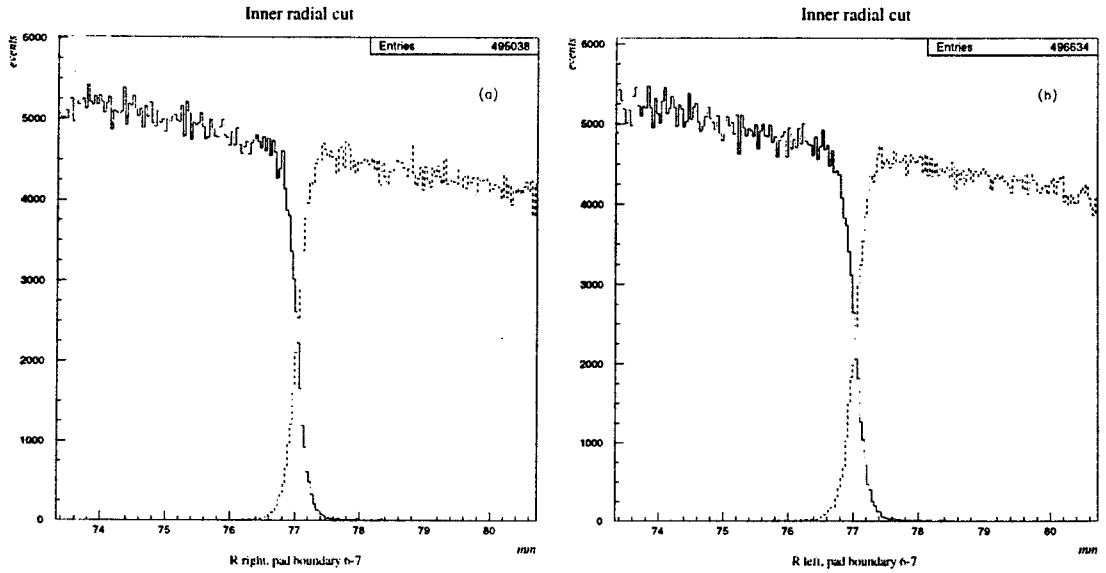

Figure 6.6: The image of a typical pad boundary. The solid histograms show the distribution of the reconstructed radial coordinate R for Bhabha events for which the largest pad signal in layer 7 is in pad 6 or at a smaller radius. The dashed histograms show the same distribution, but for events whose largest pad signal is in pad 7 or at a larger radius. Plot (a) is for the right calorimeter, while plot (b) is for the left one.

in the testbeam was explained. It remains to be shown that the reconstruction method for the radial coordinate R does not introduce any further biases. In order to ensure that the reconstructed coordinate R is bias free, the concept of "anchoring" the coordinate to the pad boundaries was developed. The R distribution for events with the maximum pad signal inside and outside of a particular pad boundary was plotted for a given layer. Figure 6.6 shows a typical plot for the left and right calorimeter. Then the *reconstructed* position R_n^l of the pad boundary between pad rows n and $n-1$ in a given layer l was defined as the R position for which the number of events with $R \geq R_n^l$ equalled the number of events in layer l for which the maximum energy was found in a pad i with $i \geq n$. Biases in the reconstructed pad boundary position R_n^l could then directly be measured as the difference between R_n^l and the geometric position of the pad boundary which

is known from the metrology of the detector. The reconstructed coordinate was then corrected for the offset from the true pad boundary and for the pad boundary bias determined in the testbeam. The reconstructed coordinate was anchored in this manner using the boundary between pad rows 6 and 7 in the 7th layer. This boundary lies within 20 μm of the acceptance cut at $R = 7.7$ cm. To confirm that the offset of the reconstructed coordinate obtained for this anchor point does not change as a function of R, the large number of pad rows and layers in the detector provided the opportunity to check the consistency of the method. The boundaries between two given pad rows, when projected along a particle trajectory into the reference plane at $7X_0$, are displaced by about 200 μm for consecutive layers. The images of the radial pad boundaries between pad rows 5 and 6, 6 and 7, and 7 and 8 were calculated as described above for layers 3 to 14. These images were now determined in terms of the reconstructed coordinate, corrected for the offsets derived at the anchoring point between pads 6 and 7 in layer 7. The residual differences between these pad boundary images and the true positions of the corresponding pad boundaries vary on the level of about $10 \sim 20$ μm within a layer and the precision of the luminosity measurement is determined by how well these changes are simulated by the Monte Carlo. In the Monte Carlo, the acceptance cuts are applied on the radial coordinate obtained from the produced four-vectors, which corresponds to a perfectly reconstructed coordinate. For the radial position of the image of a given anchor point, the difference of the number of Monte Carlo events and data events was calculated, where the difference is defined to be zero by the anchoring procedure at $R = 7.7$ cm. Using the $1/\theta^2$ dependence of the Bhabha cross section, this difference was compared to the difference in acceptance predicted by the residual difference of the pad boundary image and the true pad boundary position for the anchor points in different layers and at different pad

boundaries as described above. The agreement was found to be within 2 μm on the coordinate, or less than 10^{-4} on the luminosity [56].

Therefore, effects of biases in the coordinate were found to be well estimated by the error of 6 μm on the pad boundary bias from the testbeam. The resulting error on the luminosity measurement is $2.5 \cdot 10^{-4}$ for the inner acceptance and $0.6 \cdot 10^{-4}$ for the outer acceptance, resulting in a combined error of $2.6 \cdot 10^{-4}$ on the luminosity measurement due to the radial coordinate bias.

6.4.4 Stability of the Detector

The stability of the radial detector acceptance throughout the year is mainly affected by temperature variations. These effects were already taken into account in section 6.4.1. The reconstructed coordinate could suffer from small changes in the relative gain of neighboring pads or from failures of individual pads. These effects however should be small as long as they are confined to individual layers since the radial coordinate is reconstructed from several layers. Potential instabilities of the coordinate reconstruction were examined by dividing the recorded data into subsets; then for each subset the images of the pad boundaries were determined in several layers and compared to the average over the complete data taking period [51]. The results were consistent with a coordinate reconstruction which is not subject to systematical changes, where the test was sensitive to shifts in the coordinate of about 1 μm. This corresponds to an error on the luminosity of about $0.5 \cdot 10^{-4}$ which will be assigned as the error due to instabilities of the radial coordinate reconstruction.

The changes of the half distance between the two detectors due to temperature or pressure changes in the pressure bell were tracked throughout the operation of OPAL. The R.M.S. of the distribution of these changes is about 50 μm which

corresponds to an error on the luminosity of about $2 \cdot 10^{-5}$. This effect is small enough so that it is assigned as an additional error and no corrections on the z position of the detector are applied for the luminosity calculation. A total error of $0.5 \cdot 10^{-4}$ is therefore applied as a result of mechanical instabilities (as far as they are not taken into account in the measurement of the detector acceptance) and instabilities in the coordinate reconstruction.

6.4.5 MC Simulation of the Detector Response

The theoretical cross sections corresponding to the luminosities $\mathcal{L}_a$ and $\mathcal{L}_{rl}$ were calculated by applying the acceptance cuts described in section 6.2 to the four-vectors of the simulated Bhabha events, corresponding to the idealized situation of pointlike clusters, centered with respect to the SW detectors and with perfect coordinate and energy reconstruction. The resolutions of the values for the energy, radial and azimuthal coordinate as reconstructed by the SW luminometer were then parametrized and the Monte Carlo four-vectors were smeared accordingly. The change of acceptance for the smeared Monte Carlo with respect to the "perfect" MC sample was used to derive correction factors on the theoretical cross sections, with systematic errors reflecting the agreement of the smeared Monte Carlo with the data.

Differences in the energy scale between data and MC affect the luminosity according to the relation

$$\frac{\Delta\mathcal{L}}{\mathcal{L}} \approx 0.015 \cdot \frac{\Delta E}{E}$$

for a range of no more than a few percent in $\Delta E/E$. The numerical coefficient was derived directly from data by varying the energy scale and observing the resulting change of accepted Bhabha events. In the Monte Carlo, the energy distribution of

as indicated by the superscript i in equation 6.1. Correction factors—unlike for the determination of the tau cross section—are applied on the cross section rather than the selected number of events. Clearly, the precision of the theoretical cross section calculation has to match the precision of the experimental measurements in order to take full advantage of the accuracy of the experimental results.

In the most simple case of acceptance cuts, one merely needs to establish an inner and outer boundary for the acceptance and decide for each event, if it is inside or outside that acceptance. For a luminosity measurement on a level of 0.1%, a full kinematic reconstruction of Bhabha events is important for background rejection and to properly treat radiative events [53]. To define appropriate acceptance cuts for the SW luminometer, the energy E and the radial and azimuthal coordinates, R and ϕ, of an event have to be reconstructed from the recorded data.

A particle originating from the interaction point travels about 5 mm in radial direction between its point of entry and exit in the sensitive region of the calorimeter. In order to take full advantage of the position information from multiple layers provided by the detector, it is desirable to reconstruct the radial coordinate using information from more than one layer. Therefore, acceptance cuts effectively have to be applied on the polar angle θ. However, the θ coordinate is composed of the radial position of the shower centroid in a given layer and the z position of that layer within the OPAL coordinate system. The measurements of these two quantities were performed completely independently and it was found to be highly impractical to rely on the knowledge of the z position of a given layer within the OPAL reference frame in order to determine the actual radial position of the cut in that layer. Therefore, all geometric acceptance cuts were defined in terms of R rather than θ. The radial coordinate R used for the acceptance cuts is defined in a reference plane at the position of the silicon layers 7 X_0 deep into the two

calorimeter halves. The individual radial shower positions obtained in the other layers are projected along the particle trajectory onto that reference plane in order to calculate the R coordinate for an event. For this procedure, only the relative positions of the layers with respect to the reference plane have to be known, while the knowledge of the SW detector within the OPAL frame is not required.

In the following section, the acceptance cuts used for the luminosity measurement will be discussed. In section 6.3, the reconstruction of the quantities needed to define the acceptance cuts (R, ϕ, and E) from the DST data will be demonstrated. The z position of each layer within the OPAL coordinate system is determined from metrological measurements which will be discussed in section 6.4. In that section, the overall error of the luminosity will be derived, resulting from the mechanical stability of the SW calorimeter, the precision of the event reconstruction and effects due to the LEP beam conditions. Furthermore it will be discussed how the absolute scale of the luminosity is determined using BHLUMI MC, and which additional errors result from that procedure.

6.2 Event selection cuts

It is convenient to divide the acceptance cuts into "isolation" and "definition" cuts [45]. The first class of cuts isolates a background free sample, consisting of events with kinematics that ensures a 100% efficiency of the SWSEG trigger, and which are far enough away from the detector edges to ensure proper event reconstruction.

The isolation cuts are imposed on the radial coordinate and the azimuthal coordinate of the highest energetic cluster in the left and right calorimeter, and on the total reconstructed energy E in the left and right calorimeter halves:

- Safety Zone Cut Right (Left): $67 \text{ mm} < R_r(R_l) < 137 \text{ mm}$
- Minimum Energy Cut Right (Left): $E_r(E_l) > 0.5 \cdot E_{beam}$
- Average Energy Cut: $\frac{E_r+E_l}{2} > 0.75 \cdot E_{beam}$
- Acoplanarity Cut: $||\phi_r - \phi_l| - \pi| < 200 \text{ mrad}$
- Acollinearity Cut: $|R_r - R_l| < 25 \text{ mm}.$

The subscripts r and l denote the parameters of the left and right calorimeter, respectively, and E_{beam} stands for the LEP beam energy. The definition cuts are based solely on the radial coordinates R_r and R_l and define three event samples:

- SWITA: $77 \text{ mm} < R_a \equiv \frac{R_r+R_l}{2} < 127 \text{ mm}$
- SWITR: $77 \text{ mm} < R_r < 127 \text{ mm}$
- SWITL: $77 \text{ mm} < R_l < 127 \text{ mm}$.

The "IT" in the "SWITx" acronyms indicates that the selection cuts are applied on parameters derived for in-time coincidences, meaning coincidences between particles in the left and right calorimeter which were recorded for the same bunch crossings. Out-of-time coincidences are formed between a cluster in one calorimeter half for the present beam crossing and a cluster in the other calorimeter from eight beam crossings earlier for events from the sample triggered by the SWSEGA trigger described in section 5.5. The event samples defined in that manner were used for the analysis of off-momentum particle backgrounds as will be discussed in section 6.4.7.

The number of events N_{SWITA}, N_{SWITR}, and N_{SWITL} recorded during a given time period which pass the respective definition cuts are used to calculate the integrated luminosity during that time period:

$$\mathcal{L}_a \equiv \frac{N_{SWITA}}{\sigma_a}$$

$$\mathcal{L}_{rl} \equiv \frac{1}{2}(\mathcal{L}_r + \mathcal{L}_l) \equiv \frac{1}{2}\left(\frac{N_{SWITR}}{\sigma_r} + \frac{N_{SWITL}}{\sigma_l}\right) ,$$

where σ_a, σ_l, and σ_r denote the theoretically calculated cross sections*.

The $\mathcal{L}_a$ and $\mathcal{L}_{rl}$ luminosity measurements have largely complementary errors with respect to their acceptance defining radial cuts. The SWITA selection is fixed in the "beam frame", meaning that the corresponding luminosity $\mathcal{L}_a$ is (in the limit $\tan\theta \to \theta$) independent of longitudinal or transversal displacements of the LEP beam with respect to the OPAL reference frame. As a direct result of this feature, the actual position of the radial cut is not centered in either the left or right detector part. Furthermore, due to the presence of acollinear events, the mean radial coordinate R_a of a particle (even in the case of perfectly centered beams) is not uniquely correlated to values of R_r and R_l. These effects significantly complicate the assessment of biases of the coordinate reconstruction for the SWITA selection. The $\mathcal{L}_{rl}$ luminosity on the other hand has second order dependences on the beam position, while the position of the cut boundaries is well defined in the "detector frame". Since the detailed study of biases in the coordinate reconstruction turned out to be the most challenging part of the luminosity measurement, the luminosity was determined from the SWITR and SWITL selections, while the SWITA selection is used to cross check the result for $\mathcal{L}_{rl}$ [45].

In the collinear radiation approximation, the polar angles of the particles being recorded by the left and right calorimeter are related to their energies E through the relation $R_r/R_l = E_l/E_r$, where the subscripts r and l denote the parameters of the particles being recorded by the right and left calorimeter, respectively. Therefore, the acollinearity cut $|R_r - R_l| < 25$ mm was introduced to ensure that the geometric acceptance of single radiative events is indeed determined by

* These equations for the integrated luminosity have to be understood symbolically; Strictly speaking, each of the luminosities $\mathcal{L}_a$, $\mathcal{L}_r$, and $\mathcal{L}_l$ is calculated according to equation 6.1, with σ_{ee}^{theo} replaced by σ_a, σ_r, or σ_l, and the sum running over the events passing the SWITA, SWITR, or SWITL selection cuts, respectively.

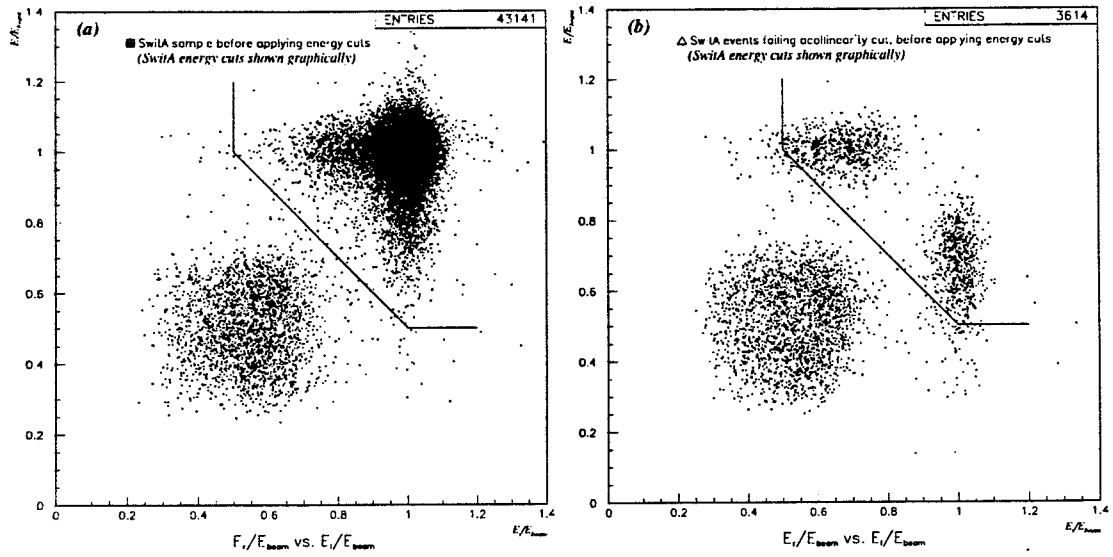

Figure 6.1: (a) The distribution of the energy recorded in the left calorimeter versus the energy recorded in the right calorimeter divided by the beam energy for events passing the SWITA selection before applying the energy cuts. (b) The same distribution for events failing the acollinearity cut but passing all other SWITA cuts, before applying the energy cuts. The acollinearity cut removes events near the energy cuts, which are shown graphically.

the radial cuts, and not by the explicit energy cuts. Figure 6.1 shows how the acollinearity cut significantly reduced the number of radiative events that are selected by the SWITA selection near the energy cut.

6.3 Event Reconstruction

6.3.1 Overview

The DST variables needed for the luminosity analysis for events recorded by the SW Calorimeter are reconstructed within the OPAL ROPE framework as described in section 4.4. The SW ROPE processor performs a number of operations on the packed dense data from the detector in order to obtain the quantities needed

for the analysis [54]. First, the data are unpacked and a cross talk correction is applied to account for the fact that a charge pulse in a given channel of an AMPLEX chip induces a small charge of opposite sign in the remaining 15 channels of the AMPLEX chip. This effect was quantified by pulsing individual channels of the AMPLEX chip on a test bench prior to the assembly of the silicon detectors. Furthermore, pads which are known to be noisy or dead are flagged in a database and their charges are set to zero for the analysis.

A fundamental design goal of the SW detector had been that it should provide enough information to estimate all effects of the shower reconstruction on the Bhabha cross section from the data themselves without relying on Monte Carlo simulations of the detector response to electrons. As will be seen, this goal made test beam measurements necessary, in particular to measure and parametrize the bias of the radial coordinate due to the curvature of the pad boundaries. In the following subsections, we will discuss the reconstruction of the energy and the radial and azimuthal coordinates of an events, which are needed for the definition of Bhabha acceptance cuts.

6.3.2 Reconstruction of the Radial Coordinate

The aim of the radial coordinate reconstruction is to allow the definition of acceptance cuts anywhere within the calorimeter such that the number of events for which the *reconstructed* coordinate lies inside the acceptance is the same as the number of events for which the *true* coordinate lies inside the acceptance. It is not necessarily required that the event sample passing the acceptance cuts based on the reconstructed coordinate is identical to the sample of events for which the true coordinate lies inside the acceptance. The precision of the reconstruction of individual events is much less critical, the spatial resolution entering only as a

weak second order correction to the acceptance, with a precision of about 1 mm at the inner edge of the acceptance resulting in a 0.1% error on the luminosity.

The first step of the coordinate reconstruction is to determine a quantity in each layer which has a 1-to-1 correspondence to the true radial position of the shower centroid in that layer and which has the property of reconstructing the true radial shower position bias-free at three "fix-points" in a given pad, namely at the pad center and at the two edges. Such a quantity is

$$Y^0 = \frac{E_1 - E_3}{2E_2 - E_1 - E_3} , \tag{6.2}$$

where E_2 is the energy in the central pad with the highest energy and E_1 and E_3 are the energies in the adjacent pads with larger and smaller radial coordinate, respectively. In a detector with cartesian geometry, this function has the value of 0 for a shower centroid positioned at the center of a pad ($E_1 = E_3$), +1 at the outer edge ($E_2 = E_1$) and −1 at the inner edge ($E_2 = E_3$) of the pad. The $r-\phi$ geometry of the SW detector spoils this symmetry, where the size of the resulting bias is a function of the pad size and of the lateral shower spread compared to the pad curvature. Rather than relying on Monte Carlo simulations of the shower spread to determine the bias, the strategy has been to determine the bias directly from the calorimeter. For this purpose, test beam studies with a partially instrumented SW calorimeter were performed [53]. The radial positions of incident electrons and muons for which the pad with the maximum energy was located within a given boundary were plotted. From fits to those distributions a turnover point was determined which marked the image of the pad boundary. Since muons do not develop electromagnetic showers but rather deposit energy through ionization, the difference of the pad image for electrons and muons directly measures the effect of the systematic biases discussed above. For this measurement, the position of

the trajectories had to be known precisely on an event-by-event basis. This was accomplished by using three delay-line proportional chambers and, for a portion of the data, through silicon micro strips that were positioned at the front face of the detector [53]. As a result of these studies, the reconstructed electron positions $4X_0$ deep into the detector were found to be systematically shifted to smaller radii by a distance of $8 \pm 2.5 \pm 5.5$ μm, where the first error is statistical and the second one systematic. The systematic error is dominated by gain variations on the order of 0.2% of the readout channels for the individual pads with respect to the mean gain variation from all available channels. Smaller systematics result from the fit-function used to determine the turnover position, effects of the corrections applied for the cross talk between the channels of a given AMPLEX chip, and from cuts applied on the muon data to reject delta rays or showering particles.

The deviation of Y^0 from the true radial position for incoming electrons at points other than the fix points depends on the lateral shower size compared to the pad size. They are largest in the middle between two fix-points and have a magnitude of up to 0.5 mm, or 20% of the pad width. From comparing the reconstructed position of muons and electrons in the testbeam data, it was found empirically that a parameter

$$Y = Y(Y^0, W^0) \text{ with } W^0 = \ln(\frac{E_1 E_3}{E_2^2})$$

can be defined, where Y preserves the fix-points of Y_0 and is smooth, meaning the Y distribution of events is directly proportional to the distribution of the true radial coordinate within a layer. The resolution of Y depends on the position of the shower centroid within a pad: It is best at the pad boundaries and worst at the pad centers. The variation of the resolution across a pad is bigger in the first layers with narrow showers and smaller in the deeper layers with broader showers.

We want to get the final coordinate for an event by combining the coordinates of the central layers, so we form the "raw" radial coordinate R^0 by averaging the radial coordinates from layers 2 to 10, weighted by the inverse square of their corresponding error[†]. The variations of the resolution within each layer have a dramatic effect when forming R^0: Events turn out to be more concentrated at radial positions with a good radial resolution, so that the overall radial distribution is subject to systematic biases as shown in figure 6.2. The distribution is characterized by an underlying $1/R^3$ dependence with a convoluted "waviness" with a pitch of 2.5 mm which is determined by the radial pad size. For obvious reasons, R^0 is referred to as "unsmoothed" radial coordinate. Similar to the procedure of deriving the parameter Y from Y^0, the distribution is smoothed by deriving a function $R(R^0)$ such that R is smooth, meaning it displays the fundamental $1/R^3$ distribution without the convoluted periodic function. Figure 6.3 shows the smoothed R distributions in the left and right calorimeter derived from the unsmoothed distributions of R^0 in figure 6.2. The average radial resolution of the final reconstructed radial coordinate is about 220 μm.

After the variety of procedures performed on the measured quantities to obtain the reconstructed radial coordinate R, on which the acceptance cuts are applied, it is not obvious that this coordinate meets the requirement set forth at the beginning. In particular, it has to be confirmed that the number of events selected by the reconstructed radial coordinate does indeed corresponds to the number of events that would have been selected by cuts on the true radial position. Effects on the measured luminosity due to the reconstruction method for the radial

[†] Recall that the radial coordinate reconstructed in each layer is extrapolated into a reference plane 7 X_0 deep into the SW detector, thereby correcting for displacements of the true radial coordinates for different layers due to the particle trajectories not being parallel with the OPAL z axis.

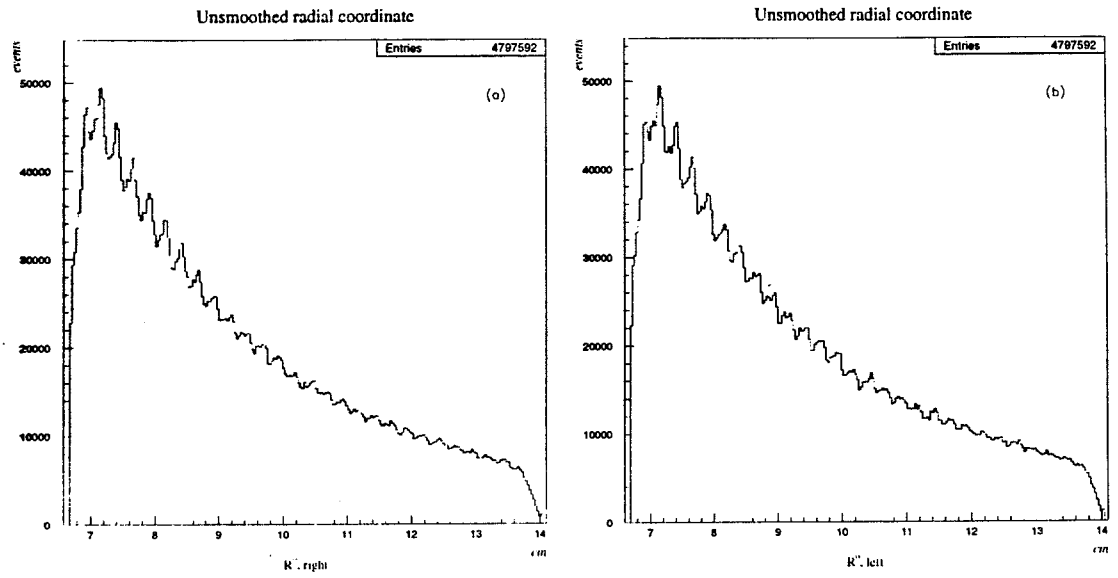

Figure 6.2: The "unsmoothed" reconstructed coordinate R^0 in (a) the right and (b) the left calorimeter. Events are shown after applying all isolation cuts except the acollinearity cut.

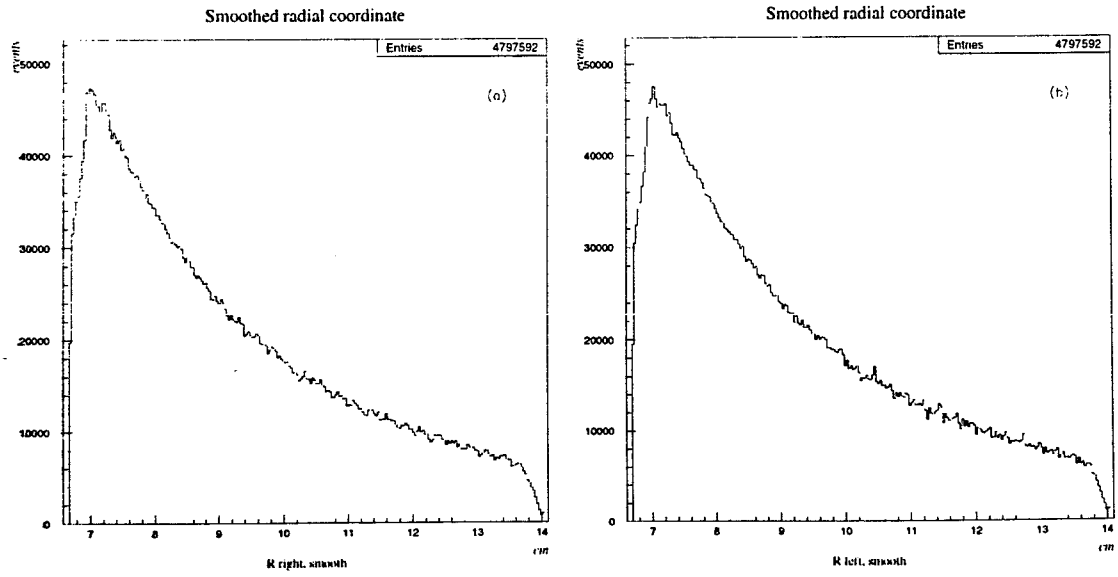

Figure 6.3: The "smoothed" reconstructed coordinate R in (a) the right and (b) the left calorimeter. Events are shown after applying all isolation cuts except the acollinearity cut.

coordinate will be discussed in section 6.4.3.

6.3.3 Reconstruction of the ϕ Coordinate

The ϕ coordinate is needed only for the acoplanarity cut which ensures that the event sample is well within the 100% efficient region of the SWSEG trigger. Since this cut rejects only about 0.7% of the events after applying all other acceptance cuts, a precise reconstruction of ϕ is not critical for the luminosity measurement. The ϕ coordinate is calculated in each layer using the same charge splitting algorithm used for the radial coordinate reconstruction: Using equation 6.2, E_2 is defined in the same manner as was done above, while E_1 and E_3 are the energies in the pads to the left and right of the central pad with energy E_2. The resulting function Φ^0, corresponding to the Y^0 function for the radial coordinate, then has a 1-to-1 relation to the true ϕ coordinate of the shower centroid, with $\Phi^0 = 0$ for a shower that is centered in the pad center and $\Phi^0 = +1(-1)$ for a shower centered at the left(right) edge of the pad. Unlike for the radial coordinate, no attempt was made to correct deviations of the Φ^0 function from the true ϕ position. Due to the large size of the pads in azimuthal direction, the ϕ coordinate of a shower is determined with a better resolution for the deeper layers where the shower has spread out. The ϕ coordinate is therefore determined from the average of the coordinates obtained from all 19 layers, but with the deeper layers having a bigger weight assigned than the earlier layers.

6.3.4 Energy Reconstruction

Energy cuts are applied to separate Bhabha events from the machine dependent background. For this purpose, the energy must be reconstructed with a high reso-

lution and a good linearity. A good linearity is important since the reconstructed energy can only be tuned to the beam energy near the Z^0 peak, while the actual cuts are applied at much smaller energies, namely at $0.5 \cdot E_{beam}$ and $0.75 \cdot E_{beam}$ for the minimum energy cut and the average energy cut, respectively. For the acollinearity cut and for the definition cuts, the reconstructed radial coordinate from the highest energetic cluster is used. Which pads are used for the reconstruction of the radial coordinate depends on the characteristics of the shower reconstruction, in particular on the ability of the algorithm to separate nearby electron and photon peaks for events with final state radiation. Therefore, the development of an adequate clustering algorithm and the tuning of its parameters is crucial to optimize the precision of the acceptance cuts.

The algorithm developed for the energy reconstruction searches the detector for energy "peaks" and then clusters the pad energy around these peaks to determine the total energy of the cluster. A peak is defined as the energy sum from an area of 2×2 pads in the $r-\phi$ plane of the detector. Then the difference of this four-pad sum and the two adjacent pads on both sides of the peak is formed in both azimuthal and radial direction. If either difference is above a predefined cutoff value, the peak is assumed to be the centroid of a showering particle. The two-cluster resolution in radial and azimuthal direction therefore is one pad between two four-pad peaks. The energies of the pads around a given peak above a predetermined threshold are summed to yield the total cluster energy, where in the case of more than one peak in a calorimeter the pad energy was assigned to the nearest peak. The absolute energy scale of a cluster is determined by choosing a factor to convert the ADC counts in a pad to the energy.

The energy response of the calorimeter is significantly affected by the presence of preshowering material which represents up to 2 radiation length in the left

calorimeter and up to 1.5 radiation length in the right calorimeter. The amount of material near the edges of the SW acceptance was kept to a minimum, while cables leading to the silicon micro vertex detector are responsible for the larger preshowering in the left than in the right calorimeter. Near the detector edges, energy is also lost due to leakage effects. The energy lost by these two effects has been parametrized as a function of both the polar angle and the ratio E_{pre}/E_{main}, where E_{pre} denotes the energy deposited by a shower in the first four layers of the calorimeter, and E_{main} the energy in the remaining 15 layers [45]. The effect of this correction is shown in figure 6.4. Besides correcting the reconstructed energy locally, an overall scaling is applied to scale the reconstructed energy to the beam energy. The average resolution of the energy is about $\sigma_E/E = 24\%/\sqrt{E}$.

Applying the corrections discussed above to the energy improves the resolution in regions with large amounts of preshowering material and is important for a proper Monte Carlo simulation of the energy response in SW. On the other hand it introduces a new source of potential systematic errors, since radiative events might have failed the threshold of the SWSEG trigger, while in the off-line analysis—had they been triggered—the correction might have pushed their energy above the cuts applied for the Bhabha selection. This effect will be investigated in section 6.4.9.

6.4 Corrections and Systematic Errors

The determination of the luminosity consists of two parts: First, the integrity of the relative luminosity is established by ensuring that the counted number of event for the three energy points are not distorted with respect to each other. Then the absolute luminosity is determined by a Monte Carlo calculation of the Bhabha cross section at the peak energy. This cross section can be extrapolated

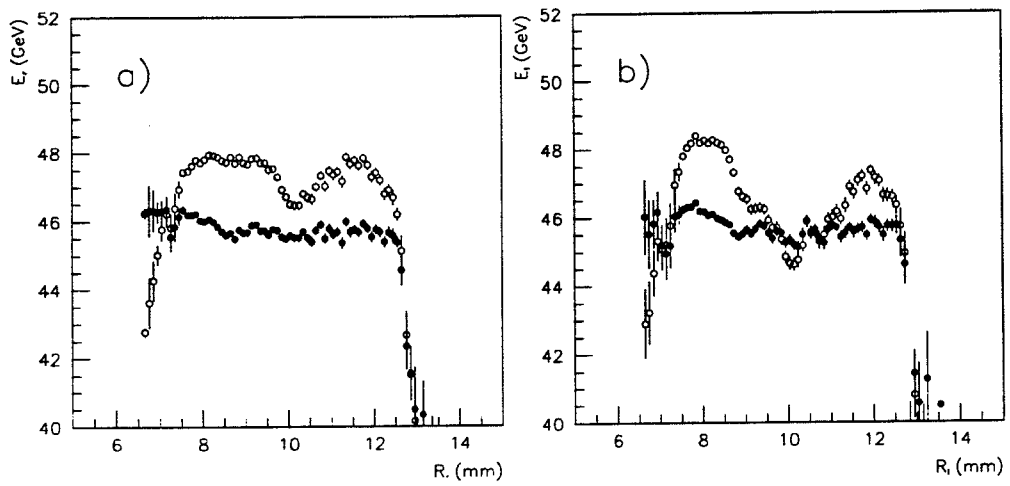

Figure 6.4: The energy of the most energetic cluster versus its radial position in (a) the right calorimeter and (b) the left calorimeter for a typical run. The open circles show the uncorrected energy, the solid circles show the corrected energy after applying corrections for leakage and preshowering.

to the off-peak points, taking into account the dominant $1/s$ dependence of the Bhabha cross section and effects on the level of 10^{-4} due to the interference term of the photonic t-channel and the s-channel of Z^0 decay. The errors resulting from the determination of the absolute luminosity apply to all three energy points. Contributions to the error that are potentially different for the three energy points are quite small and will be discussed where necessary.

The error on the absolute luminosity is dominated by the imperfect understanding of the detector geometry, the coordinate reconstruction and the effective energy response of the calorimeters. For the specific acceptance cuts introduced in section 6.2, the errors determining the inner and outer radius translate into errors on the luminosity according to the relations

$$\frac{\Delta\mathcal{L}}{\mathcal{L}} \approx +\frac{\Delta R_{in}}{25\ \mu\mathrm{m}} \cdot 10^{-3}\ ,$$

the events recorded by the SW detector was simulated by a Gaussian distribution for the main Bhabha peak, superimposed with a detailed parametrization of the non-Gaussian tails. The systematic error of the parametrization was estimated by observing the change of the number of accepted events when scaling the tail by $\pm$ 50% and the Gaussian distribution by $\pm$ 10%, resulting in errors of $2.1 \cdot 10^{-4}$ and $1.5 \cdot 10^{-4}$, respectively.

The energy resolution is expected to scale with $1/\sqrt{E}$, so that the resolution is worse by a factor of about 1.4 near the minimum energy cut of $0.5 \cdot E_{beam}$. This dependence of the resolution on the energy could not be accurately confirmed from the data. By observing the change in acceptance when assuming a resolution which is independent of the energy, an additional systematic error of $1.0 \cdot 10^{-4}$ was derived.

To check the linearity of the energy, and the effect of the preshowering and leakage corrections at low energies, acollinear events were used. As was described in section 6.2, these events allow one to predict the energy of the low energy electron according to the relation $R_\tau/R_l = E_l/E_\tau$ when the other electron is required to have an energy consistent with the beam energy. Comparing the reconstructed energy in the cluster with the lower energy to the energy expected from the acollinearity of the event, non-linearities in the data were found to be no bigger than $\pm 1\%$ at half the beam energy. Implementing this non-linearity into the Monte Carlo, a systematic error of $2.1 \cdot 10^{-4}$ on the luminosity measurement was obtained.

All effects combined yield a systematic error of $3.4 \cdot 10^{-4}$. The correction factor necessary to account for changes in the cross section due to the energy response of the detector was determined as $-7.1 \cdot 10^{-4}$ from the Monte Carlo.

The parametrization of the detector response that is implemented in the Monte

Carlo was derived from the 1993 data recorded with SW and was not optimized for the the 1994 data. The energy distribution of the 1994 data differs from the 1993 data in two measurable points [14]. First, a slight change in the gains in both the left and the right calorimeter were observed. These however modify the acceptance by only about $0.5 \cdot 10^{-4}$. A potentially more important effect was a slight change in the non-gaussian tails of the energy response. These changes were found to be within the range of 50% over which the scale of the tail was varied to obtain the systematic error as described above. Therefore, the same correction factor of $(-7.1 \pm 3.4) \cdot 10^{-4}$ has been assumed for the 1993 and 1994 data, fully correlated between the years.

To a smaller degree, the number of accepted events depends on the resolution of the radial coordinate due to the presence of the definition and acollinearity cuts, and on the azimuthal resolution due to the acoplanarity cut. Effects of the radial and azimuthal resolution both contributed an error of $1 \cdot 10^{-4}$ to the luminosity error. An additional error of $1 \cdot 10^{-4}$ was assigned due to the detector granularity which resulted in uncertainties of clustering the energy around nearby peaks. As the combined result of all the effects discussed in this subsection, a correction of $(-7.3 \pm 0.3 \pm 3.8) \cdot 10^{-4}$ was assigned for both 1993 and 1994 data. Here the first error is statistical and uncorrelated between 1993 and 1994, while the second error is systematic and fully correlated between the two years.

6.4.6 LEP Beam parameters

Transverse offsets of the LEP beam collision point in x and y direction, as well as tilts of the beam axis are quantified in terms of "eccentricities". The eccentricities are defined as the displacement of the intersection of the LEP beam in the $x - y$ plane, at the reference plane 7 X_0 deep into the SW calorimeter. The eccentricities

in the left and right detector, respectively, are 2-dimensional vectors, which will be denoted by $\vec{\mathcal{E}}_l$ and $\vec{\mathcal{E}}_r$ for the left and right calorimeter. The absolute value of the eccentricity is given by $\mathcal{E}_{l,r} = \sqrt{(\mathcal{E}^x_{l,r})^2 + (\mathcal{E}^y_{l,r})^2}$ and eccentricities different from zero introduce a modulation of the accepted number of events as a function of the azimuthal angle ϕ. We will first consider the effect of beam offsets and tilts on the definition cuts. For those cuts, when integrating the accepted number of events over ϕ, first order effects of beam tilts and offsets cancel while second order effects result in a net gain of acceptance. For the SWITA selection, transverse beam offsets cancel, with only beam tilts causing intensity modulations. For the SWITR and SWITL selection, both beam tilts and offsets modify the number of accepted events. Quantitatively, this means that the change in accepted events for the SWITA selection depends only on the difference of the eccentricities in the left and right side, $\Delta\mathcal{E} = 1/2 \cdot |\vec{\mathcal{E}}_r - \vec{\mathcal{E}}_l|$, while SWITR and SWITL depend on the respective eccentricities $\mathcal{E}_l$ and $\mathcal{E}_r$. A second order analytic calculation of the net gain of events due to beam eccentricities yields for the definition cuts [51]

$$\frac{\Delta N_{SWITR,L}}{N_{SWITR,L}} \approx \left(\frac{\mathcal{E}_{r,l}}{1.46 \text{ mm}}\right)^2 \cdot 10^{-3}$$

$$\frac{\Delta N_{SWITA}}{N_{SWITA}} \approx \left(\frac{\Delta\mathcal{E}}{1.46 \text{ mm}}\right)^2 \cdot 10^{-3} \,. \tag{6.3}$$

Figure 6.7 shows the intensity modulations as a function of ϕ for the SWITR, SWITL, and SWITA selections for a typical run, where the intensity in this context is defined as the number of events recorded in a given ϕ bin. The eccentricities have been extracted from simular plots for each run by fitting a function of the form $I(\phi) = I_0 \cdot (1 + a\cos(\phi - \phi_0))$ to the observed intensity distribution, allowing the calculation of the resulting increase of the number of accepted events. The fit parameters a and ϕ_0 indicate the amplitude and the phase of the intensity modulation.

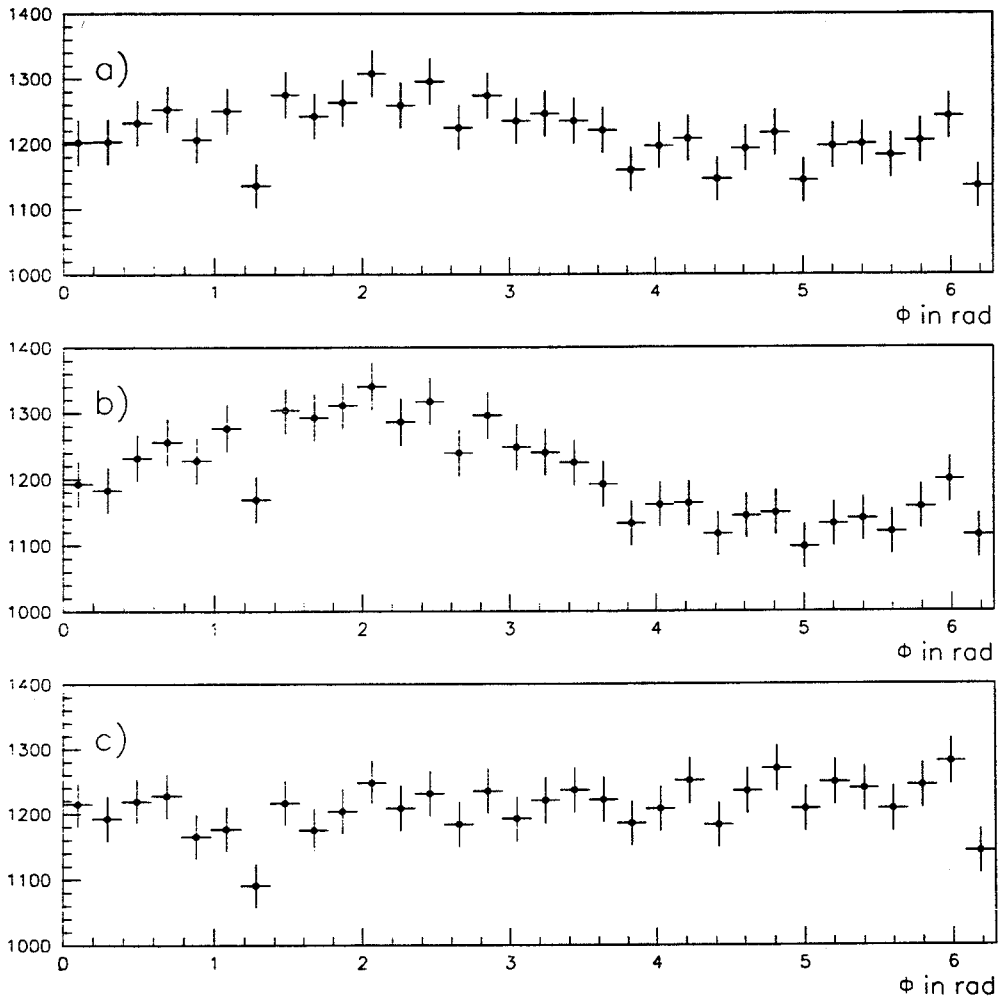

Figure 6.7: Modulation of the intensity observed with in the SW calorimeter as a function of ϕ for a typical run from 1993. Each bin is one pad wide and therefore corresponds to a tower. Shown are events selected by (a) the SWITA, (b) the SWITR, and (c) the SWITL selection.

Effects of longitudinal offsets of the position of the beam collision point on the definition cuts cancel to all orders for the SWITA selection, while for the combined SWITR and SWITL selections second order corrections remain. The residual second order correction for each the SWITR and SWITL selection is given by [51]

$$\frac{\Delta N_{SWITR,L}}{N_{SWITR,L}} \approx \left(\frac{\Delta Z}{77.8 \text{ mm}}\right) \cdot 10^{-3} .$$

The longitudinal offsets can be extracted from the data as well, albeit with a much worse resolution than the transverse beam offsets. A longitudinal beam offset will result in an asymmetry of the number of recorded events in the left and right calorimeter of the size

$$A_{rl} \equiv \frac{C_{SWITR}}{C_{SWITL}} - 1 = -\frac{2\Delta Z}{1.23 \text{ mm}} \cdot 10^{-3} , \tag{6.4}$$

where C_{SWITR} and C_{SWITL} refer to the eccentricity corrected SWITR and SWITL rates, respectively. The correction factors on the Bhabha cross section resulting from beam eccentricities and longitudinal beam offsets have been calculated for each run according to equations 6.3 and 6.4 and have been implemented into ROPE for the final luminosity measurement.

The longitudinal and transverse beam offsets result in an apparent acollinearity for events which truly have a back-to-back kinematics, allowing an independent check of the beam offsets calculated above. Longitudinal offsets result in a sinodial dependence of the difference between the reconstructed radial position in the left and right side on ϕ, while longitudinal offsets result in a offset of $R_r - R_l$ from zero which is constant in ϕ. This is shown in figure 6.8. The effect of the transverse and longitudinal beam offsets on the luminosity extracted from these distributions were found to agree with the values derived from the azimuthal intensity modulations on a level of about $5 \cdot 10^{-5}$ [51].

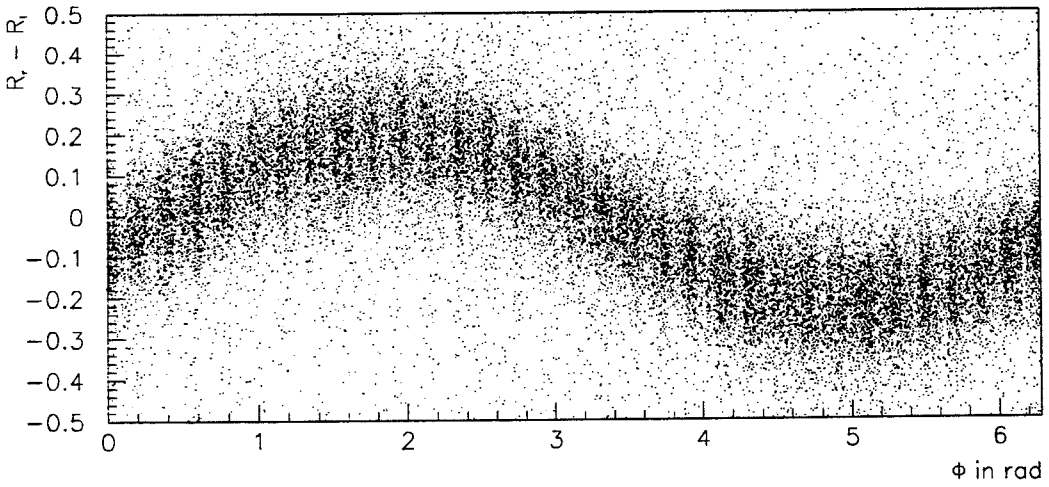

Figure 6.8: The difference of the reconstructed radial coordinate in the right and left calorimeter for a typical run as a function of the azimuthal angle for events passing the SWITA cuts and for which the energy in both calorimeters is close to the beam energy. The sinodial variations are due to beam offsets as described in the text.

The effects of beam tilts and transverse and longitudinal beam offsets are much more difficult to calculate for the isolation cuts, mainly due to the presence of the acollinearity cut. These effects have been calculated from the Monte Carlo by implementing the mean eccentricities observed for a given year into a Monte Carlo simulation specifically produced for this purpose. The change in the number of accepted events predicted by the Monte Carlo for the definition cuts was found to agree with the analytic calculation to a relative accuracy of about 1%. This gives us confidence in the MC predictions for the isolation cuts, for which no analytic calculations are possible.

For 1993, the results for the combined effect of the longitudinal and transverse beam offsets on the isolation cuts were determined as $(-3.9 \pm 0.5) \cdot 10^{-4}$ for the luminosity measurement based on the SWITR and SWITL selection, and $(-3.6 \pm 0.7) \cdot 10^{-4}$ for the SWITA selection. These results have to be combined with the effect of the definition cuts of +1.9 (SWITA selection) and +7.0 (combined SWITR and SWITL selection). The latter corrections have negligible statistical errors.

Since the main difference of the luminosities $\mathcal{L}_a$ and $\mathcal{L}_{rl}$ is their sensitivity to beam displacements, the two luminosities can be used to check the consistency of the relative luminosity. Applying the respective corrections derived above, the ratio $\mathcal{L}_{rl}/\mathcal{L}_a$ was found to be consistent with unity throughout the year and between the three energy points.

For reasons described in section 6.2, the $\mathcal{L}_{rl}$ luminosity is used for the final luminosity measurement. The overall correction factor applied to the cross section for 1993 therefore is $(+3.1 \pm 0.5) \cdot 10^{-4}$. To obtain the correction factors for the 1994 data, the average beam eccentricities and offsets for that year were implemented in the Monte Carlo. The resulting correction factor is $(+4.4 \pm 0.5) \cdot 10^{-4}$.

The resolution of both the acollinearity and acoplanarity directly affect the number of events passing the respective parts of the acceptance cuts. These resolutions in turn are dominated by beam tilts, divergences and the bunch size and the simulation of these machine parameters in the Monte Carlo contributes to the error of the luminosity measurement. Qualitatively, these parameters affect the cross section similar to beam offsets: An increase of events passing the definition cuts is compensated by a decrease of events passing the isolation cuts. Unlike beam offsets, however, they affect both the $\mathcal{L}_a$ and $\mathcal{L}_{rl}$ luminosity measurement. Quantitatively, these effects are much harder to assess. Varying these machine parameters over a reasonable range resulted in an overall change in acceptance of less then $1 \cdot 10^{-4}$, the largest individual contribution of $2 \cdot 10^{-4}$ coming from the acollinearity cut. Therefore, $2 \cdot 10^{-4}$ was assigned as an additional error to the error of the average LEP beam parameters, fully correlated between 1993 and 1994.

6.4.7 Machine Dependent Background

Background from off-momentum particles was studied using the delayed coincidence trigger SWSEGA described in section 5.5. On the event sample selected by that trigger, acceptance cuts identical to the SWITR, SWITL, and SWITA selection described in section 6.2 were imposed and denoted as SWOTR, SWOTL, and SWOTA, respectively. For SWSEGA events, the full information needed for the acceptance cuts, namely the pre-shower corrected cluster energy, and the reconstructed θ and ϕ coordinates described in section 6.3, was only available for the in-time cluster. To circumvent this problem, the distributions of the cut variables were plotted as a function of the raw energy for the in-time cluster of the SWSEGA sample. The raw energy was available for both the in-time and out-of-time cluster,

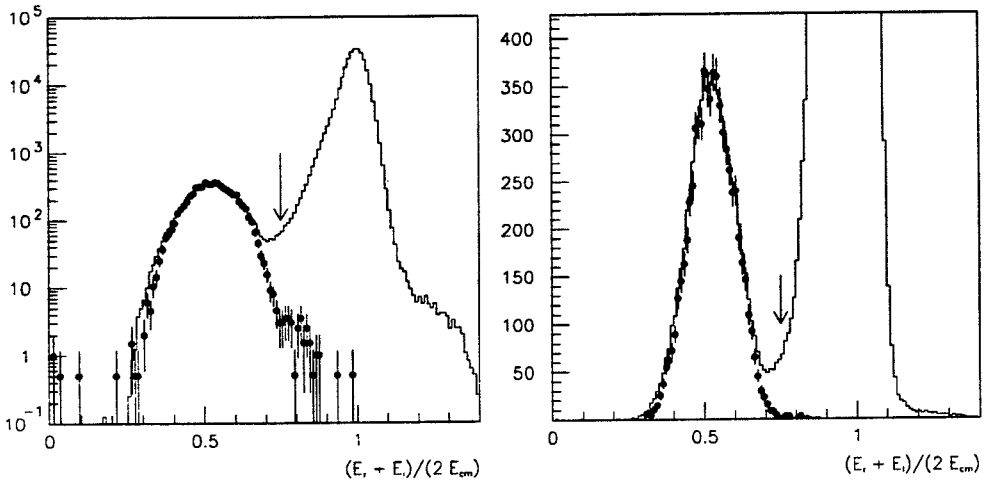

Figure 6.9: The spectra of reconstructed energies for the SWITA selection (open histogram) and the SWOTA selection (full circles) before the energy cuts. The same distribution is shown on a logarithmic scale (left) and a linear scale (right). The average energy cut at $0.75 \cdot E_{beam}$ is indicated by an arrow.

and the cut-variables could be extracted from those distributions by using the raw energy of the out-of-time cluster as an index.

The reconstructed energy distributions for the SWITA selection, overlayed with the distribution for the SWOTA sample before applying the energy cuts are shown in figure 6.9 for 1993 data, where the SWOTA sample was corrected for the prescaling applied for the SWSEGA selection. It can be observed that the background peak near an energy of $0.5 \cdot E_{cm}$ is well reconstructed by the SWOTA selection. Similar plots can be obtained for the SWOTR and SWOTL selections. From the number of events passing the acceptance cuts for delayed coincidences (SWOTR, SWOTL, and SWOTA events), the background from off-momentum particles was estimated. The arrow in figure 6.9 indicates the average energy cut—the additional minimum energy cuts that are imposed on the right and left calorimeter are of no relevance for the background from off-momentum particles. The increase of

the experimental luminosity due to accidental coincidence background was estimated at 1.0 ± 0.1 for the 1993 data. For the 1994 data, slightly modified trigger conditions result in somewhat different background conditions which are not quit as well simulated by the SWOTA, SWOTR, and SWOTL selections as for the 1993 data[61]. The correction factor and error applied for 1994 are 0.1 ± 1.0 [14].

Another potential source of machine-dependent background are off-momentum particles which overlap with true Bhabha events and cause the event to fail or pass the acceptance cuts inappropriately. To study this effect, the spectrum of accidental cluster energies recorded by the out-of-time cluster in SWSEGA triggered events was convoluted with the spectrum of reconstructed energies for Bhabha events for each calorimeter. It was found that the number of events passing the energy cuts increases by about $0.5 \cdot 10^{-4}$ as a result of overlap, which is almost exactly compensated by a decrease of events passing the acoplanarity cut and the respective definition cuts. As a result, an uncertainty of $0.1 \cdot 10^{-4}$ is applied due to overlap background.

6.4.8 The $\gamma - Z^0$ Interference Term

The main dependence of the Bhabha scattering cross section on the center-of-mass energy is given by the $1/s$ dependence of the photon t-channel in the center-of-mass frame. However, near the Z^0 peak, effects of the interference term between the photon t-channel and the Z^0 s-channel have to be taken into account. Since the Bhabha cross section calculated with BHLUMI does not include effects of this interference term, a correction factor [51]

$$c(s) = \frac{\sigma(s) \cdot s}{\sigma_t(s_{ref}) \cdot s_{ref}}$$

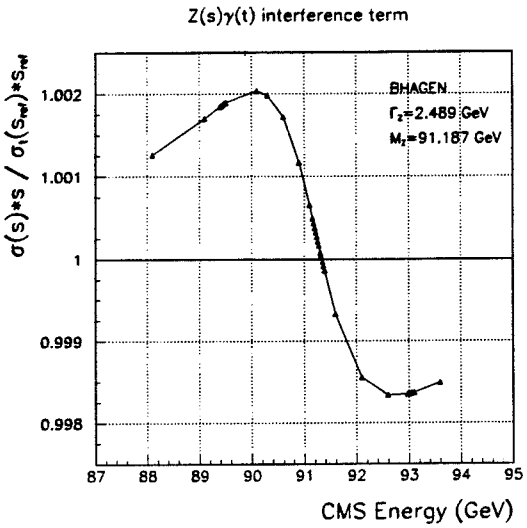

Figure 6.10: The calculated correction factor for the effect of the $\gamma - Z^0$ interference term.

has to be applied. Here $\sigma(s)$ denotes the total cross section at the energy point s, while $\sigma_t(s_{ref})$ denotes the Bhabha cross section without the $\gamma - Z^0$ interference contribution at a reference center of mass energy of s_{ref}. The correction $c(s)$ is shown in figure 6.10. The values for $\sigma(s)$ and $\sigma_t(s_{ref})$ were obtained from the Monte Carlo program BHAGEN [59], and the physical precision of the obtained factor $c(s)$ was estimated at $2 \cdot 10^{-4}$ by comparing it to published results obtained with ALIBABA [60].

6.4.9 Trigger Efficiency

The importance of a 100% efficient trigger for the luminosity measurement was pointed out in section 5.5. An important source for potential inefficiencies of the trigger are events which due to preshowering or leakage fall below the SWSEG threshold. Since in the off-line analysis energy corrections are applied to compensate effects of preshowering and leakage, these events—had they been triggered—

could have a large enough correction to pass the acceptance cuts. Furthermore, trigger thresholds are applied in terms of the absolute energy, and not relative to the beam energy, such that potential inefficiencies are likely to be larger for lower beam energies, introducing a possible source of error for the relative luminosity.

The original forward detector (FD) overlaps partially with the SW detector, providing a limited opportunity to independently check the efficiency of the SW detector, in a small region close to the outer acceptance of the SW detector. In order to check the efficiency of the SWSEG trigger over the complete acceptance of SW, the SWSEG trigger efficiency was determined for the sample of events triggered by the SWHILO trigger. The SWHILO trigger, using the energy deposited in the complete detector, is inherently less reliable than the SWSEG trigger since it is about eight times more sensitive to coherent pedestal shifts than the SWSEG trigger. It is therefore important that the SWSEG trigger alone provides a 100% trigger efficiency and before using the SWHILO trigger for checks of the SWSEG trigger, it was confirmed that pedestal shifts did not affect the performance of the trigger. It was then confirmed for a sample of events triggered by FD that the SWHILO trigger efficiency is 100% efficient in the overlap region of SW and FD, and then the efficiency of the SWSEG trigger was checked for events triggered by SWHILO over the complete acceptance of the SW detector. Since the SWHILO trigger has a much lower threshold than the SWSEG trigger for the energy deposited in either side of the luminometer, this check yields an estimate of events which fail the SWSEG trigger due to preshowering or leakage. As a result of these studies, the SWSEG trigger was found to be efficient at a level of better than 10^{-6} with no significant differences in the trigger efficiency for the three different energy points.

Effect	Correction $\cdot 10^{-4}$ 1993	1994	Systematic $\cdot 10^{-4}$ 1993	1994
SW radial dimension ($\pm 5\mu$m)	–	–	$2.0 \oplus 0.0$	$2.0 \oplus 0.0$
Radial coordinate bias	–	–	$2.6 \oplus 0.0$	$2.6 \oplus 0.0$
Monte Carlo, detector response	-7.3	-7.3	$3.8 \oplus 0.3$	$3.8 \oplus 0.3$
Monte Carlo, stat. for cross sec. calc.	–	–	$3.7 \oplus 0.0$	$3.7 \oplus 0.0$
Detector instab. (mech. + response)	–	–	$0.5 \oplus 0.0$	$0.5 \oplus 0.0$
Trigger inefficiency	–	–	< 0.01	< 0.01
LEP beam parameters (average)	$+3.1$	$+4.4$	$2.0 \oplus 0.5$	$2.0 \oplus 0.4$
fluctuations in LEP beam parameters	–	–	$0.0 \oplus 0.5$	$0.0 \oplus 0.5$
accidental coincidence background	$+1.0$	$+0.1$	$0.0 \oplus 0.1$	$0.0 \oplus 1.0$
$\gamma\gamma$ background	$+2.0$	$+2.0$	$0.1 \oplus 0.0$	$0.1 \oplus 0.0$
total			$6.6 \oplus 0.8$	$6.6 \oplus 1.2$

Table 6.1: Summary of corrections applied to the cross section corresponding to the $\mathcal{L}_{\tau l}$ luminosity and their errors. The first parts of each error is the part which is correlated between the 1993 and 1994 data, while the second part is uncorrelated.

6.5 Overall Systematic Error and Correction

The corrections and errors derived in the previous section are summarized in table 6.1. Furthermore, some additional sources of backgrounds and errors have been taken into account in the table. An error of $3.7 \cdot 10^{-4}$ due to the Monte Carlo statistics has been added, as well as a conservative error of $0.5 \cdot 10^{-4}$ to account for fluctuations of the LEP beam parameters. The latter error was derived from the RMS of the distribution of the energy reconstructed in the two SW calorimeters, divided by the beam energy. Finally, a background contribution of $(2.0 \pm 0.1) \cdot 10^{-4}$ due to two-photon reactions was added.

The cross section corresponding to the $\mathcal{L}_{\tau l}$ luminosity was calculated with BHLUMI for the cuts described in section 6.2 as 78.809 ± 0.029 nb, where the error is due to the limited statistics of the MC sample. This cross section contains the correction of $-7.3 \cdot 10^{-4}$ shown in table 6.1 for effects due to the detector

response implemented in the Monte Carlo. The corrections for accidental coincidence and two-photon background have to be applied explicitly to the theoretical cross section from above. These corrections, together with the part of the LEP beam parameter correction which is *not* due to effects of the eccentricity on the definition cuts, form the correction factor f_{sim} in equation 6.1.

The contributions to the correction f_{LEP} are taken into account directly in the ROPE code on an event-by-event basis. These corrections are due to the $\gamma - \mathrm{Z}^0$ interference term and to the effect of the eccentricities on the definition cuts as described in section 6.4.6. The correction f_{LEP} also contains a term $(E^0_{cm}/E_{cm})^2$, where $E^0_{cm} = 91.1$ GeV is the center of mass energy at which the BHLUMI MC was produced, and E_{cm} is the center of mass energy of the LEP beam for a given event. This factor scales the energy according to the $1/s$ behavior of the Bhabha cross-section to the off-peak points and also accounts for small fluctuations of the LEP beam energy of a few tens of MeV at the nominal peak and off-peak points.

To the experimental error, a theoretical error due to the BHLUMI simulation and the simulation of the $\gamma - \mathrm{Z}^0$ interference term has to be added. This theoretical error was estimated at 0.25% in [45]. Even though the theoretical uncertainty has been reduced since then [14], we will assume a theoretical error of 0.25% in this dissertation since the error is quite small compared to the systematic and statistical error of the tau pair selection.

Chapter 7

Tau Pair Analysis

7.1 Overview

To measure the mass of the Z^0, its total decay width and the peak cross section for the process $Z^0 \rightarrow \tau^+\tau^-$, the cross section for tau pair final states,

$$\sigma_{\tau\tau} = \frac{f_{\tau\tau} \cdot N_{\tau\tau}}{\mathcal{L}} ,$$

has to be determined at a minimum of three energy points. The measurement of the integrated luminosity $\mathcal{L}$ was discussed in the previous chapter. In this chapter we will derive the cuts to select $\tau^+\tau^-$ final states from the 1993 and 1994 OPAL DST data, where the number of events passing these selection cuts over a given time period is denoted by $N_{\tau\tau}$.

The τ lepton decays after traveling about 2.2 mm in the rest frame of the OPAL detector, requiring the tau pair selection cuts to be sensitive to the two leptonic and the whole range of hadronic decay channels of the tau. To determine the lineshape parameters for the process $Z^0 \rightarrow \tau^+\tau^-$, the experimental results will be compared in chapter 8 to the semi-analytical cross section calculations performed with the program ZFITTER [3]. In ZFITTER, the cross sections are calculated without geometric or kinematic cuts so that the experimental measurements have

to be corrected to correspond to the same acceptance. Therefore, the factor $f_{\tau\tau}$ is introduced to correct the number $N_{\tau\tau}$ of events selected by the tau pair selection cuts for backgrounds leaking into the sample and for genuine tau events discarded by the cuts.

In section 7.2 we will define a set of geometric and topological cuts to select events from the data which are consistent with a Z^0 decaying into a tau pair. Then the $\tau^+\tau^-$ Monte Carlo will be used to derive an acceptance correction factor to scale the selected number of data events to the full acceptance with no geometric or topological cuts. After deriving the MC acceptance correction, the main task of the analysis presented in this chapter is to ensure that all backgrounds are removed from the data sample and that correction factors are applied for all discrepancies in the inefficiency of the tau pair selection cuts between data and $\tau^+\tau^-$ MC. This will be done in sections 7.3 to 7.12. In the last section, all corrections will be combined to yield the overall correction factor $f_{\tau\tau}$.

7.2 Selection of $\tau^+\tau^-$ Final States

Since tau pair events should be selected independently of the decay channel of the τ leptons, a strategy is required which does not so much aim at selecting events with a topology consistent with $\tau^+\tau^-$ final states, but rather at *rejecting* all other final states of e^+e^- collisions. In particular, cuts have to be defined to reject $\mu^+\mu^-$ and e^+e^- final states as well as multihadronic events, which result from fragmenting quark pair final states. The probability that both taus of a tau pair decay into either muons or electrons is about 4% for each case. The reaction $\tau^+\tau^- \to \ell^+\ell^-\nu_\tau\bar{\nu}_\tau\nu_\ell\bar{\nu}_\ell$ with $\ell^+\ell^- = e^+e^-$ or $\mu^+\mu^-$ differs from decays of the form $\gamma, Z^0 \to \ell^+\ell^-$ by the presence of the neutrinos. Since neutrinos can not be detected

by OPAL, their kinetic energy is missing from the visible energy of an event. Therefore, the reaction $\gamma, Z^0 \rightarrow e^+e^-$ is rejected by removing events with high shower energy, and the reaction $\gamma, Z^0 \rightarrow \mu^+\mu^-$ is rejected by removing events with a high track momentum. Multihadronic events are rejected by removing events for which a large number of charged tracks and clusters in the electromagnetic calorimeter were observed. Two-photon events, in which the initial state e^+e^- pair interacts without forming a Z^0 resonance to yield a $e^+e^-\ell^+\ell^-$ final state have to be rejected as well. Here $\ell^+\ell^-$ denotes any lepton pair, where the production cross section decreases rapidly with increasing mass of the lepton pair. Since in general only the $\ell^+\ell^-$ pair is recorded in the OPAL detector while the e^+e^- pair travels unrecorded down the beam pipe, two-photon events are characterized by a low visible energy. Apart from the decay products of e^+e^- collisions, cosmic ray events can mimic $\tau^+\tau^-$ final states in which both taus decay into a muon and have to be rejected. Cosmic rays in general can be identified by being not in coincidence with the time at which beam collisions occur at the OPAL interaction point.

Backgrounds which result from the decay of a Z^0, namely, the backgrounds from electron pairs, muon pairs and multihadronic events, are expected to scale with the Z^0 production cross section, each background being a more or less constant fraction of the number of tau pair events selected at each energy point. These backgrounds are referred to as resonant backgrounds. Cosmic rays and two-photon backgrounds are not mediated by a Z^0 resonance. The cross section for two-photon events shows only a very weak dependence on the center-of-mass energy, while the cosmic ray cross section is obviously independent of the LEP beam energy. These backgrounds are expected to scale with the luminosity of the three energy points, independent of their center-of-mass energy, and are referred to as non-resonant backgrounds.

7.2.1 Definition of Event Parameters

Only tracks and electromagnetic clusters from the DST data which pass certain quality cuts are used for the analysis. A track is accepted as a quality track if it has a transverse momentum of $p_t \geq 0.1$ GeV/c, and if it is constrained to the interaction point by $d_0^{track} \leq 1.0$ cm and $z_0^{track} \leq 40.0$ cm. The definition of the impact parameters d_0 and z_0 was given in section 4.1.2. The track momentum for a given event is defined as the scalar sum of the track momenta from all quality tracks. The relative track momentum R_{trk} is defined as the ratio of the track momentum for an event and the center of mass energy of the colliding e^+e^- pair. The track multiplicity N_{trk} is defined as the number of quality tracks of an event.

For quality electromagnetic clusters it is required that the raw energy of the cluster be at least 0.1 GeV in the barrel region and at least 0.2 GeV in the endcap region. In the endcap region it is furthermore required that a cluster be formed from at least two lead glass blocks and that the energy fraction in the most energetic block be less than 0.99.

The shower energy for a given event is defined as the sum of all quality electromagnetic clusters. The relative shower energy R_{shw}, is defined as the ratio of the shower energy for an event and the center of mass energy of the colliding e^+e^- pair and N_{cls} is defined as the number of quality electromagnetic clusters of an event.

Finally, the relative visible energy is defined as $R_{vis} = R_{shw} + R_{trk}$ (the absolute visible energy is defined accordingly) and the total multiplicity as $N_{tot} = N_{cls} + N_{trk}$. The definition of the visible energy double-counts energy in the case of showering charged particles which is taken into account when cuts are applied on that parameter.

The quality tracks and electromagnetic clusters of an event are combined to form cones according to the following algorithm: First, all tracks and electromagnetic clusters are sorted in order of descending energy. In a first loop, the highest energetic cluster or track which has not yet been assigned to a cone is searched. This track or cluster is used as the seed for a new cone. In a second, nested loop over the remaining tracks and clusters with lower energy, the next track or cluster not yet assigned to a cone that is within an opening angle of 35 deg around the cone axis is merged with the cone. For this cone, the new axis is calculated as the energy weighted mean of the axes from all tracks and clusters in the cone and the second loop is repeated until no more tracks or clusters can be merged with the cone. Then the first loop searches for the next highest track or cluster not yet assigned to an existing cone, which is used as the seed to form a new cone. After all tracks and clusters in an event have been assigned in this manner, the number of cones found for an event which contain at least one charged track and have a visible energy $\geq 0.005 \cdot E_{cm}$ is denoted as N_{cone}. The total shower energy and the scalar sum of the track momenta in each cone, divided by the beam energy, yield the relative shower and track energy per cone, their sum yields the relative visible energy. While these quantities are not used for the cuts to select tau pair events, they are used frequently to define enhancement cuts for the investigation of a particular backgrounds.

The θ direction of a cone is calculated from the energy weighted average of the tracks and clusters in that cone. The average $|\cos\theta|$ for an event is defined as the mean of the two $|\cos\theta|$ values from its two highest energetic charged cones. The acollinearity of an event is calculated from the θ and ϕ of these two cones, using both track and electromagnetic cluster information. The magnetic field

of the OPAL detector bends charged tracks in the $x-y$ plane. By the time a particle enters the electromagnetic calorimeter, it can be bent far enough from its original direction to bias the ϕ coordinate determined from the electromagnetic clusters for the particle. The ϕ direction of a cone is therefore calculated from the tracks only. For the same reason, the acoplanarity of an event is calculated from the x and y components of only the tracks in the two highest energetic charged cones. Since the acoplanarity is insensitive to loss of momentum through initial state radiation, but sensitive to the momentum lost through neutrinos for tau pair events, the acoplanarity distribution is used frequently to separate tau pair final states from other leptonic final states.

7.2.2 Monte Carlo

For the three leptonic and the multihadronic Z^0 decay processes, Monte Carlo (MC) simulations exist for the 1994 detector at the peak energy and for the 1993 detector at the peak energy as well as the two off-peak points. The simulations for 1993 and 1994 differ in both the generator versions used to create the four-vectors and the GOPAL [33] code to simulate the detector response. Tau pair and muon pair event four-vectors were generated with the program KoralZ [37] version 3.8 for 1993 MC and version 4.0 for 1994 MC. KoralZ is a program to generate lepton or quark final states of e^+e^- collisions near the Z^0 peak, taking into account effects of initial and final state radiation. To simulate the decay of $\tau^+\tau^-$ final states, the tau decay library "tauola" [62] is used. For e^+e^- final states of large angle Bhabha scattering, the t-channel of both the Z^0 and γ decay have to be taken into account. Bhabha MC was produced with the program BABAMC [63], where the same version of the program was used for the production of the 1993 and 1994 simulation. To correct for some deficiencies of the program BABAMC at

the generator level, a weighting factor is applied for each event within the ROPE framework. This weighting factor was derived from fitting Born level differential cross sections to distributions predicted by the Monte Carlo [64]. Multihadronic events were produced with Jetset [36] version 7.3 for the 1993 MC and with version 7.4 for 1994 MC. Jetset is a program to simulate the formation of multihadronic events from the fragmentation of quark final states.

Two-photon Monte Carlo was produced using the Vermaseren [65] event generator, where differences between the 1993 and 1994 simulations result only from the different GOPAL versions. For the processes $e^+e^- \to e^+e^-e^+e^-$ and $e^+e^- \to e^+e^-\mu^+\mu^-$ Monte Carlo simulations exist for both the 1993 and 1994 detector, while for the process $e^+e^- \to e^+e^-\tau^+\tau^-$ MC was available only for the 1994 detector. Since two-photon processes are non-resonant, all Monte Carlo simulations were produced at the peak energy.

In the remainder of this chapter, whenever it is referred to "1994 background MC", it is referred to the 1994 MC for the three resonant and three non-resonant processes other than $\tau^+\tau^-$ MC. The "1993 background MC" at a particular energy point is composed of the three resonant background processes for that energy, of the $e^+e^-e^+e^-$ and $e^+e^-\mu^+\mu^-$ two-photon background for the 1993 detector at peak energy, and of the $e^+e^-\tau^+\tau^-$ two-photon background for the 1994 detector. For some of the background estimates, special Monte Carlo samples were used as will be discussed in the corresponding sections.

For the analysis, 1993 data was compared with 1993 MC and 1994 data with 1994 MC. Even though the 1994 MC simulation for most checks agrees better with the 1993 data than the 1993 MC, using different $\tau^+\tau^-$ MC samples to derive the acceptance correction and the individual correction factors is a powerful check whether the analysis is independent of the details of the detector simulations. At

various occasions, cross checks were done by comparing the 1993 peak data with the 1994 MC and vice versa.

The number of Monte Carlo events passing a given cut were scaled to the number of data events according to the luminosities of the samples. For the Monte Carlo events, the luminosity was derived by dividing the number of produced events by the production cross section. The analysis must not depend on the specific value of the production cross section implemented in the Monte Carlo, since the determination of this quantity is the aim of the analysis. Therefore, the luminosity of the data for the purpose of scaling the Monte Carlo samples was derived by dividing the number of data events that pass the tau pair selection cuts by the total cross section of Monte Carlo tau pair and background events that pass the tau pair selection cuts. The resulting luminosity is subject to small distortions due to the fact that the inefficiencies of the tau pair selection cuts for tau pair events and the number of background events passing the tau pair selection cuts is not perfectly simulated by the Monte Carlo. It was checked explicitly that these distortions do not affect the analysis after the overall correction factor for the selected data events had been derived, and the "true" cross section of tau pair production could be compared to the cross section implemented in the Monte Carlo [68].

7.2.3 The Selection Cuts

The strategy for rejecting events with final states other than tau pairs was discussed at the beginning of section 7.2. Using the parameters defined in section 7.2.1, the cuts that were applied for the selection of tau pair events from the OPAL DST data will now be described.

a) Cosmic ray rejection:

Different rejection cuts are applied for events that lie inside the acceptance of the time-of-flight counters (TOF) and those which lie outside.

- Inside the TOF acceptance region ($|\cos\theta| < 0.8$):

Reject events which are found by TOF not to be in coincidence with the expected timing of e^+e^- collisions and which fail a tight vertex cut.

- Outside the TOF acceptance region reject events that fail a loose vertex cut.

The algorithm to reject cosmic rays will be explained in more detail in section 7.8.1.

b) Bhabha rejection:

Since the energy resolution of the electromagnetic calorimeter is not uniform over its acceptance, different cuts are applied in the barrel region ($|\cos\theta| \leq 0.7$) and forward region ($|\cos\theta| > 0.7$) *.

- Require $R_{shw} \leq 0.80$ over the whole acceptance.
- If $|\cos\theta| > 0.7$, require in addition $R_{vis} \leq 1.05$ or $R_{shw} \leq 0.25$.

c) Muon pair rejection:

- Events classified as muon pairs by the criteria described in [66] are discarded from the tau pair sample. In addition, events are rejected which have been identified as muon candidates failing the muon selection cuts due to tracking problems. The muon selection will be described in more detail in section 7.5.

---

* The separation between barrel and forward region for the purpose of the Bhabha-rejection does *not* correspond to the separation between the barrel and endcap part of the electromagnetic calorimeter. The particular choice of the separation will be motivated in section 7.4.

d) Multihadron rejection:

- Require $N_{tot} < 16$.
- Require $N_{trk} < 7$.
- Require exactly 2 charged cones.

e) Acollinearity Cut:

- Require acollinearity as defined from cones ≤ 15 deg .

This cut rejects bhabha events with high final state radiation as well as two-photon and multihadronic events in the far forward region which have a big portion of missing energy along the beam pipe and consequently have a badly reconstructed cone direction.

f) Two-photon rejection:

- Require $R_{vis} \geq 0.18$.

g) Geometric acceptance cut:

- Require $|\cos\theta| \leq 0.90$.

To ensure the integrity of the subdetectors which contribute the quantities on which the tau pair event selection cuts are applied, only events for which the relevant status bits indicate no problems with the subdetectors or the corresponding triggers are considered. The number of events passing the tau pair selection cuts and the detector and trigger status cuts, and the corresponding luminosity (for purposes of scaling the MC samples) derived as described in section 7.2.2 are

data sample	data events used in analysis	$\int \mathcal{L} dt$ derived for data
1994	56015	48.9 pb^{-1}
1993 peak	15699	13.8 pb^{-1}
1993 p−2	3420	8.9 pb^{-1}
1993 p+2	4775	9.2 pb^{-1}

Table 7.1: The data events which pass the tau pair selection cuts, the detector and trigger status cuts and were used in the analysis. The luminosities shown are the approximate values of the luminosity derived from the MC cross sections as described in section 7.2.2.

shown in table 7.1.

7.2.4 Selection Efficiency

After applying all the tau pair selection cuts described in the previous section, the overall acceptance correction is determined by calculating the ratio of generated $\tau^+\tau^-$ MC events and the number of $\tau^+\tau^-$ MC events selected by the cuts. Figure 7.1 shows the $\cos\theta$ distribution of these event samples for 1994 $\tau^+\tau^-$ MC, where $\cos\theta$ was derived from the four-vector for each generated event. The selection efficiency is worse in the region $|\cos\theta| > 0.7$ as a result of the tighter bhabha rejection cuts applied in that region. Table 7.2 shows the acceptance corrections from the four different $\tau^+\tau^-$ Monte Carlo samples corresponding to the four data samples.

7.3 Acceptance Cuts on $|\cos\theta|$

The systematic error due to the acceptance cut is determined by comparing how many events are accepted into the sample in data and MC when $\cos\theta$ is determined differently than from the charged tracks and electromagnetic clusters as

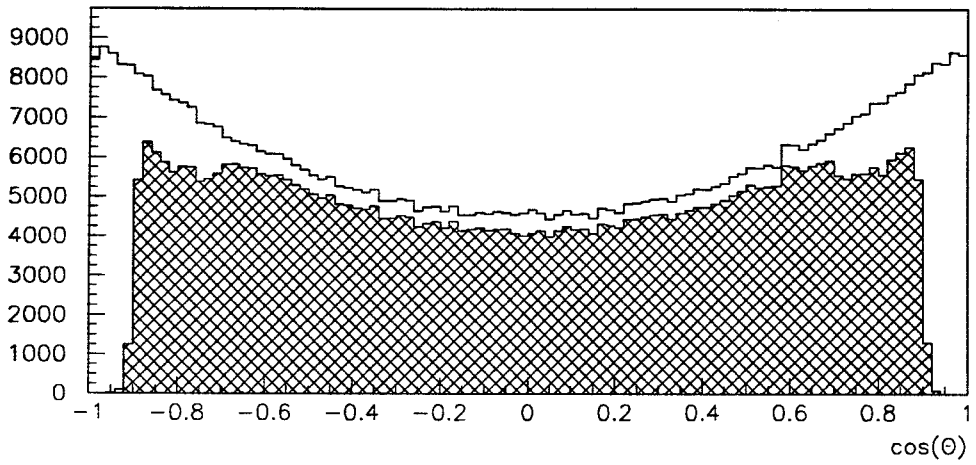

Figure 7.1: The selection efficiency from 94 $\tau^+\tau^-$ MC. On the x-axis, the difference of the $\cos\theta$ derived from the generated four-vector of the τ^- and τ^+ is shown. The open histogram is the distribution of all produced MC events, the cross-hatched histogram is the distribution of events which pass all tau pair selection cuts described in section 7.2.3.

MC Sample	acceptance correction
94	1.3257 ± 0.0010
93 peak	1.3218 ± 0.0014
93 p−2	1.3364 ± 0.0025
93 p+2	1.3353 ± 0.0024

Table 7.2: The overall acceptance correction for the tau-pair selection cuts for the different $\tau^+\tau^-$ MC runs. The error is purely statistical.

described in section 7.2.1. Specifically, $|\cos\theta|$ was alternatively calculated from the cones as before, but using only the information from the charged tracks, and using only the information from the electromagnetic calorimeter. Furthermore, the thrust axis was used to determine the $\cos\theta$ of an event, where the thrust axis was calculated from charged tracks only, from electromagnetic clusters only, and from both combined. Figure 7.2 shows the data and MC distributions using these different definitions for $|\cos\theta|$. The cut value of 0.9 is indicated by the arrows. The data MC difference for the number of selected events for each of these definitions of $|\cos\theta|$ was compared to the data MC difference obtained using the original definition of $|\cos\theta|$. The largest deviation of any of these methods from the data MC difference observed for the original definition of $|\cos\theta|$ was used as a measure of the systematic error due to this cut. In addition, a 1 mrad uncertainty in $\cos\theta$ is added to the systematic error, which results from studies of muon pair events where the $\cos\theta$ measurement using tracks is compared to that from the muon chambers [66]. The final total systematic errors are shown in table 7.3 for the different data sets.

data sample	systematic error
1994	$0.0009 \oplus 0.0007 = 0.0011$
1993 peak	$0.0015 \oplus 0.0006 = 0.0016$
1993 p$-$2	$0.0041 \oplus 0.0006 = 0.0041$
1993 p+2	$0.0028 \oplus 0.0007 = 0.0029$

Table 7.3: Systematic error due to $|\cos\theta|$ acceptance cut.

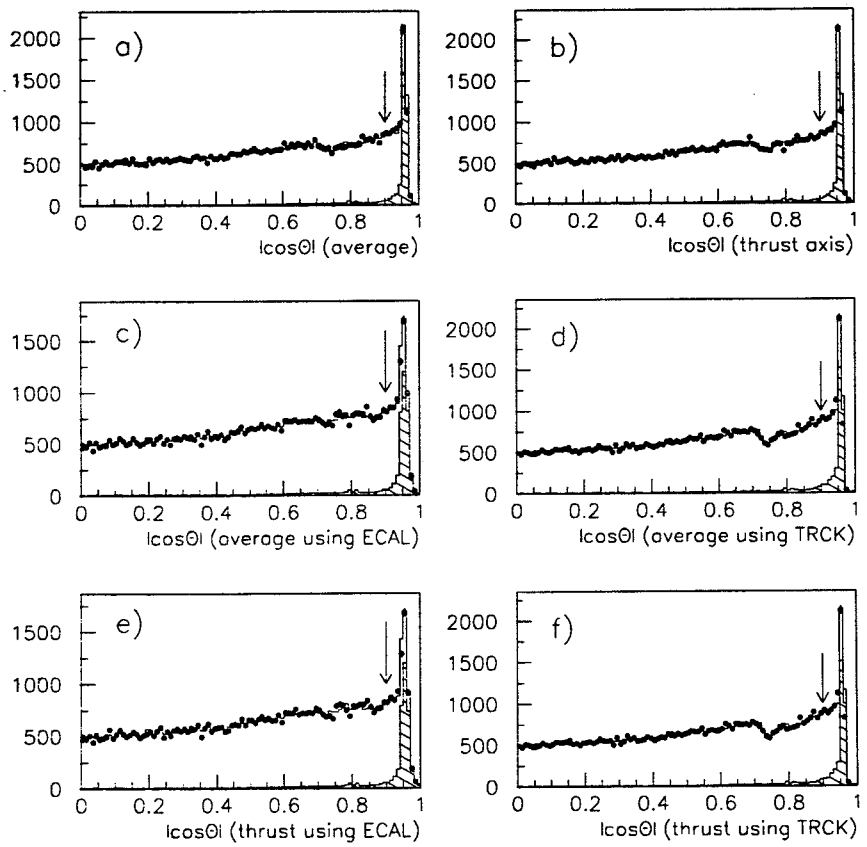

Figure 7.2: The distributions of $|\cos\theta|$ for 1994 data and 1994 MC using different definitions of $|\cos\theta|$ as indicated in each plot. Here ECAL denotes the clusters from the electromagnetic calorimeter, and TRCK the charged tracks from the central detector.

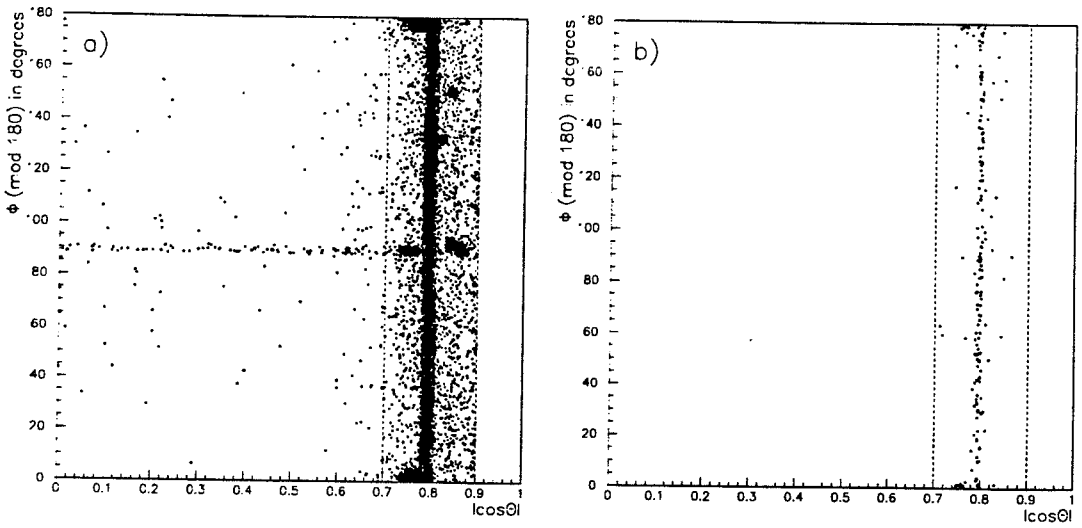

Figure 7.3: The ϕ versus $|\cos\theta|$ distribution of 1994 Bhabha MC events (a) with $R_{shw} < 0.8$ and (b) which pass the tau pair selection cuts in the forward region. The forward region is indicated by the broken lines at $|\cos\theta| = 0.7$ and 0.9. In plot (b), events in the barrel region with $|\cos\theta| \leq 0.7$ are not shown.

7.4 Bhabha Events

Bhabha background is rejected by a cut on the shower energy of an event since Bhabha events are expected to loose basically all their energy through showering in the lead glass blocks of the electromagnetic calorimeter. As a result of the different geometry of the barrel and endcap calorimeter, and due to preshowering material near the edges of the electromagnetic calorimeter barrel, the resolution of the measured shower energy is not uniform over θ. Figure 7.3a shows the ϕ versus $|\cos\theta|$ distribution for 1994 Bhabha MC events with $R_{shw} \leq 0.8$. The large amount of events for $|\cos\theta|$ just below 0.8 is due to preshowering in the pressure bell, which due to its concave shape presents a large amount of material at that angle in the radial direction from the interaction point outwards (cf. figure 4.2). The additional accumulation of events in the forward region near $\phi = 0$ (modulo 90 deg) is due to the support structure of the CJ detector. Clearly, Bhabha events

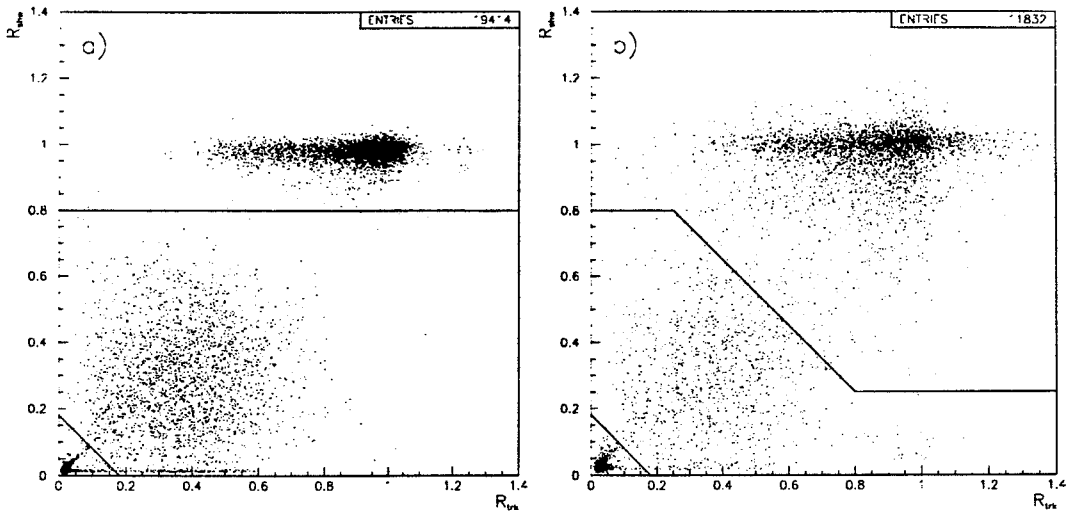

Figure 7.4: The R_{shw} versus R_{trk} distribution after all other tau pair selection cuts in (a) the barrel and (b) the forward region for roughly 20% of the 1994 data. The energy cuts applied in each region are shown graphically. The Bhabha background can be seen at $R_{shw} \approx 1$ and the two photon background at small values of R_{shw} and R_{trk}. The separation between Bhabhas and tau pair events is much worse in the forward region than in the barrel region.

in the forward region with $|\cos\theta| > 0.7$ are not effectively rejected by requiring $R_{shw} \leq 0.8$ alone, so that in this region tighter cuts have to be applied. The Bhabha MC passing all cuts in the forward region are shown in figure 7.3b. While the total number of Bhabha events has been reduced significantly compared to figure 7.3a, the remaining background is clearly concentrated in the regions with high preshowering near the edges of the lead glass barrel calorimeter. Figure 7.4 shows the R_{shw} versus R_{trk} distribution of events that pass all tau pair selection cuts in the barrel and forward region before applying any energy cuts for a part of the 1994 data. Bhabha background is clearly visible at $R_{shw} \approx 1$. The separation between tau pair events and Bhabhas is much worse in the forward region and the cuts were chosen in that region to reject most of the Bhabha background at the cost of efficiency for tau pair events. The Bhabha rejection cuts are shown graphically; also indicated are the two-photon background rejection cuts at $R_{vis} = 0.18$.

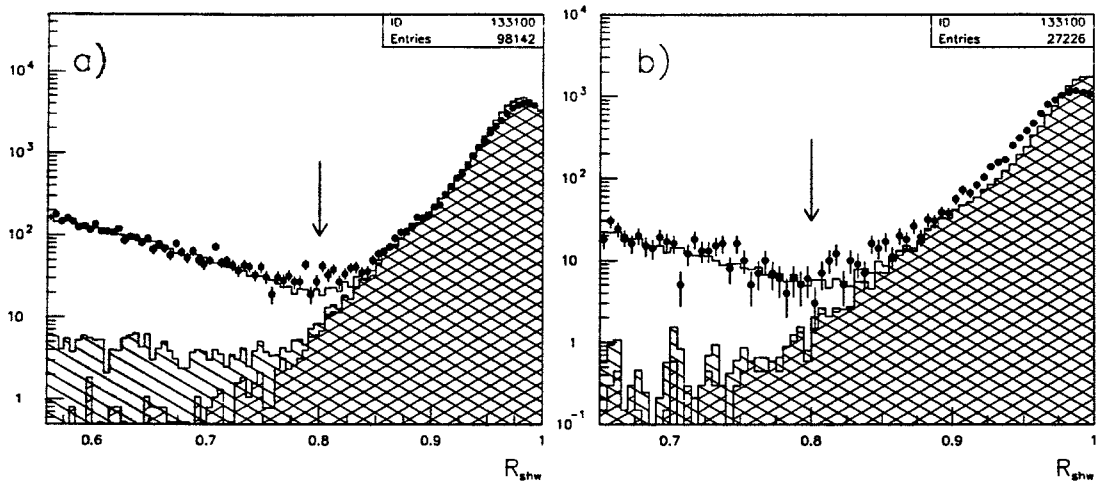

Figure 7.5: The R_{shw}-distribution after all other tau pair selection cuts in the barrel region (a) for 1994 data and MC, and (b) for 1993 peak data and MC. The Bhabha rejection cut at $R_{shw} = 0.8$ is indicated. The points are data, the open histograms total MC, the hatched histograms total background, and the cross-hatched histograms Bhabha MC only.

In figure 7.5 the 1993 and 1994 Bhabha MC is compared to data. The Bhabha peak for 1994 can be observed at a slightly lower shower energy for MC than for data, while for 1993 the Bhabha peak for MC is located at a higher energy than for data. The two Monte Carlo distributions differ appreciably due to significant improvements of the simulation of the electromagnetic calorimeter in GOPAL between the two years. Since the 1994 Bhabha MC models data much better than the 1993 MC, Bhabha MC was produced at the off-peak points with the 1994 detector simulation as well. For the investigation of the Bhabha background in the tau pair sample, results obtained with the Bhabha Monte Carlo from different years will be compared at all energy points.

7.4.1 Efficiency of Bhabha Rejection Cuts

The efficiency of the Bhabha rejection cuts for data and MC will be compared first in the barrel region and then in the forward region. The following strategy will be used for the analysis of both regions: First, we will define cuts to enhance tau events in the respective regions, where the forward region will be further divided into subregions. For the barrel region and each of the subregions in the forward region we will estimate the data excess over Monte Carlo after applying the respective enhancement cuts. To arrive at the final result, we will apply a correction for the efficiency of the enhancement cuts as derived from tau MC.

To enhance Bhabha events in the barrel region, events in the region $0.8 < R_{shw} < 0.9$ were investigated, for which the relative track momentum in the cone with the smaller track momentum (R_{pc}^{min}), fulfills $R_{pc}^{min} < 0.4$. The R_{pc}^{min} distribution and the acoplanarity distribution after requiring $R_{pc}^{min} < 0.4$ are shown in figures 7.6a and b, respectively. Since a large number of Bhabha events can also be found in the region $\theta_{acop} > 0.5$, it is conceivable that part of the data-MC difference in that region stems from the Bhabha background rather than from tau pair events. We therefore calculate an additional error based on the ratio of the number of data and MC events in the region $\theta_{acop} < 0.5$. Denoting this ratio as r^{la}, the additional error is calculated as $\sqrt{(1-r^{la})^2 + (\Delta r^{la}/r^{la})^2}$ times the number of background Monte Carlo events in the region $\theta_{acop} > 0.5$ and is added to the statistical error of the data-MC difference in the high acoplanarity region. Here Δr^{la} denotes the statistical error on r^{la}. The results for the data excess in the barrel region are $-1.1 \pm 13.5 \pm 10.7$ for 1994, $1.7 \pm 6.8 \pm 4.2$ for 1993 peak, $1.6 \pm 3.7 \pm 1.4$ for 1993 p$-$2, and $2.7 \pm 3.8 \pm 1.9$ for 1993 p+2, where the first error was derived from the statistics of data and MC events passing the enhancement cuts, while

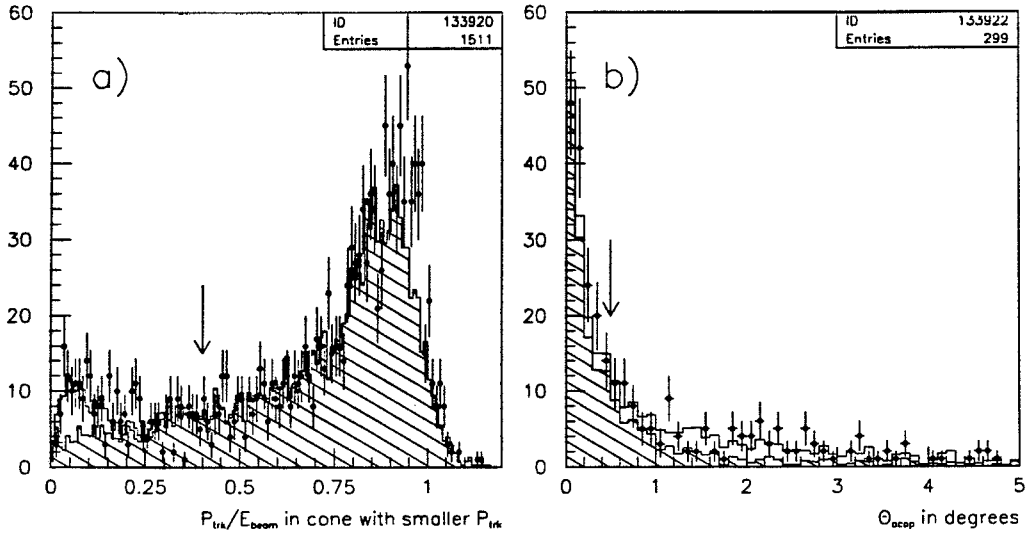

Figure 7.6: (a) The distribution of the track momentum P_{trk} divided by the beam energy in the cone with the smaller P_{trk} (R_{pc}^{min}) for events in the barrel region with $0.8 < R_{shw} < 0.9$ which pass all other tau pair selection cuts. (b) The acoplanarity distribution for events from plot (a) with $R_{pc}^{min} < 0.4$. The points are 94 data, the open histogram total MC, and the hatched histogram the total background.

the second error is the additional error as was just discussed.

Figure 7.7 shows the R_{shw} versus R_{trk} distribution for tau pair MC and Bhabha MC in the forward region. In the figure, four different regions are indicated, which due to the complicated cuts in the forward region will be investigated separately. Region 1 contains events that are rejected by the R_{vis} cut at 1.05. From 1994 tau MC it was found that 94.1% of the rejected tau events in the forward region fall into that subregion, making it the most important one to investigate. Region 2 contains events that fail the R_{shw} cut at 0.8, while events in region 3 fail the R_{shw} cut at 0.25. Region 4 does not border on the region accepted as tau events. However, a bad simulation of the R_{shw} or R_{trk} distribution in the tau MC might cause events to leak across the border into region 2 or 3, or vice versa, resulting in a data MC difference in those region which will be falsely attributed to a leakage

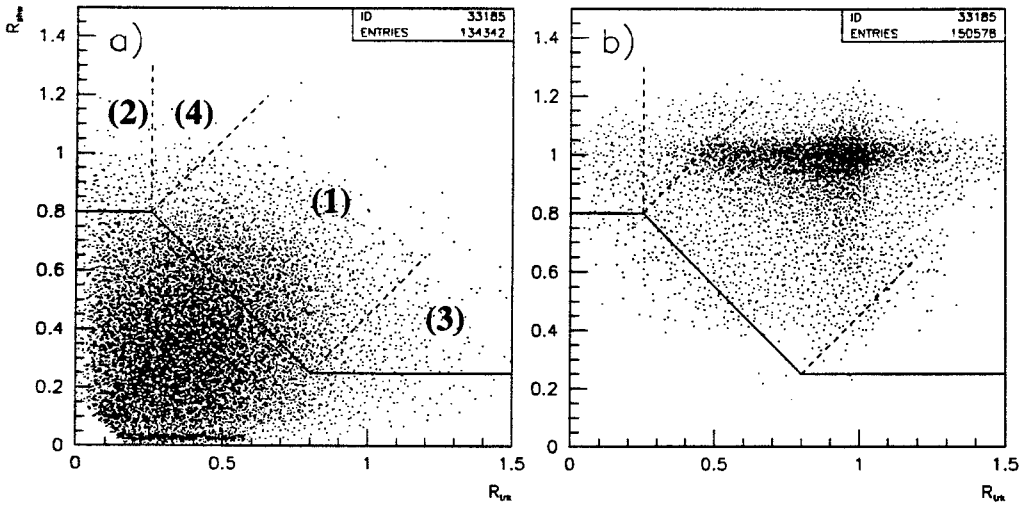

Figure 7.7: The R_{shw} versus R_{trk} distribution for (a) 1994 tau MC and (b) 1994 Bhabha MC in the forward region. The Bhabha rejection cuts are indicated by solid lines. The broken lines and corresponding numbers in plot (a) indicate the four subregions which were used for the analysis as described in the text.

of events into or from the region where events are accepted as tau pair events. It is of course irrelevant if an event fails the R_{vis} cut, the low R_{shw} cut or the high R_{shw} cut and in principal, one does not need to distinguish between subregions outside of the Bhabha acceptance. However, it was found most convenient for the analysis to define one subregion (region 1) which contains the bulk of the tau pair events, while the remaining regions contain only a small number of tau pair events with specific characteristics which determine the strategy to separate those events from the Bhabha events. It is conceivable that the distribution of tau pair MC events amongst the four subregions is different than for tau data, which could affect the total estimated data excess outside of the tau acceptance if the efficiencies for tau MC are very different in the subregions. Potential additional errors due to this effect will be investigated at the end of this subsection.

In region 1 of the forward region we will investigate events with $1.05 < R_{vis} < 1.45$. For 1994 tau MC, 94.4% of the tau events in region 1 which are rejected only by the Bhabha rejection cut fall into this R_{vis} range. As could be seen in

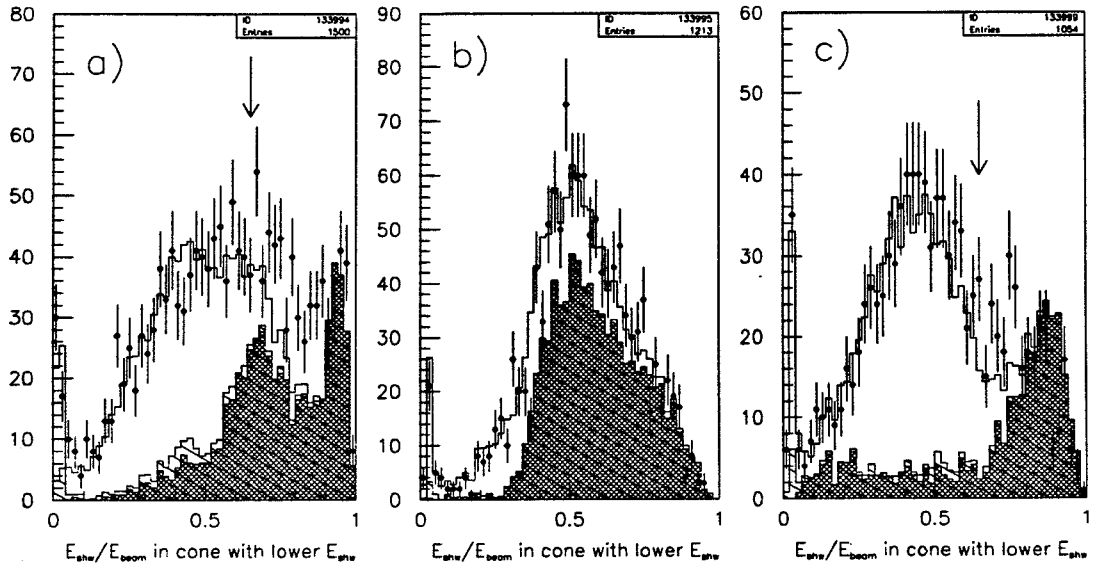

Figure 7.8: The distribution of E_{shw}/E_{beam} in the cone with the lower shower energy for events with $1.05 < R_{vis} < 1.45$ which fail only the Bhabha rejection cut in subregion 1 shown in figure 7.7. The three plots correspond to the regions (a) $0.90 > |\cos\theta| > 0.82$, (b) $0.82 > |\cos\theta| > 0.78$, and (c) $0.78 > |\cos\theta| > 0.70$. The points are 94 data, the open histogram total MC, the hatched histogram total background, and the shaded histogram Bhabha MC only.

figure 7.3, the Bhabha background in the tau sample is concentrated in the region with high preshowering at a value of $|\cos\theta|$ just below 0.8, and we assume that the same is true for Bhabha events that fail the tau pair selection cuts. Figure 7.8 shows the distribution of the relative shower energy in the cone with the smaller shower energy (R_{pc}^{min}) in the regions $0.90 > |\cos\theta| > 0.82$, $0.82 > |\cos\theta| > 0.78$ and $0.78 > |\cos\theta| > 0.70$. In the region $0.78 < |\cos\theta| < 0.82$, both Bhabha and tau MC are distributed over a wide range of R_{ec}^{min} values, making an enhancement of the tau events by a cut on R_{ec}^{min} impossible. In the remaining two $|\cos\theta|$ regions, tau events can be effectively enhanced by requiring $R_{ec}^{min} < 0.65$. Table 7.4 shows the number of events in the high acoplanarity region $\theta_{acop} > 0.5$ after the tau enhancement cuts, where for the regions $0.70 < |\cos\theta| < 0.78$ and

	data	Monte Carlo total	$\tau^+\tau^-$	e^+e^-	data−MC
94					
$.82 < \lvert\cos\theta\rvert < .90$	678 ± 26.0	659.6 ± 9.8	554.5	61.4	$18.4 \pm 27.8 \pm 8.1$
$.78 < \lvert\cos\theta\rvert < .82$	570 ± 23.9	555.6 ± 9.8	343.9	201.2	$14.4 \pm 25.8 \pm 12$
$.70 < \lvert\cos\theta\rvert < .78$	560 ± 23.7	543.3 ± 8.5	496.1	26.7	$16.7 \pm 25.1 \pm 6.4$
93 p					
$.82 < \lvert\cos\theta\rvert < .90$	190 ± 13.8	172.0 ± 3.7	149.1	18.2	$18.0 \pm 14.3 \pm 6.1$
$.78 < \lvert\cos\theta\rvert < .82$	150 ± 12.2	147.3 ± 3.7	98.9	46.1	$2.7 \pm 12.8 \pm 4.5$
$.70 < \lvert\cos\theta\rvert < .78$	153 ± 12.4	144.9 ± 3.3	134.2	7.2	$8.1 \pm 12.8 \pm 2.2$
93 p−2					
$.82 < \lvert\cos\theta\rvert < .90$	46 ± 6.8	48.8 ± 2.4	35.3	11.9	$-2.8 \pm 7.2 \pm 4.6$
$.78 < \lvert\cos\theta\rvert < .82$	54 ± 7.3	48.9 ± 3.1	22.1	26.6	$5.1 \pm 8.0 \pm 4.5$
$.70 < \lvert\cos\theta\rvert < .78$	28 ± 5.3	33.5 ± 1.4	31.1	1.7	$-5.5 \pm 5.5 \pm 0.8$
93 p+2					
$.82 < \lvert\cos\theta\rvert < .90$	78 ± 8.8	61.0 ± 2.5	46.8	13.4	$17.0 \pm 9.2 \pm 3.0$
$.78 < \lvert\cos\theta\rvert < .82$	58 ± 7.6	40.5 ± 2.1	26.8	13.3	$17.5 \pm 7.9 \pm 2.1$
$.70 < \lvert\cos\theta\rvert < .78$	55 ± 7.4	40.7 ± 1.7	38.2	1.9	$14.3 \pm 7.6 \pm 0.9$

Table 7.4: The number of events in the high acoplanarity region ($\theta_{acop} > 0.5$) that fail the tau selection cuts in region 1 of the forward region, and which have $1.05 < R_{vis} < 1.45$. In the regions $.82 < \lvert\cos\theta\rvert < .90$ and $.70 < \lvert\cos\theta\rvert < .78$, it was also required that events have $R_{ec}^{min} < 0.65$. The events are separated into three subregions according to the value of $\lvert\cos\theta\rvert$ for the event as described in the text. The first error in the column "data−MC" is statistical, the second was derived from the data MC agreement in the low acoplanarity region as described in the text.

$0.82 < \lvert\cos\theta\rvert < 0.90$ it was also required that the events have $R_{ec}^{min} < 0.65$. The second error in the column "data−MC" was calculated in the same manner as for the barrel region.

The R_{shw} distribution in region 2 is shown in figure 7.9. To fall into this region, Bhabha events need to have a very low track momentum, and a large number of events in that region have at least one badly reconstructed track. Consequently,

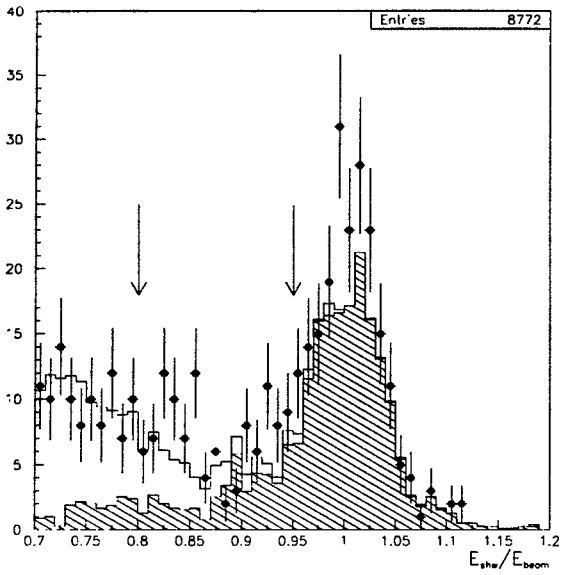

Figure 7.9: Background in subregion 2 from figure 7.7: The R_{shw} distribution for events in the forward region with $R_{trk} < 0.25$ which pass all tau pair selection cuts before applying the Bhabha rejection cuts. The points are 94 data, the open histogram total MC, and the hatched histogram the total background.

the acoplanarity is not well simulated for many Bhabha events and the acoplanarity is not useful for separating Bhabha events and tau events. Therefore, events will be selected in the region $0.8 < R_{shw} < 0.95$, without applying cuts on the acoplanarity. The excess of data over MC events in this region is $29.4 \pm 11.3 \pm 12.5$ for 1994, $3.5 \pm 5.5 \pm 3.8$ for 1993 peak, $1.9 \pm 3.6 \pm 2.2$ for 1993 p$-$2, and $0.4 \pm 3.2 \pm 4.1$ for 1993 p+2. The first error is statistical and, in absence of acoplanarity cuts, the second error was calculated from the data MC ratio in the region $R_{shw} > 0.95$.

The R_{shw} distribution in region 3 for events that pass all tau pair selection cuts before applying the Bhabha rejection cuts is shown in figure 7.10a. Events with $R_{shw} < 0.25$ are mainly muon events, while Bhabha background is located at $R_{shw} \gtrsim 0.4$. The accumulation of events around $R_{shw} \approx 1$ is presumably due to Bhabha events with bad tracking: In order to fall into region 3, an event with $R_{shw} = 1$ needs a total track momentum with $R_{trk} \geq 1.55$. The acopla-

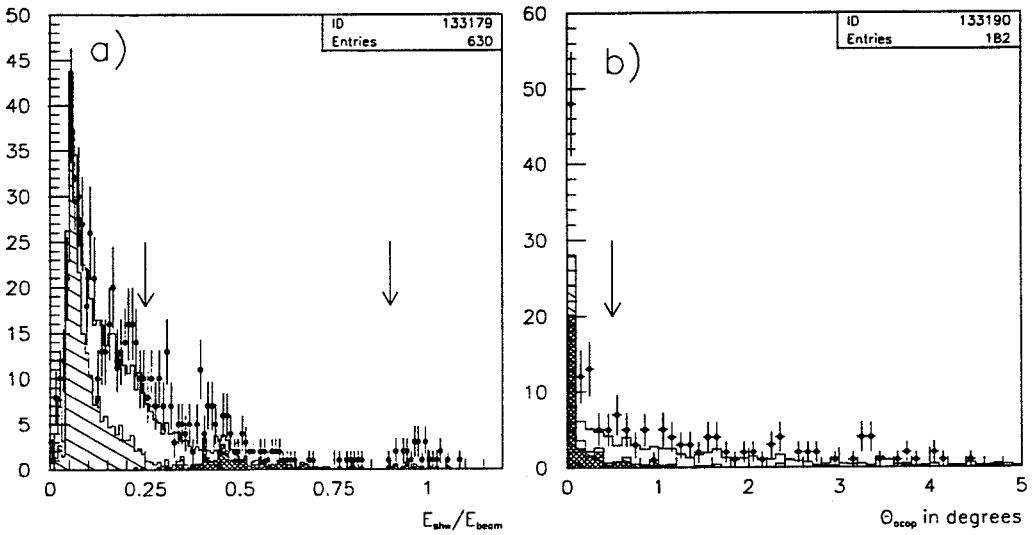

Figure 7.10: Background in subregion 3 from figure 7.7: (a) The R_{shw} distribution for events in the forward region with $R_{trk} > 0.8$ which pass all tau pair selection cuts before applying the Bhabha rejection cuts. (b) The acoplanarity distribution of events that fail the Bhabha rejection cuts in the region $0.25 < R_{shw} < 0.90$. The points are 94 data, the open histograms total MC, the hatched histograms total background, and the shaded histograms Bhabha MC only.

narity distribution for events from figure 7.10a with $0.25 < R_{shw} < 0.90$ is shown in figure 7.10b. The data excess in region 3 for events with an acoplanarity of $\theta_{acop} > 0.5$ was determined as $41.1 \pm 10.3 \pm 5.6$ for 1994, $5.0 \pm 4.5 \pm 0.6$ for 1993 peak, $3.1 \pm 2.5 \pm 0.1$ for 1993 p$-$2, and $-2.7 \pm 1.8 \pm 0.9$ for 1993 p+2. The two errors were calculated in the same manner as described above.

In region 4 only a very small number of tau MC events can be found, and tau pair events can not be separated well from the Bhabha events. We therefore will assume a data MC difference of zero in region 4 and assign as error the number of tau MC events in that region scaled to the respective data luminosity. The resulting errors are ± 14.8 for 1994, ± 3.9 for 1993 peak, ± 0.9 for 1993 p$-$2, and ± 1.1 for 1993 p+2.

The estimated data-MC difference in the barrel region and in subregions 1, 2, and 3 of the forward region were divided by the efficiency of the respective cuts from tau MC to yield the final estimates of the data excess in each region. The efficiencies in the three $|\cos\theta|$ regions of subregion 1 were calculated individually, taking into account a factor of roughly 0.95 for inefficiencies of selecting events in the region $1.05 < R_{vis} < 1.45$ out of the total region $1.05 < R_{vis}$. The highest efficiency of about 0.9 for each tau MC was observed for the enhancement cuts in subregion 2, while the remaining efficiencies were in the range $0.7 \sim 0.8$. To check if the different efficiencies in the barrel region and the subregions of the forward region effect the results, the data MC difference were added first for each data sample and then corrected by the average of all efficiencies from the barrel region and the subregions in the forward region, with an error of half the difference between the largest and smallest efficiency. The results of this calculation were only marginally different from the ones derived by applying the efficiency corrections to each region separately, since the error of the data MC difference in each region

	correction:	
data sample	events	factor
94	151±75	1.0027 ± 0.0013
93 peak	51±36	1.0033 ± 0.0023
93 p−2	3±20	1.0008 ± 0.0058
93 p+2	69±22	1.0144 ± 0.0046

Table 7.5: The final correction factors for the differences in the efficiencies of the Bhabha cuts for data and MC.

far exceeds additional errors introduced by uncertainties of the efficiency.

Any excess of data events failing the Bhabha rejection cuts is missing from the sample passing those cuts, requiring a correction factor of one plus the ratio of data excess and the total number of data events passing the tau pair selection cuts for a given data sample. The total data excess of events failing the Bhabha rejection cuts for each data point and the resulting correction factors are shown in table 7.5.

7.4.2 Background in the Barrel Region

Bhabha background in the tau pair sample was enhanced by requiring a high shower energy or track momentum in *either* of the two cones of the event. This choice should select the majority of the Bhabha background, since detector cracks or dead lead glass counters are unlikely to be located exactly back-to-back, and even if they are (in the case of the gaps between the detector modules, as will be discussed below) they can be assumed to be small enough, so that the bending of the electron and positron due to the magnetic field results in only one of the particles entering a gap.

Figure 7.11 shows the distribution of shower energy versus track momentum divided by the beam energy in the cone with the higher visible energy for 1994

Bhabha MC events after all tau pair selection cuts have been applied. The cuts that were applied to enhance the Bhabha background,

$$(R^{hc}_{trk} > 0.8 \text{ AND } R^{hc}_{shw} > 0.4) \text{ OR } (R^{hc}_{shw} > 0.7 \text{ AND } R^{hc}_{trk} > 0.4) , \qquad (7.1)$$

are shown graphically in figure 7.11. The superscript *hc* denotes the cone with the higher visible energy.

These cuts still accept a fairly large amount of multihadronic events, which can be effectively rejected by requiring

$$N^{hc}_{trk} + N^{hc}_{cls} < 4 , \qquad (7.2)$$

where N^{hc}_{trk} (N^{hc}_{cls}) denotes the number of charged tracks (electromagnetic clusters) in the cone with the higher visible energy.

The electromagnetic calorimeter is split into five modules in polar direction as was described in section 4.1.4. The resulting four gaps are located at $\cos\theta = \pm 0.213$ and ± 0.596. Furthermore, each module is split into a near and far part, resulting in gaps at $\phi = 90\,\text{deg}$ and $270\,\text{deg}$. Most of the Bhabha background in the barrel region is located near these gaps. The effect of the gaps in azimuthal direction could be seen in figure 7.3a as a band of Bhabha events leaking into the tau pair sample for $\phi = 90\,\text{deg}$ modulo $180\,\text{deg}$. The implementation of these gaps into the GOPAL code cannot be trusted since after opening and re-closing the Electromagnetic Calorimeter during technical stops, the modules do not come back together precisely in the same way. The data excess due to Bhabha background and the efficiency of the enhancement cuts for Bhabha Monte Carlo were investigated in the region near the gaps and away from the gaps. It was found that neither the efficiency of the enhancement cuts for Bhabha MC nor the agreement between $\tau^+\tau^-$ MC and data showed any appreciable dependence on whether an

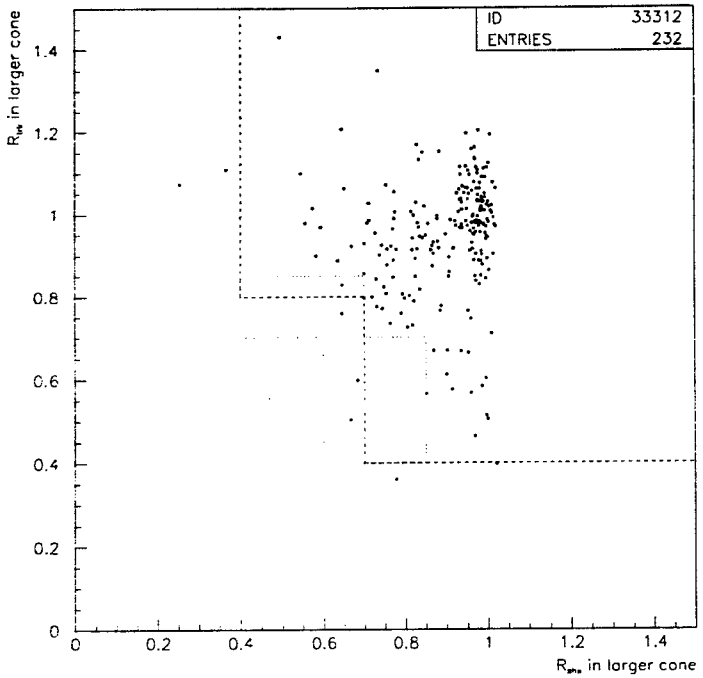

Figure 7.11: The R^{hc}_{trk} versus R^{hc}_{shw} distribution for 1994 Bhabha MC events that pass the tau pair selection cuts in the barrel region. The broken line indicates the cuts used for Bhabha enhancement and the dotted lines shows the region with little Bhabha background used for cross-checks as will be described at the end of this subsection.

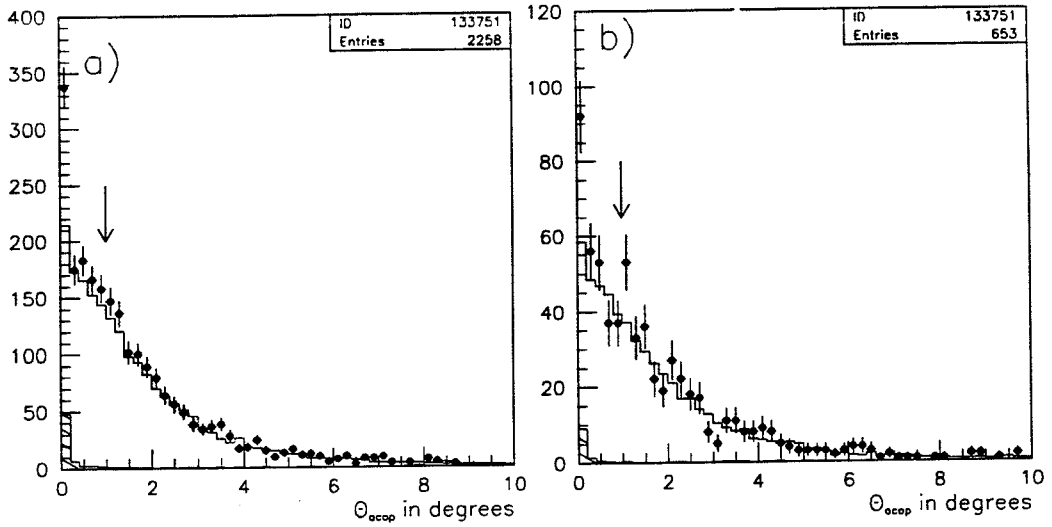

Figure 7.12: Acoplanarity distribution for events after all Bhabha enhancement cuts in the barrel region for (a) 1994 and (b) 1993 peak data and MC. The points are data, the open histograms total MC, and the hatched histograms MC background.

event was located near a gap or not. Therefore, the background estimate was done for the complete barrel region.

Figure 7.12 shows the acoplanarity distribution after all the Bhabha enhancement cuts in the barrel region have been applied. The data excess in the low acoplanarity region is assumed to be due to Bhabha events. In the region with $\theta_{acop} > 1.0$, a data MC ratio of 1.05 ± 0.03 for 1994 data and 1994 MC and a data MC ratio of 1.12 ± 0.06 for 1993 peak data and MC was observed. The statistics for the 1993 off-peak points is too low to deduce any statement about the data MC agreement, but it seems like a reasonable assumption that the 1993 off-peak data behaves qualitatively like the 1993 peak data. This data excess is due to somewhat different efficiencies of the Bhabha enhancement cuts for data and $\tau^+\tau^-$ MC. It was assumed that simular disagreements between data and tau MC exist in the regions $\theta_{acop} < 1.0$ and $\theta_{acop} > 1.0$, such that the excess of data over MC in the low acoplanarity region is not only due to a genuine excess of Bhabha background

year			Monte Carlo			
data	MC	data	$\tau\tau$ scaled	bkgr	total	data−MC
94	94	1020 ± 32	830 ± 27	60.9 ± 4.0	891 ± 27	129 ± 42
94	93	1020 ± 32	830 ± 30	41.5 ± 4.6	871 ± 30	149 ± 44
93 p	93	275 ± 17	253 ± 14	11.7 ± 1.3	265 ± 14	10 ± 22
93 p	94	275 ± 17	253 ± 14	17.1 ± 1.1	271 ± 14	5 ± 22
93 p−2	93	65 ± 8.1	48.4 ± 5.8	3.2 ± 1.0	51.6 ± 5.9	13 ± 10
93 p−2	94	65 ± 8.1	48.2 ± 5.8	5.6 ± 1.3	53.7 ± 5.9	11 ± 10
93 p+2	93	76 ± 8.7	76.5 ± 7.9	6.4 ± 1.2	82.9 ± 8.0	−7 ± 12
93 p+2	94	76 ± 8.7	76.7 ± 7.9	5.0 ± 0.7	81.6 ± 7.9	−6 ± 12

Table 7.6: Estimated excess of Bhabha background in the barrel region after Bhabha enhancement cuts and scaling tau pair MC as described in the text for different data MC combinations. For the off-peak 1994 MC, only Bhabha MC is for the 1994 detector, while all other MC is for the 1993 detector.

in the data, but at least partially also due to a disagreement of data and $\tau^+\tau^-$ MC. To check this assumption, the control region $\theta_{acop} > 1.0$ was separated into three subregions. The ratio of data to MC events in each of those subregions was consistent with the ratio of the whole region $\theta_{acop} > 1.0$. This indicates that the data and MC acoplanarity distributions agree well up to an overall scale factor. An additional test of the validity of the procedure to scale the $\tau^+\tau^-$ MC in the region $\theta_{acop} < 1.0$ by the data MC ratio observed in the region $\theta_{acop} > 1.0$ will be performed below.

In table 7.6 the excess of data over MC after scaling the $\tau^+\tau^-$ MC in the region $\theta_{acop} < 1.0$ as discussed above has been calculated. In the table, the 1993 and 1994 data was also combined with the MC of the respective other year. As expected, the excess is bigger in the case of 1993 MC, since for that MC the energy scale is higher, resulting in less events to fall below the cut at $R_{shw} = 0.8$ and to be consequently accepted in the tau sample. The difference between the data simulations for the two years could be observed in figure 7.5. The overall error of

Bhabha MC events after all tau pair selection cuts have been applied. The cuts that were applied to enhance the Bhabha background,

$$(R^{hc}_{trk} > 0.8 \text{ AND } R^{hc}_{shw} > 0.4) \text{ OR } (R^{hc}_{shw} > 0.7 \text{ AND } R^{hc}_{trk} > 0.4) \,, \qquad (7.1)$$

are shown graphically in figure 7.11. The superscript *hc* denotes the cone with the higher visible energy.

These cuts still accept a fairly large amount of multihadronic events, which can be effectively rejected by requiring

$$N^{hc}_{trk} + N^{hc}_{cls} < 4 \,, \qquad (7.2)$$

where N^{hc}_{trk} (N^{hc}_{cls}) denotes the number of charged tracks (electromagnetic clusters) in the cone with the higher visible energy.

The electromagnetic calorimeter is split into five modules in polar direction as was described in section 4.1.4. The resulting four gaps are located at $\cos\theta = \pm 0.213$ and ± 0.596. Furthermore, each module is split into a near and far part, resulting in gaps at $\phi = 90\,\text{deg}$ and $270\,\text{deg}$. Most of the Bhabha background in the barrel region is located near these gaps. The effect of the gaps in azimuthal direction could be seen in figure 7.3a as a band of Bhabha events leaking into the tau pair sample for $\phi = 90\,\text{deg}$ modulo $180\,\text{deg}$. The implementation of these gaps into the GOPAL code cannot be trusted since after opening and re-closing the Electromagnetic Calorimeter during technical stops, the modules do not come back together precisely in the same way. The data excess due to Bhabha background and the efficiency of the enhancement cuts for Bhabha Monte Carlo were investigated in the region near the gaps and away from the gaps. It was found that neither the efficiency of the enhancement cuts for Bhabha MC nor the agreement between $\tau^+\tau^-$ MC and data showed any appreciable dependence on whether an

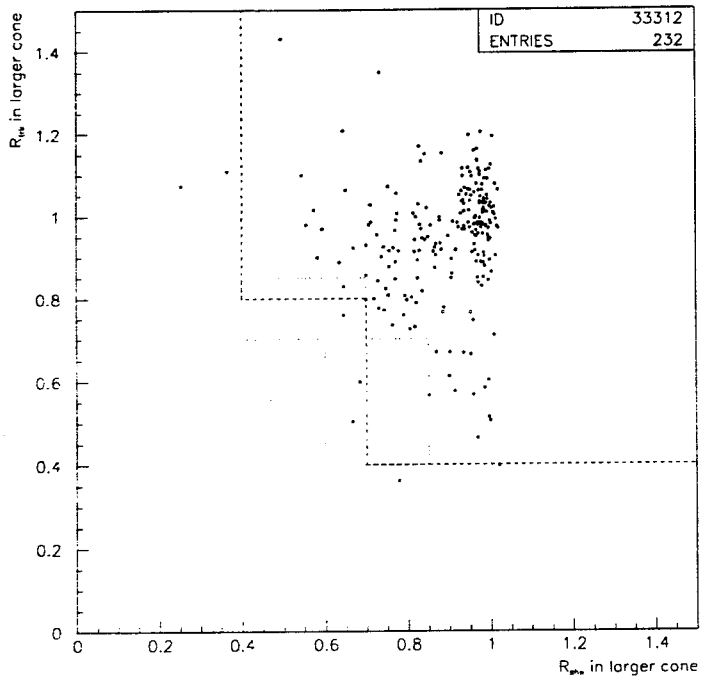

Figure 7.11: The R^{hc}_{trk} versus R^{hc}_{shw} distribution for 1994 Bhabha MC events that pass the tau pair selection cuts in the barrel region. The broken line indicates the cuts used for Bhabha enhancement and the dotted lines shows the region with little Bhabha background used for cross-checks as will be described at the end of this subsection.

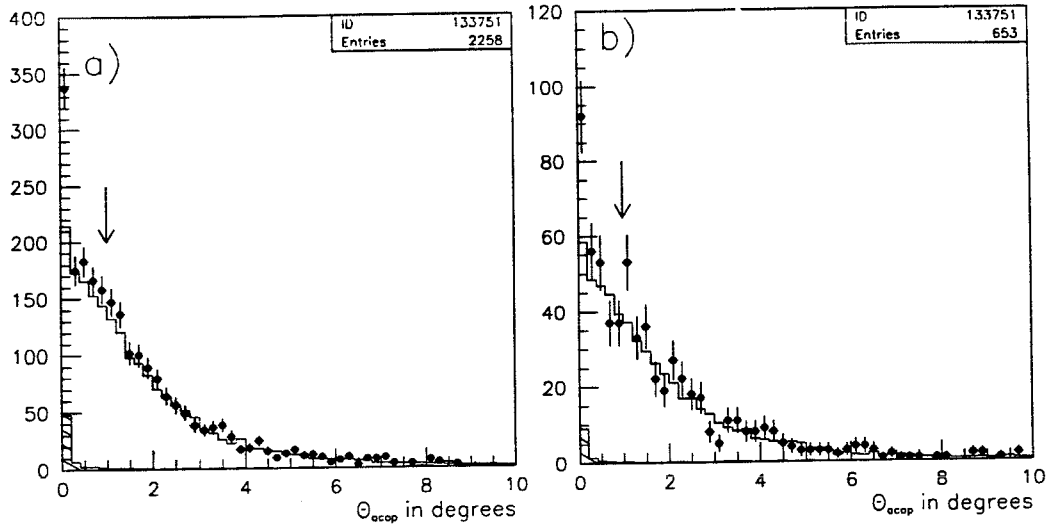

Figure 7.12: Acoplanarity distribution for events after all Bhabha enhancement cuts in the barrel region for (a) 1994 and (b) 1993 peak data and MC. The points are data, the open histograms total MC, and the hatched histograms MC background.

event was located near a gap or not. Therefore, the background estimate was done for the complete barrel region.

Figure 7.12 shows the acoplanarity distribution after all the Bhabha enhancement cuts in the barrel region have been applied. The data excess in the low acoplanarity region is assumed to be due to Bhabha events. In the region with $\theta_{acop} > 1.0$, a data MC ratio of 1.05 ± 0.03 for 1994 data and 1994 MC and a data MC ratio of 1.12 ± 0.06 for 1993 peak data and MC was observed. The statistics for the 1993 off-peak points is too low to deduce any statement about the data MC agreement, but it seems like a reasonable assumption that the 1993 off-peak data behaves qualitatively like the 1993 peak data. This data excess is due to somewhat different efficiencies of the Bhabha enhancement cuts for data and $\tau^+\tau^-$ MC. It was assumed that simular disagreements between data and tau MC exist in the regions $\theta_{acop} < 1.0$ and $\theta_{acop} > 1.0$, such that the excess of data over MC in the low acoplanarity region is not only due to a genuine excess of Bhabha background

year			Monte Carlo			
data	MC	data	$\tau\tau$ scaled	bkgr	total	data−MC
94	94	1020 ± 32	830 ± 27	60.9 ± 4.0	891 ± 27	129 ± 42
94	93	1020 ± 32	830 ± 30	41.5 ± 4.6	871 ± 30	149 ± 44
93 p	93	275 ± 17	253 ± 14	11.7 ± 1.3	265 ± 14	10 ± 22
93 p	94	275 ± 17	253 ± 14	17.1 ± 1.1	271 ± 14	5 ± 22
93 p−2	93	65 ± 8.1	48.4 ± 5.8	3.2 ± 1.0	51.6 ± 5.9	13 ± 10
93 p−2	94	65 ± 8.1	48.2 ± 5.8	5.6 ± 1.3	53.7 ± 5.9	11 ± 10
93 p+2	93	76 ± 8.7	76.5 ± 7.9	6.4 ± 1.2	82.9 ± 8.0	−7 ± 12
93 p+2	94	76 ± 8.7	76.7 ± 7.9	5.0 ± 0.7	81.6 ± 7.9	−6 ± 12

Table 7.6: Estimated excess of Bhabha background in the barrel region after Bhabha enhancement cuts and scaling tau pair MC as described in the text for different data MC combinations. For the off-peak 1994 MC, only Bhabha MC is for the 1994 detector, while all other MC is for the 1993 detector.

in the data, but at least partially also due to a disagreement of data and $\tau^+\tau^-$ MC. To check this assumption, the control region $\theta_{acop} > 1.0$ was separated into three subregions. The ratio of data to MC events in each of those subregions was consistent with the ratio of the whole region $\theta_{acop} > 1.0$. This indicates that the data and MC acoplanarity distributions agree well up to an overall scale factor. An additional test of the validity of the procedure to scale the $\tau^+\tau^-$ MC in the region $\theta_{acop} < 1.0$ by the data MC ratio observed in the region $\theta_{acop} > 1.0$ will be performed below.

In table 7.6 the excess of data over MC after scaling the $\tau^+\tau^-$ MC in the region $\theta_{acop} < 1.0$ as discussed above has been calculated. In the table, the 1993 and 1994 data was also combined with the MC of the respective other year. As expected, the excess is bigger in the case of 1993 MC, since for that MC the energy scale is higher, resulting in less events to fall below the cut at $R_{shw} = 0.8$ and to be consequently accepted in the tau sample. The difference between the data simulations for the two years could be observed in figure 7.5. The overall error of

year		e^+e^- bkgr.	e^+e^- excess	efficiency	add'l	total
data	MC	from MC	in data	for e^+e^- MC	bkgr.	bkgr.
94	94	61.1 ± 4.0	129 ± 42	0.880 ± 0.021	147 ± 48	208 ± 48
94	93	46.4 ± 4.9	149 ± 44	0.830 ± 0.039	179 ± 54	226 ± 54
93 p	93	13.1 ± 1.4	10 ± 22	0.830 ± 0.039	12 ± 26	25 ± 26
93 p	94	17.2 ± 1.1	5 ± 22	0.880 ± 0.021	5 ± 24	22 ± 24
93 p−2	93	3.5 ± 1.1	13 ± 10	0.800 ± 0.124	17 ± 13	20 ± 13
93 p−2	94	6.3 ± 1.3	11 ± 10	0.818 ± 0.081	14 ± 12	20 ± 12
93 p+2	93	6.6 ± 1.2	-7 ± 12	0.934 ± 0.045	-7 ± 13	-1 ± 13
93 p+2	94	4.9 ± 0.7	-6 ± 12	0.941 ± 0.034	-6 ± 13	-1 ± 13

Table 7.7: Total Bhabha background from MC in the barrel region and the estimate for additional background in the data that is not properly modeled in MC. The additional MC background was calculated by scaling the results from table 7.6 by the efficiency of the cuts from Bhabha MC.

the data MC difference is dominated by the statistical error of the data, which is 100% correlated when using the same data with different MC samples, such that the different size of the data excess for the two different Monte Carlo samples is indeed statistically significant.

In table 7.7 the complete Bhabha background in the barrel region is shown. For this table, the excess calculated in table 7.6 was first corrected for the efficiency of the Bhabha enhancement cuts as determined from Bhabha MC and then added to the Bhabha background observed directly from Bhabha MC. Results are shown in the table for combining data with the MC of the same year, and with the respective other year. It was checked that the total Bhabha background estimates for the same year with different MC agree within their statistical errors when taking into account only the uncorrelated part of the overall error due to the different MC samples.

The procedure of scaling the tau MC in the region $\theta_{acop} < 1.0$ according to the agreement in the region $\theta_{acop} > 1.0$ was checked by investigating the acoplanarity

distribution after the multihadron rejection cuts $N^{hc}_{trk} + N^{hc}_{cls} < 4$ in the region

$$(R^{hc}_{trk} > 0.7 \text{ AND } R^{hc}_{trk} < 0.85 \text{ AND } R^{hc}_{shw} > 0.4 \text{ AND } R^{hc}_{shw} < 0.7)$$

OR

$$(R^{hc}_{shw} > 0.6 \text{ AND } R^{hc}_{shw} < 0.85 \text{ AND } R^{hc}_{trk} > 0.4 \text{ AND } R^{hc}_{trk} < 0.7)\,,$$

where mainly tau pair events are expected. This region is indicated in figure 7.11 and was chosen to yield roughly the same statistics as the Bhabha enhancement cuts. The fraction of Bhabha events accepted by these cuts is negligible. For all four data sets it was found that the data MC ratios agree well for the low and the high acoplanarity region. Furthermore, the ratio of the number of events in the high and low acoplanarity region was found to be consistent for data and $\tau^+\tau^-$ MC, validating the scaling procedure used for the $\tau^+\tau^-$ MC.

As a further check of the background estimates in table 7.6, the distribution of R^{sc}_{trk}, the track momentum in the cone with the *smaller* visible energy (i.e. the cone on which the cuts (7.1) and (7.2) were *not* applied) after the Bhabha enhancement cuts, but without applying an acoplanarity cut, was investigated. This distribution is shown in figure 7.13. A clear excess of data in the region $R^{sc}_{trk} > 0.8$ can be observed for 1994, while for 1993 peak any potential excess is small compared to the statistical significance of the check.

Since the Bhabha MC distribution in figure 7.13 does not show a sharp cutoff for any value of R^{sc}_{trk}, Bhabha background was estimated from the excess observed in both the regions $R^{sc}_{trk} > 0.6$ and $R^{sc}_{trk} > 0.8$. A data MC disagreement was observed over the whole range of $R^{sc}_{trk} > 0.8$ with a size simular to that for the acoplanarity distribution discussed above, making it necessary to scale the $\tau^+\tau^-$ MC in the region where the data excess was calculated. The $\tau^+\tau^-$ MC in the region $R^{sc}_{trk} > 0.6$ was scaled by the data MC ratio observed in the region $R^{sc}_{trk} < 0.6$ and the $\tau^+\tau^-$ MC in the region $R^{sc}_{trk} > 0.8$ was correspondingly scaled by the data

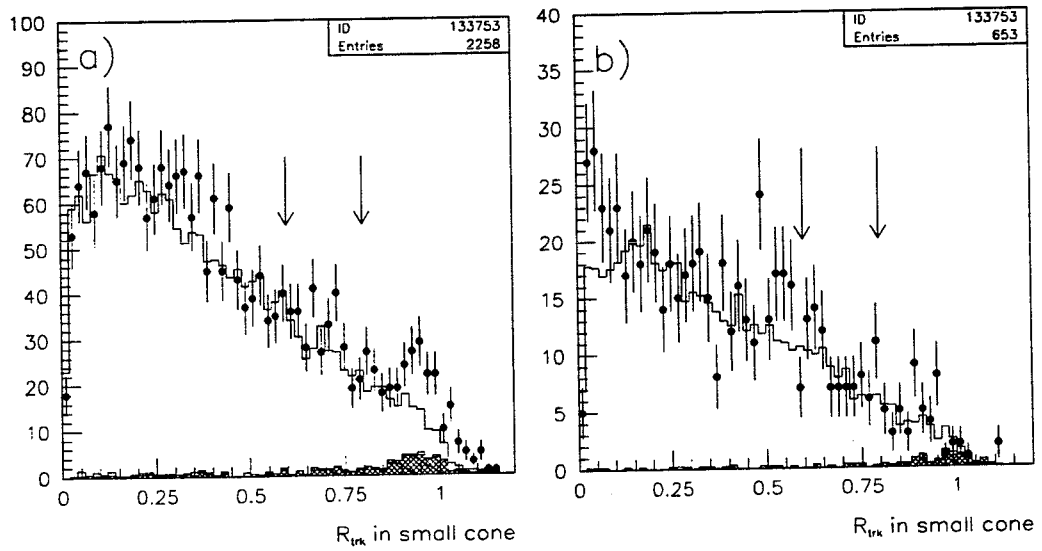

Figure 7.13: The relative track momentum distribution in the cone with the *smaller* visible energy after the Bhabha enhancement cuts on R^{hc}_{trk}, R^{hc}_{shw} and $N^{hc}_{trk}+N^{hc}_{cls}$ for (a) 1994 data and MC and (b) 1993 peak data and MC. The points are data, the open histograms total MC, the hatched histograms total background, and the shaded histograms Bhabha MC only. Bhabha background is expected to be concentrated near $R^{sc}_{trk} \approx 1$.

MC ratio in the region $R_{trk}^{sc} < 0.8$. The excess of data over MC in the two regions was calculated and the results were corrected by the respective Bhabha efficiency of the enhancement cuts from MC. The agreement with the results from table 7.7 was found to be quite good. In figure 7.13 one can observe the effect that would be expected from final state radiation: The Bhabha background shows tails extending down to $R_{trk}^{sc} \approx 0$. Consequently the efficiencies for this check are worse than for the Bhabha enhancement cuts used above and the estimates of the Bhabha excess rely quite heavily on an accurate simulation of bremsstrahlung in the Monte Carlo.

7.4.3 Background in the Forward Region

From studying Bhabha Monte Carlo, it was found that the Bhabha background in the tau pair sample can be basically divided into two classes: First, events in regions with high preshowering and second, highly radiative events, which are highly acollinear, and for which one electron has its track at $|\cos\theta| > 0.9$. For tracks beyond $|\cos\theta| \approx 0.9$, the tracking performance is rapidly degraded, and the track momentum is measured systematically too low. This is demonstrated in figure 7.14, where the difference of the track momentum and shower energy is shown for the individual cones versus the $|\cos\theta|$ value derived from the track momenta in the respective cone. The $\cos\theta$ derived from the track information in each cone separately will be denoted by $\cos\theta_{trk}^{cone}$. The difference between cone energy and shower energy is systematically below zero, since the tracking chamber does not record neutral particles. Over a large range of $|\cos\theta_{trk}^{cone}|$, data and MC show very good agreement. In the region of $0.7 \lesssim |\cos\theta_{trk}^{cone}| \lesssim 0.8$ one can see the effect of the preshowering material. Apart from that region, the difference between track momentum and shower energy is constant over $|\cos\theta_{trk}^{cone}|$, up to a sharp falloff

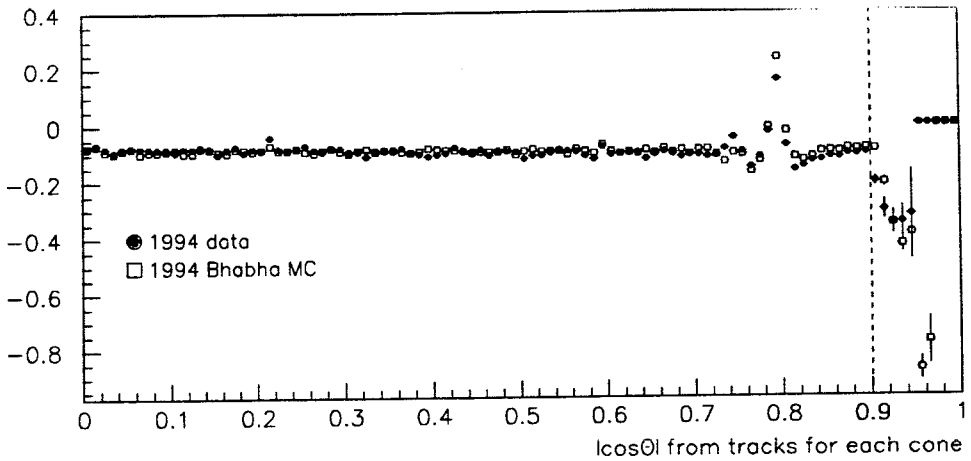

Figure 7.14: Track momentum minus shower energy per cone relative to the beam energy versus $|\cos\theta|$ derived from the track information in each cone, $|\cos\theta^{cone}_{trk}|$. Plotted are events which fail the Bhabha rejection cuts but pass all other tau pair selection cuts. The track momentum measurement becomes unreliable at $|\cos\theta^{cone}_{trk}| \approx 0.9$.

at $|\cos\theta^{cone}_{trk}| = 0.9$, as indicated by a broken line in the figure. The agreement between data and MC appears to be quite good, even though the MC seems to fall off at a slightly larger value of $|\cos\theta^{cone}_{trk}|$ and somewhat steeper than the data. These radiative events will be investigated first and then will be exclude from the study of the remaining Bhabha background.

Figure 7.15a shows the distribution of R^{cos}_{shw}, the shower energy divided by the beam energy in the cone with the larger value of $|\cos\theta^{cone}_{trk}|$, for events for which one cone fulfills $|\cos\theta^{cone}_{trk}| > 0.90$. The Bhabha background was estimated from the data excess in the region $R^{cos}_{shw} > 0.9$. In that region, good data-MC agreement was found for all four data sets. To check for potential underlying discrepancies of the data and $\tau^+\tau^-$ MC, a control region with $0.8 < R^{cos}_{shw} < 0.9$ was investigated. In that region with no significant Bhabha background, data was found to agree well with the Monte Carlo predictions. The procedure of estimating the Bhabha background from the region $R^{cos}_{shw} > 0.9$ and checking the

data MC agreement in the region $0.8 < R_{shw}^{cos} < 0.9$ was repeated for the cuts $|\cos\theta_{trk}^{cone}| > 0.85$ and 0.89. The results agreed well with the results obtained for the cut $|\cos\theta_{trk}^{cone}| > 0.90$. As a further check of the agreement between data

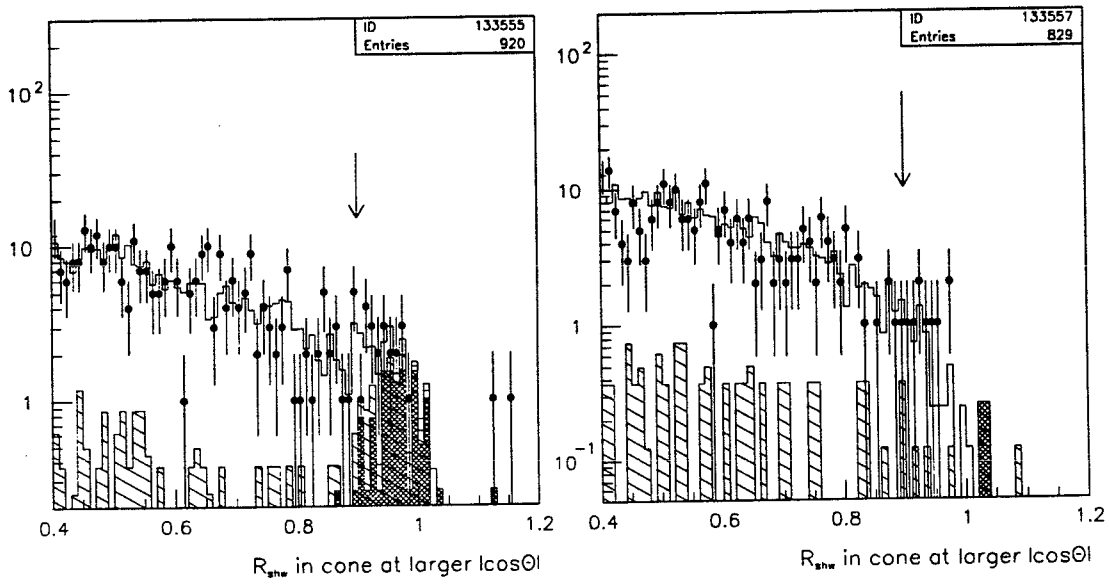

Figure 7.15: The R_{shw} distribution in cone with the larger $|\cos\theta_{trk}^{cone}|$ after all tau pair selection cuts and after requiring that the one cone have (a) $|\cos\theta_{trk}^{cone}| > 0.90$ or (b) $0.90 > |\cos\theta_{trk}^{cone}| > 0.89$ for 1994 data and MC. The points are data, open histograms MC, hatched histograms MC background and shaded histograms Bhabha MC. In figure b the Bhabha background in the region $R_{shw} > 0.9$ is largely suppressed.

and $\tau^+\tau^-$ MC, the Bhabha background was suppressed by choosing events in the region $0.89 < |\cos\theta_{trk}^{cone}| < 0.90$. The R_{shw}^{cos}-distribution for this selection is shown in figure 7.15b. For all four data sets, good agreement of data and MC was found after applying the cuts $0.89 < |\cos\theta_{trk}^{cone}| < 0.90$ for both the regions $0.8 < R_{shw}^{cos} < 0.9$ and $R_{shw}^{cos} > 0.9$.

The estimated background of radiative Bhabha events from the data MC difference in the region $|\cos\theta_{trk}^{cone}| > 0.90$ is shown in table 7.8 for the four data sets, each one compared with both 1993 and 1994 MC and corrected for the efficiency of the R_{shw} cut from Bhabha MC.

year data	MC	data−MC	eff. from e^+e^- MC	estimated bkgr.
94	94	-1.02 ± 5.26	0.958 ± 0.029	-1.06 ± 5.49
94	93	2.01 ± 5.62	0.798 ± 0.081	2.52 ± 7.05
93 p	93	2.09 ± 2.95	0.798 ± 0.081	2.62 ± 3.71
93 p	94	1.24 ± 2.89	0.958 ± 0.029	1.29 ± 3.02
93 p−2	93	-1.22 ± 1.71	0.669 ± 0.135	-1.82 ± 2.58
93 p−2	94	0.37 ± 1.53	0.667 ± 0.192	0.55 ± 2.30
93 p+2	93	5.76 ± 2.68	0.750 ± 0.217	7.56 ± 4.19
93 p+2	94	5.19 ± 2.68	0.708 ± 0.111	7.33 ± 3.96

Table 7.8: The background estimate from radiative Bhabha events with one badly measured track at $|\cos\theta_{trk}^{cone}| > 0.90$.

From 1994 Bhabha MC it was found that 20.7% of the Bhabha events passing the tau pair selection cuts have a cone with $|\cos\theta_{trk}^{cone}| > 0.90$. Now the remaining Bhabha background that enters the tau sample as a result of reduced visible energy due to preshowering or the low resolution of the electron calorimeter and/or the tracking chambers will be investigated. Figure 7.16a shows the distribution of track momentum versus shower energy relative to the beam energy in the cone with the higher visible energy for 1994 Bhabha MC in the forward region after all tau pair selection cuts have been applied. Comparing figure 7.16a with the corresponding figure 7.11 for the barrel region, one finds that the Bhabha background in the forward region is spread out over a much wider area in the $R_{shw} - R_{trk}$ plane. In order to define Bhabha enhancement cuts with a high efficiency, much looser cuts than in the case of the barrel region have to be applied. The cuts that were chosen are shown in figure 7.16 as broken lines and select events with

$$R_{shw}^{hc} > 0.5 \text{ OR } R_{trk}^{hc} > 0.4 \ .$$

As can be seen in figure 7.16b for muon MC, those cuts accept basically all the muon background in the forward region. The muon background populates the

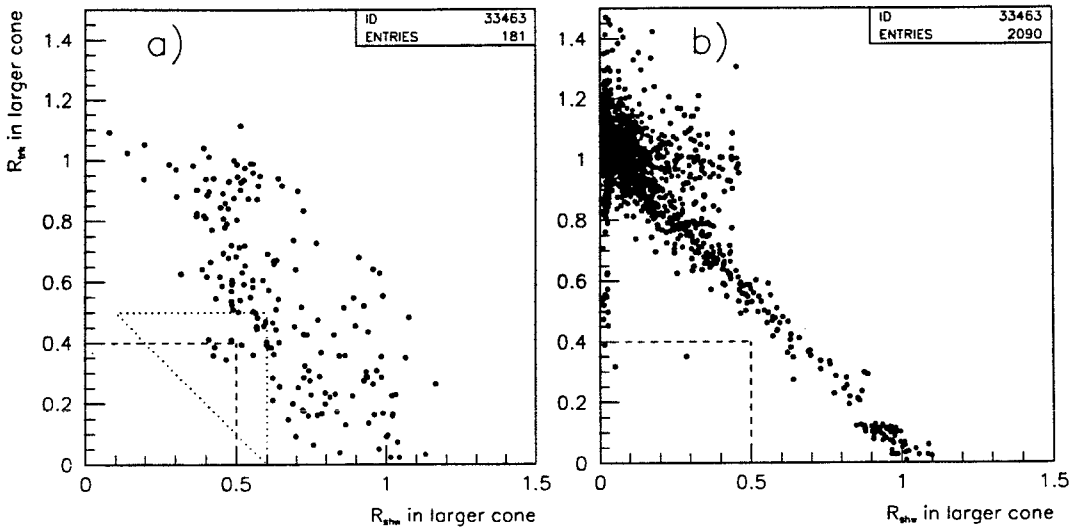

Figure 7.16: Distribution of track momentum versus shower energy divided by the beam energy in the cone with the higher visible energy after all tau pair selection cuts have been applied for (a) 1994 Bhabha MC and (b) 1994 muon MC in the forward region. Cuts to enhance the Bhabha background are shown by broken lines, while a control region with little Bhabha background is indicated in plot (a) by a dotted line. Plot (b) shows clearly that additional cuts are necessary to reject muon events.

region with $R^{hc}_{shw} + R^{hc}_{trk} \approx 1.0$, where the large shower energy of some of the muons is due to final state radiation. Therefore all events which have a muon in either cone as identified by the electromagnetic calorimeter, the muon chamber or the hadron calorimeter were rejected. As in the barrel region, multihadronic events were rejected by requiring

$$N^{hc}_{trk} + N^{hc}_{cls} < 4 \ .$$

The acoplanarity distribution after all the cuts described above is shown in figure 7.17. For the forward region, an excess of MC (rather than data) in the control region with $\theta_{acop} > 2.0$ was observed. The data MC ratio in the control region was 0.954 ± 0.024 , 0.977 ± 0.045 , 0.863 ± 0.089 , and 0.917 ± 0.079 for 1994, 1993 peak, 1993 peak-2, and 1993 peak$+2$ data and MC, respectively. The region $\theta_{acop} > 2.0$

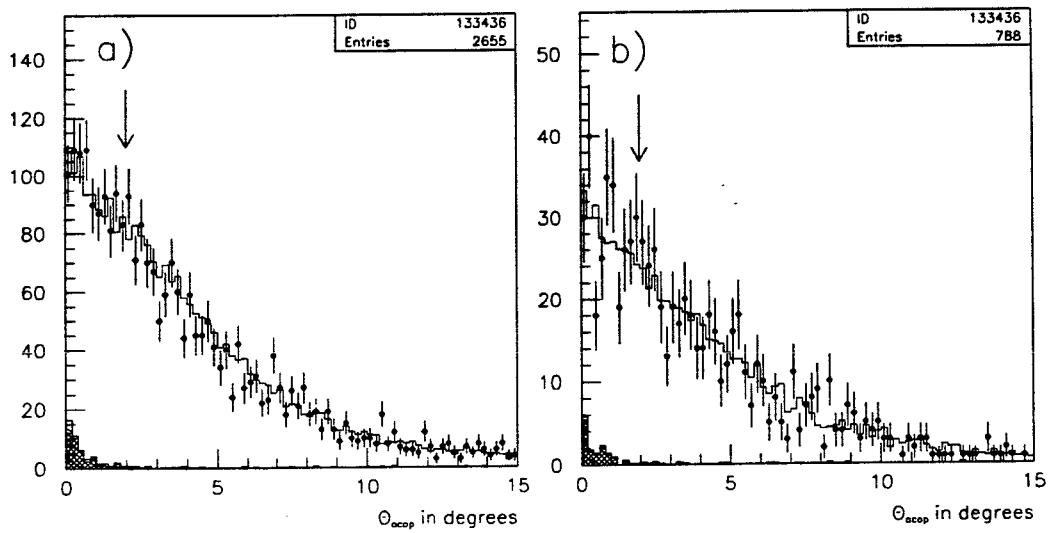

Figure 7.17: Acoplanarity distribution for events after all Bhabha enhancement cuts in the forward region for (a) 1994 and (b) 1993 peak data and MC. The points are data, the open histograms MC, the hatched histograms MC background and the shaded histograms Bhabha MC only.

was divided into three subregions and no evidence was found that the data MC disagreement shows any dependence on the acoplanarity angle. Therefore, the tau pair MC in the region $\theta_{acop} < 2.0$ was scaled by the data MC ration observed in the region $\theta_{acop} > 2.0$. The excess of data over MC in the region $\theta_{acop} < 2.0$ was then corrected for the Bhabha efficiency of the enhancement cuts as obtained from Bhabha MC. The resulting estimate of the data excess in the forward region is shown in table 7.9.

In order to check the assumption that the data-MC disagreement is independent of the acoplanarity angle, a control region was defined by selecting events with

$$R^{hc}_{shw} < 0.6 \text{ AND } R^{hc}_{trk} < 0.5 \text{ AND } R^{hc}_{shw} + R^{hc}_{trk} > 0.6 \, .$$

These cuts are shown as dotted lines in figure 7.16a. The same multiplicity cut and

year data	year MC	data	tot MC with $\tau\tau$ scaled	data−MC	e^+e^- eff. from MC	estimted excess
94	94	955 ± 31	897 ± 24	58 ± 39	0.839 ± 0.027	70 ± 47
94	93	955 ± 31	920 ± 28	35 ± 41	0.815 ± 0.036	42 ± 51
93 p	93	284 ± 17	272 ± 13	12 ± 21	0.815 ± 0.036	15 ± 26
93 p	94	284 ± 17	265 ± 12	19 ± 21	0.839 ± 0.027	22 ± 25
93 p−2	93	53 ± 7.3	52.9 ± 5.2	0.1 ± 8.9	0.727 ± 0.094	0 ± 12
93 p−2	94	53 ± 7.3	55.4 ± 5.2	-2.4 ± 9.0	0.900 ± 0.054	-3 ± 10
93 p+2	93	83 ± 9.1	77.8 ± 6.7	5.2 ± 11.3	0.853 ± 0.079	6 ± 13
93 p+2	94	83 ± 9.1	76.6 ± 6.6	6.5 ± 11.3	0.864 ± 0.065	8 ± 13

Table 7.9: Estimated excess of Bhabha background in the forward region for $|\cos\theta_{trk}^{cone}| < 0.90$ after Bhabha enhancement cuts and scaling $\tau^+\tau^-$ MC as described in the text. Combinations of data with different MC are shown. For the off-peak 1994 MC, only Bhabha MC is for the 1994 detector, while all other MC is for the 1993 detector.

muon rejection as described above are also applied. The acoplanarity distribution for events passing these cuts was investigated. Since the Bhabha events are much less localized in the $R_{trk}^{hc} - R_{shw}^{hc}$ plane for the forward region than for the barrel region, the control sample has only about 40% of the statistics of the event sample selected by Bhabha enhancement cuts. The fraction of Bhabha background compared to figure 7.17 was reduced by about 60%. On this level of statistics, the data-MC ratio was found to be consistent for the regions $\theta_{acop} > 2.0$ and $\theta_{acop} < 2.0$. Furthermore, the ratio of events between the two regions agreed well for data and MC. We conclude that the procedure of scaling the $\tau^+\tau^-$ MC in the region $\theta_{acop} < 2.0$ by the data-MC ratio observed in the region $\theta_{acop} < 2.0$ is indeed valid.

In order to conduct a cross check of the Bhabha background estimate in the forward region, Bhabha enhancement cuts were applied which were somewhat

modified from those above. First, events were required to have $R_{trk} < 0.8$. This cut effectively rejects muon events, since a large number of muon events leak into the tau sample in the geometric region $70\,\text{deg} \lesssim \phi \lesssim 110\,\text{deg}$ of the endcap region. The muon detector endcaps are not sensitive in those regions, resulting in muon pair events in those regions to be less likely identified as such. If a genuine muon pair event is not selected by the muon pair selection cuts, it is consequently not rejected from the tau pair sample. These events can be seen in figure 7.4 for low R_{shw} values at $R_{trk} \approx 1.0$ and in figure 7.10 at $R_{shw} < 0.25$. The R^{hc}_{trk} versus R^{hc}_{shw} distribution for events with $R_{trk} < 0.8$ in the forward region is shown in figure 7.18. It was then required

$$R^{hc}_{shw} + R^{hc}_{trk} > 0.8 \text{ AND } R^{hc}_{shw} > 0.2$$

and multihadronic events were as before rejected by the cut $N^{hc}_{trk} + N^{hc}_{cls} < 4$. Requiring $R^{hc}_{shw} > 0.2$ rejects most of the remaining background from muon events emitting final state radiation.

The acoplanarity distribution after these "alternative" Bhabha enhancement cuts is shown in figure 7.19. This distribution shows a qualitative behavior very simular to the acoplanarity distribution after the original Bhabha enhancement cuts shown in figure 7.17: The region $\theta_{acop} > 2.0$ shows an excess of MC over data which however does not seem to have any dependence on the acoplanarity. As before, the $\tau^+\tau^-$ MC in the region $\theta_{acop} < 2.0$ was scaled by the data MC ratio observed in the region $\theta_{acop} > 2.0$.

The data excess in the region $\theta_{acop} < 2.0$ for the alternative Bhabha enhancement cuts, after scaling the $\tau^+\tau^-$ MC and after applying an efficiency correction derived from Bhabha MC, was compared to the results from table 7.9. The only data MC comparison for which a fairly big difference between the two methods

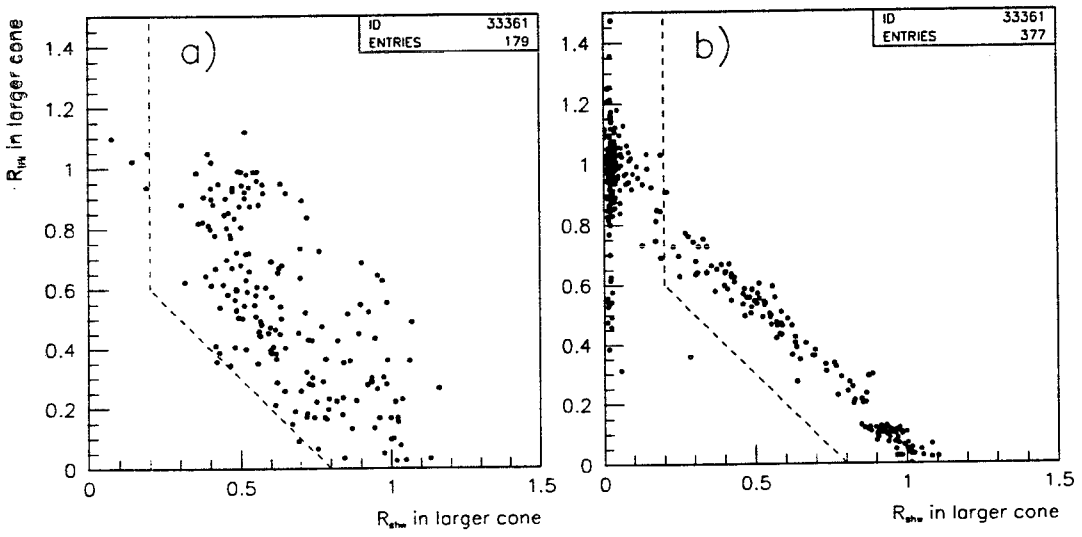

Figure 7.18: The distribution of the track momentum versus the shower energy divided by the beam energy in the cone with the larger visible energy after all tau pair selection cuts and requiring $R_{trk} < 0.8$ in the forward region. Plot (a) shows 1994 Bhabha MC and plot (b) 1994 muon MC. The alternative cuts to enhance the Bhabha background as described in the text are shown by broken lines. The muon background in plot (b) is much stronger suppressed than in figure 7.16.

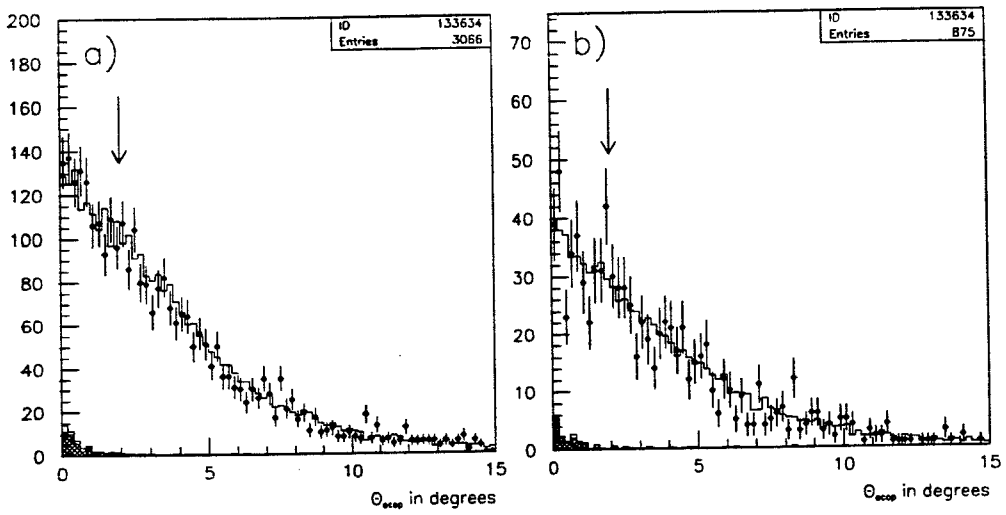

Figure 7.19: Acoplanarity distribution after the "alternative" Bhabha enhancement cuts described in the text for 1994 (a) and 1993 peak (b). The points are data, the open histograms MC, the hatched histograms MC background and the shaded histograms Bhabha MC.

could be observed was 1994 data with 1993 peak MC. Taking error correlations into account, it was found that the two results agreed on a level of no worse than 1.3σ, which was considered acceptable [68].

For the final Bhabha background estimate in the forward region, the results from the tables 7.9 and 7.8 and the Bhabha background from MC were added. The results are shown in table 7.10.

In analogy to the background estimate in the barrel region, it was checked that the total Bhabha background estimates in the forward region for the same year compared to different MC samples agree within their statistical errors when taking into account only the uncorrelated part of the overall error due to the different MC samples.

year		e^+e^- MC	excess from	remaining	total
data	MC	bkgr.	radiative events	excess	bkgr.
94	94	58.84 ± 3.88	-1.06 ± 5.49	69.63 ± 46.78	127.41 ± 47.26
94	93	71.20 ± 6.03	2.52 ± 7.05	42.36 ± 50.90	116.08 ± 51.74
93 p	93	20.03 ± 1.70	2.62 ± 3.71	14.59 ± 25.85	37.24 ± 26.17
93 p	94	16.56 ± 1.09	1.29 ± 3.02	22.54 ± 24.54	40.39 ± 24.75
93 p−2	93	11.57 ± 1.96	-1.82 ± 2.58	0.10 ± 12.30	9.85 ± 12.72
93 p−2	94	10.23 ± 1.69	0.55 ± 2.30	-2.61 ± 9.97	8.17 ± 10.37
93 p+2	93	5.28 ± 1.08	7.56 ± 4.19	6.12 ± 13.26	18.96 ± 13.95
93 p+2	94	4.67 ± 0.70	7.33 ± 3.96	7.47 ± 13.06	19.47 ± 13.08

Table 7.10: Total Bhabha background from MC and the estimate for additional background in the data that is not properly modeled in MC for the forward region for different data MC combinations.

7.4.4 Total Bhabha background

In table 7.11 the estimates for the Bhabha background in the barrel and the forward region from tables 7.7 and 7.10 were added to yield the final correction factor. The final background estimate is virtually independent of the MC samples that were used to derive the results.

7.5 Muon Events

The procedure of discarding events which are classified as muon pair events from the tau pair sample has the effect that the single muon rejection cut from section 7.2.3 really is composed of multiple cuts, each one applied on quantities which are not identical to the quantities used for the tau pair analysis. This does not have any serious consequences for the assessment of background from muon events leaking into the tau pair sample, but it does make a comparison of data and MC for genuine tau pair events, which are classified as muon pair events and consequently are discarded from the tau pair sample, more difficult. However, the

year					correction
data	MC	barrel	forward	total	factor
94	94	208 ± 48	127 ± 47	336 ± 67	0.9940 ± 0.0012
94	93	226 ± 54	116 ± 52	342 ± 75	0.9939 ± 0.0013
93 p	93	25 ± 26	37 ± 26	62 ± 37	0.9960 ± 0.0024
93 p	94	22 ± 24	40 ± 25	63 ± 35	0.9960 ± 0.0022
93 p−2	93	20 ± 13	10 ± 13	30 ± 18	0.9912 ± 0.0053
93 p−2	94	20 ± 12	8 ± 10	28 ± 16	0.9917 ± 0.0047
93 p+2	93	-1 ± 13	19 ± 14	18 ± 19	0.9962 ± 0.0040
93 p+2	94	-1 ± 13	19 ± 13	18 ± 18	0.9961 ± 0.0038

Table 7.11: Combined background from the barrel and endcap region and final estimate for the correction and systematic error due to the Bhabha background. The correction factors resulting from combining data with the MC of the respective other year are shown for comparison.

discarded muon events are characterized by a high visible energy as defined in section 7.2.1. Figure 7.20 shows the R_{vis} distribution for events discarded from the tau pair sample as muon pair events but passing all other tau pair selection cuts. Clearly, by investigating the region $R_{vis} \lesssim 0.85$, most of the muon pair events which are discarded from the tau pair sample are rejected, while basically all tau pair events are selected. This separation between tau pair and muon pair events will allow for an investigation of tau pair events being mistakenly discarded as muon pair events, as will be described in section 7.5.2.

A detailed description of the cuts applied to select muon events can be found in [66]. The basic elements of the cuts are the following [14]: Two tracks, each having a momentum greater than 6 GeV, matched to the beam interaction point and identified as a muon by at least one outer detector (the electromagnetic calorimeter, the hadron calorimeter or the muon chambers), are required. Multihadronic events are rejected by removing events with more than three charged tracks, after applying corrections for additional tracks due to photon conversion and "track

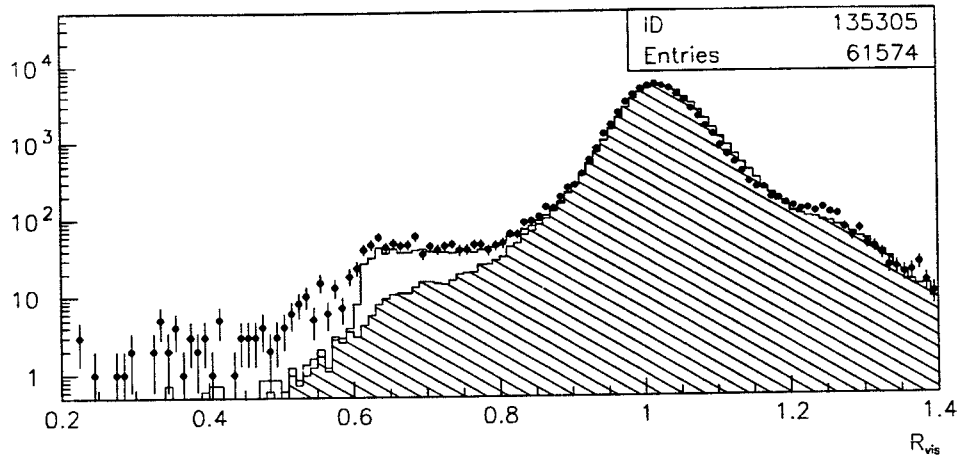

Figure 7.20: The R_{vis} distribution for events that are discarded as muon pair events but pass all other tau pair selection cuts for 94 data and MC. The points are data, the open histogram is the total MC and the hatched histogram is the background MC.

splitting" of tracks close to the anode wires in the jet chamber. Remaining tau pair and two-photon backgrounds are rejected by a requirement that the sum of the two highest momentum tracks plus the highest energy electromagnetic cluster be at least $0.6 \cdot \sqrt{s}$.

These cuts fail to identify a large number of genuine muon events which have a track close to a CJ anode wire: In those regions, the momentum measurement is not very accurate, resulting in reconstructed track momenta which are up to several tens of GeV different from the true value. To reduce the number of muon pair events with too low a reconstructed track momentum that are leaking into the tau pair sample, events which pass "alternative" muon selection cuts are also discarded from the tau sample. For this selection, events with back-to-back segments in the muon chamber and the electromagnetic calorimeter consistent with a muon pair event are investigated. An event then passes the alternative selection, if at least one of its tracks is close to an anode or cathode wire, or if one of the charged tracks is classified as a "very high quality" track. A "very high quality"

track is defined by tightened requirements on the proximity of the track to the interaction point, the track momentum and the number of axial CV wires that fired.

7.5.1 Efficiency of Muon Rejection Cuts

Events that fail the tau pair selection due to the muon pair rejection only were investigated and tau pair events in this sample were enhanced by the following cuts:

- $\theta_{acop} \geq 0.5\,\mathrm{deg}$
- event should not be within 1 deg of an anode plane.

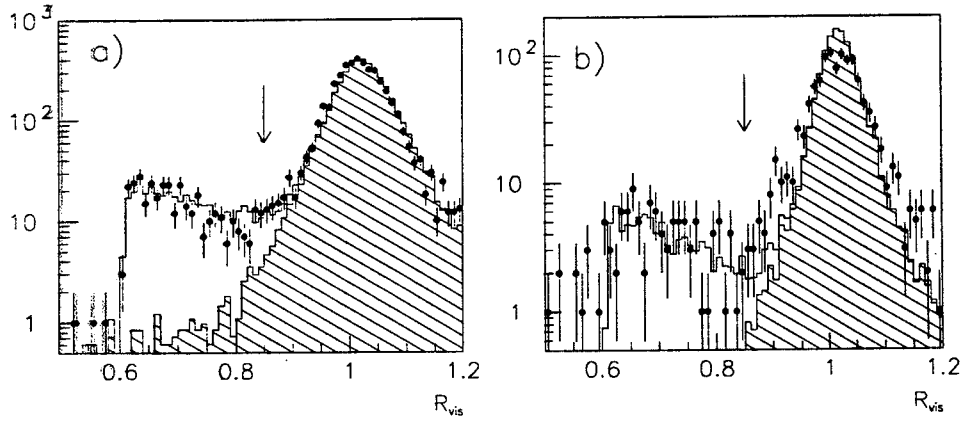

Figure 7.21: The distribution of the relative visible energy for events which fail the tau pair selection cuts due to the muon pair rejection only and pass the tau enhancement cuts explained in the text. Shown are (a) 1994 data and MC and (b) 1993 peak data and MC. The points are the data, the open histograms contain all MC samples and the hashed histograms are the background MC, which is almost exclusively muon pair MC.

In figure 7.20 an excess of data events that are discarded from the tau pair event sample in the region $R_{vis} < 0.6$ could be observed. Data events in this region were found to be located near the CJ wires and having a very low shower energy, a low

acoplanarity angle and a muon identified by the outer detectors in at least one cone. These events were therefore assumed to be muon pair events that have too low a track momentum assigned and were not assumed to be candidates for tau pair events failed by the muon rejection cuts.

Figure 7.21 shows the distribution of the relative visible energy for events passing the tau pair enhancement cuts from above for 1994 and 1993 peak data and MC. The muon pair events can be seen at high R_{vis} values. The agreement between data and MC was examined in the region $0.4 \leq R_{vis} \leq 0.85$ as indicated by the arrow in the plots. The muon peak is much better simulated by the 1994 MC, while the region $0.85 \leq R_{vis} \leq 1.0$ shows some disagreement between data and MC for all Monte Carlo samples. This disagreement is presumably due to a bad simulation of the muon pair events and could affect the muon pair MC in the region $0.4 \leq R_{vis} \leq 0.85$ as well. Therefore, the muon pair MC in the region $0.4 \leq R_{vis} \leq 0.85$ was multiplied by the data MC ratio in the region $0.85 \leq R_{vis} \leq 1.0$ minus 1, and the result assigned as an additional error. The errors derived in this fashion are $(1.19 - 1) \cdot 33.0 = 6.3$ for 1994 data and MC, $(1.23 - 1) \cdot 5.5 = 1.3$ for 1993 peak data and MC, $(1.34 - 1) \cdot 1.9 = 0.6$ for 1993 p$-$2 data and MC, and $(1.09 - 1) \cdot 2.6 = 0.2$ for 1994 p+2 data and MC. The data MC difference in the region $0.9 \leq R_{vis} \leq 1.0$ is -23.7 ± 29.1 for 1994 data and MC, 17.8 ± 10.5 for 1993 peak data and MC, -2.4 ± 4.2 for 1993 p$-$2 data and MC, and 8.2 ± 6.1 for 1994 p+2 data and MC. Here the error is composed of the statistical error from the data MC difference and the additional error due to the data MC disagreement in the region $0.85 \leq R_{vis} \leq 1.0$, which were conservatively added linearly. The result was then divided by the efficiency of about 0.58 for the cuts derived from tau pair MC. The results are shown in table 7.12.

data sample	estimated data excess	correction factor
1994	-40.6 ± 44.5	0.9993±0.0008
1993 peak	30.4 ± 20.0	1.0019±0.0013
1993 p−2	-4.2 ± 7.4	0.9988±0.0022
1993 p+2	14.1 ± 10.5	1.0030±0.0022

Table 7.12: The estimated data excess of events discarded as muon pair events. In the last column, the resulting correction factors and errors are shown.

7.5.2 Muon Background

The muon pair background in the tau pair sample is estimated from MC to be about 0.75%. A part of the muon pair events leak into the tau pair sample because one of the muons has radiated a photon, such that the acoplanarity is degraded and should not be relied on for enhancing muon pair events. Radiative muon pair events could already be observed in figure 7.16b as events with a shower energy much bigger than zero and a relative visible energy of about 1 in the cone with the higher visible energy. Therefore, muon pair events were enhanced by using cuts which require a low shower energy in one cone and a visible energy of about 1. Figure 7.22 shows examples of plots from these samples. The events in figure 7.22a were selected by requiring that the cone with R_{vis}^{cone} closest to 1 has $R_{shw}^{cone} < 0.2$. The visible energy divided by the beam energy of the opposite cone (R_{vis}^{opp}) is then plotted. Figure 7.22b shows the relative visible energy for events in which one cone has a relative visible energy in the range 0.7 to 1.3 and a relative shower energy of less than 0.2. Muon pair events (shown by the shaded histograms) should appear at values around 1 in these distribution and there is good agreement between data and MC in the region indicated by the arrows. From the agreement of the number of data and MC events in the region $0.8 < R_{vis}^{opp} < 1.3$ from figure 7.22a, the background correction factor was derived. First, the data MC ratio outside

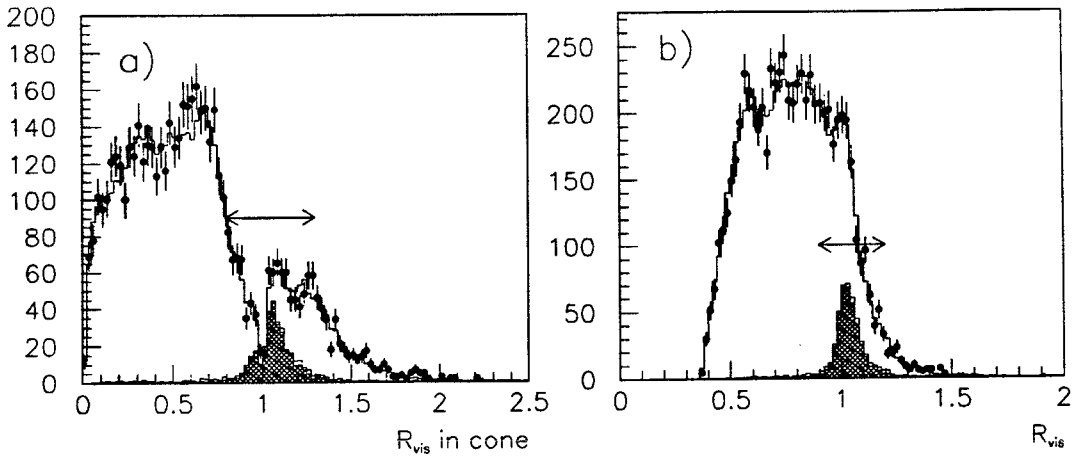

Figure 7.22: The points are data, the open histogram contains all MC samples, the hashed histogram the MC background samples and the shaded histogram is the muon pair MC only. Plot (a) shows the relative visible energy in an individual cone and plot (b) shows the total visible energy for events selected as described in the text.

this region was calculated, and the tau MC in the region $0.8 < R_{vis}^{opp} < 1.3$ was scaled by this ratio. The resulting scaling factors were 1.017 ± 0.015 for 1994 data and MC, 0.962 ± 0.028 for 1993 peak data and MC, 1.081 ± 0.065 for 1993 p$-$2 data and MC, and 0.953 ± 0.052 for 1994 p+2 data and MC. Then the data MC difference was calculated in the region $0.8 < R_{vis}^{opp} < 1.3$, and the result divided by the efficiency of the cuts for muon pair MC. The efficiencies were about 0.65 for the four different muon MC samples. The resulting estimate for the background that is not modelled by the MC and the background predictions from MC are shown in table 7.13. Varying the region of the R_{vis}^{opp} cuts had no significant effect on the results.

It was also investigated if events failed the muon pair selection cuts due to bad tracking and hence end up in the tau pair sample. Such events may not show up in the above checks because the badly measured track would lead to a visible energy significantly different from the beam energy. In order not to rely

data sample	MC prediction	extra bckgnd	correction factor
1994	424.3 ± 7.2	-33.4 ± 49.2	0.9930 ± 0.0009
1993 peak	116.1 ± 3.4	8.9 ± 24.6	0.9920 ± 0.0016
1993 p−2	24.6 ± 1.0	-4.7 ± 11.9	0.9942 ± 0.0035
1993 p+2	36.5 ± 1.5	3.2 ± 14.0	0.9917 ± 0.0029

Table 7.13: Muon pair background estimates from the MC and the estimate of additional background in the data samples.

on any track information, a sample of events in which the muon pair background has been enhanced is selected using muon identification from the outer detectors. For events with at least one identified muon in each cone and an acoplanarity of $\theta_{acop} < 2$ deg, figure 7.23 shows the ϕ distribution modulo 15 deg (i.e. a CJ sector). With the alternative muon pair selection cuts used to reject muon pair events with bad tracking, the extra muon pair background not modelled by the MC was dramatically reduced [68]. In figure 7.23, no significant extra muon pair background can be noticed near the CJ wires. Figure 7.24 shows the acoplanarity distribution for events with at least 1 identified muon in each cone for 1994 data compared to 1994 MC. The excess of events seen at low θ_{acop}, indicated by the arrow in figure 7.24 is assumed to be due to background muon pair events in the tau sample which are not well simulated by the $e^+e^- \rightarrow \mu^+\mu^-$ MC *and* due to muons from cosmic ray events. The Monte Carlo simulations that were compared to data did not include cosmic ray events and as will be discussed in section 7.8, cosmic ray events consist essentially of muons. If these traverse the detector close to the interaction point, their apparent acoplanarity is near zero. The excess in the region $\theta_{acop} < 0.5$ deg was found to be almost completely due to cosmic ray events. After subtracting the contribution expected from cosmic ray events, the data MC agreement observed in the region $\theta_{acop} < 0.5$ deg was found to be consistent with

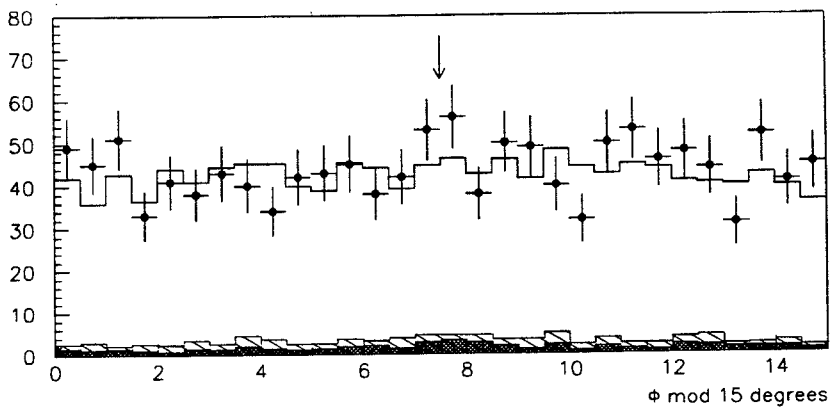

Figure 7.23: The ϕ(mod 15 deg) distribution for events with one identified muon in each cone and $\theta_{acop} < 2\,\mathrm{deg}$ which pass all tau pair selection cuts. The arrow indicates the position of the CJ-wires. The points are data, the open histogram total MC, the hashed histogram background MC only and the shaded histogram muon pair MC only.

the results of a data excess consistent with zero from table 7.13.

From figure 7.24 it can be seen that the low acoplanarity region being used for this check also contains background from sources other than muon pairs. This background (the hashed region of the plot) was found to be mostly from two photon events with final state $e^+e^-\mu^+\mu^-$ and to a smaller degree from multihadron events. A cut was applied on the transverse momentum ($p_T \geq 0.02\ E_{beam}$) to remove the two photon events and on the number of tracks (N_{trk} <5) to remove the multihadron events. These cuts reduces the fraction of $e^+e^-\mu^+\mu^-$ events in the background sample from 41% to 6% and the multihadron fraction from 11% to 1.5%, respectively. The data MC agreement in the low acoplanarity region was not affected by the cuts.

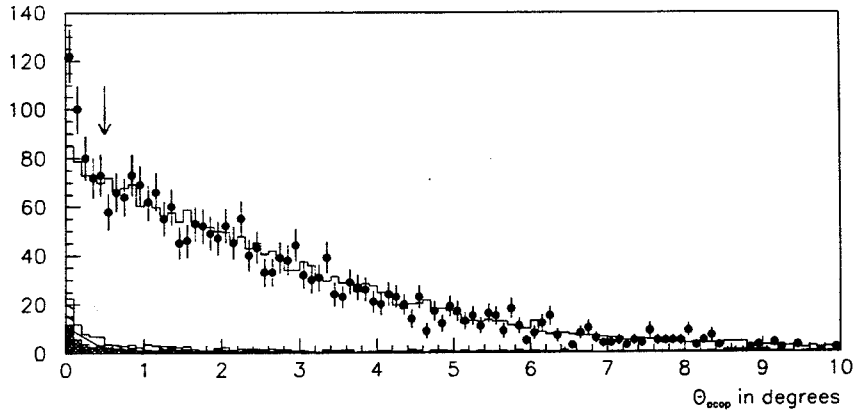

Figure 7.24: Acoplanarity distribution for events with one identified muon in each cone for 1994 data and 1994 MC. The points are data, the open histogram contains all MC samples, the hashed histogram background MC, abd the shaded histogram is the muon pair MC only.

7.6 Multihadronic Events

Due to its hadronic decay modes, a decaying τ lepton can mimic a fragmenting quark. The tau lepton has a probability of about 14% to decay into three or more charged particles, the probability for both taus to decay into a combined number of six or more charged tracks is about 2%. Figure 7.25 shows the distribution of the number of charged tracks N_{trk} and of the total multiplicity N_{tot} after all other tau pair selection cuts have been applied. The cuts on the total multiplicity and the number of charged tracks that are applied to reject multihadronic events from the tau pair sample are indicated by arrows. Figure 7.26 compares the data and MC distributions of the number of charged cones. The background discarded by the the N_{cone} cut consists to 97% of multihadronic events.

Monte Carlo predictions for the multihadron background in the tau pair sample vary considerably between different MC samples as shown in table 7.14. There

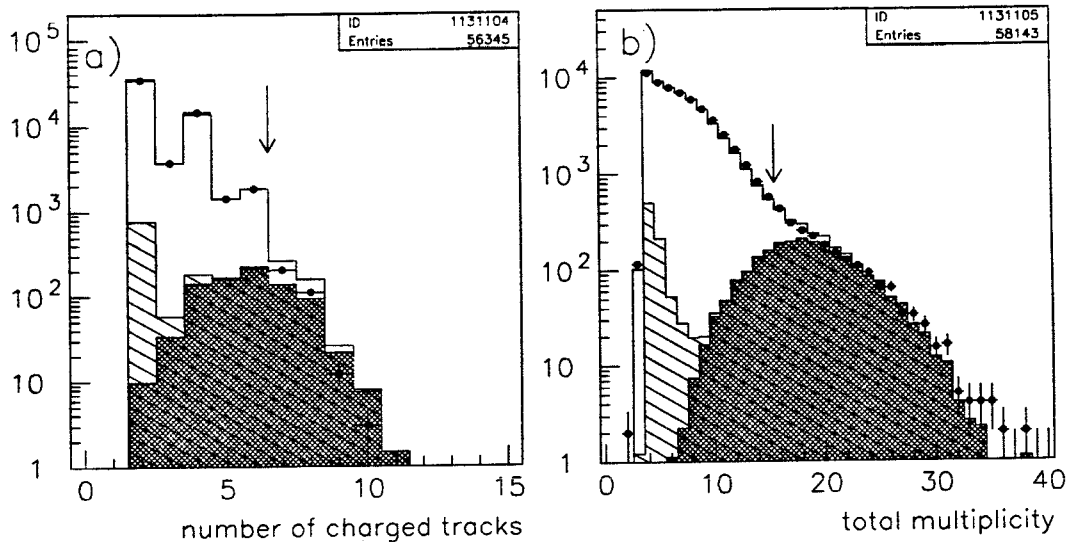

Figure 7.25: (a) The distribution of the charged track multiplicity and (b) the distribution of the total multiplicity after applying all other tau pair selection cuts for 1994 data and MC. The points are data, the open histogram the complete MC, the hatched histogram the background MC, and the shaded histogram multihadron MC only.

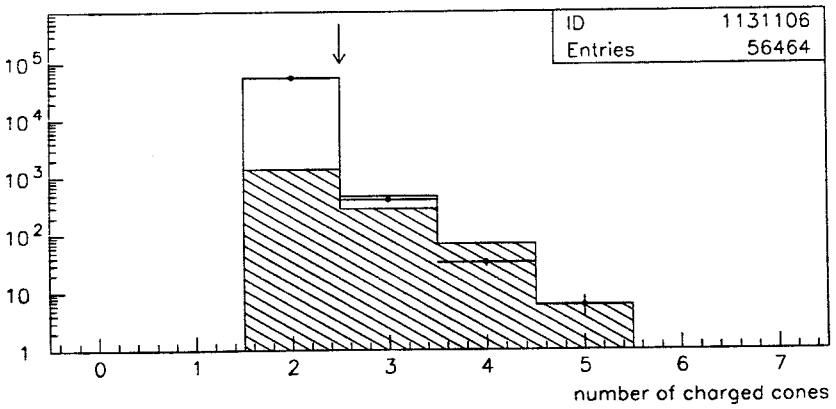

Figure 7.26: The distribution of the number of charged cones after all other tau pair selection cuts have been applied for 1994 data and MC. The points are data, the open histogram the complete MC and the hatched histogram the background MC.

year	generator	$\int \mathcal{L}dt$ $(pb)^{-1}$	predicted background
1994	Jetset	131.6	$(1.014 \pm 0.026)\%$
1993	Jetset	65.4	$(0.393 \pm 0.023)\%$
1994	Herwig	15.0	$(0.833 \pm 0.069)\%$
1992	Herwig	17.4	$(0.822 \pm 0.066)\%$

Table 7.14: Monte Carlo predictions for multihadron background in the tau pair samples for different MC samples and the luminosity corresponding to the number of produced Monte Carlo events.

is a large change in the background predicted by Jetset between the 1993 and 1994 MC samples. This is mostly due to changes in the distribution of clusters in the electromagnetic calorimeter as a result of tuning Jetset production rates and decay tables [69], [70].

It was found most effective to define a set of cuts to enhance multihadronic events which were then used for both the assessment of inefficiencies of the multihadronic rejection cuts and the multihadronic background in the tau pair sample. In order to use this background estimate for the calculation of the inefficiency of the multiplicity cuts, the cuts on the total multiplicity and on the number of charged tracks were relaxed until almost no tau pair MC events were rejected by the cuts. For these relaxed cuts, the multihadronic background was estimated and subtracted from the number of data events accepted by the relaxed cuts. The result was compared to the tau pair MC and any discrepancies were attributed to discrepancies between the data and tau pair MC. This procedure (which does not include any effects of the cut on the number of charged cones) will be described in subsection 7.6.1.

Unfortunately, it is rather difficult to define enhancement cuts for multihadronic events which do not depend heavily on the efficiencies predicted for those cuts by

multihadronic MC. Therefore it has to be shown that the corrections that will be derived for the multihadronic background account for the differences between the uncorrected Monte Carlo predictions from table 7.14.

The remainder of this section is divided into four subsections: In the first one, the cuts to enhance multihadronic events will be derived. In the second subsection, the agreement between data and tau pair MC for events that fail the multihadron rejection cuts will be investigated. In the third subsection, the multihadronic background in the tau pair sample will be estimated. For the assessment of multihadron background, cross checks will be presented in which events with three or more charged cones are investigated. This leads to the fourth subsection, where the inefficiencies due to the cut on the number of charged cones will be compared for data and tau pair MC.

7.6.1 Enhancment Cuts for Multihadronic Events

The following cuts were applied to enhance multihadronic events:

- $min(M_{inv}^{cone}) > 1.0$
- $6 < \Sigma(M_{inv}^{cone}) < 15$,

where $min(M_{inv}^{cone})$ is the minimum invariant mass of the two cones and $\Sigma(M_{inv}^{cone})$ is the sum of the invariant masses of the two cones. The invariant mass is derived for each cone from the combined information of the electromagnetic clusters and the charged tracks. The efficiency of these cuts depends very strongly on the total multiplicity. For events accepted by the tau pair selection cuts in the region $12 \leq N_{tot} \leq 15$, the efficiency varies from about 0.4 to about 0.65. As will be seen, the efficiency for values of the total multiplicity of less than 12 is too small to yield meaningful results. For events discarded by the tau pair selection cuts

in the region $16 \leq N_{tot} \leq 19$, the efficiency varies from ~ 0.7 to ~ 0.9. For this reason, the corrected number of multihadronic events was derived for each N_{tot} bin individually in the following manner: The number of tau pair MC events passing the enhancement cuts for a given multiplicity bin was subtracted from the number of data events passing the enhancement cuts. This difference was assumed to be due to multihadronic events, and the estimate for the total number of multihadronic events in a given multiplicity bin was calculated by dividing this difference by the efficiency obtained from a given multihadron Monte Carlo for that bin. Unfortunately, this estimate is quite sensitive to the correct modeling of the tau pair MC in each multiplicity bin and effects due to discrepancies of the tau pair MC with the data have to be investigated.

7.6.2 Inefficiency of Multiplicity Cuts

To estimate the number of genuine tau pair events discarded in excess of tau pair MC events, the multiplicity cuts were loosened stepwise, leading from the original requirement $N_{trk} < 7$, $N_{tot} < 16$ in four steps to requiring $N_{trk} < 11$, $N_{tot} < 20$. Since the N_{tot} and N_{trk} cuts are not independent, they were loosened at the same time. The ratio of events discarded by the multiplicity cuts with $N_{tot} < 20$ and $N_{trk} < 11$ to the total number of events discarded by the multiplicity cuts is 86.9% for 1994 tau pair MC and 86.3% for 1993 peak tau pair MC.

For each step, the multihadron enhancement cuts described above were applied and the multihadronic background was estimated for each N_{tot} bin starting with $N_{tot} = 12$ up to the highest value allowed for a given step of loosening the cuts. We are estimating the number of genuine tau pair data events which are discarded *in excess* of the number of tau pair MC events for each step of loosening the multiplicity cuts as follows: The total number of events which are accepted in

excess of the number accepted for the original cuts ($N_{trk} < 7$, $N_{tot} < 16$) are calculated for data and tau pair MC. From the difference of the two numbers, the estimated additional multihadron background introduced by loosening the cuts was subtracted. The remaining number of events is assumed to be due to tau pair data which is not properly modeled by the tau pair MC.

Figure 7.27 shows the N_{tot} distribution after requiring $min(M_{inv}^{cone}) > 1.0$ and $6 < \Sigma(M_{inv}^{cone}) < 15$, for $N_{trk} < 11$ and $N_{tot} < 20$. The distributions shown in that figure for $1 \leq N_{tot} < 16$ do *not* exactly correspond to the distributions of accepted events which pass the enhancement cuts for the original multiplicity cuts since the N_{trk} cut was loosened in the figure as well.

Figure 7.28 shows the data excess for each step of loosening the multiplicity cuts. One can observe a data excess, which is bigger for 1994 tau pair MC, but which is appreciable for both 1993 and 1994 MC. This excess seems to "level out", so that we do not expect the excess to increase when the multiplicity cuts are relaxed any further. Therefore, the excess for the cuts $N_{tot} < 20$ and $N_{trk} < 11$ was used as the estimate of the data excess, without applying any efficiency corrections.

The observation that the N_{tot} distribution in the tau pair MC does not simulate the data very well unfortunately affects the procedure to estimate this disagreement: to calculate the multihadron background for each value of N_{tot}, the tau pair MC prediction was subtracted from the data for events passing the multihadron enhancement cuts. If the number of tau pair MC events is underestimated, the number of multihadron events in the data will be overestimated by that amount. The following procedure was applied to estimate the bias due to that effect: The calculation of the multihadronic background as described in section 7.6.1 for each N_{tot} bin was modified by introducing a scaling factor f which was applied to the number of tau pair MC events passing the enhancement cuts. To estimate an

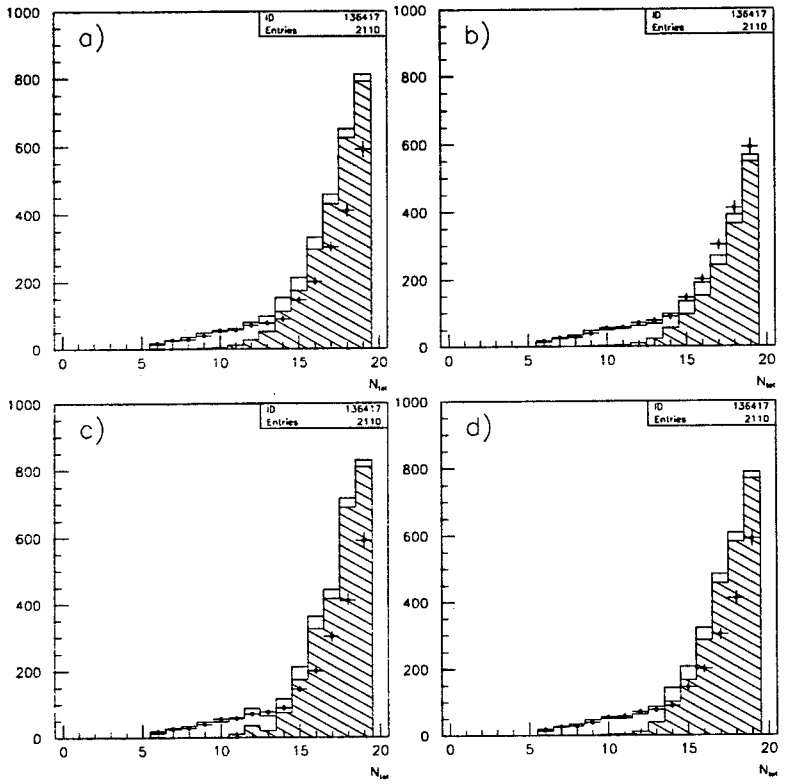

Figure 7.27: The total multiplicity (N_{tot}) distribution of events passing the multihadron enhancement cuts $min(M_{inv}^{cone}) > 1$ and $6 < \Sigma(M_{inv}^{cone}) < 15$ with multiplicity cuts loosened to $N_{tot} < 20$ and $N_{trk} < 11$. Shown are 1994 data and multihadron MC (a) 1994 Jetset, (b) 1993 Jetset, (c) 1994 Herwig and (d) 1992 Herwig, with the remaining MC from 1994. The points are data, the open histograms total MC, and the hatched histograms total background. Backgrounds other than from multihadronic events are negligible.

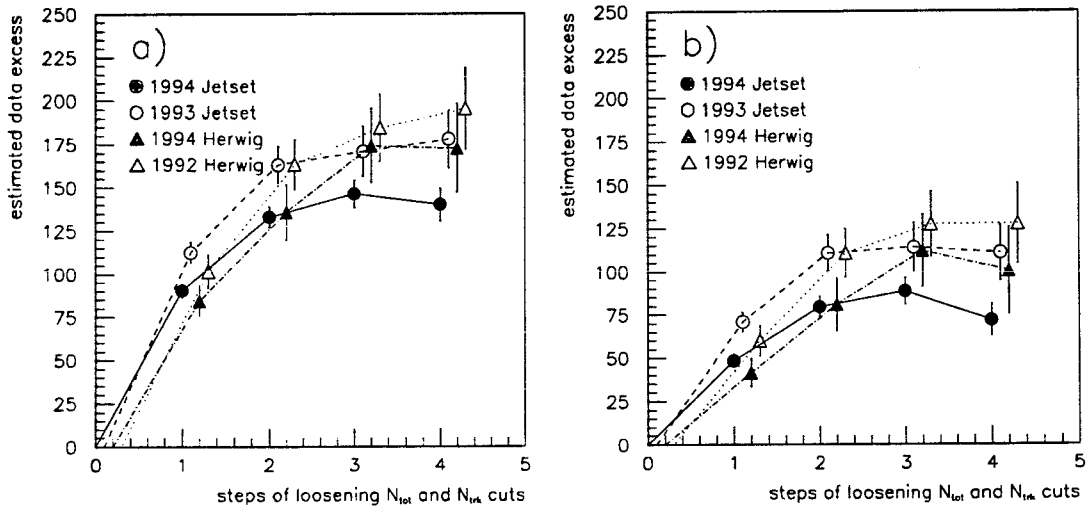

Figure 7.28: The estimated data excess when loosening the multiplicity cuts as described in the text. To allow a direct comparison of the quality of the tau pair MC, 1994 data was used in both plots. MC other than multihadronic MC is for (a) the 1994 detector and (b) the 1993 detector. For better clarity, the values corresponding to the four different multihadron MC samples for the same step of loosening the multiplicity cuts are slightly displaced from each other. The errors shown are only due to the multihadron MC efficiency, which is the part of the error which is uncorrelated amongst the data excess estimated for the four different MC samples in each plot.

appropriate value for the scaling factor f, the "relative data excess" was used in the following manner: Assuming that f is independent of the multiplicity, then for the "true" value of f the multihadronic background estimate is the "true" background estimate. If the additional multihadron background for a particular step of loosening the cuts is then subtracted from the additional number of data events, the result has no biases from the estimate of the multihadron background and is the "true" excess of genuine tau pair data events over tau pair MC events. If we divide this excess by the number of additional tau pair MC events accepted by loosening the multiplicity cuts, we obtain the "relative data excess". Assuming that the ratio of additional tau pair data events to additional tau pair MC events is the same before and after the multihadron enhancement cuts, the relative data excess is just $f-1$. From varying f and observing the change in the relative data excess, a range covering the average f for all multiplicity bins was determined. For 1994 tau pair MC, a scaling factor of $f = 1.2$ was used to calculate the data excess of events discarded by the multiplicity cuts, and half of the difference of the data excesses for $f = 1.1$ and 1.3 was assigned as systematic error. For 1993 peak tau pair MC, due to its better agreement with data, a scaling factor $f = 1.1$ was used to calculate the data excess with an error of half the difference in the excess observed for $f = 1.0$ and 1.2.

The estimate of the data excess after loosening the multihadron rejection cuts to $N_{trk} < 17, N_{tot} < 20$ for each of the four multihadron MC samples is shown in figure 7.29. The results for $f = 1.0$ and for the final scaling factor f applied for the respective tau pair MC are compared. Errors due to varying f over the ranges described above are not included in the figure. Table 7.15 summarizes the results for the tau pair MC inefficiency for the 1994 data and the three 1993 data points. The 1994 and 1993 peak data were compared to both 1994 and 1993 tau

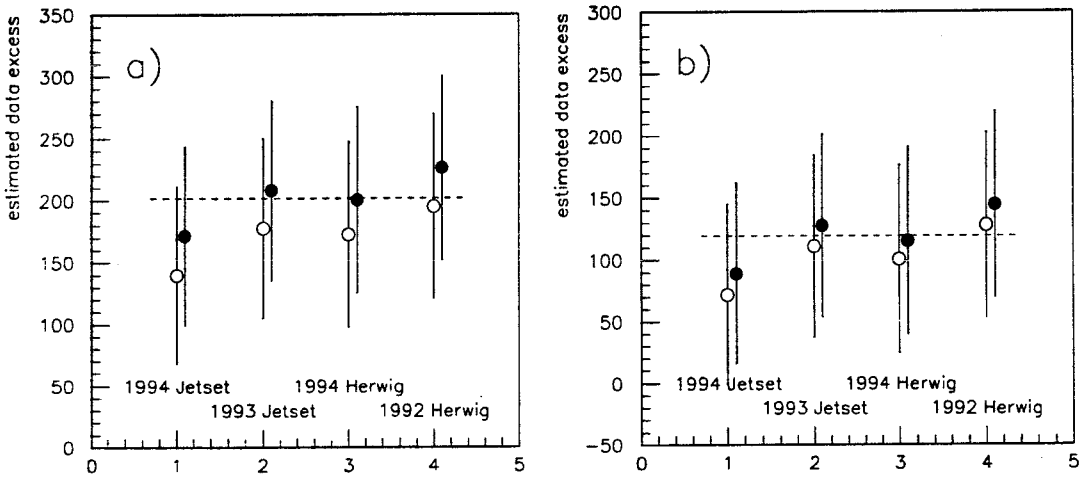

Figure 7.29: The estimate of the data excess for the four multihadron MC samples for (a) 1994 data and all other MC from 1994, and (b) for 1994 data with all other MC from 1993. The open circles show the estimated data excess using $f = 1.0$ (i.e. no correction applied to tau pair MC) and are equivalent to the results of the "forth step of loosening the multiplicity cuts" in figure 7.28. The full circles show the estimated data excess using the respective final scaling factors, $f = 1.2$ in plot (a) and $f = 1.1$ in plot (b). The errors are purely statistical. The average from the four results for the data excess with the respective scaling factors applied to the tau pair MC is shown as a dotted line. (Note the offsets between the y axes in plots (a) and (b)!)

year		tau data excess	stat	error from	correction factor
data	$\tau\tau$ MC	using respective f	error	varying f	
94	94	201.7 ± 27.3	± 73.5	± 15.1	1.0036 ± 0.0014
94	93	119.3 ± 27.8	± 74.5	± 16.4	—
93	94	62.7 ± 6.7	± 35.9	± 4.3	—
93	93	39.5 ± 6.9	± 36.1	± 4.6	1.0025 ± 0.0024
93p−2	93p−2	-14.5	± 18.3	± 4.9	0.9958 ± 0.0055
93p+2	93p+2	15.1	± 21.5	± 1.8	1.0032 ± 0.0045

Table 7.15: Estimate of the excess of tau pair data events failing the multihadron rejection cuts. The estimated tau pair data excess for the peak points is the average from the results for the four multihadron MC samples, where the error is half the difference of the maximum and minimum estimate. To derive these results, the appropriate value for f as described in the text was used. Furthermore, the statistical error and the error of varying f over a reasonable range are shown. For the peak points, these errors are the averages from the four multihadron MC samples. For the off-peak points, only the corresponding 1993 Jetset MC was used.

pair MC. As expected, the size of the scaling factor f depends on the tau pair MC used, with only a small dependence on the data which was used. The final scaling factors f, and the range over which they were varied for the error estimate, therefore are the same for a given tau pair MC, independent of the data sample used.

For the off-peak points, only 1993 Jetset MC was available. However, as can be seen in figure 7.29, the prediction for the 1993 peak Jetset MC is very close to the final data excess estimate for the peak points, and the error resulting from using different multihadron MC samples is small compared to the statistical error. Given that the statistical error is bigger for the off-peak points, the inefficiency of the multihadron cuts was estimated from the 1993 Jetset MC only. Otherwise, the same methods were used for the estimate as for the peak points. Figure 7.30 shows the change of the excess of data over tau pair MC when loosening the multiplicity

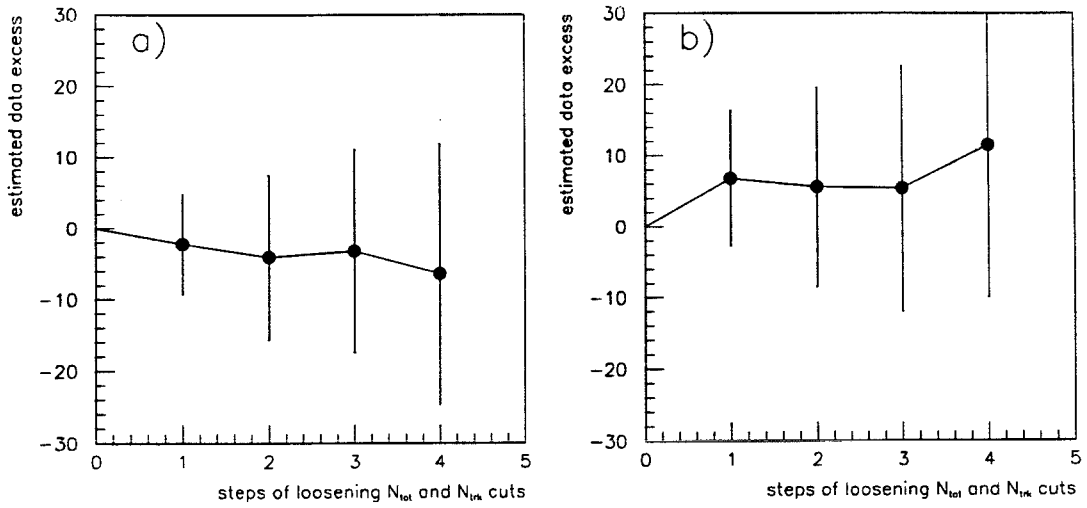

Figure 7.30: Estimate of the inefficiency of the multihadron rejection cuts for the 1993 off-peak points corresponding to figure 7.28 for the peak points. Plot (a) shows the estimated data excess over MC when loosening the multiplicity cuts for 1993p−2, plot (b) for 1993p+2. The errors shown here are the complete statistical errors.

cuts for the off-peak points. The tau pair MC scaling factors were $f = 0.75$ for 1993 peak−2 and $f = 1.2$ for 1993 peak+2, the corresponding ranges over which f was varied to estimate the systematic errors of the corrections were $f = 0.9$ to 0.6 and $f = 1.1$ to 1.3. The results are shown in table 7.15.

For the final estimate of the inefficiency of the multihadron rejection cuts, the three errors (two errors in the case of the off-peak points) shown in table 7.15 were added in quadrature. The resulting correction factors are shown in the last column of the table.

7.6.3 Multihadronic Background

The total multiplicity distribution from different multihadron Monte Carlo samples for events which leak into the tau pair acceptance is shown in figure 7.31a. Figure 7.31b show the efficiency of the enhancement cuts described in section 7.6.1

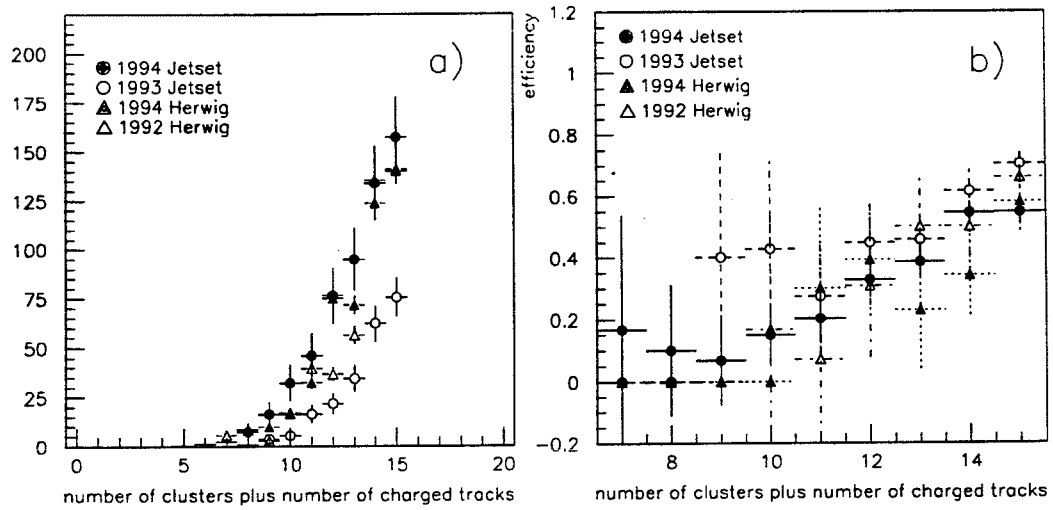

Figure 7.31: (a) Multihadron background accepted by the tau pair selection cuts as a function of the total multiplicity N_{tot}. The predictions of the four MC samples from table 7.14 are shown. (b) The efficiency of the multihadron enhancement cuts $min(M_{inv}^{cone}) > 1$ and $6 < \Sigma(M_{inv}^{cone}) < 15$ as described in the text for the four different multihadron MC samples as a function of the total multiplicity N_{tot}.

for multihadron MC as a function of the total multiplicity. Figure 7.32 compares the total multiplicity distributions for data and MC after applying the enhancement cuts. Clearly, the data MC agreement depends strongly on the multiplicity. The straightforward procedure of applying the efficiency corrections from figure 7.31b on a bin-by-bin basis to the corresponding data MC difference in figure 7.32 can only be applied to the region with large total multiplicities due to the low efficiency of the cuts for multihadron MC at low multiplicities. It therefore was required that the size of the multihadronic background passing the enhancement cuts should have at least about the same size as the statistical error of the data for a given bin of the N_{tot} distribution, and a bin-by-bin correction was only applied for the region $12 \leq N_{tot} \leq 15$. For the remaining region $N_{tot} \leq 11$, the average of the 1993 and 1994 Jetset predictions was used as the background estimate and half the difference between the two predictions was assigned as error. The uncor-

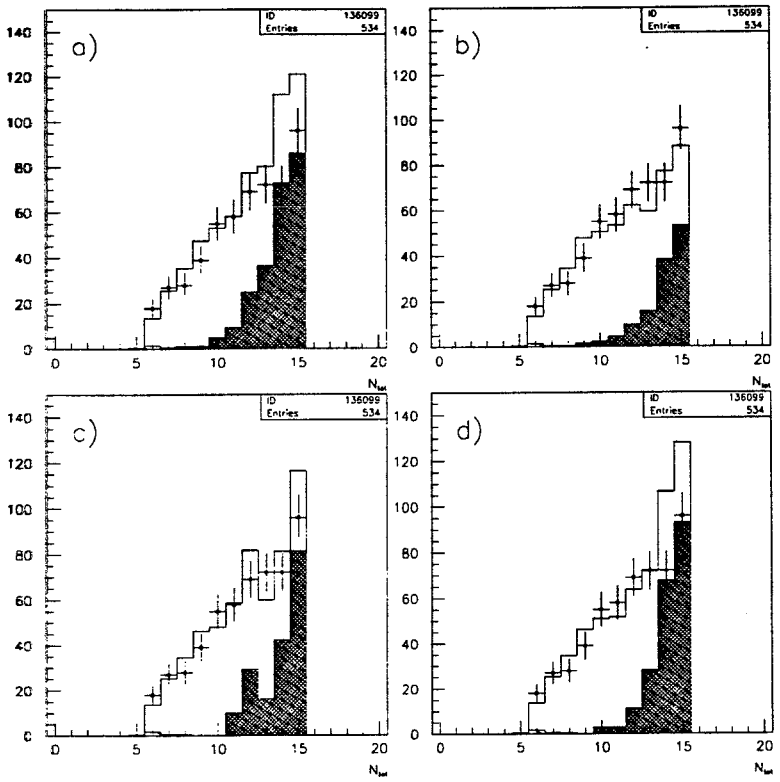

Figure 7.32: The distribution of the total multiplicity N_{tot} for events passing the multihadron enhancement cuts $min(M_{inv}^{cone}) > 1$ and $6 < \Sigma(M_{inv}^{cone}) < 15$ for 1994 data compared to the four different multihadron MC samples: (a) 1994 Jetset, (b) 1993 Jetset, (c) 1994 Herwig and (d) 1992 Herwig. The remaining MC is for the 1994 detector simulation. The points are data, the open histograms total MC, the hatched histograms total background and the shaded histograms multihadron MC only. Small backgrounds other than from multihadronic events can only be observed for small values of N_{tot}.

Monte Carlo	$N_{tot} \leq 11$	$12 \leq N_{tot} \leq 15$
94 Jetset	105.9±6.3	461.9±13.1
93 Jetset	26.2±4.4	193.7±12.0
94 Herwig	58.6±13.8	410.0±52.4
92 Herwig	73.2±14.4	368.8±32.2
average	66.1±3.8 ± 39.9	327.8±8.9 ± 134.1

Table 7.16: The predicted multihadronic background for the different multihadron MC samples, scaled to the luminosity of the 1994 data sample, for low and high total multiplicities. The average shown in the last row is the average of the results for the 1993 and 1994 Jetset multihadron samples, where the first error is purely statistical and the second is half the difference between the two predictions. The MC background estimate in the region $N_{tot} \leq 11$ from this table will be used as multihadron background estimate, while for the region $12 \leq N_{tot} \leq 15$ corrections will be derived. The high multiplicity region is only listed here for completeness.

rected multihadron MC background predictions in the low and high multiplicity regions are shown in table 7.16. The predictions of the Herwig MC fall somewhere inbetween the two Jetset estimates.

Given a difference between the number of data and MC events of $\sim$ 10% for 1993 and $\sim$ 20% for 1994 observed in the previous subsection for events failing the tau pair selection cuts, it is a reasonable assumption that similar differences exist for the multiplicity distribution inside the tau pair acceptance. Due to the larger fraction of tau pair events after the multihadron enhancement cuts *inside* the tau pair acceptance (shown in figure 7.32) one would expect a larger effect than *outside* of the tau pair acceptance (shown in figure 7.27).

The procedure used here to determine the multihadronic background inside the tau pair acceptance differs from the one used in the previous subsection only in the following points: First, a scaling factor f will be calculated for each value of N_{tot} in the range $12 \leq N_{tot} \leq 15$ passing the multihadron enhancement cuts individually and will be denoted as f^m, where the superscript m indicates the

multiplicity. The cut on N_{trk} remains unchanged. Second, rather than "scanning a region of f by hand", the ratio of the data excess and tau pair MC will be formed for each N_{tot} value individually. By taking this ratio as $f^m - 1$, a new value for f^m will be derived and fed back into the next iteration of the calculation of the data excess. Here the same relation between the relative data excess for a given multiplicity bin m and the quantity f^m holds as described in the previous subsection for the average scaling factor f when loosening the multiplicity cuts. Performing this iterative process it was observed that the change of the background estimate was large after the first step, while for subsequent iterations changes in the background estimate are rather small compared to the statistical error of the background estimate.

Figure 7.33 shows the scaling factor f^m minus 1 after the zero-th iteration, i.e. the result for the ratio of data excess and tau pair MC events for each multiplicity bin in the range $12 \leq N_{tot} \leq 15$ when $f^m = 1.0$ was implemented. The data MC agreement improves with smaller values of the total multiplicity as one would expect, since we are moving away from the tails of the distribution, for which we expect the worst agreement between data and MC. For a given data sample, the data excess for each value of the total multiplicity should in theory only be determined by the tau pair MC, and should within its statistical errors not depend on the multihadron Monte Carlo sample that was used. This appears to be the case in figure 7.33, where the agreement between different multihadron MC samples gets better for smaller values of N_{tot} since less multihadron MC is present in those bins. However, the results for 1994 Herwig Monte Carlo are not in very good agreement with the other three Monte Carlo samples for $N_{tot} = 13$ and 14, which is precisely where we observe the low efficiencies of the multihadron enhancement cuts in figure 7.31b. These low efficiencies result in a much bigger error for the relative

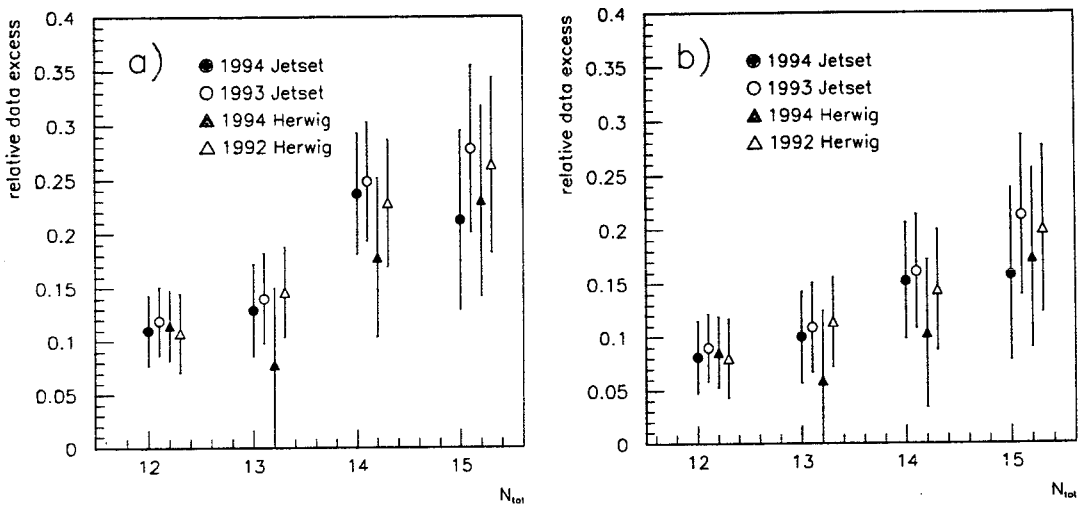

Figure 7.33: The excess of data minus the estimated multihadron background over tau pair MC, divided by the number of tau pair MC events for values of the total multiplicity from 12 to 15. To allow a direct comparison of the tau pair MC, the 1994 data was used in both plots, where for plot (a) all MC other than multihadron MC is from 1994, in plot (b) from 1993. In each case, the results using the four different multihadron MC samples are shown. Ideally, the relative data excess should be independent of the multihadron MC that was used.

data excess for 1994 Herwig Monte Carlo in figure 7.33. For this reason, and due to the low statistics of the Herwig MC, the correction factors will be derived only from the Jetset MC. Furthermore, Herwig generally seems to simulate particle production rates worse than Jetset [69].

Systematic errors on f^m are expected from two sources: First, from differences between the true multihadronic background in the data and the multihadronic background predicted for each multiplicity bin from the data MC difference after scaling the tau pair MC. This effect should be covered by using the four different multihadron MC samples for the background estimate with their full statistical errors. Second, we are *deriving* the scaling factor f^m from comparing data to MC without applying any enhancement cuts, while we are *applying* it to the tau pair MC which passes the multihadron enhancement cuts. The scaling factor f^m therefore is sensitive to potential differences in the efficiencies of the enhancement cuts for data and MC. The effect of the multihadron enhancement cuts on the data MC agreement was estimated by comparing the data MC agreement in a N_{tot} region with minimal background before and after the multihadron enhancement cuts. A good region for this estimate is $7 \leq N_{tot} \leq 9$ as demonstrated in figure 7.34. For those three bins of the total multiplicity, the maximum background in a bin is about 35% of the statistical error of the data before the multihadron enhancement cuts, and about 20% after the enhancement cuts. We therefore can directly calculate the scaling factor f^m before and after applying the multihadron enhancement cuts by dividing the corresponding number of data and tau pair MC events for these bins, without being sensitive to the multihadron MC background predictions. The two ratios were found to agree well for all three values of N_{tot} within their statistical uncertainties.

Applying the procedure lined out so far, we will now calculate the multi-

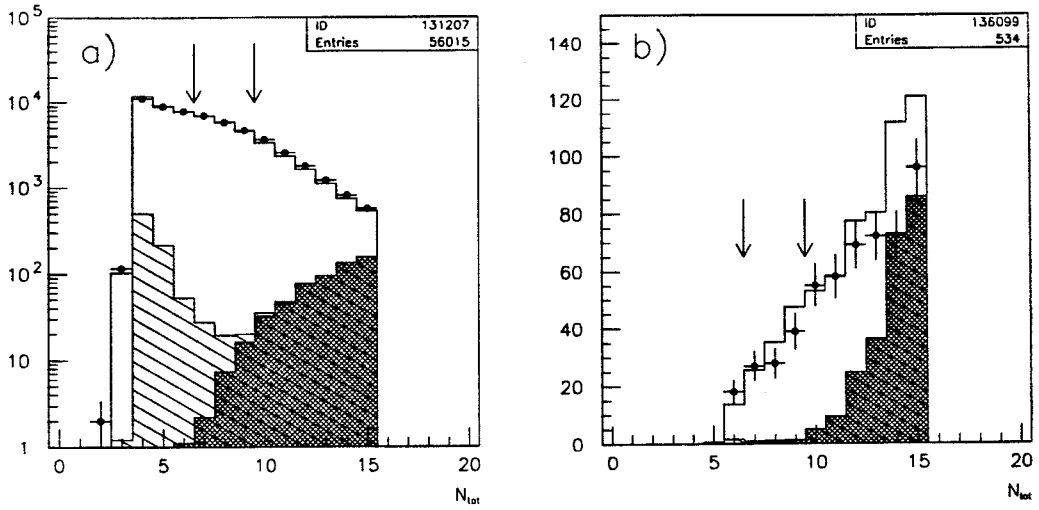

Figure 7.34: The distribution of the total multiplicity for 1994 data and MC (the multihadron MC is 1994 Jetset) (a) for all events selected by the tau pair selection cuts and (b) after the multihadron enhancement cuts. The arrows indicate a region with small background in each plot. This region was used to check if the data MC ratios before and after the multihadron enhancement cuts show good agreement.

hadronic background estimate in the high multiplicity region in an iterative process as follows: We start without applying any corrections by implementing $f_0^m = 1.0$ for all multiplicity bins. The resulting relative data excess is equal to $f^m - 1$, where f^m now is the scaling factor for the next iteration which is used to calculate the final estimate of the multihadron background. We are using the full statistical errors on f^m resulting from the data and tau pair MC statistics of events which pass the tau pair pair selection per multiplicity bin. The results of this procedure are shown in table 7.17. The results without applying the scaling factors to the number of tau pair MC events are also shown for comparison. The disagreement between the background estimates when using different tau pair MC with the same data has decreased by about 40%. Also, the background estimate itself has decreased significantly. With the exception of 1994 Herwig MC, the background estimates for different multihadron Monte Carlo show decent agreement

among each other. Problems with the 1994 Herwig MC prediction due to low statistics and low efficiencies for $N_{tot} = 13$ and 14 were discussed above. As the final background estimate, we are taking the average of the highest and lowest Jetset background estimate for a given data sample compared to either 1993 or 1994 tau pair MC. In practice this means that we are using the average of the estimates for 1994 tau pair MC with 1994 Jetset and 1993 tau pair MC with 1993 Jetset. As the statistical error, we take the average of the two statistical errors and as an additional error we assign half the difference of the two estimates. The background estimate was also performed with slightly modified multihadron enhancement cuts, where the cut on $min(M_{inv}^{cone})$ was tightened from 1.0 to 1.5. Differences between these two cuts were quite small compared to the statistical error of each estimate.

As an alternative method of estimating the agreement of multihadron MC and data, the N_{tot} distribution for events which *fail* the tau pair selection cuts because they have more than two charged cones was investigated before applying the N_{tot} or N_{trk} cut. The N_{tot} distributions for these events are shown in figure 7.35 for different multihadron MC samples. Events fulfilling those conditions are almost exclusively multihadron events, giving us an opportunity to directly compare the data MC agreement for multihadron in the N_{tot} region of interest, albeit for multihadrons that fail the tau pair selection cuts. Clearly, all multihadron MC runs except the 1993 Jetset in figure 7.35c greatly overestimate the number of events in the region $13 \leq N_{tot} \leq 15$. We will use the distributions in figure 7.35 to estimate the multihadron background as follows: For each multihadron MC sample, we will subtract the tau pair MC from the data and divide the difference by the Monte Carlo prediction for the multihadronic events on a bin-by-bin basis. This ratio will be used on a bin-by-bin basis to correct the number of multihadron MC

year		Multihadron	without	with tau MC
data	$\tau\tau$ MC	Monte Carlo	tau MC scaling	scaling by f^m
94	94	1994 Jetset	296.7±43.8	233.9±44.6
		1993 Jetset	239.5±36.9	182.5±36.7
		1994 Herwig	368.3±78.2	303.7±73.7
		1992 Herwig	269.0±50.9	206.1±46.6
		bkgr. est.	268.1±40.3 ± 28.6	208.2±40.7 ± 25.7
94	93	1994 Jetset	262.9±45.1	213.2±46.4
		1993 Jetset	211.9±37.5	166.0±37.9
		1994 Herwig	323.8±74.1	274.3±70.6
		1992 Herwig	239.2±49.6	189.5±47.9
		bkgr. est.	237.4±41.3 ± 25.5	189.6±42.15± 23.6
94	ave	bkgr. est.		200.0±41.3 ± 34.0
93	94	1994 Jetset	78.7±21.8	65.0±22.2
		1993 Jetset	63.4±17.6	50.6±17.8
		1994 Herwig	93.8±29.5	80.0±29.3
		1992 Herwig	72.3±22.0	59.2±21.9
		bkgr. est.	71.1±19.7 ± 7.7	57.8±20.0 ± 7.2
93	93	1994 Jetset	69.2±22.1	59.1±22.6
		1993 Jetset	55.6±17.7	45.9±18.0
		1994 Herwig	81.3±29.1	71.6±29.3
		1992 Herwig	63.9±22.0	54.4±22.2
		bkgr. est.	62.4±19.9 ± 6.8	52.5±20.3 ± 6.6
93	ave	bkgr. est.		55.5±20.1 ± 9.6

Table 7.17: The multihadronic background estimate for the 1994 and 1993 peak points. The results without applying any scaling to the tau pair MC are shown for comparison. The background estimate for each combination of data and tau pair MC was obtained by taking the average of the 1993 and 94 Jetset predictions. The first error is the average of the statistical errors, the second error is half the difference between the two estimates. The final background estimate for each data sample was derived in the same manner by averaging the highest and lowest Jetset estimate from the results of comparing each data set to both 1994 and 1993 tau pair MC.

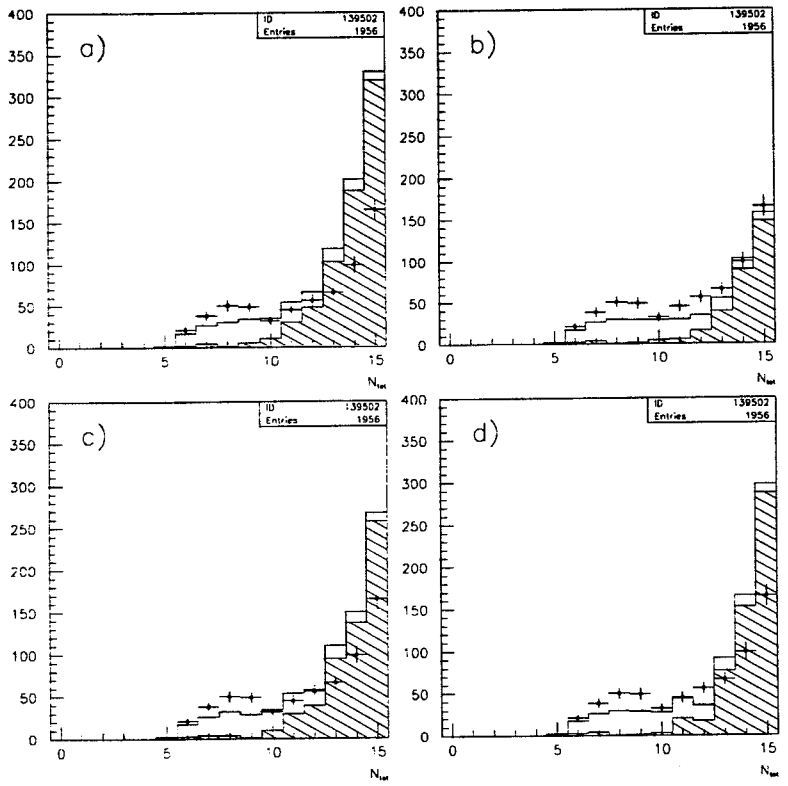

Figure 7.35: The N_{tot} distribution of events with $N_{cone} > 2$ which pass all other tau pair selection cuts before applying the N_{tot} or N_{trk} cut. Shown are 1994 data and multihadron MC (a) 1994 Jetset, (b) 1993 Jetset, (c) 1994 Herwig and (d) 1992 Herwig, with the remaining MC from 1994. The points are data, the open histograms total MC, and the hatched histograms total background. Backgrounds other than multihadronic events are negligible for $N_{tot} > 10$.

multipl. region	1994	1993 peak
$N_{tot} < 12$	66.1± 3.8 ± 39.9	18.6± 2.2 ± 11.2
$12 \leq N_{tot} \leq 15$	200.0±41.3 ± 34.0	55.5±20.1 ± 9.6
total	266.1±41.5 ± 73.9	74.1±20.2 ± 20.8

Table 7.18: Estimate of the multihadron background for 1994 and 1993 peak for the low and high total multiplicity regions combined. The first error in each column is statistical, the second one is the contribution from half the difference between the maximum and the minimum estimate. For each year, the statistical error was added in quadrature, while the second error was added linearly.

events leaking into the tau pair acceptance for multihadron MC which are shown in figure 7.31a. This method is not expected to work for small multiplicities since the portion of tau pair MC in a bin is getting larger with smaller multiplicities, affecting the calculation of the correction factor if the tau pair MC is badly simulated. Just as for the method using enhancement cuts described above, we will only calculate a correction factor in the region $12 \leq N_{tot} \leq 15$. The average of the predictions using 1993 Jetset and 1994 Jetset is about 235 events for the 1994 data and about 70 events for the 1993 data. These results are in decent agreement with the results from table 7.17.

In figure 7.35 one could observe a data MC disagreement in the region $N_{tot} \leq 10$ which presumably is due to a disagreement of tau pair data and tau pair MC events that are discarded by the cut on the number of charged cones. In the next subsection, the distribution from figure 7.35 will be used almost directly to estimate the inefficiency of the cut on the number of charged cones for tau pair data and tau pair MC.

Finally, in table 7.18 the background estimates for the low multiplicity region from table 7.16 have been added to the background estimates for the high multiplicity region in table 7.17. The error estimates which were obtained from

Monte Carlo	1993 p−2	1993 p+2
93 Jetset (p−2)	13.3±2.2	—
93 Jetset (p+2)	—	17.9±3.0
93 Jetset (peak)	13.3±0.8	18.9±1.1
94 Jetset	34.3±0.9	48.9±1.3
94 Herwig	28.2±2.4	40.2±3.4
92 Herwig	26.7±2.1	37.9±3.0
average	23.8±1.2	33.9±1.7
Estimated bkgr	13.3±2.2 ± 10.5	17.9±3.0 ± 16.0

Table 7.19: Peak multihadron background estimates from Monte Carlo scaled to the off-peak points. The average shown in the last but one row is the average of the 1993 and 1994 Jetset predictions. As the final result, the 1993 Jetset prediction for each off-peak point was used. The first error of the estimated background is statistical, the second is the difference between the estimated background and the average value from the previous row.

taking half the difference of the maximum and minimum background predicted by different multihadron MC samples were added linearly for the low and high multiplicity: The errors for the uncorrected background predictions from multihadron MC were originally correlated in table 7.16 and it is conceivable that despite the variety of procedures performed to obtain the multihadronic background estimates for the high multiplicity region in table 7.17, part of the correlation is still present.

In table 7.19 the multihadron MC for the peak energy point was scaled to the off-peak points, taking into account the different luminosities and cross sections. As one would expect, the predictions of the 1993 Jetset MC agree well for the off-peak points and for the scaled MC from the peak point. As the multihadronic background estimate for the off-peak points, we directly use the Jetset MC predictions for the respective energy point. We know from the peak data that the average of the predictions from 1994 and 1993 peak Jetset MC is well above the

data sample	MH background	correction factor
94	266.1 ± 84.8	0.9952 ± 0.0015
93 peak	74.1 ± 29.0	0.9953 ± 0.0018
93 p−2	13.3 ± 10.7	0.9961 ± 0.0031
93 p+2	17.9 ± 16.3	0.9963 ± 0.0034

Table 7.20: The final estimate of the multihadron background from table 7.18 for the peak points and table 7.19 for the off-peak points.

actual multihadronic background (compare tables 7.18 and 7.16). We therefore assign the difference between that average and the 1993 Jetset prediction for each off-peak point as an additional error. Due to the lower statistics for the off-peak points, the size of this error is acceptable. The results are shown in the last row of table 7.19. The final results for the background estimate from multihadronic events for all data samples are shown in table 7.20.

7.6.4 Inefficiency of the Charged Cone Cut

The inefficiency of the cut on the number of charged cones was compared for data and tau pair MC by investigating the distribution of the total multiplicity in the region $N_{tot} \leq 15$ for events with more than two charged cones after applying all other tau pair selection cuts. These distributions correspond almost exactly to those shown in figure 7.35, with small differences resulting from applying the cut $N_{trk} < 7$ on the multiplicity of charged tracks. Due to the large contribution from multihadronic events for high total multiplicities, the data excess was estimated in the regions $N_{tot} \leq 11$ and $12 \leq N_{tot} \leq 15$ separately. In the low multiplicity region, the difference between data and MC was calculated as $58.8 \pm 15.4 \pm 16.6$ for 1994 data and MC, $21.3 \pm 8.4 \pm 4.7$ for 1993 peak data and MC, $2.6 \pm 3.5 \pm 1.0$ for 1993 p−2 data and MC, and $11.1 \pm 6.2 \pm 2.7$ for 1994 p+2 data and MC.

Here the first error is purely statistical, while the second one is half the difference of the predicted number of events using 1993 and 1994 Jetset MC. The number of multihadronic MC events used to calculate the data excess was the average of those two MC predictions. For the off-peak points, the peak Jetset MC predictions were scaled according to luminosity and cross section. In the previous subsections it was found that the data MC agreement depends on the total multiplicity such that it does not seem advisable to extrapolate the disagreement in the region with low total multiplicity into the region with high total multiplicity. For events in the region $12 \leq N_{tot} \leq 15$ that pass the tau pair selection cuts, it could be observed in figure 7.33 that the excess of genuine tau pair events in the data over tau pair MC events is in the range of $10\% \sim 25\%$. Assuming that a similar disagreement applies for events that fail the tau pair selection cuts with more than two charged cones, the excess of tau pair data over tau pair MC in the region $12 \leq N_{tot} \leq 15$ was estimated as 0.25 ± 0.25 times the number of tau pair MC events in that region. The resulting estimates for the data excess, scaled to the respective data luminosity, are 12.2 ± 12.2 from 1994 tau pair MC, 4.1 ± 4.1 from 1993 peak tau pair MC, 0.8 ± 0.8 from 1993 p$-$2 tau pair MC, and 1.5 ± 1.5 from 1994 p+2 tau pair MC. These errors, and the errors obtained for the low multiplicity region, were added in quadrature. The resulting corrections and errors are shown in table 7.21.

7.7 Two Photon Events

Two photon events constitute the most dominant non-resonant background to the Z^0 lineshape. The dominant two photon backgrounds are from $e^+e^-e^+e^-$ and $e^+e^-\mu^+\mu^-$ final states, and, to a smaller degree, from the final state $e^+e^-\tau^+\tau^-$.

year	data excess	correction factor
94	71.0 ± 25.7	1.0013 ± 0.0005
93 peak	25.4 ± 10.5	1.0016 ± 0.0007
93 p−2	3.4 ± 3.7	1.0010 ± 0.0011
93 p+2	12.6 ± 6.9	1.0026 ± 0.0014

Table 7.21: The excess of genuine tau pair data events over tau pair MC events rejected by the cut on the number of cones and the resulting correction factors.

Two photon events, having a cross section which is strongly peaked in forward direction, have a small transverse momentum component and a missing momentum vector which due to leakage along the beam pipe points into the forward direction. All two photon events in general have a low visible energy (see section 7.2), where the distribution of $e^+e^-e^+e^-$ events is characterized by $R_{trk} \approx R_{shw}$, while the distribution of $e^+e^-\mu^+\mu^-$ final states has a constant, low R_{shw}, but varying R_{trk}. Figure 7.36 shows the R_{vis} distribution before the two photon rejection cut at $R_{vis} = 0.18$.

7.7.1 Inefficiency of the Two Photon Cuts

To investigate potential discrepancies between the number of tau pair events discarded in data and MC by the two photon rejection cut, events in the regions $0.06 < R_{vis} < 0.18$, $0.10 < R_{vis} < 0.18$, $0.125 < R_{vis} < 0.18$, and $0.15 < R_{vis} < 0.18$ have been selected. For each region, the number of data and MC events with a ratio of the transverse momentum to the beam energy of $R_{p_t} > 0.04$ were compared. In this region, mainly tau pair events are expected. Figure 7.37 shows the R_{p_t} distribution for the regions $0.06 < R_{vis} < 0.18$ and $0.15 < R_{vis} < 0.18$ for 1994 data and MC. Clearly, in the first region (figure 7.37a), a large amount of two photon background can be observed at low values of R_{p_t}.

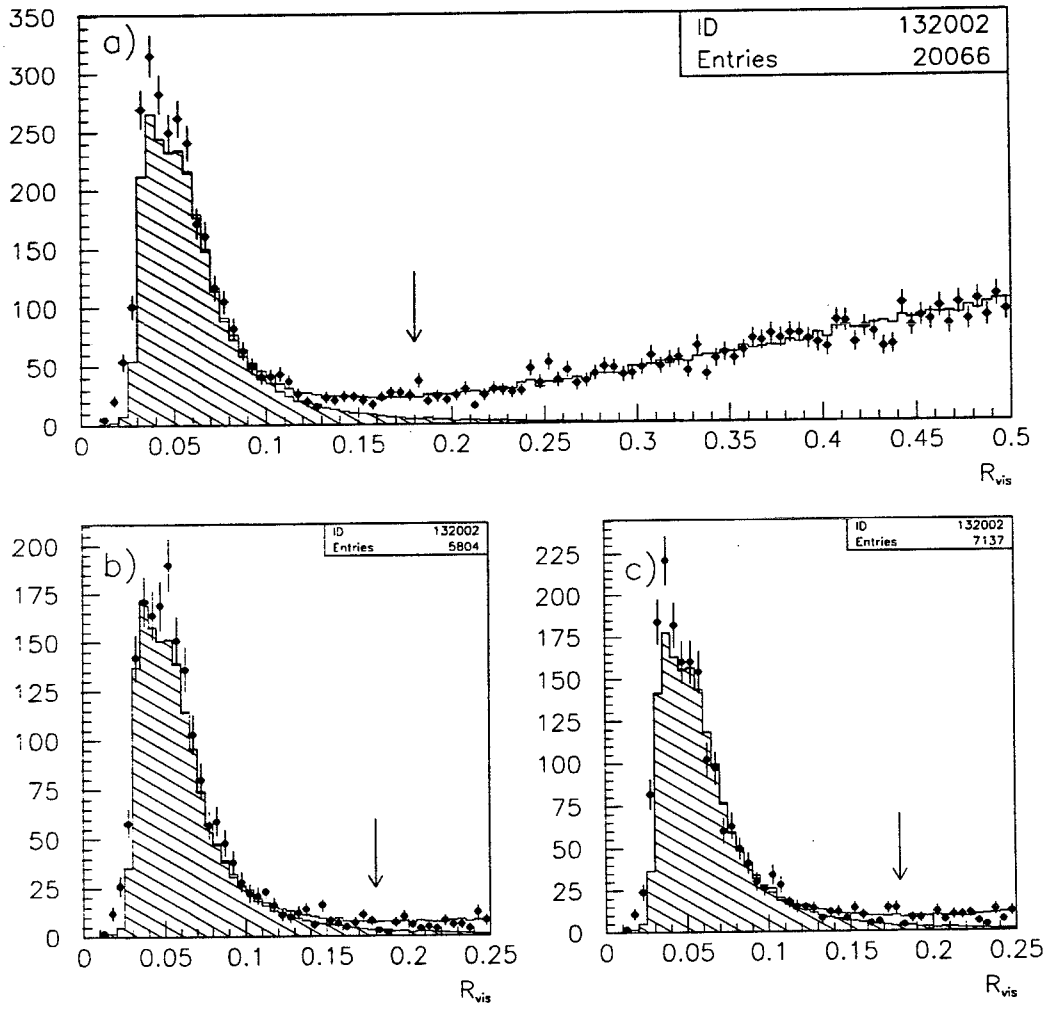

Figure 7.36: The R_{vis} distribution after all other cuts tau pair selection cuts for 1993 at (a) peak, (b) peak−2, and (c) peak+2. The points are data, the open histograms total MC and the hatched histograms the background. The background peak at low visible energy is from two photon events and is rejected by a cut at $R_{vis} = 0.18$. Two photon reactions are non-resonant, and when comparing figure (a) to (b) and (c) one can clearly see that for the off-peak points the two photon background constitutes a higher background fraction near the cut at $R_{vis} = 0.18$.

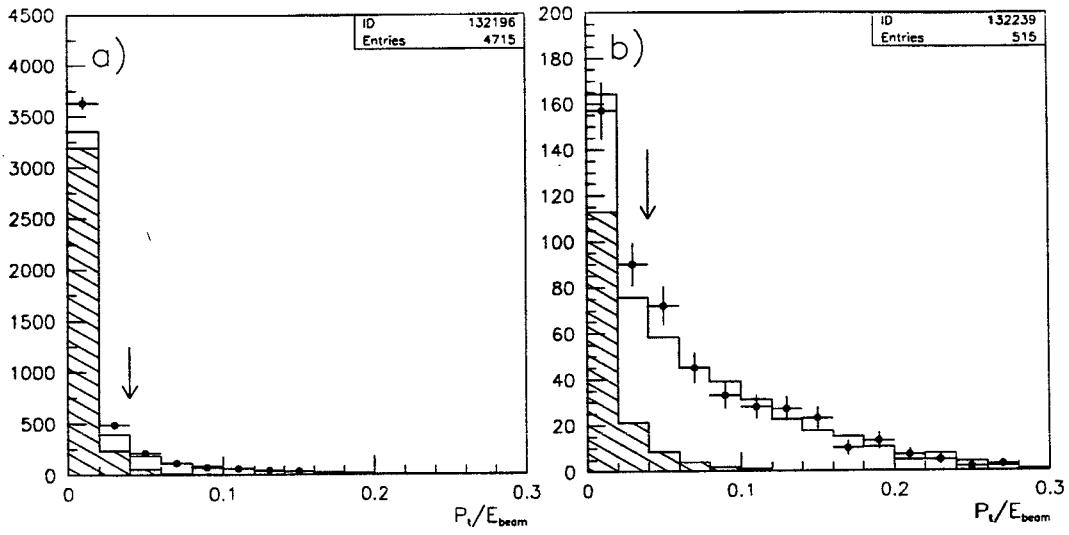

Figure 7.37: The distribution of P_t/E_{beam} in the regions (a) $0.06 < R_{vis} < 0.18$ and (b) $0.15 < R_{vis} < 0.18$ for 1994 data and MC. The points are data, the open histograms the total MC and the hatched histograms background MC only. The background is almost exclusively from two photon MC.

The data MC disagreement in that region is obviously due to two photon events. For figure 7.37b, the two photon background is strongly suppressed and one can observe that the data MC agreement in the low R_{p_t} region has much improved. In figure 7.38, the data MC difference in the region $R_{p_t} > 0.04$ for the four different cuts on R_{vis}, divided by the efficiency of the R_{p_t} cut for tau pair MC, is shown for each data sample as full circles. The solid line in each of the 4 plots is *not* a fit, but is simply the value for the region $0.15 < R_{vis} < 0.18$. Since all events from that region are also contained in the three other R_{vis} regions, the total errors of the four data MC differences for each data set are correlated. The error bars for the remaining three regions of each plot in figure 7.38 were obtained only from the events with $R_{vis} < 0.15$, so that the χ^2 of those three errors with respect to the data MC difference in the region $0.15 < R_{vis} < 0.18$ indicates whether the data MC difference shows any serious dependence on the choice of the R_{vis} region. For

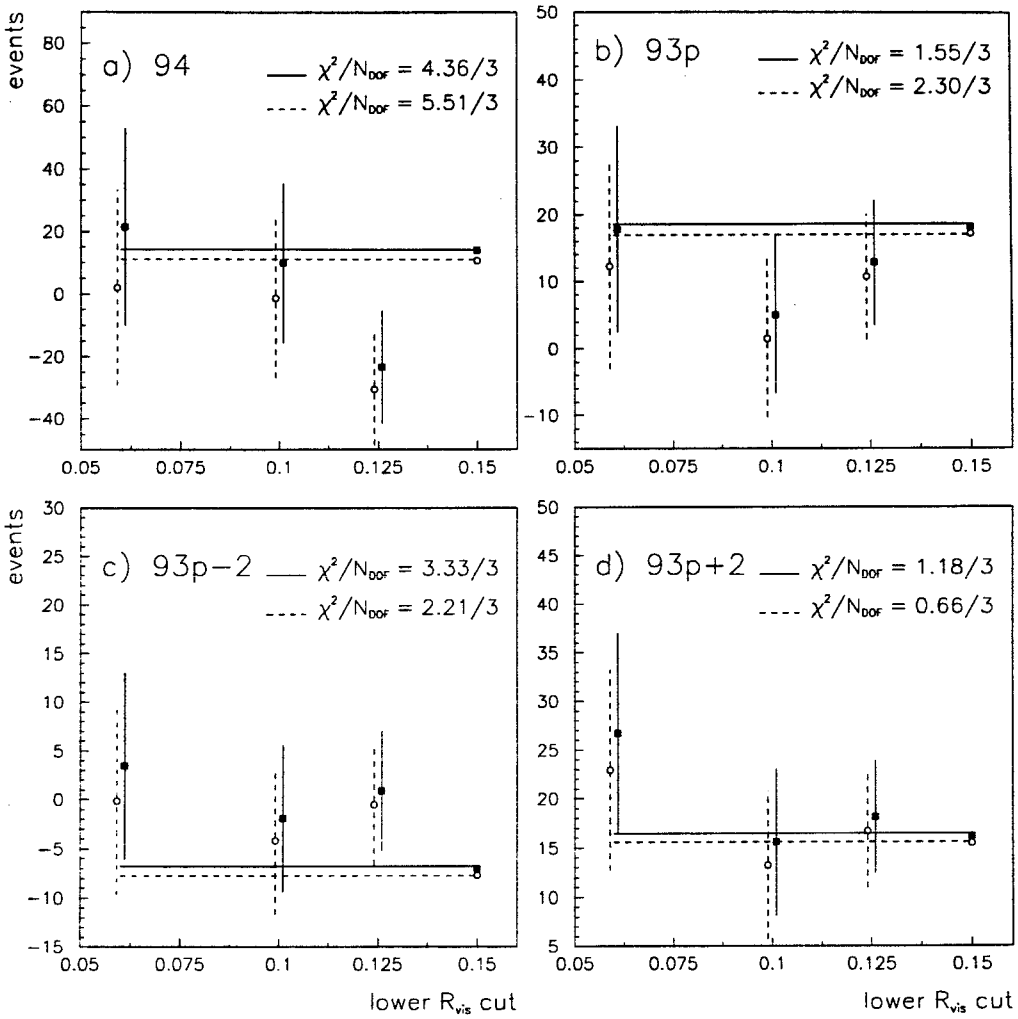

Figure 7.38: Excess of data over MC in the four different R_{vis} regions described in the text for (a) 1994, (b) 1993 peak, (c) 1993 p−2, and (d) 1993 p+2. The full circles and solid line correspond to the results obtained without scaling the two photon MC, where all error bars are with respect to the data excess in the region $0.15 < R_{vis} < 0.18$. The open circles and broken line indicate the data excess after scaling the two photon MC. The line indicates the respective result for the region $0.15 < R_{vis} < 0.18$, and the χ^2's are those of the remaining three measurements with respect to that result.

all the data samples, the resulting χ^2 is reasonably close to 1. The sum of the χ^2's from all four data samples is $10.41/12 \simeq 0.87$.

In figure 7.36 it could be observed that the two photon MC does not model the data very well at its peak at about $R_{vis} \approx 0.05$. The following procedure was applied to account for potential biases of the data MC difference due to bad simulation of the two photon MC: First the data MC ratio in the region $R_{vis} < 0.1$ was calculated, which is clearly dominated by two photon events. These ratios are 1.144 for 1994 data and MC, 1.153, 1.136, 1.107 for 1993 data and MC at the peak, at p−2 and at p+2, respectively. As an approximation for all four data samples, the two photon MC in the region $R_{p_t} > 0.04$ was scaled by 1.15 and the data MC difference for the four R_{vis} regions was recalculated. The results of this procedure are shown in figure 7.38 as open circles, where the error bars are again excluding events in the region $0.15 < R_{vis} < 0.18$, and the broken line indicates the data MC difference in that region. The χ^2 has improved with respect to the fit to the results without scaling two photon MC for the off-peak points while it got worse for the peak points. The sum of the χ^2's for the four data sets however has remained almost constant and is $10.67/12 \simeq 0.89$.

We conclude that the estimate of the data MC agreement outside the R_{vis} cut is well estimated by the agreement observed in the region $0.15 < R_{vis} < 0.18$. For the final result, the correction factors derived from that region *without* applying the scaling for two photon MC were used. To account for any effects of a bad modelling of the two photon MC, the difference of the data excess observed with and without scaling the two photon MC in the region $0.15 < R_{vis} < 0.18$ was added linearly to the statistical error.

The data MC difference for events with $R_{p_t} > 0.04$ in the four R_{vis} regions was divided by the efficiency of the R_{p_t} cut as calculated from $\tau^+\tau^-$ MC. These

	estimated data excess	add'l error from scaling 2γ MC	correction factor
94	14.08 ± 24.88	± 3.30	1.0004 ± 0.0005
93 peak	18.07 ± 13.54	± 1.01	1.0012 ± 0.0009
93 p$-$2	-7.05 ± 5.15	± 0.64	0.9979 ± 0.0017
93 p+2	16.16 ± 8.65	± 0.67	1.0034 ± 0.0020

Table 7.22: The final correction factors and errors to account for differences in the data and MC efficiencies of the two photon rejection cut.

efficiencies are between 0.6 and 0.7 depending on the R_{vis} cuts that were applied and it was checked that the R_{p_t} distribution is modelled reliably by the $\tau^+\tau^-$ MC by investigating the R_{p_t} distribution for events that pass the tau pair selection cuts in the regions $0.18 < R_{vis} < 0.25$ and $0.25 < R_{vis} < 0.30$. For none of the four data sets did these checks indicate any discrepancies between data and MC which would necessitate additional errors or correction factors. Table 7.22 shows the final correction factors that were applied for the inefficiency of the two photon rejection cut.

7.7.2 Background from Two Photon Events

To investigate the two photon background, the following enhancement cuts have been applied on events that pass the tau pair event selection cuts:

For $e^+e^- \rightarrow e^+e^-\mu^+\mu^-$ events require:

- $R_{trk} < 0.5$
- $R_{shw}^{hc} < 0.05$,

  where R_{shw}^{hc} is the shower energy in the cone with the higher shower energy.

For $e^+e^- \rightarrow e^+e^-e^+e^-$ events require:

- $R_{trk} < 0.4$,
- $0.8 < R^1_{EP} < 1.2$ AND $0.4 < R^2_{EP} < 1.6$,

  where R^1_{EP} (R^2_{EP}) is the ratio of shower energy and track momentum in the cone for which this ratio is closer to (further away from) 1.
- $N^{hc}_{trk} + N^{hc}_{cls} \leq 3$,

  where N^{hc}_{trk} and N^{hc}_{cls} are the number of tracks and clusters, respectively, in the cone with the higher visible energy. This cut removes some residual multihadronic events and $e^+e^-\tau^+\tau^-$ events.

Since for a two photon process $e^+e^- \rightarrow e^+e^-\ell^+\ell^-$ usually only the $\ell^+\ell^-$-pair is recorded, isolating the $e^+e^-\tau^+\tau^-$ background from tau pair events is extremely difficult. From Monte Carlo, the background from events with $e^+e^-\tau^+\tau^-$ final states was found to be only about 0.03% for the peak energy and about 0.07% for the off-peak points, such that the background estimate was obtained from the Monte Carlo prediction and a 100% error was assigned.

Using the kinematic properties of two photon events discussed at the beginning of this section, two distributions were investigated after applying the respective enhancement cuts to estimate the two photon background: First, the $|\cos\theta^{mis}_{trk}|$ distribution, where the missing longitudinal momentum component is defined as $\cos\theta^{mis}_{trk} = -\sum_{i=1}^{N_{trk}} p^i_z / |\sum_{i=1}^{N_{trk}} \vec{p}^{\,i}|$ and two photon events are expected to have low values of $|\cos\theta^{mis}_{trk}|$. Second, as for the investigation of the efficiency of the two photon cuts, the distribution of the transverse momentum divided by the beam energy for an event, R_{p_t}, was investigated. Two photon events are expected to have low values of R_{p_t}.

The $|\cos\theta^{mis}_{trk}|$ and R_{p_t} distributions after applying all $e^+e^-\mu^+\mu^-$ enhancement

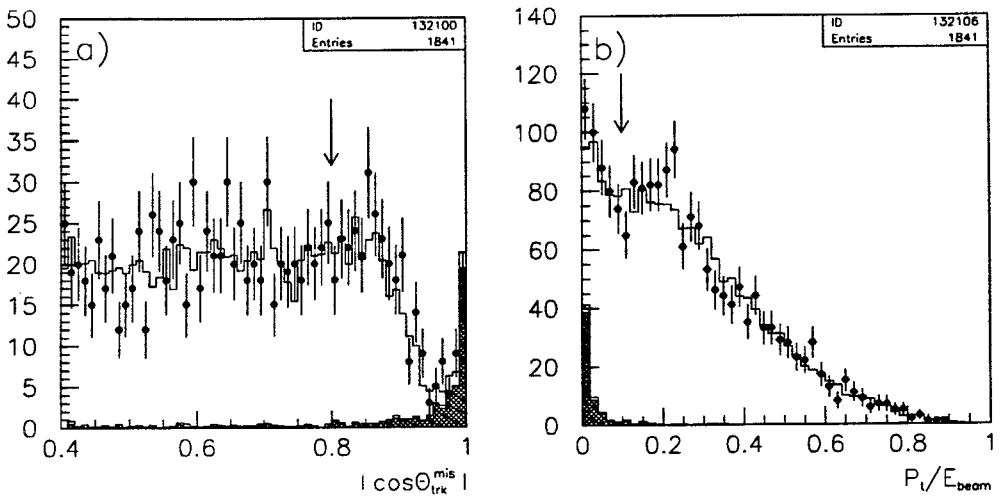

Figure 7.39: (a) The $|\cos\theta^{mis}_{trk}|$ and (b) the R_{p_t} distributions after all $e^+e^-\mu^+\mu^-$ enhancement cuts for 1994 data and MC. The points are data, the open histograms the total MC, the hatched histograms the total background MC, and the shaded histograms $e^+e^-\mu^+\mu^-$ MC only.

cuts are shown in figure 7.39, while figure 7.40 shows the same distributions after all $e^+e^-e^+e^-$ enhancement cuts. The $|\cos\theta^{mis}_{trk}|$ distributions show a very pronounced peak due to two photon events near $|\cos\theta^{mis}_{trk}| = 1$. However, the distribution has large tails, with two photon events being found all the way down to $|\cos\theta^{mis}_{trk}| \approx 0$. The R_{p_t} distribution on the other hand shows less pronounced tails, but the low R_{p_t} region is not only populated by two photon events but also by a large number of tau pair events. Since the $|\cos\theta^{mis}_{trk}|$ distribution in general shows better data MC agreement than the R_{p_t} distribution, it will be used to derive all correction factors, while the R_{p_t} distribution will be used to cross check the results.

First the $e^+e^-\mu^+\mu^-$ background will be discussed. The excess of data over MC was calculated after applying all $e^+e^-\mu^+\mu^-$ enhancement cuts in the region $|\cos\theta^{mis}_{trk}| > 0.8$. The ratio of data and MC events in the control region $|\cos\theta^{mis}_{trk}| < 0.8$ was found to be consistent with a ratio of 1 and did not show any dependence on $|\cos\theta^{mis}_{trk}|$ for 1994 and 1993 peak data and MC. For the off-peak points, the data

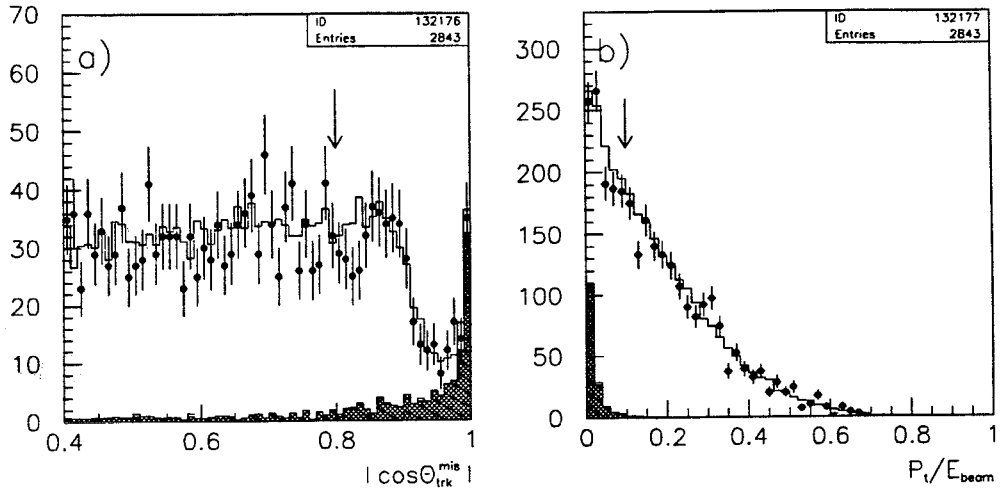

Figure 7.40: (a) The $|\cos\theta^{mis}_{trk}|$ and (b) the R_{p_t} distributions after all $e^+e^-e^+e^-$ enhancement cuts for 1994 data and MC. The points are data, the open histograms the total MC, the hatched histograms the total background MC, and the shaded histograms $e^+e^-e^+e^-$ MC only.

MC ratio in the control region was 0.839 ± 0.097 for 1993 p$-$2 and 0.900 ± 0.085 for 1993 p+2 data and MC. The tau pair MC for the off-peak points in the region $|\cos\theta^{mis}_{trk}| < 0.8$ was corrected by this factor. The difference between data and MC was then divided by the efficiency of the enhancement cuts for $e^+e^-\mu^+\mu^-$ MC to yield the estimate for the excess of $e^+e^-\mu^+\mu^-$ background in the data. The efficiencies after requiring $|\cos\theta^{mis}_{trk}| < 0.8$ were 0.709 ± 0.019 for 1994 MC and 0.746 ± 0.019 for 1993 MC.

For the R_{p_t} distribution, after applying the $e^+e^-\mu^+\mu^-$ enhancement cuts, the quality of the data MC agreement was found to be similar to that of the $|\cos\theta^{mis}_{trk}|$ distribution: In the control region $R_{p_t} > 0.1$ a good data MC agreement was observed for the 1994 and 1993 peak points, but some disagreement was found for the off-peak points. Therefore, the same procedure was applied as for the $|\cos\theta^{mis}_{trk}|$-distribution: For the off-peak points, the tau pair MC in the region $R_{p_t} < 0.1$ was corrected by the data MC ratio observed in the region $R_{p_t} < 0.1$.

Then the excess of $e^+e^-\mu^+\mu^-$ background was estimated from the data excess in the region $R_{p_t} < 0.1$, divided by the efficiency of the enhancement cuts. The efficiencies for the requirement $R_{p_t} < 0.1$ were 0.880 ± 0.014 for 1994 MC and 0.895 ± 0.013 for 1993 MC.

The excess of $e^+e^-e^+e^-$ events in the data was estimated in the same manner as for the $e^+e^-\mu^+\mu^-$ background. The enhancement cuts for these events result in larger discrepancies between the number of selected data and MC events. Therefore, the tau pair MC in the region $|\cos\theta^{mis}_{trk}| > 0.8$ was corrected by the data MC ratio in the region $|\cos\theta^{mis}_{trk}| < 0.8$ for all four data sets. These correction factors were 0.970 ± 0.021, 0.946 ± 0.038, 0.930 ± 0.080, and 0.933 ± 0.068 for 1994, 1993 peak, 1993 p$-$2, and 1993 p+2 data and MC, respectively. The $\tau^+\tau^-$ MC in the region $R_{p_t} < 0.1$ was corrected by the data MC ratio observed in the region $0.1 < R_{p_t}$. The correction factors in this case were 0.973 ± 0.025, 0.889 ± 0.043, 0.988 ± 0.098, and 0.963 ± 0.081 for 1994, 1993 peak, 1993 p$-$2, and 1993 p+2 data and MC, respectively. To yield the $e^+e^-e^+e^-$ background estimate, the data excess in the respective regions populated by the background were corrected for the efficiencies from $e^+e^-e^+e^-$ MC. The efficiencies for events in the region $|\cos\theta^{mis}_{trk}| > 0.8$ were 0.534 ± 0.013 for 1994 MC and 0.547 ± 0.013 for 1993 MC, for the region $0.1 < R_{p_t}$ the efficiencies were 0.790 ± 0.010 for 1994 MC and 0.800 ± 0.011 for 1993 MC.

Since the two photon background is not expected to depend on the energy or the year the data was recorded, the average $e^+e^-\mu^+\mu^-$ and $e^+e^-e^+e^-$ background for the four data samples was calculated. To do so, the excess observed in the data was added to the estimated background from $e^+e^-\mu^+\mu^-$ MC in the tau pair sample. The resulting number of events was divided by the luminosity of each data sample to get an estimate for the cross section of the background which is

expected to be independent of the center-of-mass energy. Figure 7.41 shows a fit to the estimated $e^+e^-\mu^+\mu^-$ background cross section from the $|\cos\theta^{mis}_{trk}|$ and the R_{p_t} distributions. The $|\cos\theta^{mis}_{trk}|$ results are shown as full circles and the fit to the four data samples as solid line, while the results from the R_{p_t} distribution are shown as open circles with a broken line indicating the fit. Figure 7.41a shows the results for the combination of data with MC of the same year, figure 7.41b shows the combinations of data with MC from the respective other year. The fit to the cross sections with the different MC samples agree very well, the difference being -0.019 pb for the $|\cos\theta^{mis}_{trk}|$ distribution and 0.088 pb for the R_{p_t} distribution. For figure 7.41a, the fitted cross sections from the $|\cos\theta^{mis}_{trk}|$ and the R_{p_t} disagree by 0.270 pb. This is within the error of either fit, but the errors for the two fits are correlated to some degree. The biggest disagreement between the cross sections from the $|\cos\theta^{mis}_{trk}|$ and the R_{p_t} distributions was observed for the 1993 p+2 point. When the fit for the $|\cos\theta^{mis}_{trk}|$ distribution is repeated without the 1993 p+2 result, a cross section of 1.364 ± 0.386 pb is obtained. The difference of $|1.234\text{ pb} - 1.364\text{ pb}| = 0.130$ pb has been added as an additional error. Table 7.23 shows the final result for the estimate of the background cross section and the additional errors that have been assigned.

Figure 7.42 shows a fit to the estimated $e^+e^-e^+e^-$ background cross sections. Shown are the results from the $|\cos\theta^{mis}_{trk}|$ distribution (full circles and solid line), and from the R_{p_t} distribution (open circles and broken line). Figure 7.42a shows the results for the combination of data with MC from the same year, figure 7.42b for the combination of data with MC from the respective other year. We observe a bigger disagreement when using different MC samples than we did in the case of $e^+e^-\mu^+\mu^-$ MC: For each fit in figure 7.42, combining data with the MC from the respective other year yields a higher background estimate than combining data

year		e^+e^- bkgr.	e^+e^- excess	efficiency	add'l	total
data	MC	from MC	in data	for e^+e^- MC	bkgr.	bkgr.
94	94	61.1 ± 4.0	129 ± 42	0.880 ± 0.021	147 ± 48	208 ± 48
94	93	46.4 ± 4.9	149 ± 44	0.830 ± 0.039	179 ± 54	226 ± 54
93 p	93	13.1 ± 1.4	10 ± 22	0.830 ± 0.039	12 ± 26	25 ± 26
93 p	94	17.2 ± 1.1	5 ± 22	0.880 ± 0.021	5 ± 24	22 ± 24
93 p−2	93	3.5 ± 1.1	13 ± 10	0.800 ± 0.124	17 ± 13	20 ± 13
93 p−2	94	6.3 ± 1.3	11 ± 10	0.818 ± 0.081	14 ± 12	20 ± 12
93 p+2	93	6.6 ± 1.2	-7 ± 12	0.934 ± 0.045	-7 ± 13	-1 ± 13
93 p+2	94	4.9 ± 0.7	-6 ± 12	0.941 ± 0.034	-6 ± 13	-1 ± 13

Table 7.7: Total Bhabha background from MC in the barrel region and the estimate for additional background in the data that is not properly modeled in MC. The additional MC background was calculated by scaling the results from table 7.6 by the efficiency of the cuts from Bhabha MC.

the data MC difference is dominated by the statistical error of the data, which is 100% correlated when using the same data with different MC samples, such that the different size of the data excess for the two different Monte Carlo samples is indeed statistically significant.

In table 7.7 the complete Bhabha background in the barrel region is shown. For this table, the excess calculated in table 7.6 was first corrected for the efficiency of the Bhabha enhancement cuts as determined from Bhabha MC and then added to the Bhabha background observed directly from Bhabha MC. Results are shown in the table for combining data with the MC of the same year, and with the respective other year. It was checked that the total Bhabha background estimates for the same year with different MC agree within their statistical errors when taking into account only the uncorrelated part of the overall error due to the different MC samples.

The procedure of scaling the tau MC in the region $\theta_{acop} < 1.0$ according to the agreement in the region $\theta_{acop} > 1.0$ was checked by investigating the acoplanarity

distribution after the multihadron rejection cuts $N^{hc}_{trk} + N^{hc}_{cls} < 4$ in the region

$$(R^{hc}_{trk} > 0.7 \text{ AND } R^{hc}_{trk} < 0.85 \text{ AND } R^{hc}_{shw} > 0.4 \text{ AND } R^{hc}_{shw} < 0.7)$$

OR

$$(R^{hc}_{shw} > 0.6 \text{ AND } R^{hc}_{shw} < 0.85 \text{ AND } R^{hc}_{trk} > 0.4 \text{ AND } R^{hc}_{trk} < 0.7)\,,$$

where mainly tau pair events are expected. This region is indicated in figure 7.11 and was chosen to yield roughly the same statistics as the Bhabha enhancement cuts. The fraction of Bhabha events accepted by these cuts is negligible. For all four data sets it was found that the data MC ratios agree well for the low and the high acoplanarity region. Furthermore, the ratio of the number of events in the high and low acoplanarity region was found to be consistent for data and $\tau^+\tau^-$ MC, validating the scaling procedure used for the $\tau^+\tau^-$ MC.

As a further check of the background estimates in table 7.6, the distribution of R^{sc}_{trk}, the track momentum in the cone with the *smaller* visible energy (i.e. the cone on which the cuts (7.1) and (7.2) were *not* applied) after the Bhabha enhancement cuts, but without applying an acoplanarity cut, was investigated. This distribution is shown in figure 7.13. A clear excess of data in the region $R^{sc}_{trk} > 0.8$ can be observed for 1994, while for 1993 peak any potential excess is small compared to the statistical significance of the check.

Since the Bhabha MC distribution in figure 7.13 does not show a sharp cutoff for any value of R^{sc}_{trk}, Bhabha background was estimated from the excess observed in both the regions $R^{sc}_{trk} > 0.6$ and $R^{sc}_{trk} > 0.8$. A data MC disagreement was observed over the whole range of $R^{sc}_{trk} > 0.8$ with a size simular to that for the acoplanarity distribution discussed above, making it necessary to scale the $\tau^+\tau^-$ MC in the region where the data excess was calculated. The $\tau^+\tau^-$ MC in the region $R^{sc}_{trk} > 0.6$ was scaled by the data MC ratio observed in the region $R^{sc}_{trk} < 0.6$ and the $\tau^+\tau^-$ MC in the region $R^{sc}_{trk} > 0.8$ was correspondingly scaled by the data

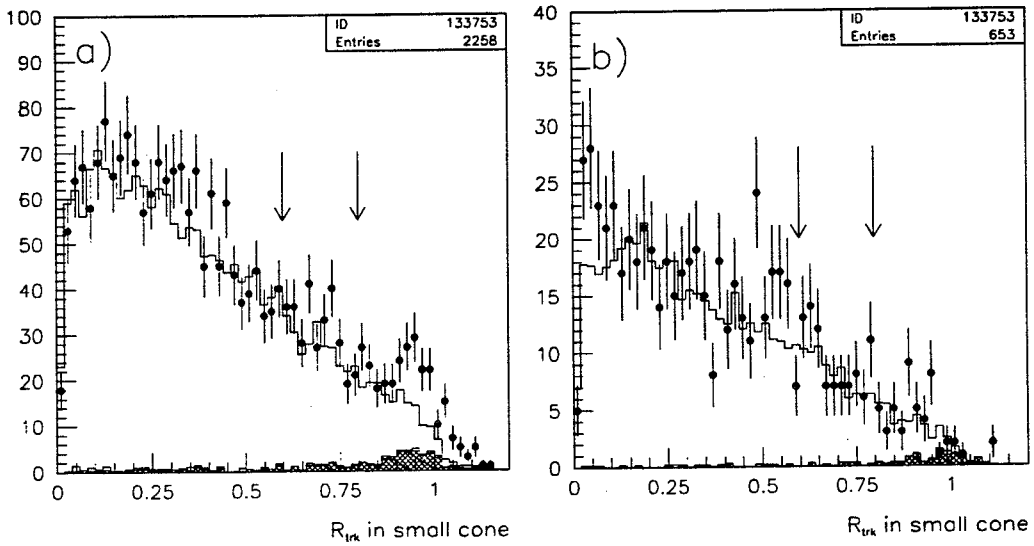

Figure 7.13: The relative track momentum distribution in the cone with the *smaller* visible energy after the Bhabha enhancement cuts on R^{hc}_{trk}, R^{hc}_{shw} and $N^{hc}_{trk}+N^{hc}_{cls}$ for (a) 1994 data and MC and (b) 1993 peak data and MC. The points are data, the open histograms total MC, the hatched histograms total background, and the shaded histograms Bhabha MC only. Bhabha background is expected to be concentrated near $R^{sc}_{trk} \approx 1$.

MC ratio in the region $R_{trk}^{sc} < 0.8$. The excess of data over MC in the two regions was calculated and the results were corrected by the respective Bhabha efficiency of the enhancement cuts from MC. The agreement with the results from table 7.7 was found to be quite good. In figure 7.13 one can observe the effect that would be expected from final state radiation: The Bhabha background shows tails extending down to $R_{trk}^{sc} \approx 0$. Consequently the efficiencies for this check are worse than for the Bhabha enhancement cuts used above and the estimates of the Bhabha excess rely quite heavily on an accurate simulation of bremsstrahlung in the Monte Carlo.

7.4.3 Background in the Forward Region

From studying Bhabha Monte Carlo, it was found that the Bhabha background in the tau pair sample can be basically divided into two classes: First, events in regions with high preshowering and second, highly radiative events, which are highly acollinear, and for which one electron has its track at $|\cos\theta| > 0.9$. For tracks beyond $|\cos\theta| \approx 0.9$, the tracking performance is rapidly degraded, and the track momentum is measured systematically too low. This is demonstrated in figure 7.14, where the difference of the track momentum and shower energy is shown for the individual cones versus the $|\cos\theta|$ value derived from the track momenta in the respective cone. The $\cos\theta$ derived from the track information in each cone separately will be denoted by $\cos\theta_{trk}^{cone}$. The difference between cone energy and shower energy is systematically below zero, since the tracking chamber does not record neutral particles. Over a large range of $|\cos\theta_{trk}^{cone}|$, data and MC show very good agreement. In the region of $0.7 \lesssim |\cos\theta_{trk}^{cone}| \lesssim 0.8$ one can see the effect of the preshowering material. Apart from that region, the difference between track momentum and shower energy is constant over $|\cos\theta_{trk}^{cone}|$, up to a sharp falloff

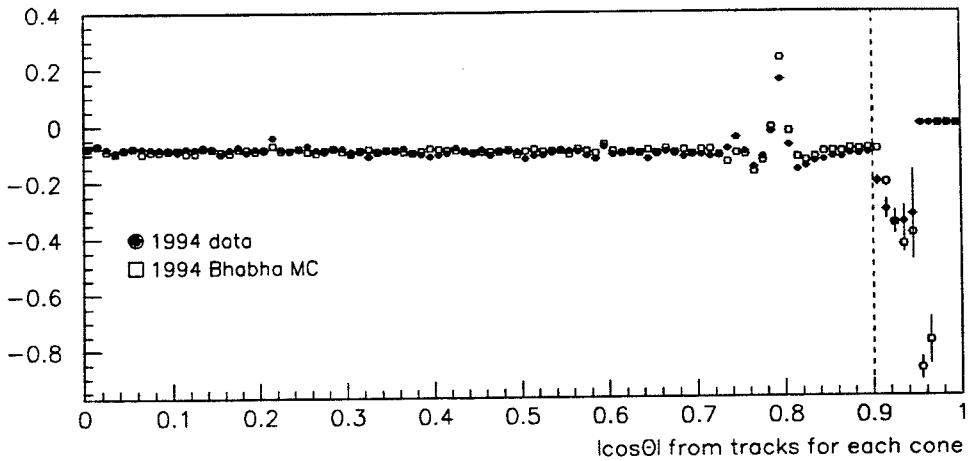

Figure 7.14: Track momentum minus shower energy per cone relative to the beam energy versus $|\cos\theta|$ derived from the track information in each cone, $|\cos\theta^{cone}_{trk}|$. Plotted are events which fail the Bhabha rejection cuts but pass all other tau pair selection cuts. The track momentum measurement becomes unreliable at $|\cos\theta^{cone}_{trk}| \approx 0.9$.

at $|\cos\theta^{cone}_{trk}| = 0.9$, as indicated by a broken line in the figure. The agreement between data and MC appears to be quite good, even though the MC seems to fall off at a slightly larger value of $|\cos\theta^{cone}_{trk}|$ and somewhat steeper than the data. These radiative events will be investigated first and then will be exclude from the study of the remaining Bhabha background.

Figure 7.15a shows the distribution of R^{cos}_{shw}, the shower energy divided by the beam energy in the cone with the larger value of $|\cos\theta^{cone}_{trk}|$, for events for which one cone fulfills $|\cos\theta^{cone}_{trk}| > 0.90$. The Bhabha background was estimated from the data excess in the region $R^{cos}_{shw} > 0.9$. In that region, good data-MC agreement was found for all four data sets. To check for potential underlying discrepancies of the data and $\tau^+\tau^-$ MC, a control region with $0.8 < R^{cos}_{shw} < 0.9$ was investigated. In that region with no significant Bhabha background, data was found to agree well with the Monte Carlo predictions. The procedure of estimating the Bhabha background from the region $R^{cos}_{shw} > 0.9$ and checking the

data MC agreement in the region $0.8 < R_{shw}^{cos} < 0.9$ was repeated for the cuts $|\cos\theta_{trk}^{cone}| > 0.85$ and 0.89. The results agreed well with the results obtained for the cut $|\cos\theta_{trk}^{cone}| > 0.90$. As a further check of the agreement between data

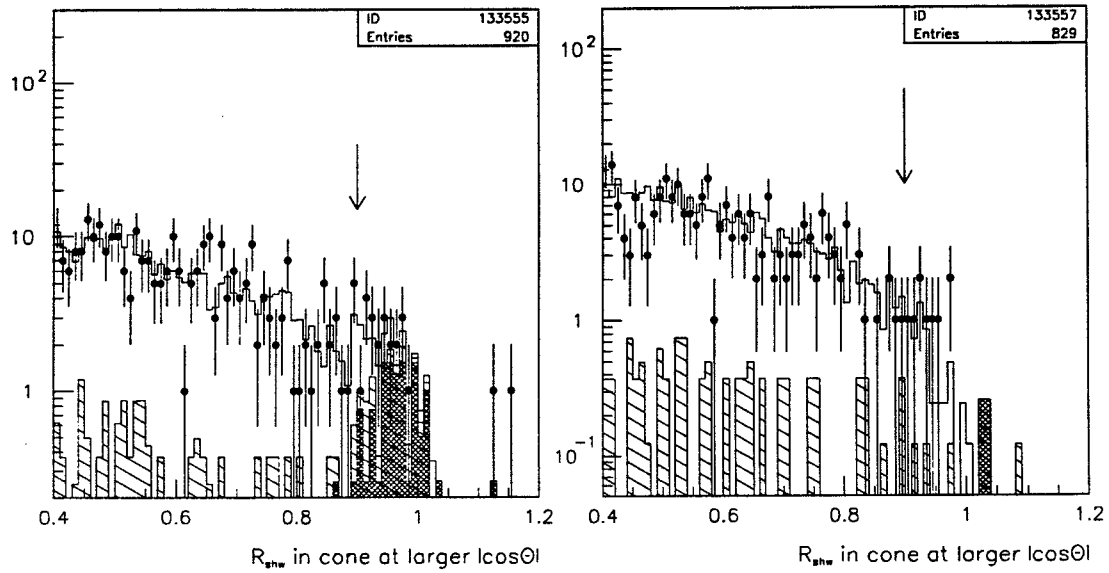

Figure 7.15: The R_{shw} distribution in cone with the larger $|\cos\theta_{trk}^{cone}|$ after all tau pair selection cuts and after requiring that the one cone have (a) $|\cos\theta_{trk}^{cone}| > 0.90$ or (b) $0.90 > |\cos\theta_{trk}^{cone}| > 0.89$ for 1994 data and MC. The points are data, open histograms MC, hatched histograms MC background and shaded histograms Bhabha MC. In figure b the Bhabha background in the region $R_{shw} > 0.9$ is largely suppressed.

and $\tau^+\tau^-$ MC, the Bhabha background was suppressed by choosing events in the region $0.89 < |\cos\theta_{trk}^{cone}| < 0.90$. The R_{shw}^{cos}-distribution for this selection is shown in figure 7.15b. For all four data sets, good agreement of data and MC was found after applying the cuts $0.89 < |\cos\theta_{trk}^{cone}| < 0.90$ for both the regions $0.8 < R_{shw}^{cos} < 0.9$ and $R_{shw}^{cos} > 0.9$.

The estimated background of radiative Bhabha events from the data MC difference in the region $|\cos\theta_{trk}^{cone}| > 0.90$ is shown in table 7.8 for the four data sets, each one compared with both 1993 and 1994 MC and corrected for the efficiency of the R_{shw} cut from Bhabha MC.

year data	MC	data−MC	eff. from e^+e^- MC	estimated bkgr.
94	94	-1.02 ± 5.26	0.958 ± 0.029	-1.06 ± 5.49
94	93	2.01 ± 5.62	0.798 ± 0.081	2.52 ± 7.05
93 p	93	2.09 ± 2.95	0.798 ± 0.081	2.62 ± 3.71
93 p	94	1.24 ± 2.89	0.958 ± 0.029	1.29 ± 3.02
93 p−2	93	-1.22 ± 1.71	0.669 ± 0.135	-1.82 ± 2.58
93 p−2	94	0.37 ± 1.53	0.667 ± 0.192	0.55 ± 2.30
93 p+2	93	5.76 ± 2.68	0.750 ± 0.217	7.56 ± 4.19
93 p+2	94	5.19 ± 2.68	0.708 ± 0.111	7.33 ± 3.96

Table 7.8: The background estimate from radiative Bhabha events with one badly measured track at $|\cos\theta_{trk}^{cone}| > 0.90$.

From 1994 Bhabha MC it was found that 20.7% of the Bhabha events passing the tau pair selection cuts have a cone with $|\cos\theta_{trk}^{cone}| > 0.90$. Now the remaining Bhabha background that enters the tau sample as a result of reduced visible energy due to preshowering or the low resolution of the electron calorimeter and/or the tracking chambers will be investigated. Figure 7.16a shows the distribution of track momentum versus shower energy relative to the beam energy in the cone with the higher visible energy for 1994 Bhabha MC in the forward region after all tau pair selection cuts have been applied. Comparing figure 7.16a with the corresponding figure 7.11 for the barrel region, one finds that the Bhabha background in the forward region is spread out over a much wider area in the $R_{shw} - R_{trk}$ plane. In order to define Bhabha enhancement cuts with a high efficiency, much looser cuts than in the case of the barrel region have to be applied. The cuts that were chosen are shown in figure 7.16 as broken lines and select events with

$$R_{shw}^{hc} > 0.5 \text{ OR } R_{trk}^{hc} > 0.4 \ .$$

As can be seen in figure 7.16b for muon MC, those cuts accept basically all the muon background in the forward region. The muon background populates the

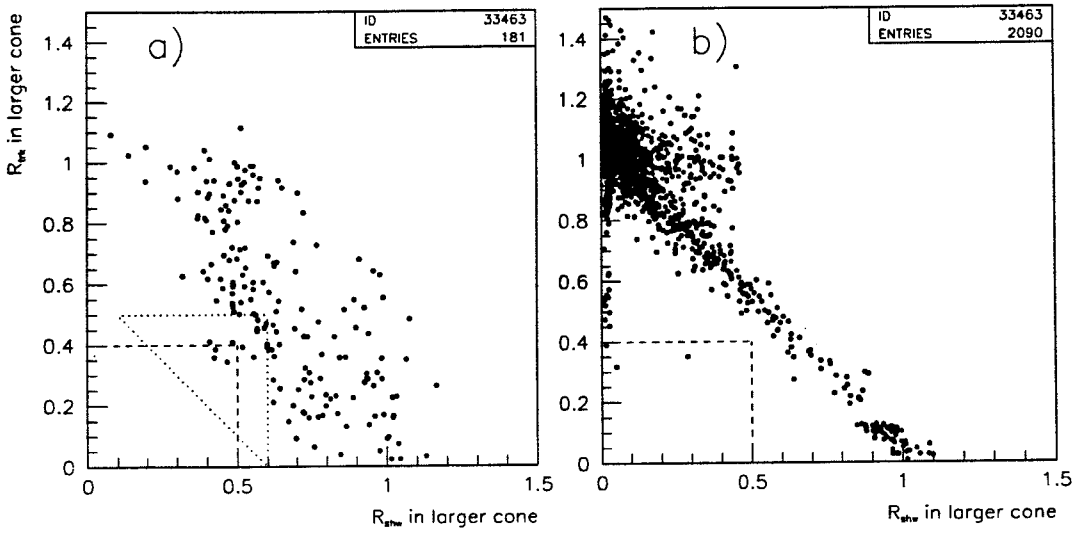

Figure 7.16: Distribution of track momentum versus shower energy divided by the beam energy in the cone with the higher visible energy after all tau pair selection cuts have been applied for (a) 1994 Bhabha MC and (b) 1994 muon MC in the forward region. Cuts to enhance the Bhabha background are shown by broken lines, while a control region with little Bhabha background is indicated in plot (a) by a dotted line. Plot (b) shows clearly that additional cuts are necessary to reject muon events.

region with $R^{hc}_{shw} + R^{hc}_{trk} \approx 1.0$, where the large shower energy of some of the muons is due to final state radiation. Therefore all events which have a muon in either cone as identified by the electromagnetic calorimeter, the muon chamber or the hadron calorimeter were rejected. As in the barrel region, multihadronic events were rejected by requiring

$$N^{hc}_{trk} + N^{hc}_{cls} < 4 \, .$$

The acoplanarity distribution after all the cuts described above is shown in figure 7.17. For the forward region, an excess of MC (rather than data) in the control region with $\theta_{acop} > 2.0$ was observed. The data MC ratio in the control region was 0.954 ± 0.024 , 0.977 ± 0.045 , 0.863 ± 0.089 , and 0.917 ± 0.079 for 1994, 1993 peak, 1993 peak-2, and 1993 peak$+2$ data and MC, respectively. The region $\theta_{acop} > 2.0$

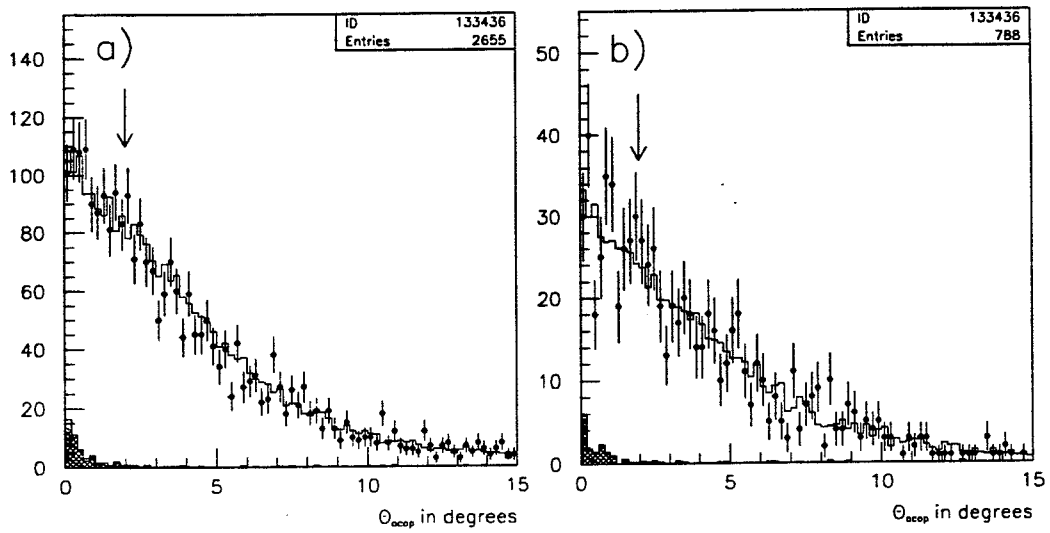

Figure 7.17: Acoplanarity distribution for events after all Bhabha enhancement cuts in the forward region for (a) 1994 and (b) 1993 peak data and MC. The points are data, the open histograms MC, the hatched histograms MC background and the shaded histograms Bhabha MC only.

was divided into three subregions and no evidence was found that the data MC disagreement shows any dependence on the acoplanarity angle. Therefore, the tau pair MC in the region $\theta_{acop} < 2.0$ was scaled by the data MC ration observed in the region $\theta_{acop} > 2.0$. The excess of data over MC in the region $\theta_{acop} < 2.0$ was then corrected for the Bhabha efficiency of the enhancement cuts as obtained from Bhabha MC. The resulting estimate of the data excess in the forward region is shown in table 7.9.

In order to check the assumption that the data-MC disagreement is independent of the acoplanarity angle, a control region was defined by selecting events with

$$R^{hc}_{shw} < 0.6 \text{ AND } R^{hc}_{trk} < 0.5 \text{ AND } R^{hc}_{shw} + R^{hc}_{trk} > 0.6 \ .$$

These cuts are shown as dotted lines in figure 7.16a. The same multiplicity cut and

year data	year MC	data	tot MC with $\tau\tau$ scaled	data−MC	e^+e^- eff. from MC	estimted excess
94	94	955 ± 31	897 ± 24	58 ± 39	0.839 ± 0.027	70 ± 47
94	93	955 ± 31	920 ± 28	35 ± 41	0.815 ± 0.036	42 ± 51
93 p	93	284 ± 17	272 ± 13	12 ± 21	0.815 ± 0.036	15 ± 26
93 p	94	284 ± 17	265 ± 12	19 ± 21	0.839 ± 0.027	22 ± 25
93 p−2	93	53 ± 7.3	52.9 ± 5.2	0.1 ± 8.9	0.727 ± 0.094	0 ± 12
93 p−2	94	53 ± 7.3	55.4 ± 5.2	-2.4 ± 9.0	0.900 ± 0.054	-3 ± 10
93 p+2	93	83 ± 9.1	77.8 ± 6.7	5.2 ± 11.3	0.853 ± 0.079	6 ± 13
93 p+2	94	83 ± 9.1	76.6 ± 6.6	6.5 ± 11.3	0.864 ± 0.065	8 ± 13

Table 7.9: Estimated excess of Bhabha background in the forward region for $|\cos\theta^{cone}_{trk}| < 0.90$ after Bhabha enhancement cuts and scaling $\tau^+\tau^-$ MC as described in the text. Combinations of data with different MC are shown. For the off-peak 1994 MC, only Bhabha MC is for the 1994 detector, while all other MC is for the 1993 detector.

muon rejection as described above are also applied. The acoplanarity distribution for events passing these cuts was investigated. Since the Bhabha events are much less localized in the $R^{hc}_{trk} - R^{hc}_{shw}$ plane for the forward region than for the barrel region, the control sample has only about 40% of the statistics of the event sample selected by Bhabha enhancement cuts. The fraction of Bhabha background compared to figure 7.17 was reduced by about 60%. On this level of statistics, the data-MC ratio was found to be consistent for the regions $\theta_{acop} > 2.0$ and $\theta_{acop} < 2.0$. Furthermore, the ratio of events between the two regions agreed well for data and MC. We conclude that the procedure of scaling the $\tau^+\tau^-$ MC in the region $\theta_{acop} < 2.0$ by the data-MC ratio observed in the region $\theta_{acop} < 2.0$ is indeed valid.

In order to conduct a cross check of the Bhabha background estimate in the forward region, Bhabha enhancement cuts were applied which were somewhat

modified from those above. First, events were required to have $R_{trk} < 0.8$. This cut effectively rejects muon events, since a large number of muon events leak into the tau sample in the geometric region $70\,\text{deg} \lesssim \phi \lesssim 110\,\text{deg}$ of the endcap region. The muon detector endcaps are not sensitive in those regions, resulting in muon pair events in those regions to be less likely identified as such. If a genuine muon pair event is not selected by the muon pair selection cuts, it is consequently not rejected from the tau pair sample. These events can be seen in figure 7.4 for low R_{shw} values at $R_{trk} \approx 1.0$ and in figure 7.10 at $R_{shw} < 0.25$. The R^{hc}_{trk} versus R^{hc}_{shw} distribution for events with $R_{trk} < 0.8$ in the forward region is shown in figure 7.18. It was then required

$$R^{hc}_{shw} + R^{hc}_{trk} > 0.8 \text{ AND } R^{hc}_{shw} > 0.2$$

and multihadronic events were as before rejected by the cut $N^{hc}_{trk} + N^{hc}_{cls} < 4$. Requiring $R^{hc}_{shw} > 0.2$ rejects most of the remaining background from muon events emitting final state radiation.

The acoplanarity distribution after these "alternative" Bhabha enhancement cuts is shown in figure 7.19. This distribution shows a qualitative behavior very simular to the acoplanarity distribution after the original Bhabha enhancement cuts shown in figure 7.17: The region $\theta_{acop} > 2.0$ shows an excess of MC over data which however does not seem to have any dependence on the acoplanarity. As before, the $\tau^+\tau^-$ MC in the region $\theta_{acop} < 2.0$ was scaled by the data MC ratio observed in the region $\theta_{acop} > 2.0$.

The data excess in the region $\theta_{acop} < 2.0$ for the alternative Bhabha enhancement cuts, after scaling the $\tau^+\tau^-$ MC and after applying an efficiency correction derived from Bhabha MC, was compared to the results from table 7.9. The only data MC comparison for which a fairly big difference between the two methods

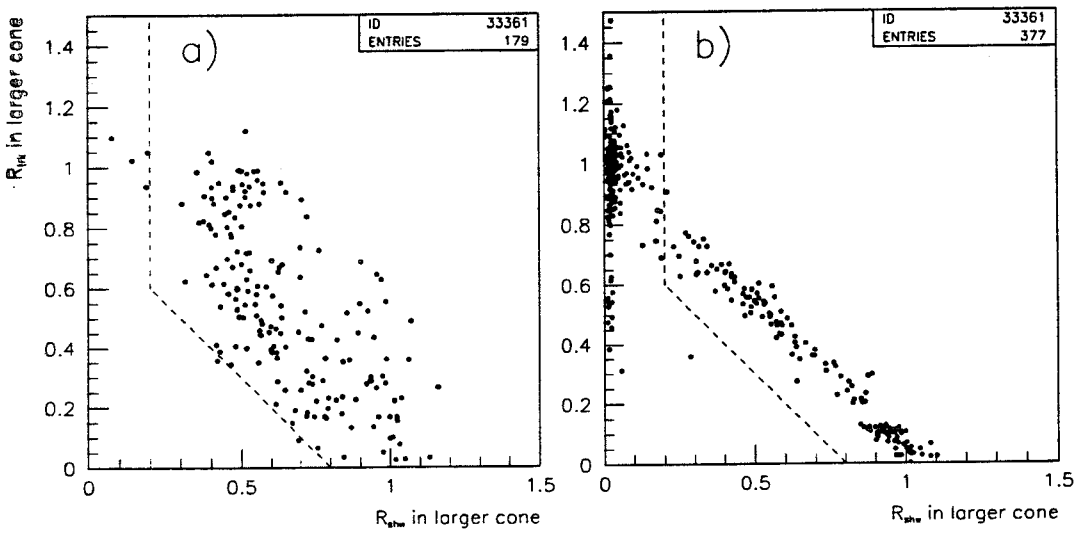

Figure 7.18: The distribution of the track momentum versus the shower energy divided by the beam energy in the cone with the larger visible energy after all tau pair selection cuts and requiring $R_{trk} < 0.8$ in the forward region. Plot (a) shows 1994 Bhabha MC and plot (b) 1994 muon MC. The alternative cuts to enhance the Bhabha background as described in the text are shown by broken lines. The muon background in plot (b) is much stronger suppressed than in figure 7.16.

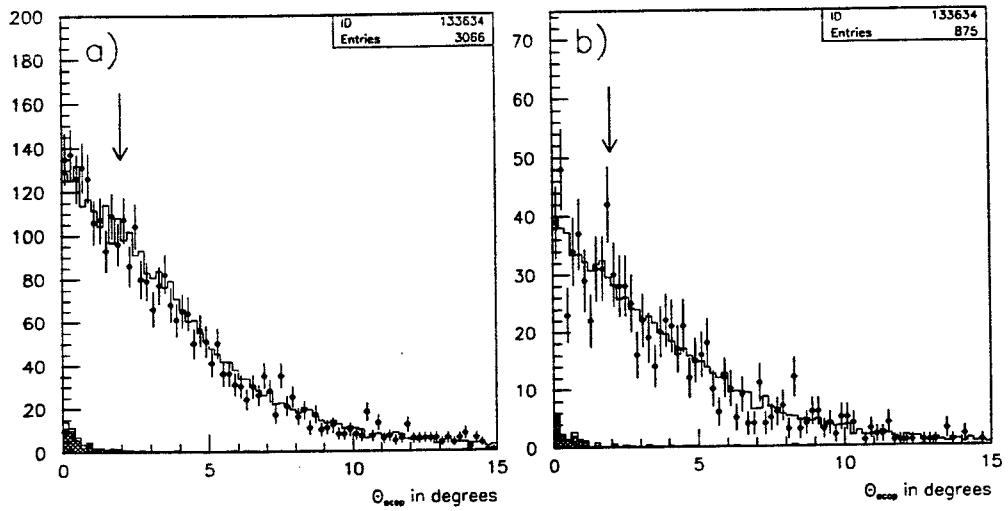

Figure 7.19: Acoplanarity distribution after the "alternative" Bhabha enhancement cuts described in the text for 1994 (a) and 1993 peak (b). The points are data, the open histograms MC, the hatched histograms MC background and the shaded histograms Bhabha MC.

could be observed was 1994 data with 1993 peak MC. Taking error correlations into account, it was found that the two results agreed on a level of no worse than 1.3σ, which was considered acceptable [68].

For the final Bhabha background estimate in the forward region, the results from the tables 7.9 and 7.8 and the Bhabha background from MC were added. The results are shown in table 7.10.

In analogy to the background estimate in the barrel region, it was checked that the total Bhabha background estimates in the forward region for the same year compared to different MC samples agree within their statistical errors when taking into account only the uncorrelated part of the overall error due to the different MC samples.

year		e^+e^- MC	excess from	remaining	total
data	MC	bkgr.	radiative events	excess	bkgr.
94	94	58.84 ± 3.88	-1.06 ± 5.49	69.63 ± 46.78	127.41 ± 47.26
94	93	71.20 ± 6.03	2.52 ± 7.05	42.36 ± 50.90	116.08 ± 51.74
93 p	93	20.03 ± 1.70	2.62 ± 3.71	14.59 ± 25.85	37.24 ± 26.17
93 p	94	16.56 ± 1.09	1.29 ± 3.02	22.54 ± 24.54	40.39 ± 24.75
93 p−2	93	11.57 ± 1.96	-1.82 ± 2.58	0.10 ± 12.30	9.85 ± 12.72
93 p−2	94	10.23 ± 1.69	0.55 ± 2.30	-2.61 ± 9.97	8.17 ± 10.37
93 p+2	93	5.28 ± 1.08	7.56 ± 4.19	6.12 ± 13.26	18.96 ± 13.95
93 p+2	94	4.67 ± 0.70	7.33 ± 3.96	7.47 ± 13.06	19.47 ± 13.08

Table 7.10: Total Bhabha background from MC and the estimate for additional background in the data that is not properly modeled in MC for the forward region for different data MC combinations.

7.4.4 Total Bhabha background

In table 7.11 the estimates for the Bhabha background in the barrel and the forward region from tables 7.7 and 7.10 were added to yield the final correction factor. The final background estimate is virtually independent of the MC samples that were used to derive the results.

7.5 Muon Events

The procedure of discarding events which are classified as muon pair events from the tau pair sample has the effect that the single muon rejection cut from section 7.2.3 really is composed of multiple cuts, each one applied on quantities which are not identical to the quantities used for the tau pair analysis. This does not have any serious consequences for the assessment of background from muon events leaking into the tau pair sample, but it does make a comparison of data and MC for genuine tau pair events, which are classified as muon pair events and consequently are discarded from the tau pair sample, more difficult. However, the

year					correction
data	MC	barrel	forward	total	factor
94	94	208 ± 48	127 ± 47	336 ± 67	0.9940 ± 0.0012
94	93	226 ± 54	116 ± 52	342 ± 75	0.9939 ± 0.0013
93 p	93	25 ± 26	37 ± 26	62 ± 37	0.9960 ± 0.0024
93 p	94	22 ± 24	40 ± 25	63 ± 35	0.9960 ± 0.0022
93 p−2	93	20 ± 13	10 ± 13	30 ± 18	0.9912 ± 0.0053
93 p−2	94	20 ± 12	8 ± 10	28 ± 16	0.9917 ± 0.0047
93 p+2	93	-1 ± 13	19 ± 14	18 ± 19	0.9962 ± 0.0040
93 p+2	94	-1 ± 13	19 ± 13	18 ± 18	0.9961 ± 0.0038

Table 7.11: Combined background from the barrel and endcap region and final estimate for the correction and systematic error due to the Bhabha background. The correction factors resulting from combining data with the MC of the respective other year are shown for comparison.

discarded muon events are characterized by a high visible energy as defined in section 7.2.1. Figure 7.20 shows the R_{vis} distribution for events discarded from the tau pair sample as muon pair events but passing all other tau pair selection cuts. Clearly, by investigating the region $R_{vis} \lesssim 0.85$, most of the muon pair events which are discarded from the tau pair sample are rejected, while basically all tau pair events are selected. This separation between tau pair and muon pair events will allow for an investigation of tau pair events being mistakenly discarded as muon pair events, as will be described in section 7.5.2.

A detailed description of the cuts applied to select muon events can be found in [66]. The basic elements of the cuts are the following [14]: Two tracks, each having a momentum greater than 6 GeV, matched to the beam interaction point and identified as a muon by at least one outer detector (the electromagnetic calorimeter, the hadron calorimeter or the muon chambers), are required. Multihadronic events are rejected by removing events with more than three charged tracks, after applying corrections for additional tracks due to photon conversion and "track

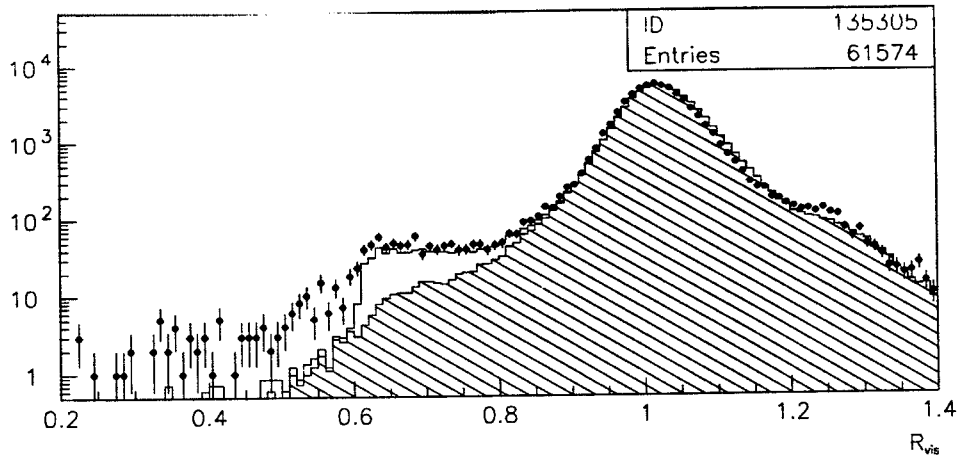

Figure 7.20: The R_{vis} distribution for events that are discarded as muon pair events but pass all other tau pair selection cuts for 94 data and MC. The points are data, the open histogram is the total MC and the hatched histogram is the background MC.

splitting" of tracks close to the anode wires in the jet chamber. Remaining tau pair and two-photon backgrounds are rejected by a requirement that the sum of the two highest momentum tracks plus the highest energy electromagnetic cluster be at least $0.6 \cdot \sqrt{s}$.

These cuts fail to identify a large number of genuine muon events which have a track close to a CJ anode wire: In those regions, the momentum measurement is not very accurate, resulting in reconstructed track momenta which are up to several tens of GeV different from the true value. To reduce the number of muon pair events with too low a reconstructed track momentum that are leaking into the tau pair sample, events which pass "alternative" muon selection cuts are also discarded from the tau sample. For this selection, events with back-to-back segments in the muon chamber and the electromagnetic calorimeter consistent with a muon pair event are investigated. An event then passes the alternative selection, if at least one of its tracks is close to an anode or cathode wire, or if one of the charged tracks is classified as a "very high quality" track. A "very high quality"

track is defined by tightened requirements on the proximity of the track to the interaction point, the track momentum and the number of axial CV wires that fired.

7.5.1 Efficiency of Muon Rejection Cuts

Events that fail the tau pair selection due to the muon pair rejection only were investigated and tau pair events in this sample were enhanced by the following cuts:

- $\theta_{acop} \geq 0.5\,\mathrm{deg}$
- event should not be within 1 deg of an anode plane.

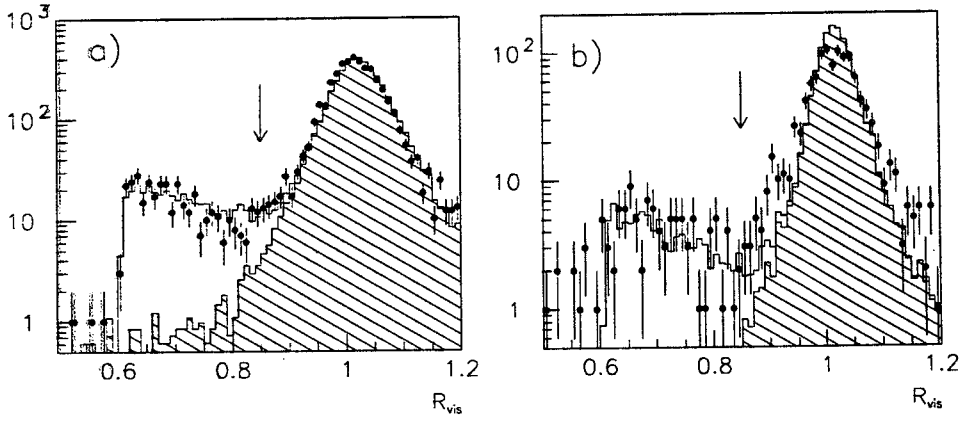

Figure 7.21: The distribution of the relative visible energy for events which fail the tau pair selection cuts due to the muon pair rejection only and pass the tau enhancement cuts explained in the text. Shown are (a) 1994 data and MC and (b) 1993 peak data and MC. The points are the data, the open histograms contain all MC samples and the hashed histograms are the background MC, which is almost exclusively muon pair MC.

In figure 7.20 an excess of data events that are discarded from the tau pair event sample in the region $R_{vis} < 0.6$ could be observed. Data events in this region were found to be located near the CJ wires and having a very low shower energy, a low

acoplanarity angle and a muon identified by the outer detectors in at least one cone. These events were therefore assumed to be muon pair events that have too low a track momentum assigned and were not assumed to be candidates for tau pair events failed by the muon rejection cuts.

Figure 7.21 shows the distribution of the relative visible energy for events passing the tau pair enhancement cuts from above for 1994 and 1993 peak data and MC. The muon pair events can be seen at high R_{vis} values. The agreement between data and MC was examined in the region $0.4 \leq R_{vis} \leq 0.85$ as indicated by the arrow in the plots. The muon peak is much better simulated by the 1994 MC, while the region $0.85 \leq R_{vis} \leq 1.0$ shows some disagreement between data and MC for all Monte Carlo samples. This disagreement is presumably due to a bad simulation of the muon pair events and could affect the muon pair MC in the region $0.4 \leq R_{vis} \leq 0.85$ as well. Therefore, the muon pair MC in the region $0.4 \leq R_{vis} \leq 0.85$ was multiplied by the data MC ratio in the region $0.85 \leq R_{vis} \leq 1.0$ minus 1, and the result assigned as an additional error. The errors derived in this fashion are $(1.19 - 1) \cdot 33.0 = 6.3$ for 1994 data and MC, $(1.23 - 1) \cdot 5.5 = 1.3$ for 1993 peak data and MC, $(1.34 - 1) \cdot 1.9 = 0.6$ for 1993 p$-$2 data and MC, and $(1.09 - 1) \cdot 2.6 = 0.2$ for 1994 p+2 data and MC. The data MC difference in the region $0.9 \leq R_{vis} \leq 1.0$ is -23.7 ± 29.1 for 1994 data and MC, 17.8 ± 10.5 for 1993 peak data and MC, -2.4 ± 4.2 for 1993 p$-$2 data and MC, and 8.2 ± 6.1 for 1994 p+2 data and MC. Here the error is composed of the statistical error from the data MC difference and the additional error due to the data MC disagreement in the region $0.85 \leq R_{vis} \leq 1.0$, which were conservatively added linearly. The result was then divided by the efficiency of about 0.58 for the cuts derived from tau pair MC. The results are shown in table 7.12.

data sample	estimated data excess	correction factor
1994	-40.6 ± 44.5	0.9993±0.0008
1993 peak	30.4 ± 20.0	1.0019±0.0013
1993 p−2	-4.2 ± 7.4	0.9988±0.0022
1993 p+2	14.1 ± 10.5	1.0030±0.0022

Table 7.12: The estimated data excess of events discarded as muon pair events. In the last column, the resulting correction factors and errors are shown.

7.5.2 Muon Background

The muon pair background in the tau pair sample is estimated from MC to be about 0.75%. A part of the muon pair events leak into the tau pair sample because one of the muons has radiated a photon, such that the acoplanarity is degraded and should not be relied on for enhancing muon pair events. Radiative muon pair events could already be observed in figure 7.16b as events with a shower energy much bigger than zero and a relative visible energy of about 1 in the cone with the higher visible energy. Therefore, muon pair events were enhanced by using cuts which require a low shower energy in one cone and a visible energy of about 1. Figure 7.22 shows examples of plots from these samples. The events in figure 7.22a were selected by requiring that the cone with R_{vis}^{cone} closest to 1 has $R_{shw}^{cone} < 0.2$. The visible energy divided by the beam energy of the opposite cone (R_{vis}^{opp}) is then plotted. Figure 7.22b shows the relative visible energy for events in which one cone has a relative visible energy in the range 0.7 to 1.3 and a relative shower energy of less than 0.2. Muon pair events (shown by the shaded histograms) should appear at values around 1 in these distribution and there is good agreement between data and MC in the region indicated by the arrows. From the agreement of the number of data and MC events in the region $0.8 < R_{vis}^{opp} < 1.3$ from figure 7.22a, the background correction factor was derived. First, the data MC ratio outside

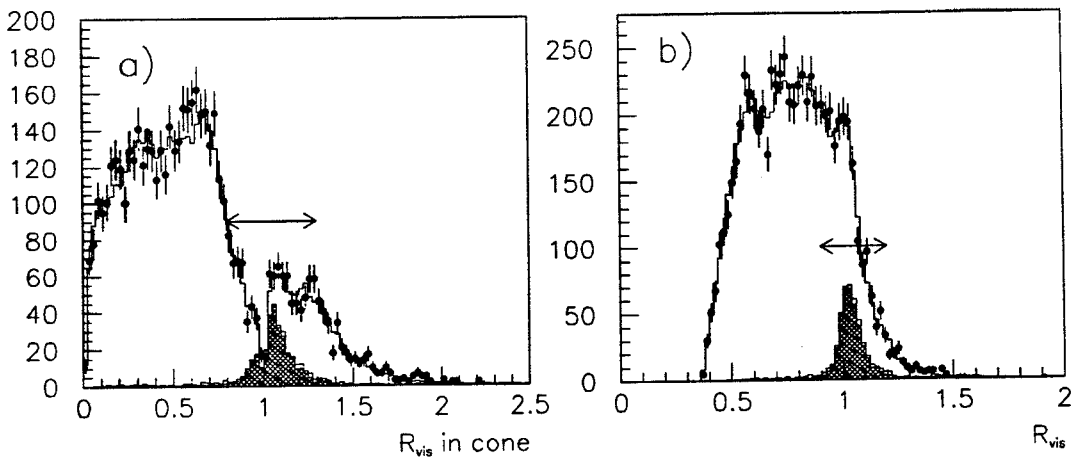

Figure 7.22: The points are data, the open histogram contains all MC samples, the hashed histogram the MC background samples and the shaded histogram is the muon pair MC only. Plot (a) shows the relative visible energy in an individual cone and plot (b) shows the total visible energy for events selected as described in the text.

this region was calculated, and the tau MC in the region $0.8 < R_{vis}^{opp} < 1.3$ was scaled by this ratio. The resulting scaling factors were 1.017 ± 0.015 for 1994 data and MC, 0.962 ± 0.028 for 1993 peak data and MC, 1.081 ± 0.065 for 1993 p$-$2 data and MC, and 0.953 ± 0.052 for 1994 p+2 data and MC. Then the data MC difference was calculated in the region $0.8 < R_{vis}^{opp} < 1.3$, and the result divided by the efficiency of the cuts for muon pair MC. The efficiencies were about 0.65 for the four different muon MC samples. The resulting estimate for the background that is not modelled by the MC and the background predictions from MC are shown in table 7.13. Varying the region of the R_{vis}^{opp} cuts had no significant effect on the results.

It was also investigated if events failed the muon pair selection cuts due to bad tracking and hence end up in the tau pair sample. Such events may not show up in the above checks because the badly measured track would lead to a visible energy significantly different from the beam energy. In order not to rely

data sample	MC prediction	extra bckgnd	correction factor
1994	424.3 ± 7.2	-33.4 ± 49.2	0.9930 ± 0.0009
1993 peak	116.1 ± 3.4	8.9 ± 24.6	0.9920 ± 0.0016
1993 p−2	24.6 ± 1.0	-4.7 ± 11.9	0.9942 ± 0.0035
1993 p+2	36.5 ± 1.5	3.2 ± 14.0	0.9917 ± 0.0029

Table 7.13: Muon pair background estimates from the MC and the estimate of additional background in the data samples.

on any track information, a sample of events in which the muon pair background has been enhanced is selected using muon identification from the outer detectors. For events with at least one identified muon in each cone and an acoplanarity of $\theta_{acop} < 2$ deg, figure 7.23 shows the ϕ distribution modulo 15 deg (i.e. a CJ sector). With the alternative muon pair selection cuts used to reject muon pair events with bad tracking, the extra muon pair background not modelled by the MC was dramatically reduced [68]. In figure 7.23, no significant extra muon pair background can be noticed near the CJ wires. Figure 7.24 shows the acoplanarity distribution for events with at least 1 identified muon in each cone for 1994 data compared to 1994 MC. The excess of events seen at low θ_{acop}, indicated by the arrow in figure 7.24 is assumed to be due to background muon pair events in the tau sample which are not well simulated by the $e^+e^- \rightarrow \mu^+\mu^-$ MC *and* due to muons from cosmic ray events. The Monte Carlo simulations that were compared to data did not include cosmic ray events and as will be discussed in section 7.8, cosmic ray events consist essentially of muons. If these traverse the detector close to the interaction point, their apparent acoplanarity is near zero. The excess in the region $\theta_{acop} < 0.5$ deg was found to be almost completely due to cosmic ray events. After subtracting the contribution expected from cosmic ray events, the data MC agreement observed in the region $\theta_{acop} < 0.5$ deg was found to be consistent with

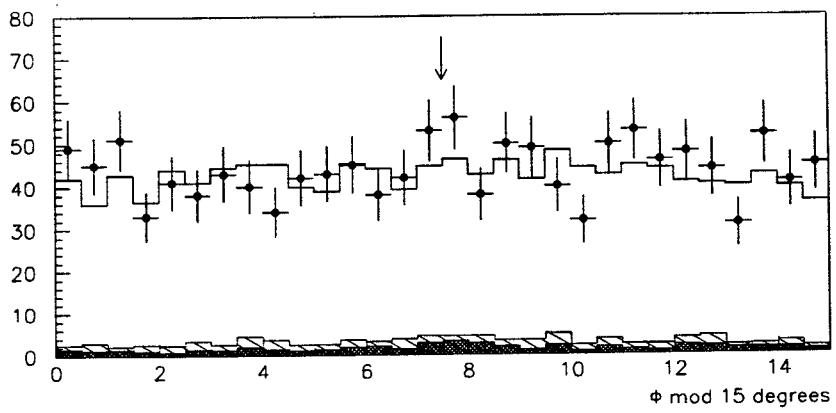

Figure 7.23: The ϕ(mod 15 deg) distribution for events with one identified muon in each cone and $\theta_{acop} < 2$ deg which pass all tau pair selection cuts. The arrow indicates the position of the CJ-wires. The points are data, the open histogram total MC, the hashed histogram background MC only and the shaded histogram muon pair MC only.

the results of a data excess consistent with zero from table 7.13.

From figure 7.24 it can be seen that the low acoplanarity region being used for this check also contains background from sources other than muon pairs. This background (the hashed region of the plot) was found to be mostly from two photon events with final state $e^+e^-\mu^+\mu^-$ and to a smaller degree from multihadron events. A cut was applied on the transverse momentum ($p_T \geq 0.02\ E_{beam}$) to remove the two photon events and on the number of tracks ($N_{trk} < 5$) to remove the multihadron events. These cuts reduces the fraction of $e^+e^-\mu^+\mu^-$ events in the background sample from 41% to 6% and the multihadron fraction from 11% to 1.5%, respectively. The data MC agreement in the low acoplanarity region was not affected by the cuts.

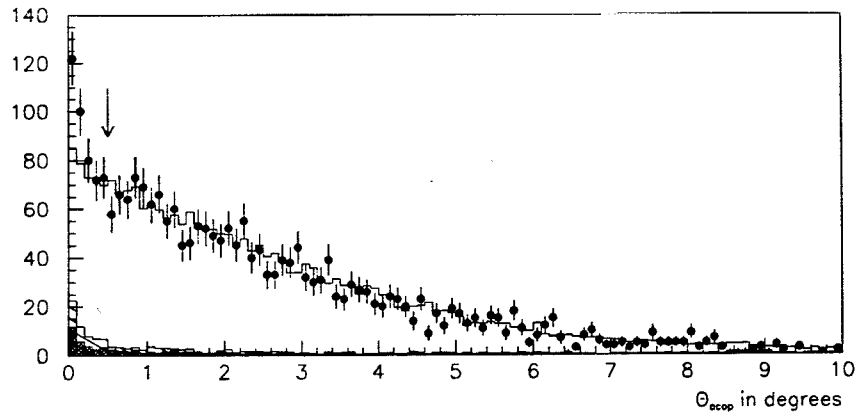

Figure 7.24: Acoplanarity distribution for events with one identified muon in each cone for 1994 data and 1994 MC. The points are data, the open histogram contains all MC samples, the hashed histogram background MC, abd the shaded histogram is the muon pair MC only.

7.6 Multihadronic Events

Due to its hadronic decay modes, a decaying τ lepton can mimic a fragmenting quark. The tau lepton has a probability of about 14% to decay into three or more charged particles, the probability for both taus to decay into a combined number of six or more charged tracks is about 2%. Figure 7.25 shows the distribution of the number of charged tracks N_{trk} and of the total multiplicity N_{tot} after all other tau pair selection cuts have been applied. The cuts on the total multiplicity and the number of charged tracks that are applied to reject multihadronic events from the tau pair sample are indicated by arrows. Figure 7.26 compares the data and MC distributions of the number of charged cones. The background discarded by the the N_{cone} cut consists to 97% of multihadronic events.

Monte Carlo predictions for the multihadron background in the tau pair sample vary considerably between different MC samples as shown in table 7.14. There

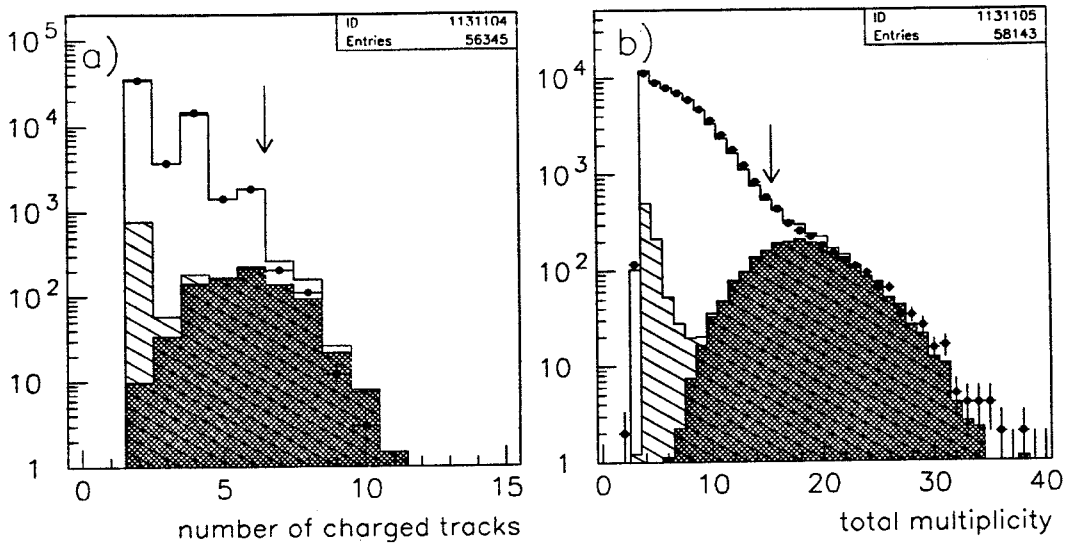

Figure 7.25: (a) The distribution of the charged track multiplicity and (b) the distribution of the total multiplicity after applying all other tau pair selection cuts for 1994 data and MC. The points are data, the open histogram the complete MC, the hatched histogram the background MC, and the shaded histogram multihadron MC only.

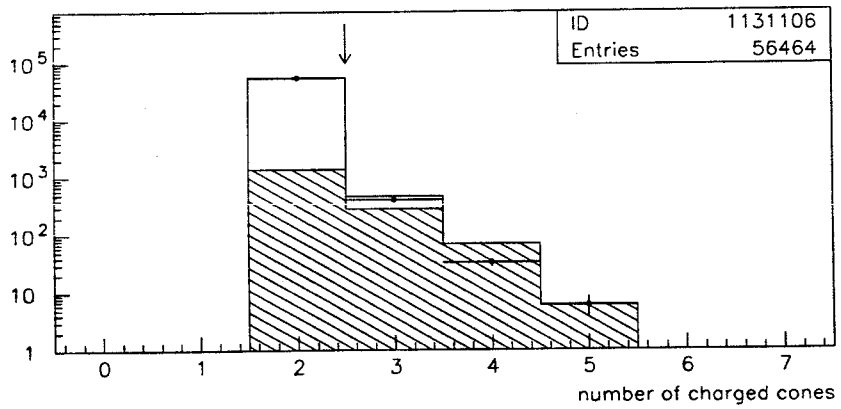

Figure 7.26: The distribution of the number of charged cones after all other tau pair selection cuts have been applied for 1994 data and MC. The points are data, the open histogram the complete MC and the hatched histogram the background MC.

year	generator	$\int \mathcal{L}dt$ $(pb)^{-1}$	predicted background
1994	Jetset	131.6	$(1.014 \pm 0.026)\%$
1993	Jetset	65.4	$(0.393 \pm 0.023)\%$
1994	Herwig	15.0	$(0.833 \pm 0.069)\%$
1992	Herwig	17.4	$(0.822 \pm 0.066)\%$

Table 7.14: Monte Carlo predictions for multihadron background in the tau pair samples for different MC samples and the luminosity corresponding to the number of produced Monte Carlo events.

is a large change in the background predicted by Jetset between the 1993 and 1994 MC samples. This is mostly due to changes in the distribution of clusters in the electromagnetic calorimeter as a result of tuning Jetset production rates and decay tables [69], [70].

It was found most effective to define a set of cuts to enhance multihadronic events which were then used for both the assessment of inefficiencies of the multihadronic rejection cuts and the multihadronic background in the tau pair sample. In order to use this background estimate for the calculation of the inefficiency of the multiplicity cuts, the cuts on the total multiplicity and on the number of charged tracks were relaxed until almost no tau pair MC events were rejected by the cuts. For these relaxed cuts, the multihadronic background was estimated and subtracted from the number of data events accepted by the relaxed cuts. The result was compared to the tau pair MC and any discrepancies were attributed to discrepancies between the data and tau pair MC. This procedure (which does not include any effects of the cut on the number of charged cones) will be described in subsection 7.6.1.

Unfortunately, it is rather difficult to define enhancement cuts for multihadronic events which do not depend heavily on the efficiencies predicted for those cuts by

multihadronic MC. Therefore it has to be shown that the corrections that will be derived for the multihadronic background account for the differences between the uncorrected Monte Carlo predictions from table 7.14.

The remainder of this section is divided into four subsections: In the first one, the cuts to enhance multihadronic events will be derived. In the second subsection, the agreement between data and tau pair MC for events that fail the multihadron rejection cuts will be investigated. In the third subsection, the multihadronic background in the tau pair sample will be estimated. For the assessment of multihadron background, cross checks will be presented in which events with three or more charged cones are investigated. This leads to the fourth subsection, where the inefficiencies due to the cut on the number of charged cones will be compared for data and tau pair MC.

7.6.1 Enhancment Cuts for Multihadronic Events

The following cuts were applied to enhance multihadronic events:

- $min(M_{inv}^{cone}) > 1.0$
- $6 < \Sigma(M_{inv}^{cone}) < 15$,

where $min(M_{inv}^{cone})$ is the minimum invariant mass of the two cones and $\Sigma(M_{inv}^{cone})$ is the sum of the invariant masses of the two cones. The invariant mass is derived for each cone from the combined information of the electromagnetic clusters and the charged tracks. The efficiency of these cuts depends very strongly on the total multiplicity. For events accepted by the tau pair selection cuts in the region $12 \leq N_{tot} \leq 15$, the efficiency varies from about 0.4 to about 0.65. As will be seen, the efficiency for values of the total multiplicity of less than 12 is too small to yield meaningful results. For events discarded by the tau pair selection cuts

in the region $16 \leq N_{tot} \leq 19$, the efficiency varies from ~ 0.7 to ~ 0.9. For this reason, the corrected number of multihadronic events was derived for each N_{tot} bin individually in the following manner: The number of tau pair MC events passing the enhancement cuts for a given multiplicity bin was subtracted from the number of data events passing the enhancement cuts. This difference was assumed to be due to multihadronic events, and the estimate for the total number of multihadronic events in a given multiplicity bin was calculated by dividing this difference by the efficiency obtained from a given multihadron Monte Carlo for that bin. Unfortunately, this estimate is quite sensitive to the correct modeling of the tau pair MC in each multiplicity bin and effects due to discrepancies of the tau pair MC with the data have to be investigated.

7.6.2 Inefficiency of Multiplicity Cuts

To estimate the number of genuine tau pair events discarded in excess of tau pair MC events, the multiplicity cuts were loosened stepwise, leading from the original requirement $N_{trk} < 7$, $N_{tot} < 16$ in four steps to requiring $N_{trk} < 11$, $N_{tot} < 20$. Since the N_{tot} and N_{trk} cuts are not independent, they were loosened at the same time. The ratio of events discarded by the multiplicity cuts with $N_{tot} < 20$ and $N_{trk} < 11$ to the total number of events discarded by the multiplicity cuts is 86.9% for 1994 tau pair MC and 86.3% for 1993 peak tau pair MC.

For each step, the multihadron enhancement cuts described above were applied and the multihadronic background was estimated for each N_{tot} bin starting with $N_{tot} = 12$ up to the highest value allowed for a given step of loosening the cuts. We are estimating the number of genuine tau pair data events which are discarded *in excess* of the number of tau pair MC events for each step of loosening the multiplicity cuts as follows: The total number of events which are accepted in

excess of the number accepted for the original cuts ($N_{trk} < 7$, $N_{tot} < 16$) are calculated for data and tau pair MC. From the difference of the two numbers, the estimated additional multihadron background introduced by loosening the cuts was subtracted. The remaining number of events is assumed to be due to tau pair data which is not properly modeled by the tau pair MC.

Figure 7.27 shows the N_{tot} distribution after requiring $min(M_{inv}^{cone}) > 1.0$ and $6 < \Sigma(M_{inv}^{cone}) < 15$, for $N_{trk} < 11$ and $N_{tot} < 20$. The distributions shown in that figure for $1 \leq N_{tot} < 16$ do *not* exactly correspond to the distributions of accepted events which pass the enhancement cuts for the original multiplicity cuts since the N_{trk} cut was loosened in the figure as well.

Figure 7.28 shows the data excess for each step of loosening the multiplicity cuts. One can observe a data excess, which is bigger for 1994 tau pair MC, but which is appreciable for both 1993 and 1994 MC. This excess seems to "level out", so that we do not expect the excess to increase when the multiplicity cuts are relaxed any further. Therefore, the excess for the cuts $N_{tot} < 20$ and $N_{trk} < 11$ was used as the estimate of the data excess, without applying any efficiency corrections.

The observation that the N_{tot} distribution in the tau pair MC does not simulate the data very well unfortunately affects the procedure to estimate this disagreement: to calculate the multihadron background for each value of N_{tot}, the tau pair MC prediction was subtracted from the data for events passing the multihadron enhancement cuts. If the number of tau pair MC events is underestimated, the number of multihadron events in the data will be overestimated by that amount. The following procedure was applied to estimate the bias due to that effect: The calculation of the multihadronic background as described in section 7.6.1 for each N_{tot} bin was modified by introducing a scaling factor f which was applied to the number of tau pair MC events passing the enhancement cuts. To estimate an

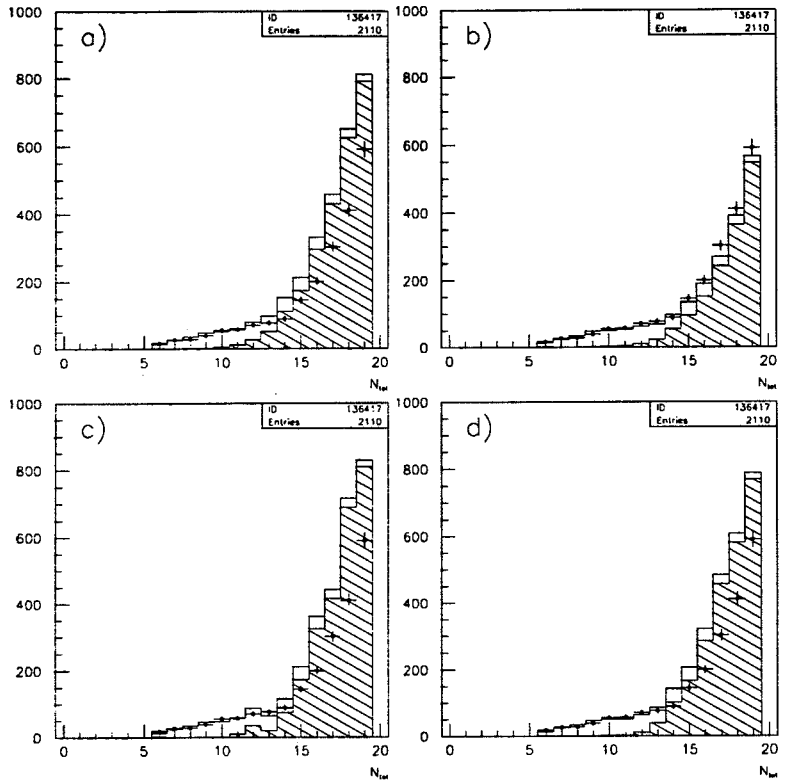

Figure 7.27: The total multiplicity (N_{tot}) distribution of events passing the multihadron enhancement cuts $min(M_{inv}^{cone}) > 1$ and $6 < \Sigma(M_{inv}^{cone}) < 15$ with multiplicity cuts loosened to $N_{tot} < 20$ and $N_{trk} < 11$. Shown are 1994 data and multihadron MC (a) 1994 Jetset, (b) 1993 Jetset, (c) 1994 Herwig and (d) 1992 Herwig, with the remaining MC from 1994. The points are data, the open histograms total MC, and the hatched histograms total background. Backgrounds other than from multihadronic events are negligible.

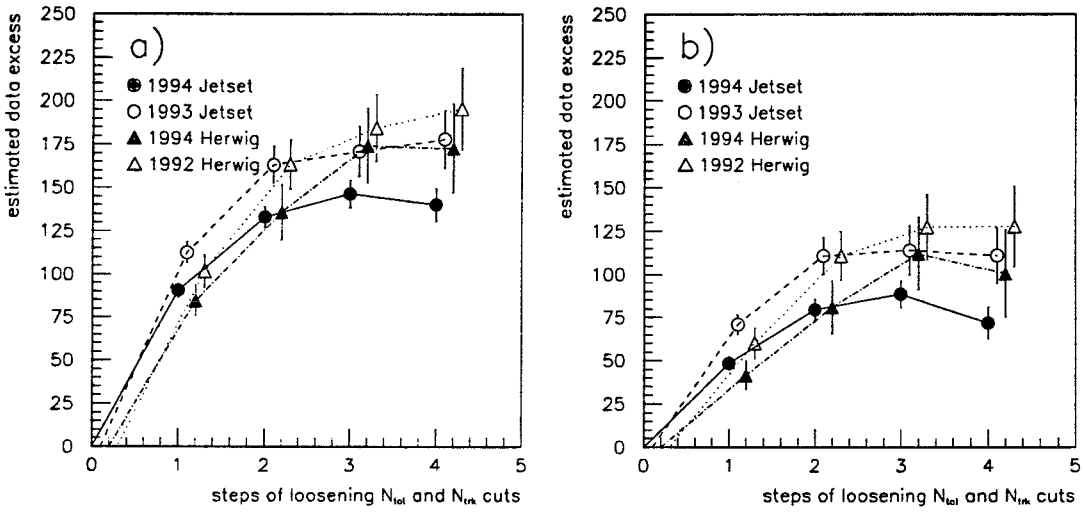

Figure 7.28: The estimated data excess when loosening the multiplicity cuts as described in the text. To allow a direct comparison of the quality of the tau pair MC, 1994 data was used in both plots. MC other than multihadronic MC is for (a) the 1994 detector and (b) the 1993 detector. For better clarity, the values corresponding to the four different multihadron MC samples for the same step of loosening the multiplicity cuts are slightly displaced from each other. The errors shown are only due to the multihadron MC efficiency, which is the part of the error which is uncorrelated amongst the data excess estimated for the four different MC samples in each plot.

appropriate value for the scaling factor f, the "relative data excess" was used in the following manner: Assuming that f is independent of the multiplicity, then for the "true" value of f the multihadronic background estimate is the "true" background estimate. If the additional multihadron background for a particular step of loosening the cuts is then subtracted from the additional number of data events, the result has no biases from the estimate of the multihadron background and is the "true" excess of genuine tau pair data events over tau pair MC events. If we divide this excess by the number of additional tau pair MC events accepted by loosening the multiplicity cuts, we obtain the "relative data excess". Assuming that the ratio of additional tau pair data events to additional tau pair MC events is the same before and after the multihadron enhancement cuts, the relative data excess is just $f-1$. From varying f and observing the change in the relative data excess, a range covering the average f for all multiplicity bins was determined. For 1994 tau pair MC, a scaling factor of $f = 1.2$ was used to calculate the data excess of events discarded by the multiplicity cuts, and half of the difference of the data excesses for $f = 1.1$ and 1.3 was assigned as systematic error. For 1993 peak tau pair MC, due to its better agreement with data, a scaling factor $f = 1.1$ was used to calculate the data excess with an error of half the difference in the excess observed for $f = 1.0$ and 1.2.

The estimate of the data excess after loosening the multihadron rejection cuts to $N_{trk} < 17, N_{tot} < 20$ for each of the four multihadron MC samples is shown in figure 7.29. The results for $f = 1.0$ and for the final scaling factor f applied for the respective tau pair MC are compared. Errors due to varying f over the ranges described above are not included in the figure. Table 7.15 summarizes the results for the tau pair MC inefficiency for the 1994 data and the three 1993 data points. The 1994 and 1993 peak data were compared to both 1994 and 1993 tau

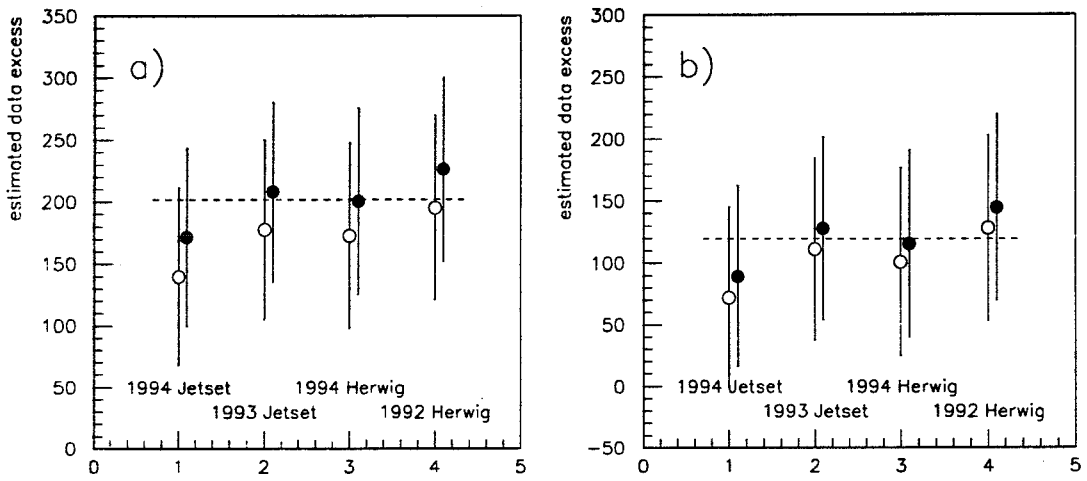

Figure 7.29: The estimate of the data excess for the four multihadron MC samples for (a) 1994 data and all other MC from 1994, and (b) for 1994 data with all other MC from 1993. The open circles show the estimated data excess using $f = 1.0$ (i.e. no correction applied to tau pair MC) and are equivalent to the results of the "forth step of loosening the multiplicity cuts" in figure 7.28. The full circles show the estimated data excess using the respective final scaling factors, $f = 1.2$ in plot (a) and $f = 1.1$ in plot (b). The errors are purely statistical. The average from the four results for the data excess with the respective scaling factors applied to the tau pair MC is shown as a dotted line. (Note the offsets between the y axes in plots (a) and (b)!)

year		tau data excess	stat	error from	correction factor
data	$\tau\tau$ MC	using respective f	error	varying f	
94	94	201.7 ± 27.3	± 73.5	± 15.1	1.0036 ± 0.0014
94	93	119.3 ± 27.8	± 74.5	± 16.4	—
93	94	62.7 ± 6.7	± 35.9	± 4.3	—
93	93	39.5 ± 6.9	± 36.1	± 4.6	1.0025 ± 0.0024
93p−2	93p−2	-14.5	± 18.3	± 4.9	0.9958 ± 0.0055
93p+2	93p+2	15.1	± 21.5	± 1.8	1.0032 ± 0.0045

Table 7.15: Estimate of the excess of tau pair data events failing the multihadron rejection cuts. The estimated tau pair data excess for the peak points is the average from the results for the four multihadron MC samples, where the error is half the difference of the maximum and minimum estimate. To derive these results, the appropriate value for f as described in the text was used. Furthermore, the statistical error and the error of varying f over a reasonable range are shown. For the peak points, these errors are the averages from the four multihadron MC samples. For the off-peak points, only the corresponding 1993 Jetset MC was used.

pair MC. As expected, the size of the scaling factor f depends on the tau pair MC used, with only a small dependence on the data which was used. The final scaling factors f, and the range over which they were varied for the error estimate, therefore are the same for a given tau pair MC, independent of the data sample used.

For the off-peak points, only 1993 Jetset MC was available. However, as can be seen in figure 7.29, the prediction for the 1993 peak Jetset MC is very close to the final data excess estimate for the peak points, and the error resulting from using different multihadron MC samples is small compared to the statistical error. Given that the statistical error is bigger for the off-peak points, the inefficiency of the multihadron cuts was estimated from the 1993 Jetset MC only. Otherwise, the same methods were used for the estimate as for the peak points. Figure 7.30 shows the change of the excess of data over tau pair MC when loosening the multiplicity

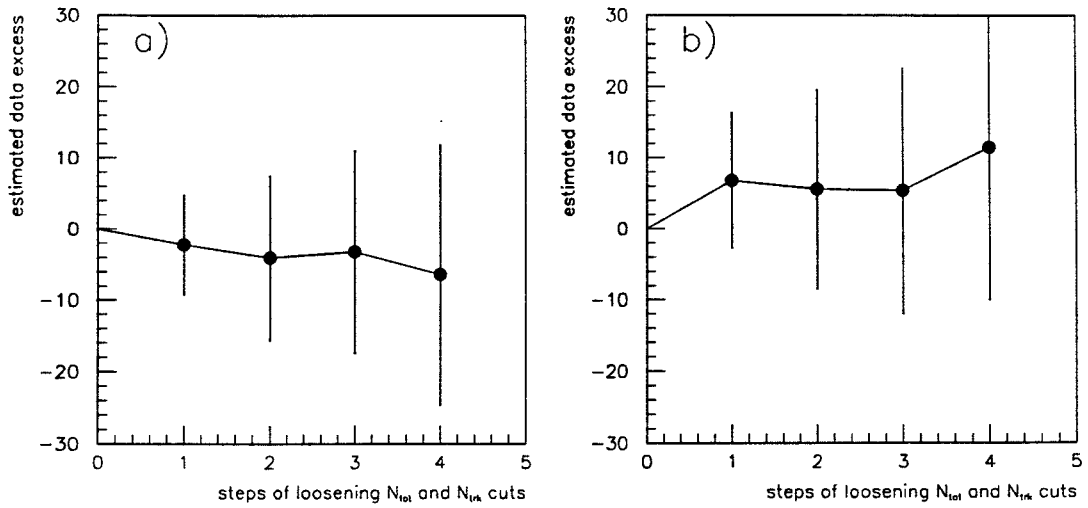

Figure 7.30: Estimate of the inefficiency of the multihadron rejection cuts for the 1993 off-peak points corresponding to figure 7.28 for the peak points. Plot (a) shows the estimated data excess over MC when loosening the multiplicity cuts for 1993p−2, plot (b) for 1993p+2. The errors shown here are the complete statistical errors.

cuts for the off-peak points. The tau pair MC scaling factors were $f = 0.75$ for 1993 peak−2 and $f = 1.2$ for 1993 peak+2, the corresponding ranges over which f was varied to estimate the systematic errors of the corrections were $f = 0.9$ to 0.6 and $f = 1.1$ to 1.3. The results are shown in table 7.15.

For the final estimate of the inefficiency of the multihadron rejection cuts, the three errors (two errors in the case of the off-peak points) shown in table 7.15 were added in quadrature. The resulting correction factors are shown in the last column of the table.

7.6.3 Multihadronic Background

The total multiplicity distribution from different multihadron Monte Carlo samples for events which leak into the tau pair acceptance is shown in figure 7.31a. Figure 7.31b show the efficiency of the enhancement cuts described in section 7.6.1

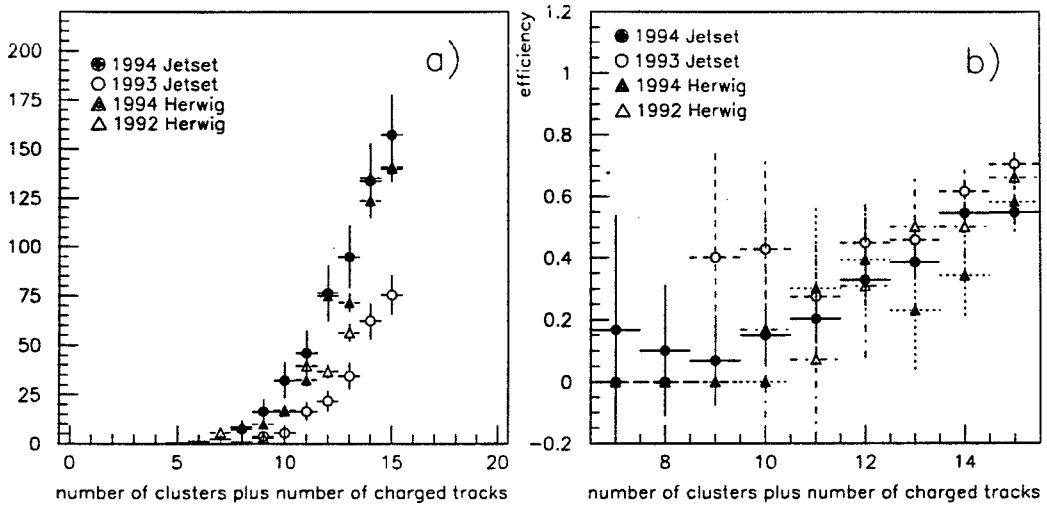

Figure 7.31: (a) Multihadron background accepted by the tau pair selection cuts as a function of the total multiplicity N_{tot}. The predictions of the four MC samples from table 7.14 are shown. (b) The efficiency of the multihadron enhancement cuts $min(M_{inv}^{cone}) > 1$ and $6 < \Sigma(M_{inv}^{cone}) < 15$ as described in the text for the four different multihadron MC samples as a function of the total multiplicity N_{tot}.

for multihadron MC as a function of the total multiplicity. Figure 7.32 compares the total multiplicity distributions for data and MC after applying the enhancement cuts. Clearly, the data MC agreement depends strongly on the multiplicity. The straightforward procedure of applying the efficiency corrections from figure 7.31b on a bin-by-bin basis to the corresponding data MC difference in figure 7.32 can only be applied to the region with large total multiplicities due to the low efficiency of the cuts for multihadron MC at low multiplicities. It therefore was required that the size of the multihadronic background passing the enhancement cuts should have at least about the same size as the statistical error of the data for a given bin of the N_{tot} distribution, and a bin-by-bin correction was only applied for the region $12 \leq N_{tot} \leq 15$. For the remaining region $N_{tot} \leq 11$, the average of the 1993 and 1994 Jetset predictions was used as the background estimate and half the difference between the two predictions was assigned as error. The uncor-

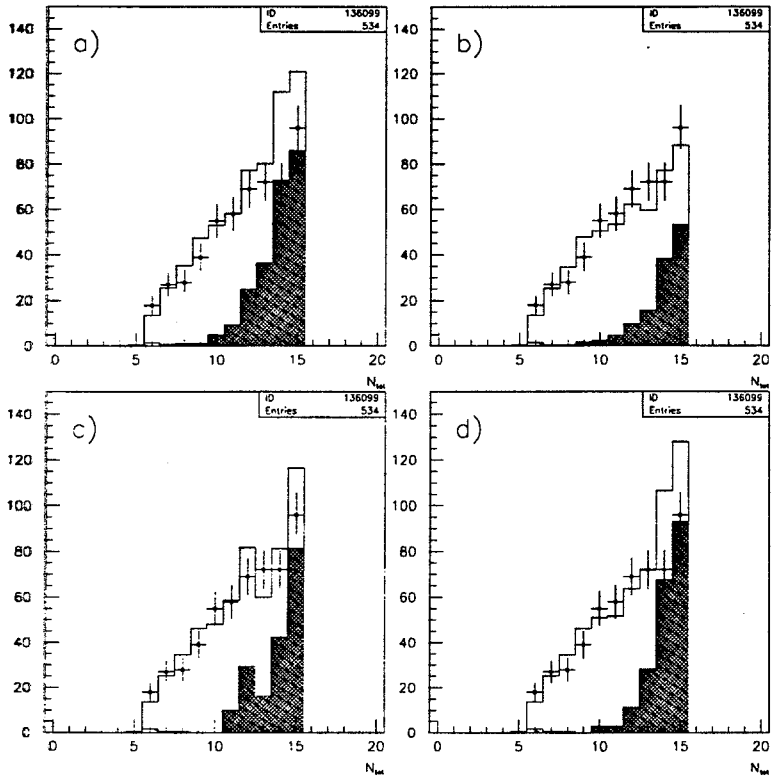

Figure 7.32: The distribution of the total multiplicity N_{tot} for events passing the multihadron enhancement cuts $min(M_{inv}^{cone}) > 1$ and $6 < \Sigma(M_{inv}^{cone}) < 15$ for 1994 data compared to the four different multihadron MC samples: (a) 1994 Jetset, (b) 1993 Jetset, (c) 1994 Herwig and (d) 1992 Herwig. The remaining MC is for the 1994 detector simulation. The points are data, the open histograms total MC, the hatched histograms total background and the shaded histograms multihadron MC only. Small backgrounds other than from multihadronic events can only be observed for small values of N_{tot}.

Monte Carlo	$N_{tot} \leq 11$	$12 \leq N_{tot} \leq 15$
94 Jetset	105.9±6.3	461.9±13.1
93 Jetset	26.2±4.4	193.7±12.0
94 Herwig	58.6±13.8	410.0±52.4
92 Herwig	73.2±14.4	368.8±32.2
average	66.1±3.8 ± 39.9	327.8±8.9 ± 134.1

Table 7.16: The predicted multihadronic background for the different multihadron MC samples, scaled to the luminosity of the 1994 data sample, for low and high total multiplicities. The average shown in the last row is the average of the results for the 1993 and 1994 Jetset multihadron samples, where the first error is purely statistical and the second is half the difference between the two predictions. The MC background estimate in the region $N_{tot} \leq 11$ from this table will be used as multihadron background estimate, while for the region $12 \leq N_{tot} \leq 15$ corrections will be derived. The high multiplicity region is only listed here for completeness.

rected multihadron MC background predictions in the low and high multiplicity regions are shown in table 7.16. The predictions of the Herwig MC fall somewhere inbetween the two Jetset estimates.

Given a difference between the number of data and MC events of $\sim$ 10% for 1993 and $\sim$ 20% for 1994 observed in the previous subsection for events failing the tau pair selection cuts, it is a reasonable assumption that similar differences exist for the multiplicity distribution inside the tau pair acceptance. Due to the larger fraction of tau pair events after the multihadron enhancement cuts *inside* the tau pair acceptance (shown in figure 7.32) one would expect a larger effect than *outside* of the tau pair acceptance (shown in figure 7.27).

The procedure used here to determine the multihadronic background inside the tau pair acceptance differs from the one used in the previous subsection only in the following points: First, a scaling factor f will be calculated for each value of N_{tot} in the range $12 \leq N_{tot} \leq 15$ passing the multihadron enhancement cuts individually and will be denoted as f^m, where the superscript m indicates the

multiplicity. The cut on N_{trk} remains unchanged. Second, rather than "scanning a region of f by hand", the ratio of the data excess and tau pair MC will be formed for each N_{tot} value individually. By taking this ratio as $f^m - 1$, a new value for f^m will be derived and fed back into the next iteration of the calculation of the data excess. Here the same relation between the relative data excess for a given multiplicity bin m and the quantity f^m holds as described in the previous subsection for the average scaling factor f when loosening the multiplicity cuts. Performing this iterative process it was observed that the change of the background estimate was large after the first step, while for subsequent iterations changes in the background estimate are rather small compared to the statistical error of the background estimate.

Figure 7.33 shows the scaling factor f^m minus 1 after the zero-th iteration, i.e. the result for the ratio of data excess and tau pair MC events for each multiplicity bin in the range $12 \leq N_{tot} \leq 15$ when $f^m = 1.0$ was implemented. The data MC agreement improves with smaller values of the total multiplicity as one would expect, since we are moving away from the tails of the distribution, for which we expect the worst agreement between data and MC. For a given data sample, the data excess for each value of the total multiplicity should in theory only be determined by the tau pair MC, and should within its statistical errors not depend on the multihadron Monte Carlo sample that was used. This appears to be the case in figure 7.33, where the agreement between different multihadron MC samples gets better for smaller values of N_{tot} since less multihadron MC is present in those bins. However, the results for 1994 Herwig Monte Carlo are not in very good agreement with the other three Monte Carlo samples for $N_{tot} = 13$ and 14, which is precisely where we observe the low efficiencies of the multihadron enhancement cuts in figure 7.31b. These low efficiencies result in a much bigger error for the relative

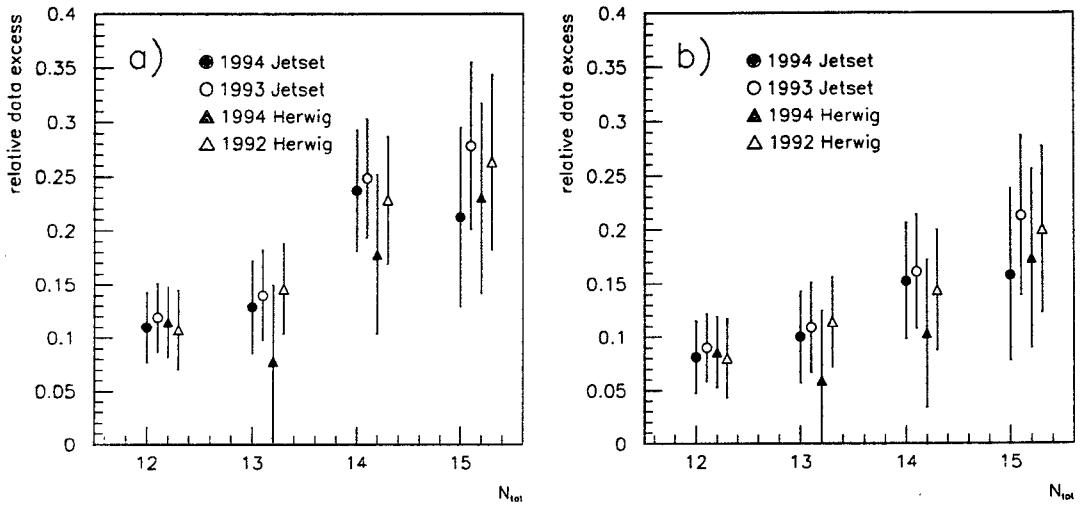

Figure 7.33: The excess of data minus the estimated multihadron background over tau pair MC, divided by the number of tau pair MC events for values of the total multiplicity from 12 to 15. To allow a direct comparison of the tau pair MC, the 1994 data was used in both plots, where for plot (a) all MC other than multihadron MC is from 1994, in plot (b) from 1993. In each case, the results using the four different multihadron MC samples are shown. Ideally, the relative data excess should be independent of the multihadron MC that was used.

data excess for 1994 Herwig Monte Carlo in figure 7.33. For this reason, and due to the low statistics of the Herwig MC, the correction factors will be derived only from the Jetset MC. Furthermore, Herwig generally seems to simulate particle production rates worse than Jetset [69].

Systematic errors on f^m are expected from two sources: First, from differences between the true multihadronic background in the data and the multihadronic background predicted for each multiplicity bin from the data MC difference after scaling the tau pair MC. This effect should be covered by using the four different multihadron MC samples for the background estimate with their full statistical errors. Second, we are *deriving* the scaling factor f^m from comparing data to MC without applying any enhancement cuts, while we are *applying* it to the tau pair MC which passes the multihadron enhancement cuts. The scaling factor f^m therefore is sensitive to potential differences in the efficiencies of the enhancement cuts for data and MC. The effect of the multihadron enhancement cuts on the data MC agreement was estimated by comparing the data MC agreement in a N_{tot} region with minimal background before and after the multihadron enhancement cuts. A good region for this estimate is $7 \leq N_{tot} \leq 9$ as demonstrated in figure 7.34. For those three bins of the total multiplicity, the maximum background in a bin is about 35% of the statistical error of the data before the multihadron enhancement cuts, and about 20% after the enhancement cuts. We therefore can directly calculate the scaling factor f^m before and after applying the multihadron enhancement cuts by dividing the corresponding number of data and tau pair MC events for these bins, without being sensitive to the multihadron MC background predictions. The two ratios were found to agree well for all three values of N_{tot} within their statistical uncertainties.

Applying the procedure lined out so far, we will now calculate the multi-

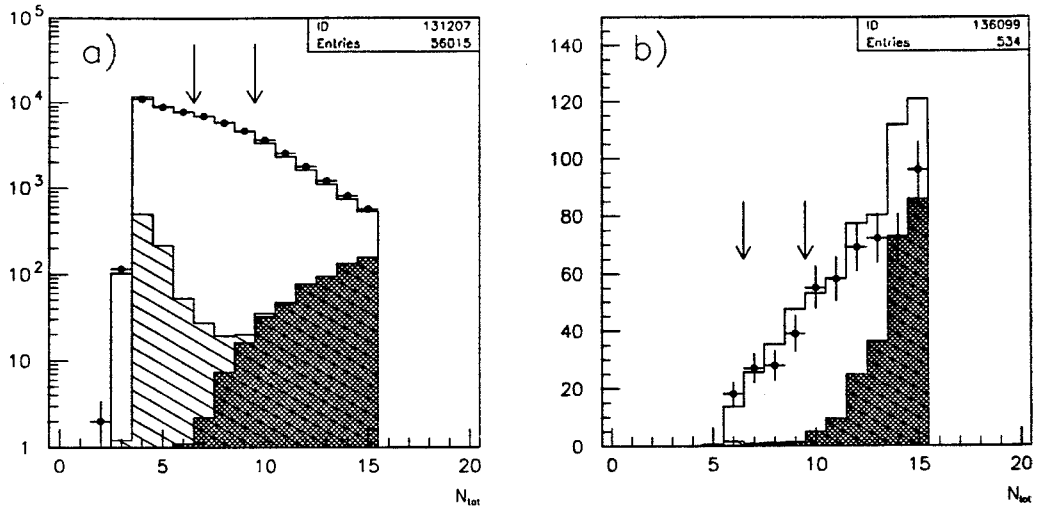

Figure 7.34: The distribution of the total multiplicity for 1994 data and MC (the multihadron MC is 1994 Jetset) (a) for all events selected by the tau pair selection cuts and (b) after the multihadron enhancement cuts. The arrows indicate a region with small background in each plot. This region was used to check if the data MC ratios before and after the multihadron enhancement cuts show good agreement.

hadronic background estimate in the high multiplicity region in an iterative process as follows: We start without applying any corrections by implementing $f_0^m = 1.0$ for all multiplicity bins. The resulting relative data excess is equal to $f^m - 1$, where f^m now is the scaling factor for the next iteration which is used to calculate the final estimate of the multihadron background. We are using the full statistical errors on f^m resulting from the data and tau pair MC statistics of events which pass the tau pair pair selection per multiplicity bin. The results of this procedure are shown in table 7.17. The results without applying the scaling factors to the number of tau pair MC events are also shown for comparison. The disagreement between the background estimates when using different tau pair MC with the same data has decreased by about 40%. Also, the background estimate itself has decreased significantly. With the exception of 1994 Herwig MC, the background estimates for different multihadron Monte Carlo show decent agreement

among each other. Problems with the 1994 Herwig MC prediction due to low statistics and low efficiencies for $N_{tot} = 13$ and 14 were discussed above. As the final background estimate, we are taking the average of the highest and lowest Jetset background estimate for a given data sample compared to either 1993 or 1994 tau pair MC. In practice this means that we are using the average of the estimates for 1994 tau pair MC with 1994 Jetset and 1993 tau pair MC with 1993 Jetset. As the statistical error, we take the average of the two statistical errors and as an additional error we assign half the difference of the two estimates. The background estimate was also performed with slightly modified multihadron enhancement cuts, where the cut on $min(M_{inv}^{cone})$ was tightened from 1.0 to 1.5. Differences between these two cuts were quite small compared to the statistical error of each estimate.

As an alternative method of estimating the agreement of multihadron MC and data, the N_{tot} distribution for events which *fail* the tau pair selection cuts because they have more than two charged cones was investigated before applying the N_{tot} or N_{trk} cut. The N_{tot} distributions for these events are shown in figure 7.35 for different multihadron MC samples. Events fulfilling those conditions are almost exclusively multihadron events, giving us an opportunity to directly compare the data MC agreement for multihadron in the N_{tot} region of interest, albeit for multihadrons that fail the tau pair selection cuts. Clearly, all multihadron MC runs except the 1993 Jetset in figure 7.35c greatly overestimate the number of events in the region $13 \leq N_{tot} \leq 15$. We will use the distributions in figure 7.35 to estimate the multihadron background as follows: For each multihadron MC sample, we will subtract the tau pair MC from the data and divide the difference by the Monte Carlo prediction for the multihadronic events on a bin-by-bin basis. This ratio will be used on a bin-by-bin basis to correct the number of multihadron MC

year		Multihadron	without	with tau MC
data	$\tau\tau$ MC	Monte Carlo	tau MC scaling	scaling by f^m
94	94	1994 Jetset	296.7±43.8	233.9±44.6
		1993 Jetset	239.5±36.9	182.5±36.7
		1994 Herwig	368.3±78.2	303.7±73.7
		1992 Herwig	269.0±50.9	206.1±46.6
		bkgr. est.	268.1±40.3 ± 28.6	208.2±40.7 ± 25.7
94	93	1994 Jetset	262.9±45.1	213.2±46.4
		1993 Jetset	211.9±37.5	166.0±37.9
		1994 Herwig	323.8±74.1	274.3±70.6
		1992 Herwig	239.2±49.6	189.5±47.9
		bkgr. est.	237.4±41.3 ± 25.5	189.6±42.15± 23.6
94	ave	bkgr. est.		200.0±41.3 ± 34.0
93	94	1994 Jetset	78.7±21.8	65.0±22.2
		1993 Jetset	63.4±17.6	50.6±17.8
		1994 Herwig	93.8±29.5	80.0±29.3
		1992 Herwig	72.3±22.0	59.2±21.9
		bkgr. est.	71.1±19.7 ± 7.7	57.8±20.0 ± 7.2
93	93	1994 Jetset	69.2±22.1	59.1±22.6
		1993 Jetset	55.6±17.7	45.9±18.0
		1994 Herwig	81.3±29.1	71.6±29.3
		1992 Herwig	63.9±22.0	54.4±22.2
		bkgr. est.	62.4±19.9 ± 6.8	52.5±20.3 ± 6.6
93	ave	bkgr. est.		55.5±20.1 ± 9.6

Table 7.17: The multihadronic background estimate for the 1994 and 1993 peak points. The results without applying any scaling to the tau pair MC are shown for comparison. The background estimate for each combination of data and tau pair MC was obtained by taking the average of the 1993 and 94 Jetset predictions. The first error is the average of the statistical errors, the second error is half the difference between the two estimates. The final background estimate for each data sample was derived in the same manner by averaging the highest and lowest Jetset estimate from the results of comparing each data set to both 1994 and 1993 tau pair MC.

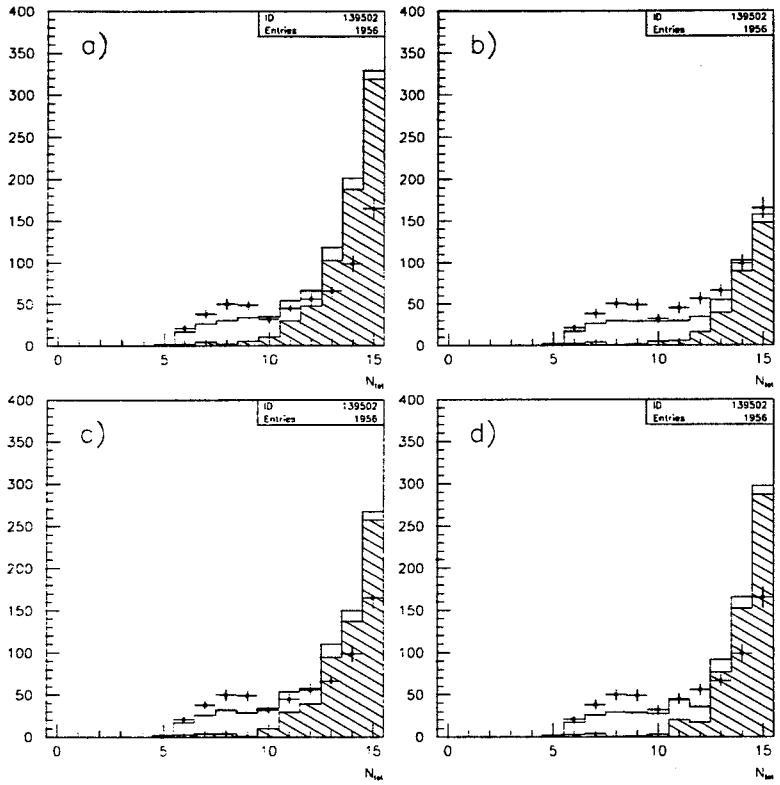

Figure 7.35: The N_{tot} distribution of events with $N_{cone} > 2$ which pass all other tau pair selection cuts before applying the N_{tot} or N_{trk} cut. Shown are 1994 data and multihadron MC (a) 1994 Jetset, (b) 1993 Jetset, (c) 1994 Herwig and (d) 1992 Herwig, with the remaining MC from 1994. The points are data, the open histograms total MC, and the hatched histograms total background. Backgrounds other than multihadronic events are negligible for $N_{tot} > 10$.

multipl. region	1994	1993 peak
$N_{tot} < 12$	66.1± 3.8 ± 39.9	18.6± 2.2 ± 11.2
$12 \leq N_{tot} \leq 15$	200.0±41.3 ± 34.0	55.5±20.1 ± 9.6
total	266.1±41.5 ± 73.9	74.1±20.2 ± 20.8

Table 7.18: Estimate of the multihadron background for 1994 and 1993 peak for the low and high total multiplicity regions combined. The first error in each column is statistical, the second one is the contribution from half the difference between the maximum and the minimum estimate. For each year, the statistical error was added in quadrature, while the second error was added linearly.

events leaking into the tau pair acceptance for multihadron MC which are shown in figure 7.31a. This method is not expected to work for small multiplicities since the portion of tau pair MC in a bin is getting larger with smaller multiplicities, affecting the calculation of the correction factor if the tau pair MC is badly simulated. Just as for the method using enhancement cuts described above, we will only calculate a correction factor in the region $12 \leq N_{tot} \leq 15$. The average of the predictions using 1993 Jetset and 1994 Jetset is about 235 events for the 1994 data and about 70 events for the 1993 data. These results are in decent agreement with the results from table 7.17.

In figure 7.35 one could observe a data MC disagreement in the region $N_{tot} \leq 10$ which presumably is due to a disagreement of tau pair data and tau pair MC events that are discarded by the cut on the number of charged cones. In the next subsection, the distribution from figure 7.35 will be used almost directly to estimate the inefficiency of the cut on the number of charged cones for tau pair data and tau pair MC.

Finally, in table 7.18 the background estimates for the low multiplicity region from table 7.16 have been added to the background estimates for the high multiplicity region in table 7.17. The error estimates which were obtained from

Monte Carlo	1993 p−2	1993 p+2
93 Jetset (p−2)	13.3±2.2	—
93 Jetset (p+2)	—	17.9±3.0
93 Jetset (peak)	13.3±0.8	18.9±1.1
94 Jetset	34.3±0.9	48.9±1.3
94 Herwig	28.2±2.4	40.2±3.4
92 Herwig	26.7±2.1	37.9±3.0
average	23.8±1.2	33.9±1.7
Estimated bkgr	13.3±2.2 ± 10.5	17.9±3.0 ± 16.0

Table 7.19: Peak multihadron background estimates from Monte Carlo scaled to the off-peak points. The average shown in the last but one row is the average of the 1993 and 1994 Jetset predictions. As the final result, the 1993 Jetset prediction for each off-peak point was used. The first error of the estimated background is statistical, the second is the difference between the estimated background and the average value from the previous row.

taking half the difference of the maximum and minimum background predicted by different multihadron MC samples were added linearly for the low and high multiplicity: The errors for the uncorrected background predictions from multihadron MC were originally correlated in table 7.16 and it is conceivable that despite the variety of procedures performed to obtain the multihadronic background estimates for the high multiplicity region in table 7.17, part of the correlation is still present.

In table 7.19 the multihadron MC for the peak energy point was scaled to the off-peak points, taking into account the different luminosities and cross sections. As one would expect, the predictions of the 1993 Jetset MC agree well for the off-peak points and for the scaled MC from the peak point. As the multihadronic background estimate for the off-peak points, we directly use the Jetset MC predictions for the respective energy point. We know from the peak data that the average of the predictions from 1994 and 1993 peak Jetset MC is well above the

data sample	MH background	correction factor
94	266.1 ± 84.8	0.9952 ± 0.0015
93 peak	74.1 ± 29.0	0.9953 ± 0.0018
93 p−2	13.3 ± 10.7	0.9961 ± 0.0031
93 p+2	17.9 ± 16.3	0.9963 ± 0.0034

Table 7.20: The final estimate of the multihadron background from table 7.18 for the peak points and table 7.19 for the off-peak points.

actual multihadronic background (compare tables 7.18 and 7.16). We therefore assign the difference between that average and the 1993 Jetset prediction for each off-peak point as an additional error. Due to the lower statistics for the off-peak points, the size of this error is acceptable. The results are shown in the last row of table 7.19. The final results for the background estimate from multihadronic events for all data samples are shown in table 7.20.

7.6.4 Inefficiency of the Charged Cone Cut

The inefficiency of the cut on the number of charged cones was compared for data and tau pair MC by investigating the distribution of the total multiplicity in the region $N_{tot} \leq 15$ for events with more than two charged cones after applying all other tau pair selection cuts. These distributions correspond almost exactly to those shown in figure 7.35, with small differences resulting from applying the cut $N_{trk} < 7$ on the multiplicity of charged tracks. Due to the large contribution from multihadronic events for high total multiplicities, the data excess was estimated in the regions $N_{tot} \leq 11$ and $12 \leq N_{tot} \leq 15$ separately. In the low multiplicity region, the difference between data and MC was calculated as $58.8 \pm 15.4 \pm 16.6$ for 1994 data and MC, $21.3 \pm 8.4 \pm 4.7$ for 1993 peak data and MC, $2.6 \pm 3.5 \pm 1.0$ for 1993 p−2 data and MC, and $11.1 \pm 6.2 \pm 2.7$ for 1994 p+2 data and MC.

Here the first error is purely statistical, while the second one is half the difference of the predicted number of events using 1993 and 1994 Jetset MC. The number of multihadronic MC events used to calculate the data excess was the average of those two MC predictions. For the off-peak points, the peak Jetset MC predictions were scaled according to luminosity and cross section. In the previous subsections it was found that the data MC agreement depends on the total multiplicity such that it does not seem advisable to extrapolate the disagreement in the region with low total multiplicity into the region with high total multiplicity. For events in the region $12 \leq N_{tot} \leq 15$ that pass the tau pair selection cuts, it could be observed in figure 7.33 that the excess of genuine tau pair events in the data over tau pair MC events is in the range of $10\% \sim 25\%$. Assuming that a similar disagreement applies for events that fail the tau pair selection cuts with more than two charged cones, the excess of tau pair data over tau pair MC in the region $12 \leq N_{tot} \leq 15$ was estimated as 0.25 ± 0.25 times the number of tau pair MC events in that region. The resulting estimates for the data excess, scaled to the respective data luminosity, are 12.2 ± 12.2 from 1994 tau pair MC, 4.1 ± 4.1 from 1993 peak tau pair MC, 0.8 ± 0.8 from 1993 p$-$2 tau pair MC, and 1.5 ± 1.5 from 1994 p+2 tau pair MC. These errors, and the errors obtained for the low multiplicity region, were added in quadrature. The resulting corrections and errors are shown in table 7.21.

7.7 Two Photon Events

Two photon events constitute the most dominant non-resonant background to the Z^0 lineshape. The dominant two photon backgrounds are from $e^+e^-e^+e^-$ and $e^+e^-\mu^+\mu^-$ final states, and, to a smaller degree, from the final state $e^+e^-\tau^+\tau^-$.

year	data excess	correction factor
94	71.0 ± 25.7	1.0013 ± 0.0005
93 peak	25.4 ± 10.5	1.0016 ± 0.0007
93 p−2	3.4 ± 3.7	1.0010 ± 0.0011
93 p+2	12.6 ± 6.9	1.0026 ± 0.0014

Table 7.21: The excess of genuine tau pair data events over tau pair MC events rejected by the cut on the number of cones and the resulting correction factors.

Two photon events, having a cross section which is strongly peaked in forward direction, have a small transverse momentum component and a missing momentum vector which due to leakage along the beam pipe points into the forward direction. All two photon events in general have a low visible energy (see section 7.2), where the distribution of $e^+e^-e^+e^-$ events is characterized by $R_{trk} \approx R_{shw}$, while the distribution of $e^+e^-\mu^+\mu^-$ final states has a constant, low R_{shw}, but varying R_{trk}. Figure 7.36 shows the R_{vis} distribution before the two photon rejection cut at $R_{vis} = 0.18$.

7.7.1 Inefficiency of the Two Photon Cuts

To investigate potential discrepancies between the number of tau pair events discarded in data and MC by the two photon rejection cut, events in the regions $0.06 < R_{vis} < 0.18$, $0.10 < R_{vis} < 0.18$, $0.125 < R_{vis} < 0.18$, and $0.15 < R_{vis} < 0.18$ have been selected. For each region, the number of data and MC events with a ratio of the transverse momentum to the beam energy of $R_{p_t} > 0.04$ were compared. In this region, mainly tau pair events are expected. Figure 7.37 shows the R_{p_t} distribution for the regions $0.06 < R_{vis} < 0.18$ and $0.15 < R_{vis} < 0.18$ for 1994 data and MC. Clearly, in the first region (figure 7.37a), a large amount of two photon background can be observed at low values of R_{p_t}.

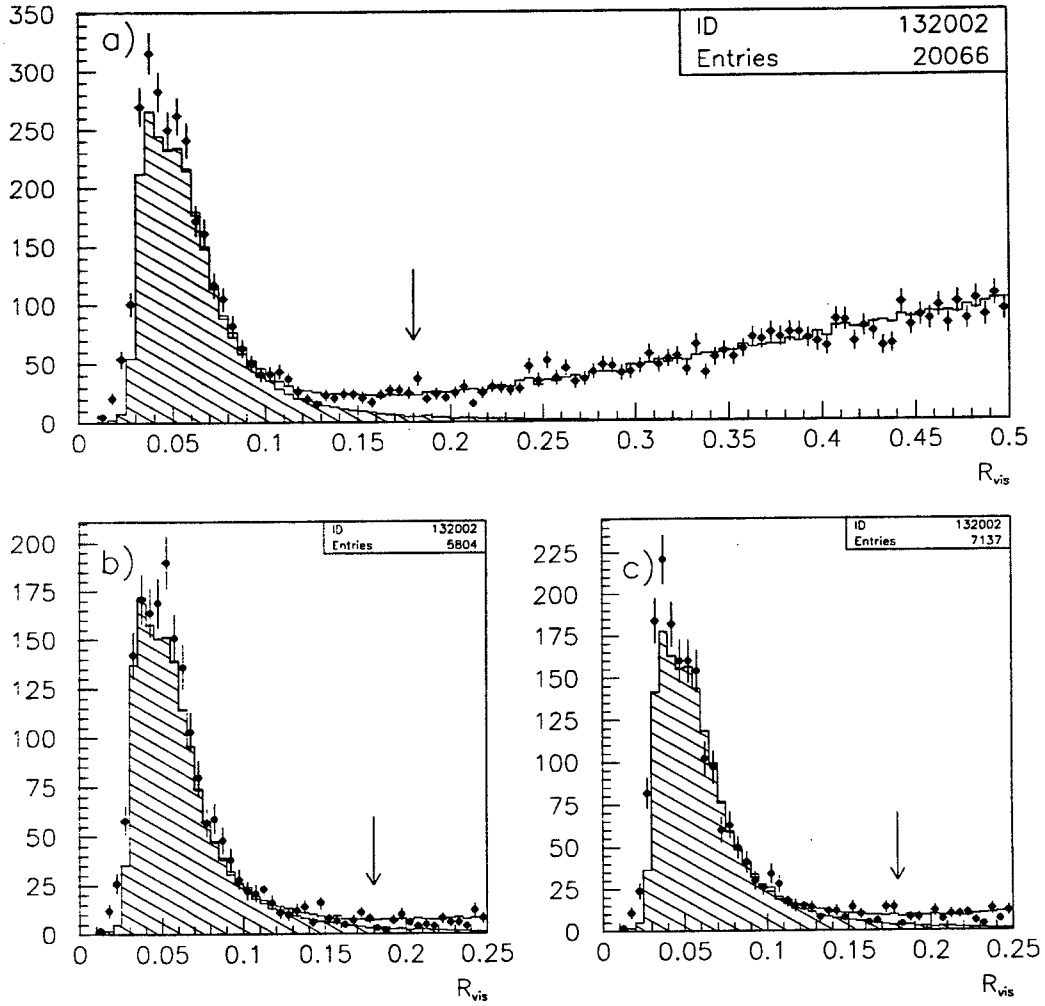

Figure 7.36: The R_{vis} distribution after all other cuts tau pair selection cuts for 1993 at (a) peak, (b) peak−2, and (c) peak+2. The points are data, the open histograms total MC and the hatched histograms the background. The background peak at low visible energy is from two photon events and is rejected by a cut at $R_{vis} = 0.18$. Two photon reactions are non-resonant, and when comparing figure (a) to (b) and (c) one can clearly see that for the off-peak points the two photon background constitutes a higher background fraction near the cut at $R_{vis} = 0.18$.

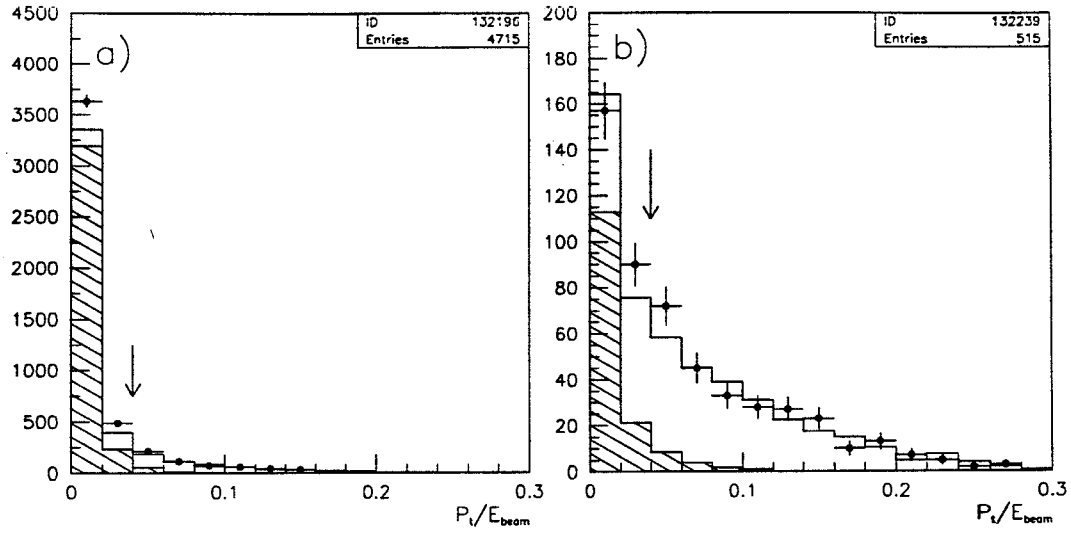

Figure 7.37: The distribution of P_t/E_{beam} in the regions (a) $0.06 < R_{vis} < 0.18$ and (b) $0.15 < R_{vis} < 0.18$ for 1994 data and MC. The points are data, the open histograms the total MC and the hatched histograms background MC only. The background is almost exclusively from two photon MC.

The data MC disagreement in that region is obviously due to two photon events. For figure 7.37b, the two photon background is strongly suppressed and one can observe that the data MC agreement in the low R_{p_t} region has much improved. In figure 7.38, the data MC difference in the region $R_{p_t} > 0.04$ for the four different cuts on R_{vis}, divided by the efficiency of the R_{p_t} cut for tau pair MC, is shown for each data sample as full circles. The solid line in each of the 4 plots is *not* a fit, but is simply the value for the region $0.15 < R_{vis} < 0.18$. Since all events from that region are also contained in the three other R_{vis} regions, the total errors of the four data MC differences for each data set are correlated. The error bars for the remaining three regions of each plot in figure 7.38 were obtained only from the events with $R_{vis} < 0.15$, so that the χ^2 of those three errors with respect to the data MC difference in the region $0.15 < R_{vis} < 0.18$ indicates whether the data MC difference shows any serious dependence on the choice of the R_{vis} region. For

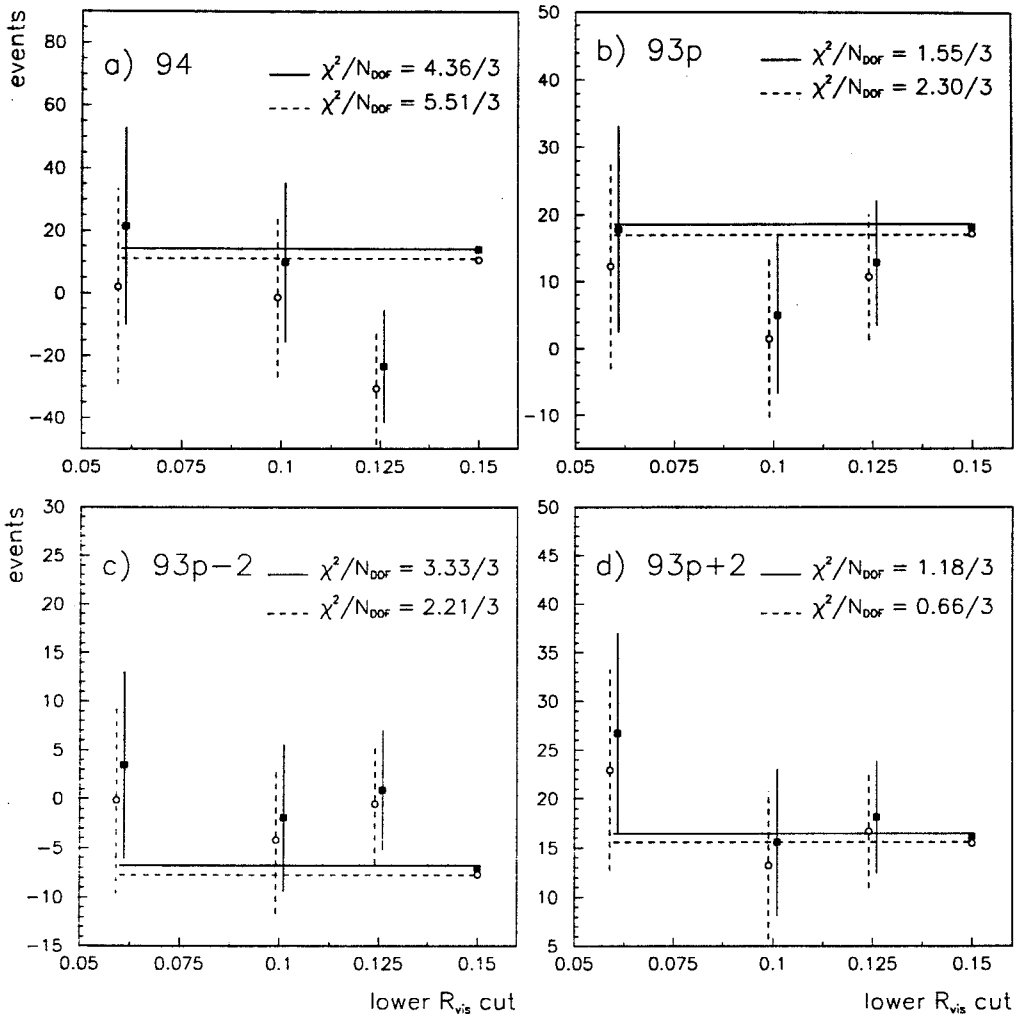

Figure 7.38: Excess of data over MC in the four different R_{vis} regions described in the text for (a) 1994, (b) 1993 peak, (c) 1993 p−2, and (d) 1993 p+2. The full circles and solid line correspond to the results obtained without scaling the two photon MC, where all error bars are with respect to the data excess in the region $0.15 < R_{vis} < 0.18$. The open circles and broken line indicate the data excess after scaling the two photon MC. The line indicates the respective result for the region $0.15 < R_{vis} < 0.18$, and the χ^2's are those of the remaining three measurements with respect to that result.

all the data samples, the resulting χ^2 is reasonably close to 1. The sum of the χ^2's from all four data samples is $10.41/12 \simeq 0.87$.

In figure 7.36 it could be observed that the two photon MC does not model the data very well at its peak at about $R_{vis} \approx 0.05$. The following procedure was applied to account for potential biases of the data MC difference due to bad simulation of the two photon MC: First the data MC ratio in the region $R_{vis} < 0.1$ was calculated, which is clearly dominated by two photon events. These ratios are 1.144 for 1994 data and MC, 1.153, 1.136, 1.107 for 1993 data and MC at the peak, at p−2 and at p+2, respectively. As an approximation for all four data samples, the two photon MC in the region $R_{p_t} > 0.04$ was scaled by 1.15 and the data MC difference for the four R_{vis} regions was recalculated. The results of this procedure are shown in figure 7.38 as open circles, where the error bars are again excluding events in the region $0.15 < R_{vis} < 0.18$, and the broken line indicates the data MC difference in that region. The χ^2 has improved with respect to the fit to the results without scaling two photon MC for the off-peak points while it got worse for the peak points. The sum of the χ^2's for the four data sets however has remained almost constant and is $10.67/12 \simeq 0.89$.

We conclude that the estimate of the data MC agreement outside the R_{vis} cut is well estimated by the agreement observed in the region $0.15 < R_{vis} < 0.18$. For the final result, the correction factors derived from that region *without* applying the scaling for two photon MC were used. To account for any effects of a bad modelling of the two photon MC, the difference of the data excess observed with and without scaling the two photon MC in the region $0.15 < R_{vis} < 0.18$ was added linearly to the statistical error.

The data MC difference for events with $R_{p_t} > 0.04$ in the four R_{vis} regions was divided by the efficiency of the R_{p_t} cut as calculated from $\tau^+\tau^-$ MC. These

	estimated data excess	add'l error from scaling 2γ MC	correction factor
94	14.08 ± 24.88	± 3.30	1.0004 ± 0.0005
93 peak	18.07 ± 13.54	± 1.01	1.0012 ± 0.0009
93 p$-$2	-7.05 ± 5.15	± 0.64	0.9979 ± 0.0017
93 p+2	16.16 ± 8.65	± 0.67	1.0034 ± 0.0020

Table 7.22: The final correction factors and errors to account for differences in the data and MC efficiencies of the two photon rejection cut.

efficiencies are between 0.6 and 0.7 depending on the R_{vis} cuts that were applied and it was checked that the R_{p_t} distribution is modelled reliably by the $\tau^+\tau^-$ MC by investigating the R_{p_t} distribution for events that pass the tau pair selection cuts in the regions $0.18 < R_{vis} < 0.25$ and $0.25 < R_{vis} < 0.30$. For none of the four data sets did these checks indicate any discrepancies between data and MC which would necessitate additional errors or correction factors. Table 7.22 shows the final correction factors that were applied for the inefficiency of the two photon rejection cut.

7.7.2 Background from Two Photon Events

To investigate the two photon background, the following enhancement cuts have been applied on events that pass the tau pair event selection cuts:

For $e^+e^- \rightarrow e^+e^-\mu^+\mu^-$ events require:

- $R_{trk} < 0.5$
- $R_{shw}^{hc} < 0.05$,

  where R_{shw}^{hc} is the shower energy in the cone with the higher shower energy.

For $e^+e^- \rightarrow e^+e^-e^+e^-$ events require:

- $R_{trk} < 0.4$,
- $0.8 < R^1_{EP} < 1.2$ AND $0.4 < R^2_{EP} < 1.6$,
  where R^1_{EP} (R^2_{EP}) is the ratio of shower energy and track momentum in the cone for which this ratio is closer to (further away from) 1.
- $N^{hc}_{trk} + N^{hc}_{cls} \leq 3$,
  where N^{hc}_{trk} and N^{hc}_{cls} are the number of tracks and clusters, respectively, in the cone with the higher visible energy. This cut removes some residual multihadronic events and $e^+e^-\tau^+\tau^-$ events.

Since for a two photon process $e^+e^- \rightarrow e^+e^-\ell^+\ell^-$ usually only the $\ell^+\ell^-$-pair is recorded, isolating the $e^+e^-\tau^+\tau^-$ background from tau pair events is extremely difficult. From Monte Carlo, the background from events with $e^+e^-\tau^+\tau^-$ final states was found to be only about 0.03% for the peak energy and about 0.07% for the off-peak points, such that the background estimate was obtained from the Monte Carlo prediction and a 100% error was assigned.

Using the kinematic properties of two photon events discussed at the beginning of this section, two distributions were investigated after applying the respective enhancement cuts to estimate the two photon background: First, the $|\cos\theta^{mis}_{trk}|$ distribution, where the missing longitudinal momentum component is defined as $\cos\theta^{mis}_{trk} = -\sum_{i=1}^{N_{trk}} p^i_z / |\sum_{i=1}^{N_{trk}} \vec{p}^{\,i}|$ and two photon events are expected to have low values of $|\cos\theta^{mis}_{trk}|$. Second, as for the investigation of the efficiency of the two photon cuts, the distribution of the transverse momentum divided by the beam energy for an event, R_{p_t}, was investigated. Two photon events are expected to have low values of R_{p_t}.

The $|\cos\theta^{mis}_{trk}|$ and R_{p_t} distributions after applying all $e^+e^-\mu^+\mu^-$ enhancement

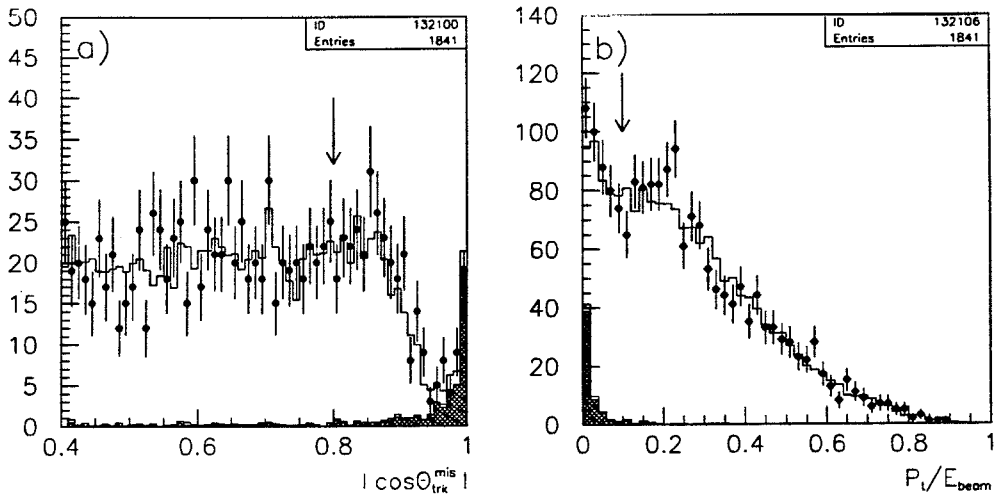

Figure 7.39: (a) The $|\cos\theta_{trk}^{mis}|$ and (b) the R_{p_t} distributions after all $e^+e^-\mu^+\mu^-$ enhancement cuts for 1994 data and MC. The points are data, the open histograms the total MC, the hatched histograms the total background MC, and the shaded histograms $e^+e^-\mu^+\mu^-$ MC only.

cuts are shown in figure 7.39, while figure 7.40 shows the same distributions after all $e^+e^-e^+e^-$ enhancement cuts. The $|\cos\theta_{trk}^{mis}|$ distributions show a very pronounced peak due to two photon events near $|\cos\theta_{trk}^{mis}| = 1$. However, the distribution has large tails, with two photon events being found all the way down to $|\cos\theta_{trk}^{mis}| \approx 0$. The R_{p_t} distribution on the other hand shows less pronounced tails, but the low R_{p_t} region is not only populated by two photon events but also by a large number of tau pair events. Since the $|\cos\theta_{trk}^{mis}|$ distribution in general shows better data MC agreement than the R_{p_t} distribution, it will be used to derive all correction factors, while the R_{p_t} distribution will be used to cross check the results.

First the $e^+e^-\mu^+\mu^-$ background will be discussed. The excess of data over MC was calculated after applying all $e^+e^-\mu^+\mu^-$ enhancement cuts in the region $|\cos\theta_{trk}^{mis}| > 0.8$. The ratio of data and MC events in the control region $|\cos\theta_{trk}^{mis}| < 0.8$ was found to be consistent with a ratio of 1 and did not show any dependence on $|\cos\theta_{trk}^{mis}|$ for 1994 and 1993 peak data and MC. For the off-peak points, the data

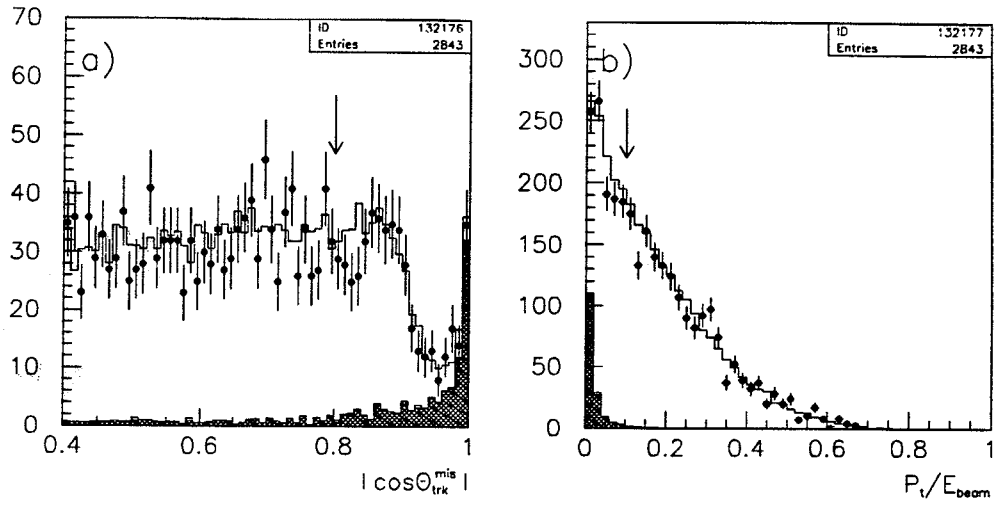

Figure 7.40: (a) The $|\cos\theta_{trk}^{mis}|$ and (b) the R_{p_t} distributions after all $e^+e^-e^+e^-$ enhancement cuts for 1994 data and MC. The points are data, the open histograms the total MC, the hatched histograms the total background MC, and the shaded histograms $e^+e^-e^+e^-$ MC only.

MC ratio in the control region was 0.839 ± 0.097 for 1993 p$-$2 and 0.900 ± 0.085 for 1993 p+2 data and MC. The tau pair MC for the off-peak points in the region $|\cos\theta_{trk}^{mis}| < 0.8$ was corrected by this factor. The difference between data and MC was then divided by the efficiency of the enhancement cuts for $e^+e^-\mu^+\mu^-$ MC to yield the estimate for the excess of $e^+e^-\mu^+\mu^-$ background in the data. The efficiencies after requiring $|\cos\theta_{trk}^{mis}| < 0.8$ were 0.709 ± 0.019 for 1994 MC and 0.746 ± 0.019 for 1993 MC.

For the R_{p_t} distribution, after applying the $e^+e^-\mu^+\mu^-$ enhancement cuts, the quality of the data MC agreement was found to be similar to that of the $|\cos\theta_{trk}^{mis}|$ distribution: In the control region $R_{p_t} > 0.1$ a good data MC agreement was observed for the 1994 and 1993 peak points, but some disagreement was found for the off-peak points. Therefore, the same procedure was applied as for the $|\cos\theta_{trk}^{mis}|$-distribution: For the off-peak points, the tau pair MC in the region $R_{p_t} < 0.1$ was corrected by the data MC ratio observed in the region $R_{p_t} < 0.1$.

Then the excess of $e^+e^-\mu^+\mu^-$ background was estimated from the data excess in the region $R_{p_t} < 0.1$, divided by the efficiency of the enhancement cuts. The efficiencies for the requirement $R_{p_t} < 0.1$ were 0.880 ± 0.014 for 1994 MC and 0.895 ± 0.013 for 1993 MC.

The excess of $e^+e^-e^+e^-$ events in the data was estimated in the same manner as for the $e^+e^-\mu^+\mu^-$ background. The enhancement cuts for these events result in larger discrepancies between the number of selected data and MC events. Therefore, the tau pair MC in the region $|\cos\theta_{trk}^{mis}| > 0.8$ was corrected by the data MC ratio in the region $|\cos\theta_{trk}^{mis}| < 0.8$ for all four data sets. These correction factors were 0.970 ± 0.021, 0.946 ± 0.038, 0.930 ± 0.080, and 0.933 ± 0.068 for 1994, 1993 peak, 1993 p$-$2, and 1993 p+2 data and MC, respectively. The $\tau^+\tau^-$ MC in the region $R_{p_t} < 0.1$ was corrected by the data MC ratio observed in the region $0.1 < R_{p_t}$. The correction factors in this case were 0.973 ± 0.025, 0.889 ± 0.043, 0.988 ± 0.098, and 0.963 ± 0.081 for 1994, 1993 peak, 1993 p$-$2, and 1993 p+2 data and MC, respectively. To yield the $e^+e^-e^+e^-$ background estimate, the data excess in the respective regions populated by the background were corrected for the efficiencies from $e^+e^-e^+e^-$ MC. The efficiencies for events in the region $|\cos\theta_{trk}^{mis}| > 0.8$ were 0.534 ± 0.013 for 1994 MC and 0.547 ± 0.013 for 1993 MC, for the region $0.1 < R_{p_t}$ the efficiencies were 0.790 ± 0.010 for 1994 MC and 0.800 ± 0.011 for 1993 MC.

Since the two photon background is not expected to depend on the energy or the year the data was recorded, the average $e^+e^-\mu^+\mu^-$ and $e^+e^-e^+e^-$ background for the four data samples was calculated. To do so, the excess observed in the data was added to the estimated background from $e^+e^-\mu^+\mu^-$ MC in the tau pair sample. The resulting number of events was divided by the luminosity of each data sample to get an estimate for the cross section of the background which is

expected to be independent of the center-of-mass energy. Figure 7.41 shows a fit to the estimated $e^+e^-\mu^+\mu^-$ background cross section from the $|\cos\theta^{mis}_{trk}|$ and the R_{p_t} distributions. The $|\cos\theta^{mis}_{trk}|$ results are shown as full circles and the fit to the four data samples as solid line, while the results from the R_{p_t} distribution are shown as open circles with a broken line indicating the fit. Figure 7.41a shows the results for the combination of data with MC of the same year, figure 7.41b shows the combinations of data with MC from the respective other year. The fit to the cross sections with the different MC samples agree very well, the difference being −0.019 pb for the $|\cos\theta^{mis}_{trk}|$ distribution and 0.088 pb for the R_{p_t} distribution. For figure 7.41a, the fitted cross sections from the $|\cos\theta^{mis}_{trk}|$ and the R_{p_t} disagree by 0.270 pb. This is within the error of either fit, but the errors for the two fits are correlated to some degree. The biggest disagreement between the cross sections from the $|\cos\theta^{mis}_{trk}|$ and the R_{p_t} distributions was observed for the 1993 p+2 point. When the fit for the $|\cos\theta^{mis}_{trk}|$ distribution is repeated without the 1993 p+2 result, a cross section of 1.364 ± 0.386 pb is obtained. The difference of $|1.234\text{ pb} - 1.364\text{ pb}| = 0.130$ pb has been added as an additional error. Table 7.23 shows the final result for the estimate of the background cross section and the additional errors that have been assigned.

Figure 7.42 shows a fit to the estimated $e^+e^-e^+e^-$ background cross sections. Shown are the results from the $|\cos\theta^{mis}_{trk}|$ distribution (full circles and solid line), and from the R_{p_t} distribution (open circles and broken line). Figure 7.42a shows the results for the combination of data with MC from the same year, figure 7.42b for the combination of data with MC from the respective other year. We observe a bigger disagreement when using different MC samples than we did in the case of $e^+e^-\mu^+\mu^-$ MC: For each fit in figure 7.42, combining data with the MC from the respective other year yields a higher background estimate than combining data

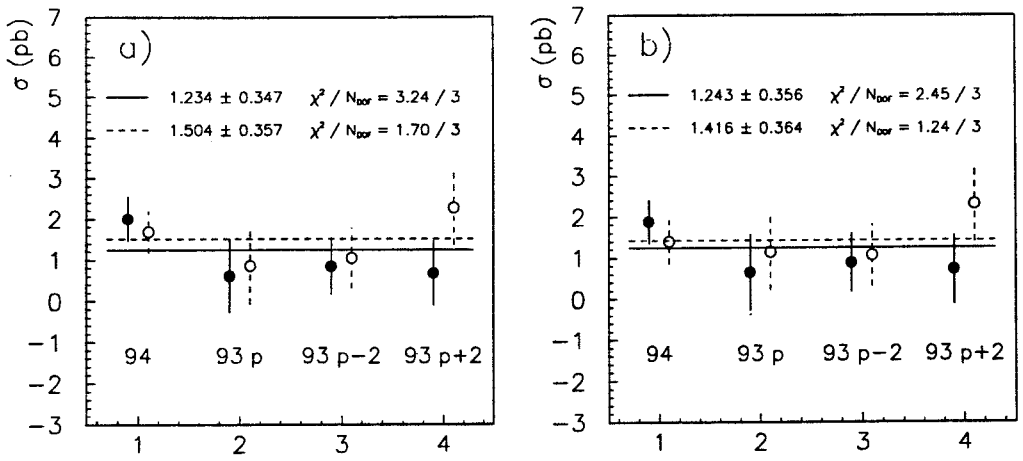

Figure 7.41: Fit to the $e^+e^-\mu^+\mu^-$ background estimates for 1994 and the three 1993 data sets. Figure (a) shows the combination of data with MC from the same year, in figure (b) data is combined with MC from the respective other year. The full circles are the cross sections estimated from the $|\cos\theta^{mis}_{trk}|$ distribution, the solid line is a fit to the four cross sections. The open circles are the estimates using the R_{p_t} distribution, the broken line is the corresponding fit.

and MC from the same year. The biggest difference of −0.104 pb was observed for the $|\cos\theta^{mis}_{trk}|$ distribution. We will add this difference to the error of the $|\cos\theta^{mis}_{trk}|$ fit. In both figure 7.42a and b we observe a discrepancy between the background estimates from the $|\cos\theta^{mis}_{trk}|$ distribution and from the R_{p_t} distribution. This difference comes mainly from the 1993 peak point. A fit to the $|\cos\theta^{mis}_{trk}|$ results excluding the 1993 peak measurement yields a background estimate of (3.200 ± 0.701) pb for the combination of data with the same year MC. The difference $|2.771\text{ pb} - 3.200\text{ pb}| = 0.429$ pb was added to the overall error. Table 7.23 shows the final result for the estimate of the background cross section, and the additional errors that have been assigned.

Using the background from $e^+e^-\tau^+\tau^-$ MC with an error of 100% yields a background estimate of (0.423 ± 0.423) pb. The total two photon background

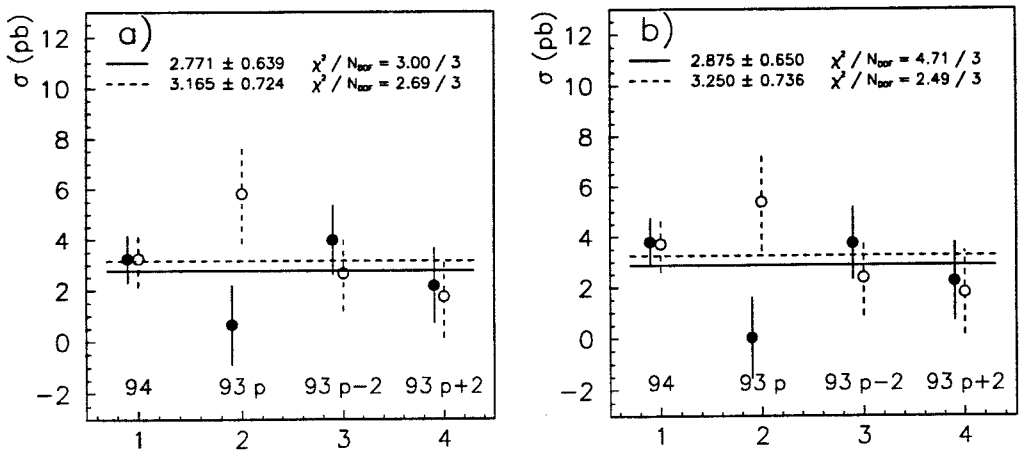

Figure 7.42: Fit to the $e^+e^-e^+e^-$ background estimates for 1994 and the three 1993 data sets. Figure (a) shows the combination of data with MC from the same year, in figure (b) data is combined with MC from the respective other year. The full circles are the cross sections estimated from the $|\cos\theta^{mis}_{trk}|$ distribution, the solid line is a fit to the four cross sections. The open circles are the estimates using the R_{p_t} distribution, the broken line is the corresponding fit.

	$e^+e^-\mu^+\mu^-$ bkgr.		$e^+e^-e^+e^-$ bkgr.	
contribution	σ (pb)	error (pb)	σ (pb)	error (pb)
fit to $\|\cos\theta^{mis}_{trk}\|$ distribution	1.234	0.347	2.771	0.639
diff. for different MCs		0.009		0.104
diff. $\|\cos\theta^{mis}_{trk}\|$ and R_{p_t}		0.130		0.429
total	1.234	0.371	2.771	0.777

Table 7.23: Estimate of the $e^+e^-\mu^+\mu^-$ and $e^+e^-e^+e^-$ background cross sections and their errors from the fits in figures 7.41 and 7.42.

	$\int \mathcal{L}dt$ (pb^{-1})	2γ bkgr. events	correction factor
94	48.9	216.6 ± 46.9	0.9961 ± 0.0008
93 peak	13.8	60.9 ± 13.2	0.9961 ± 0.0008
93 p−2	8.9	39.4 ± 8.5	0.9885 ± 0.0025
93 p+2	9.2	40.7 ± 8.8	0.9915 ± 0.0018

Table 7.24: Estimate of the complete two photon background for each data set from the background cross section estimate in equation 7.3.

from $e^+e^-\mu^+\mu^-$, $e^+e^-e^+e^-$, and $e^+e^-\tau^+\tau^-$ events is

$$\sigma_{2\gamma} = (1.234\pm0.371)\text{pb}+(2.771\pm0.777)\text{pb}+(0.423\pm0.423)\text{pb} = (4.428\pm0.959)\text{pb}\,. \tag{7.3}$$

Table 7.24 shows the background corrections and errors for each data sample resulting from this cross section of two photon reactions.

7.8 Cosmic Ray Events

7.8.1 The Cosmic Ray Rejection Algorithm

The cosmic ray rejection is done by a combination of vertex cuts and cuts on the information provided by the time-of-flight counters (TOF). For the TOF cut, the absolute time t_0 and the time difference Δt of an event are used. The absolute time t_0 is defined as the time out of all TOF hits which is closest to 0, i.e. which is closest to coinciding with the expected time of arrival after a beam crossing, assuming the particle travels with $\beta = 1$. To determine the time difference Δt for an event, a double loop over all TOF hits is performed and the time difference of each pair is calculated by subtracting the absolute time of the hit in the lower hemisphere from the absolute time of the hit in the upper hemisphere. Cosmic

rays coming from above therefore are expected to have a positive time difference which is significantly different from zero. The time difference with the smallest absolute value from all back-to-back TOF cluster pairs is assigned as Δt for the event. An event is classified as a cosmic ray event by TOF if any of the following three conditions is met:

(a) If at least one pair of back-to-back TOF hits was found, then classify the event as a cosmic ray if either of the following conditions is met:

$$10.0 \text{ ns} < \Delta t < 30.0 \text{ ns}$$

$$\text{NOT } (-10.0 \text{ ns} < t_0 < 10.0 \text{ ns}) .$$

(b) If at least 1 TOF hit was found but no back-to-back TOF hits, then classify the event as a cosmic ray if

$$\text{NOT } (-10.0 \text{ ns} < t_0 < 10.0 \text{ ns}) .$$

(c) If no TOF hits were found, classify the event as a cosmic ray.

Effectively these cuts are only applied inside the TOF acceptance. The exact definition of "inside" and "outside" of the TOF acceptance will be given below.

Figure 7.43a shows the Δt distribution for events in the TOF acceptance and figure 7.43b the t_0 distribution of events for which no back-to-back pair of TOF clusters was found. The cosmic ray background is in both cases quite well separated from the peak of tau pair events near zero. The cosmic ray rejection cuts described above are indicated by arrows.

In order to reject cosmic rays outside the TOF acceptance, and to retrieve some of the tau events mistakenly classified by TOF as cosmic ray events, an additional cosmic ray classification, based on the charged track information is

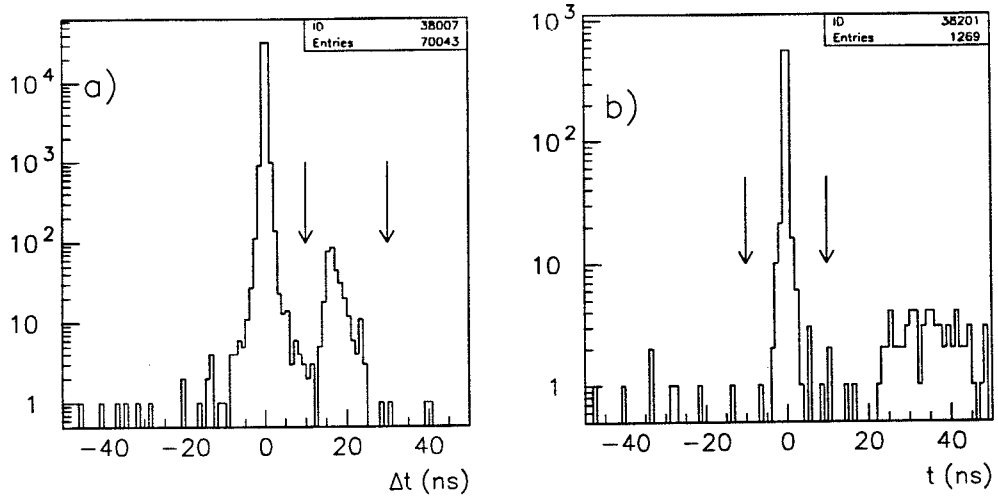

Figure 7.43: Distribution of (a) time difference and (b) absolute time for events with no back-to-back TOF hits for tau pair events before applying the cosmic ray rejection cuts inside the TOF acceptance from the combined 1993 and 1994 data sample. In plot (a) cosmic ray events can be seen in the region 10 ns $\approx< \Delta t \approx<$ 30 ns, in plot (b) they populate the region 10 ns $\approx< t_0$.

performed. For this purpose "cosmic ray quality tracks" were defined by requiring $p_t \geq 0.1$ GeV/c, $d_0^{track} \leq 20.0$ cm, and $z_0^{track} \leq 500.0$ cm. One loops over all the tracks thus defined, so that all possible pairs of tracks are formed. If the tracks are sufficiently back-to-back, the d_0 and z_0 for the *pair* of tracks are defined in the following manner:

$$d_0^{\mathrm{pair}\,ij} \equiv |d_0^{\mathrm{track}\,i}| + |d_0^{\mathrm{track}\,j}|$$
$$z_0^{\mathrm{pair}\,ij} \equiv z_0^{\mathrm{track}\,i} + z_0^{\mathrm{track}\,j} .$$

The smallest such d_0 and z_0 found among the track pairs are used for the cuts and will be called d_0^{min} and z_0^{min} hereafter. The *absolute* values of the d_0s from the tracks have been added because for out-of-time events close to the interaction point, CJ will reconstruct the two tracks as if displaced from the interaction point at opposite sides in the $x-y$ plane [67]. Therefore, the $d_0^{\mathrm{pair}\,ij}$ value for cosmic rays that traverse the detector close to the interaction point will get enhanced.

Tight and loose vertex cuts are defined by the following conditions:

$$\text{loose vertex cut} \;:\; |z_0^{min}| < 50.0 \text{ AND } d_0^{min} < 1.5 \text{ cm} \tag{7.4}$$

$$\text{tight vertex cut} \;:\; |z_0^{min}| < 10.0 \text{ AND } d_0^{min} < 0.08 \text{ cm} . \tag{7.5}$$

An event is assumed to be inside the TOF acceptance if a back-to-back pair of cosmic ray quality tracks can be found for which both tracks have $|\cos\theta| < 0.8$. An event is then *rejected* as a cosmic ray if the following conditions are met:

- inside TOF acceptance: fail TOF cut (cut (a), (b), or (c) from above) AND fail tight vertex cut (7.5).
- outside TOF acceptance: fail loose vertex cut (7.4).

The z_0^{min} versus d_0^{min} distribution of events inside the TOF acceptance with no TOF hits is shown in figure 7.44a. Those events are classified by TOF as cosmic rays, and indeed, they are rather evenly distributed over a large area, as one would expect for cosmic rays. There appears to be a slight concentration of events near the vertex, suggesting that a few events with NTOF=0 are tau pair events and should not be rejected. In figure 7.44a, the tight vertex cut is shown by broken lines. Events that lie inside this "box" near the vertex are retained in the tau sample, independent of the TOF information. The z_0^{min} versus d_0^{min} distribution of events inside the TOF acceptance which have at least one TOF hit and were classified as cosmic ray events by the cuts on t_0 or Δt are show in figure 7.44b. Again, one sees a concentration of presumed tau pair events near the vertex, which are retained in the tau sample since they pass the tight vertex cut.

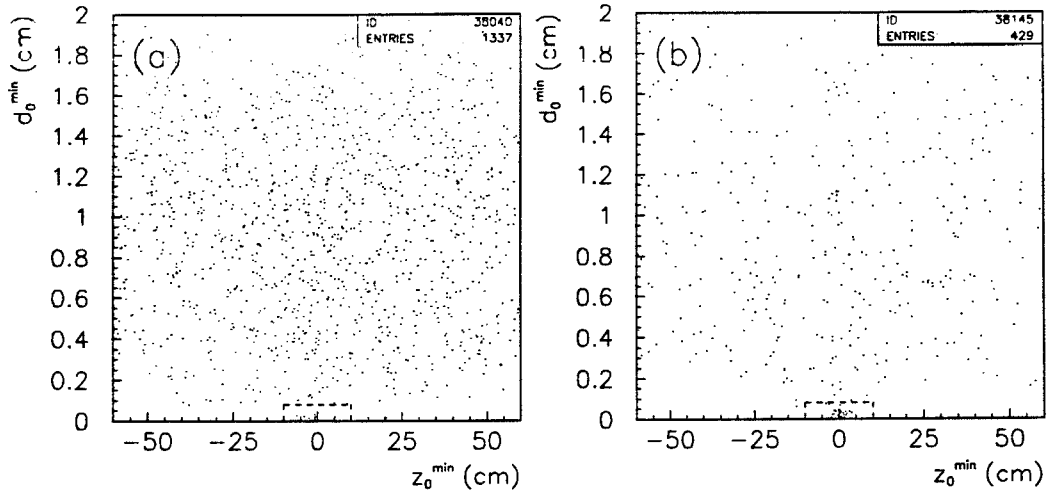

Figure 7.44: The d_0^{min} versus z_0^{min} distribution for events that are rejected by the TOF counter but pass all tau pair selection cuts before the cosmic ray rejection cuts. Shown are (a) events with no TOF hits and (b) events with at least one TOF hit inside the TOF acceptance from the combined 1993 and 1994 data sample. The broken line near the vertex shows the tight vertex cut inside which events are retained regardless of the TOF information.

7.8.2 Cosmic Ray Background Inside the TOF Acceptance

Figure 7.45a shows the d_0^{min} versus z_0^{min} distribution inside the TOF acceptance for events that pass all TOF cuts. A few events are found far away from the vertex, indicating that indeed we have some cosmic ray background leaking into the tau pair sample. A small number of cosmic rays is also expected to traverse the detector close enough to the vertex to pass the tight vertex cuts and therefore to be misclassified as tau pair events. This background is quite small and will be discussed below, while for now we are completely exempting events that pass the tight vertex cut. To assess the background of cosmic ray events, we will first look at the d_0^{min} versus z_0^{min} distribution of events that pass the tau pair selection cuts. In figure 7.45a two regions have been indicated: Region 1 near the vertex with $d_0^{min} < 1.1$ cm and $|z_0^{min}| < 20$ cm (but excluding the region $d_0^{min} < 0.08$ cm and

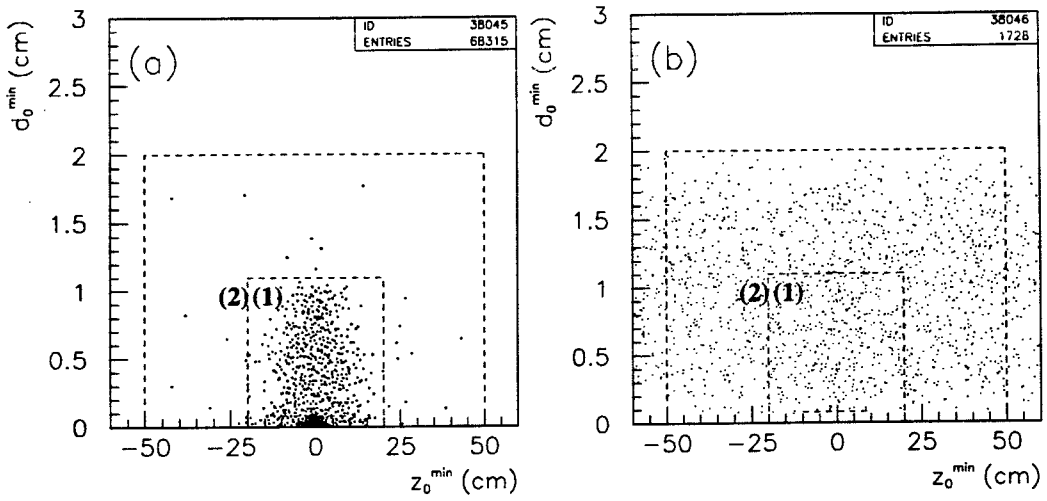

Figure 7.45: (a) Events from the combined 1993 and 1994 data sample that pass the tau pair selection cuts inside the TOF acceptance and (b) events that are rejected as cosmic rays by the TOF counter but pass all other tau pair selection cuts. The broken lines indicate the two regions used for the cosmic ray background estimate, where the region $d_0^{min} < 0.08$ cm and $|z_0^{min}| < 10$ cm is not included in region 1. This region is empty in plot (b) since events that pass the tight vertex cuts are retained as tau events independent of their TOF information.

$|z_0^{min}| < 10$ cm) and region 2 with 1.1 cm $< d_0^{min} < 2.0$ cm and 20 cm $< |z_0^{min}| <$ 50 cm which is populated only by a few events. Events in region 2 are suspected to be mainly cosmic ray events. Figure 7.45b shows the d_0^{min} versus z_0^{min} distribution for events that were rejected by the TOF counter but pass all other tau cuts. Here the same regions as in figure 7.45a are indicated. No events with $d_0^{min} >$ 2.0 cm are observed in that figure since events which pass all tau pair selection cuts except the cosmic ray rejection cuts are required to have at least one quality charged track with $d_0^{track} < 1.0$ cm in each cone. We will estimate the number of cosmic ray events by

$$N_{tot}^{CR} \leq N_{max}^{CR} \equiv \frac{N_1^{CR} + N_2^{CR}}{N_2^{CR}} N_2^{\tau} ,$$

where N_i denotes the number of events in region i for events that pass the tau cuts (superscript 'τ', corresponds to figure 7.45a) or are rejected by the TOF cut

	N_2^τ	$\frac{N_1^{CR}+N_2^{CR}}{N_2^{CR}}$	N_{max}^{CR}	N_{tot}^{CR}
94	17 ± 4.1	1.437 ± 0.036	24.4 ± 5.9	12.2 ± 13.6
93 peak	8 ± 2.8	1.455 ± 0.057	11.6 ± 4.1	5.8 ± 7.1
93 p−2	1 ± 1.0	1.463 ± 0.068	1.5 ± 1.5	0.7 ± 1.6
93 p+2	0 ± 0.0	1.368 ± 0.063	0.0 ± 0.0	0.0 ± 0.0
all data	26 ± 5.1	1.436 ± 0.025	37.3 ± 7.3	18.7 ± 20.1

Table 7.25: Estimate of the cosmic ray background in the tau pair sample inside the TOF acceptance from extrapolating presumed cosmic ray events into the vertex region according to equation (7.6).

(superscript 'CR', corresponds to figure 7.45b). We expect N_{max}^{CR} to be an upper estimate of the number of cosmic ray events in the tau sample, N_{tot}^{CR}, since some of the events in region 2 of the tau sample could indeed be tau events rather than cosmic rays. Furthermore, region 2 has been bounded at $|z_0^{min}| = 50$ cm since no events were observed that pass the tau pair selection cuts with $|z_0^{min}| > 50$ cm. While this boundary is rather arbitrary, we do observe cosmic ray events with $|z_0^{min}| > 50$ cm in figure 7.45b, so that applying a cutoff *decreases* the number N_2^{CR} and therefore *increases* the correction factor $(N_1^{CR}+N_2^{CR})/N_2^{CR}$. We estimate the number of cosmic ray events in tau pair sample, N_{tot}^{CR}, by

$$N_{tot}^{CR} = \frac{1}{2}N_{max}^{CR} \pm \frac{1}{2}N_{max}^{CR} \pm \Delta N_{max}^{CR} , \qquad (7.6)$$

where ΔN_{max}^{CR} denotes the statistical error on N_{max}^{CR}. Table 7.25 shows the results of this estimate. The results suffer of course from the extremely low statistics of the check. As a cross check of the results, the number of events that pass the TOF Δt cuts was extrapolated from the region $t_0 > 10$ ns into the region -10 ns $> t_0 > 10$ ns using the t_0 distribution of events that are rejected by the Δt cut. Also, the t_0 distribution of events without back-to-back tracks, for which consequently no value for Δt could be determined, was extrapolated into the region

-10 ns $> t_0 >$ 10 ns. The results of that check were found to be consistent with those in table 7.25 [68].

The cosmic ray background scales with the luminosities rather than with the cross sections, so that the number of cosmic ray events observed for the 1993 off-peak points should be roughly 65% of the background observed for the 1993 peak energy. However, due to the small statistics, looking at the results for the 1993 energy points individually does not allow for very conclusive comparisons of the backgrounds between the energy points. Since there is no reason to assume that the cosmic ray background depends on the beam energy or on the year the data was recorded, the combined 1993 and 1994 data samples will be used to calculate the background correction.

7.8.3 Cosmic ray background near the vertex and inefficiency of the cosmic ray cuts inside the TOF acceptance

Figure 7.46 shows the ratio of shower energy to the total visible energy, R_{shw}/R_{vis} for events that were rejected as cosmic ray events inside the TOF acceptance, and for events that would have been rejected by the TOF cuts but are inside the inner vertex box. As "inner vertex box" we denote the region with $d_0^{min} < 0.08$ cm and $|z_0^{min}| < 10$ cm, in which events are retained in the tau sample irrespective of their TOF information. As can be seen in figure 7.46a, the events failed by the TOF cut are characterized by a low fraction of shower energy. This is expected for cosmic rays, since they basically consist of muons. From the figure we see that a reasonable cutoff is at $R_{shw}/R_{vis} = 0.2$. To estimate the background of cosmic ray events inside the inner vertex box, we count events with $R_{shw}/R_{vis} < 0.2$,

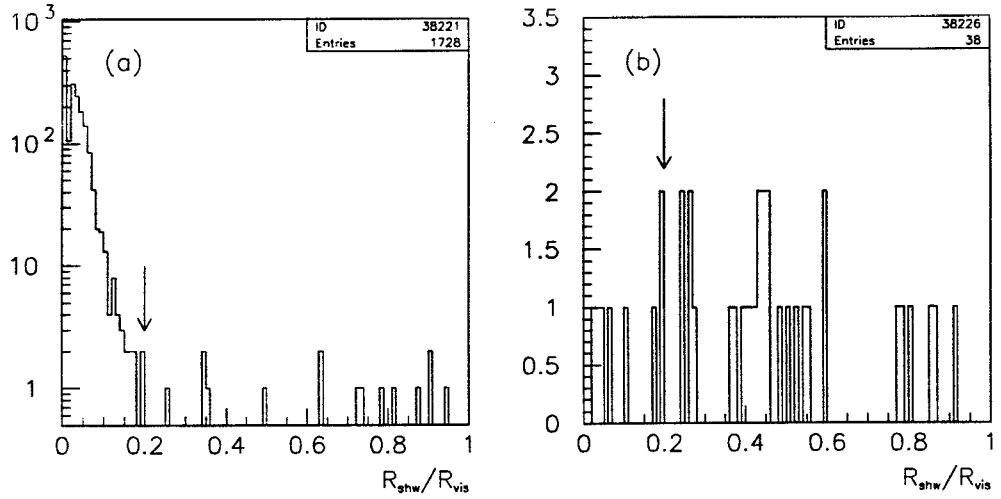

Figure 7.46: The R_{shw}/R_{vis} distribution (a) for events that were discarded by the TOF counter but pass all other tau pair selection cuts and (b) for those which were classified by the TOF cuts as cosmic ray events but were retained in the tau sample since they pass the tight vertex cuts. Both plots are for the combined 1993 and 1994 data sample.

subtract the number of tau events extrapolated from the region $R_{shw}/R_{vis} < 0.2$ into the region with $R_{shw}/R_{vis} < 0.2$, and assign a 100% error. The number of cosmic ray events thus estimated are shown in table 7.26 and will be added to the overall cosmic ray background.

We also investigated the events that fail the TOF cut and have $R_{shw}/R_{vis} > 0.2$. A visual scan of the events suggests that roughly half of those events are cosmic rays or beam-gas events overlapping with a tau pair event. The tau pair event is outside the TOF acceptance with a relatively poor z_0 and d_0 resolution, while the overlapping background tracks are inside the TOF acceptance, resulting in the whole event being classified as inside the TOF acceptance. Most of the events then fail the TOF cuts since they have no TOF hits because the overlapping background tracks are not in coincidence with the beam crossing at the OPAL interaction point. The number of tau pair events lost due to such overlapping

	Events in inner vtx box		ratio τ events:	TOF ineff.	bkgr
	fail TOF	estimated CR background	outside/inside vtx box	inner vtx box	overlap ineff.
94	23	2.0 ± 2.0	3536/44366	1.8 ± 1.8	4 ± 4
93 (peak)	10	2.6 ± 2.6	1087/12326	0.9 ± 0.9	3 ± 3
93 (p−2)	1	0 ± 1.0	245/2677	0.1 ± 0.1	0 ± 0
93 (p+2)	4	1.9 ± 1.9	308/3762	0.3 ± 0.3	0 ± 0
all data	38	6.5 ± 6.5	5176/63131	3.1 ± 3.1	7 ± 7

Table 7.26: Estimate of the inefficiency of the TOF cuts inside the TOF acceptance and estimate of the cosmic ray background that is accepted by the tight vertex cuts.

background was estimated by counting the number of events with $|\cos\theta| > 0.8$ which have a d_0^{min} and z_0^{min} value consistent with a tau pair event. An error of 100% was assigned to this "background overlap inefficiency".

To estimate the number of tau events which were mistakenly discarded by TOF but are not inside the inner vertex box, we multiply the total number of events inside the vertex box that failed the TOF cut by the ratio of events that pass all tau cuts and lie outside and inside the inner vertex box. A few events that have already been estimated by the background overlap inefficiency might be double counted by this extrapolation procedure. Also, events with a low value of R_{shw} inside the inner vertex box ($\sim$ 6.5 events for the combined 1993-94 data sample) are counted both as background *and* as potential tau pair events that are retrieved by the tight vertex cut. These double countings should be negligibly small and should be well covered by assigning a 100% error to the TOF inefficiency. The results for the inefficiency of the TOF cuts and the background overlap inefficiencies are shown in table 7.26.

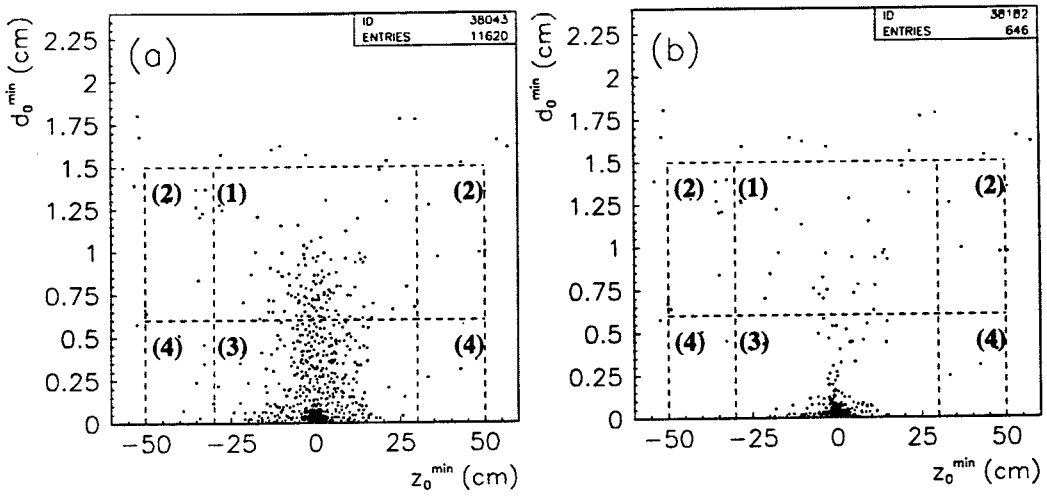

Figure 7.47: The d_0^{min} versus z_0^{min} distribution (a) for events passing the tau pair selection cuts before the cosmic ray rejection cuts outside the TOF acceptance and (b) for events remaining after requiring $R_{shw}/R_{vis} < 0.1$ for the combined 1993 and 1994 data sample. The broken lines indicate the regions used for the calculation of the cosmic ray background.

7.8.4 Cosmic Ray Background Outside of the TOF Acceptance

Figure 7.47a shows the d_0^{min} versus z_0^{min} distribution for events that pass the tau pair selection cuts before applying the cosmic ray cuts outside the TOF acceptance. The outermost broken lines show the loose vertex cut which is applied to reject cosmic ray events. Figure 7.47b shows the d_0^{min} vs. z_0^{min} distribution for tau pair events before cosmic ray cuts outside the TOF acceptance which remain after requiring $R_{shw}/R_{trk} < 0.1$. As was shown in figure 7.46a, cosmic ray events are expected to have a low fraction of shower energy. And indeed, comparing figures 7.47a and b, it can be observed that the cut significantly reduces the number of events near the vertex, while removing only a very small number of events further away from the vertex.

The cosmic ray background was estimated by estimating a minimum and a

maximum value. To estimate the minimum, events with $R_{shw}/R_{vis} < 0.1$ were counted in the region 50 cm $> |z_0^{min}| > 30$ cm, $d_0^{min} < 1.5$ cm, which corresponds to the regions 2 and 4 in figure 7.47b. The number of events was then extrapolated linearly into the region $|z_0^{min}| \leq 30$ cm, which is to say, it was simply multiplied by 2.5. A linear extrapolation should indeed yield a lower estimate of the number of events in the central region, since we expect the true distribution of cosmic ray events to peak near $|z_0^{min}| \approx 0$. To estimate the maximum, we look at regions 1 and 2 from figure 7.47b, i.e. at the regions 50 cm $> |z_0^{min}| > 30$ cm, 1.5 cm $> |d_0^{min}| > 0.6$ cm and $|z_0^{min}| \leq 30$ cm, 1.5 cm $> |d_0^{min}| > 0.6$ cm. Some of the events with $R_{shw}/R_{trk} < 0.1$ in the region 1 are expected to be tau pair events, so by counting them as cosmic rays, the result will be an upper limit for the true number of cosmic rays after requiring $R_{shw}/R_{trk} < 0.1$ in that region. The estimates of the minimum and maximum number of events in the forward region were calculated by:

$$
\begin{aligned}
N_{min} &= \frac{5}{2}(N_2^{low\ R_{shw}} + N_4^{low\ R_{shw}}) \\
N_{max} &= \frac{15}{9} N_2^{all} \frac{(N_1^{low\ R_{shw}} + N_2^{low\ R_{shw}})}{N_2^{low\ R_{shw}}} ,
\end{aligned}
$$

where N_i denotes the number of events in region i for $R_{shw}/R_{trk} < 0.1$ (superscript '*low* R_{shw}') or before any cosmic ray rejection cuts (superscript '*all*'), respectively. The factor 15/9 in the equation for N_{max} is applied to extrapolate the number of events into the region $d_0^{min} < 0.6$ cm. We are linearly extrapolating the number of events, while we indeed expect the number of events to peak around $d_0^{min} = 1$, since for the calculation of d_0^{min}, the absolute values of the d_0's from two tracks were added. So we are overestimating the true number of cosmic ray events by using a linear extrapolation. The estimate for the maximum and minimum number of events is shown in table 7.27. The cosmic ray background was then estimated

	N_{min}	N_{max}	CR bkgr estimate:
94	27.5 ± 8.3	40.0 ± 8.2	33.8 ± 13.2
93 peak	5.0 ± 3.5	13.3 ± 4.7	9.2 ± 7.2
93 p−2	0.0 ± 0.0	0.0 ± 0.0	0.0 ± 0.0
93 p+2	5.0 ± 3.5	10.0 ± 4.1	7.5 ± 6.0
all data	40.0 ± 10.0	63.3 ± 10.3	51.7 ± 18.5

Table 7.27: Estimate of cosmic ray background from extrapolating the number of events in the different regions of figures 7.47a and b as described in the text.

by

$$N^{CR} = \frac{1}{2}(N_{max} + N_{min}) \pm \frac{1}{2}(N_{max} - N_{min}) \pm \Delta N_{max} \pm \Delta N_{min} \ ,$$

where ΔN_{max} and ΔN_{min} denote the statistical errors on N_{max} and N_{min}, respectively. The result of this calculation is shown in the last column of table 7.27.

To confirm the results from that table, the ratio of events that fail the TOF cuts (but pass all other tau pair selection cuts) away from the vertex to the number of events in a large region around the vertex was extrapolated from the region $|\cos\theta| < 0.8$ into the region $|\cos\theta| > 0.8$ [68]. The two regions used in this check coincided with the combined regions 2 and 4, and with the combined regions 1, 2, 3, and 4 in figure 7.47, respectively. Using the extrapolated ratio of events, the number of cosmic ray events outside the TOF acceptance in regions 1 and 3 was estimated from the number of events in regions 2 and 4. The results of this procedure showed good agreement with the results from table 7.27.

7.8.5 Inefficiencies Outside of the TOF Acceptance

For the combined 1993 and 1994 data sample, 26 events were found which were rejected by the loose vertex cut outside the TOF acceptance. A visual scan of these events makes it quite clear that all of them are indeed cosmic rays. For a typical

event of this sample, two tracks were found which are clearly displaced from the interaction point and have very little activity in the electromagnetic calorimeter. Out of the 26 events, all have a muon identified by the muon chamber, the hadron calorimeter or the electromagnetic calorimeter in at least one cone, while for 23 events a muon was identified in both cones. A correction factor of 1 was assigned for the inefficiency and 0.18 times the number of rejected events was assigned as error. The factor 0.18 corresponds to the branching ratio of a tau decaying into a muon, so if the rejected events were indeed taus, one would only expect that fraction of events to have a muon in at least one cone. We observe 12, 4, 7, 3 events failing the loose or outer vertex cut outside the TOF acceptance for 1994, 1993 peak, 1993 p−2, 1993 p+2. This yields errors of 2.2, 0.7, 1.3, 0.5 events, respectively. These errors are taken as the contribution of the region outside the TOF acceptance to the overall inefficiency in table 7.29.

7.8.6 Combined Backgrounds and Inefficiencies for the Complete Acceptance

In table 7.28 the combined cosmic ray background from inside and outside the TOF acceptance is shown. The estimated cosmic ray background was calculated in two ways: First, the number of background events from the different sources were added for each data sample, and second, the total estimated background from the "all data" sample was scaled to the luminosity of each data sample. The two results show good agreement, except maybe in the case of the 1993 "peak−2" sample. Due to the small number of events, and since we do not expect the cosmic ray background to depend on the year or the energy, we have calculated the correction factor for each data sample using the luminosity scaled background

	$\int \mathcal{L}dt$ (pb^{-1})	total background		
		events directly	ev. scaled fr. all data	correction factor
94	48.9	48.0 ± 19.1	46.6 ± 17.0	0.9992 ± 0.0003
93 peak	13.8	17.6 ± 10.4	13.1 ± 4.8	0.9992 ± 0.0003
93 p−2	8.9	0.7 ± 1.9	8.5 ± 3.1	0.9975 ± 0.0009
93 p+2	9.2	9.4 ± 6.3	8.7 ± 3.2	0.9982 ± 0.0007
all data	80.7	76.9 ± 28.1	–	–

Table 7.28: The cosmic ray background over the whole acceptance. The total background in the 'events directly' column is the sum of the background estimates from table 7.25, from the estimated cosmic ray background inside the 'inner vertex box' in table 7.26 and from the cosmic ray background estimate outside the TOF acceptance in table 7.27.

estimate from the "all data" sample.

In table 7.29 the combined inefficiencies of the cosmic ray rejection cuts inside and outside the TOF acceptance are shown. In order to be conservative, the errors have been added linearly and not in quadrature. The correction factors derived in this section compensate for the inefficiencies of the cosmic ray rejection cuts in the data. But the cosmic ray rejection cuts have also a small inefficiency for the MC, and in order to account for this, the correction factor derived for data has been divided by the ratio of the number of tau events selected from MC *without* the cosmic ray rejection cuts and the number of tau events selected with all cuts. This ratio is 1.00015 for 1994 tau MC, 1.00012 for 1993 peak tau MC, 1.00013 for 1993 p−2 tau MC, and 1.00017 for 1993 p+2 tau MC, where the error is negligible. The results in the last column of table 7.29 were obtained by dividing the pure data correction factors by the correction for the respective MC. For the 'all data' sample, the result was divided by 1.00015. The final results are consistent with a correction factor of unity for each of the data samples and for the combined data sample. Given the extremely low statistics and that we have no reason to assume

	Inside TOF accept.		Outside TOF	total background	
	TOF	bkgr. overlap ineff.		events	data cor. divided by MC cor.
94	1.8 ± 1.8	4 ± 4	0 ± 2.2	5.8 ± 8.0	0.99995 ± 0.00014
93 peak	0.9 ± 0.9	3 ± 3	0 ± 0.7	3.9 ± 4.6	1.00013 ± 0.00029
93 p−2	0.1 ± 0.1	0 ± 0	0 ± 1.3	0.1 ± 1.4	0.99990 ± 0.00041
93 p+2	0.3 ± 0.3	0 ± 0	0 ± 0.5	0.3 ± 0.8	0.99989 ± 0.00017
all data	3.1 ± 3.1	7 ± 7	0 ± 4.7	10.1 ± 14.8	0.99998 ± 0.00019

Table 7.29: The inefficiency of the TOF and vertex cuts over the whole acceptance.

that the inefficiencies of the cuts depend on the year or the energy, we will use the correction factor from the combined data sample of 1.0000 ± 0.0002 for all the data samples as our final result.

7.9 Inefficiency of the Acollinearity Cut

Figure 7.48a shows the acollinearity distribution for events that pass all other tau pair selection cuts. By requiring an acollinearity angle of less than 15 deg, a large number of various backgrounds is discarded. The data MC agreement in the region with an acollinearity of more than 15° is not very good: For 1994 data and MC we find 11127 data events compared to 7698 luminosity scaled MC events, of which only 1100 events are from $\tau^+\tau^-$ MC. The remaining background is composed of 59% two photon MC (39% $e^+e^-e^+e^-$ + 16% $e^+e^-\mu^+\mu^-$ + 4% $e^+e^-\tau^+\tau^-$ MC), 25% Bhabha events, and 14% multihadronic events. The remaining less than 2% background is due to $\mu^+\mu^-$ events.

Figure 7.48b shows the R_{vis} distribution for events in the acollinearity regions $15\,\text{deg} < \theta_{acol} < 50\,\text{deg}$. The region $\theta_{acol} > 50\,\text{deg}$ was not investigated, since the large amount of background in that region makes it impossible to enhance the

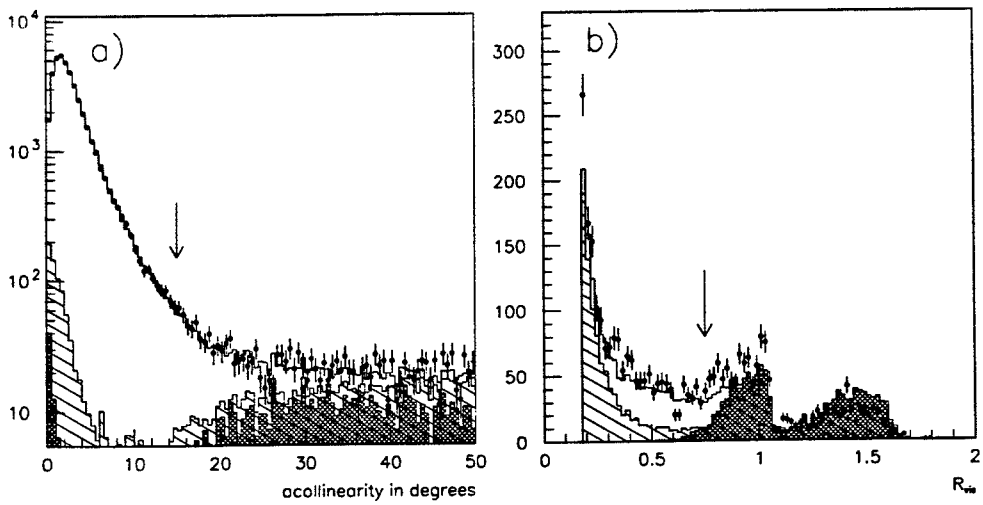

Figure 7.48: (a) The acollinearity distribution for events that pass all other tau pair selection cuts. The acollinearity cut is indicated by an arrow at 15 degrees. (b) The distribution for events that fail only the acollinearity cut and have an acollinearity of less than 50 degrees. In both plots, the points are 1994 data, the open histograms are the total 1994 MC, and the hatched histograms are the background only. The Bhabha background is indicated by the shaded histograms.

tau pair events strongly enough to allow for a comparisons of tau pair data and MC events. In the figure it can be observed that the Bhabha events which are rejected by the acollinearity cut have a high visible energy while the two photon and multihadron events have a low visible energy. This is due to the fact that most Bhabha events fail the acollinearity cut due emission of final state radiation, while two photon events and multihadronic events usually point into the forward region and have a large amount of energy lost along the beam pipe. These different properties make it necessary to reject the backgrounds in the high and low visible energy region separately, where the separation has been chosen at $R_{vis} = 0.75$ as indicated by the arrow in figure 7.48b. For the region $R_{vis} > 0.75$, tau pair events were enhanced by requiring the relative shower energy in the cone with the bigger shower energy (R^{hc}_{shw}) to fall into the region $0.1 < R^{hc}_{shw} < 0.7$. The R^{hc}_{shw} distribution of events with $R_{vis} > 0.75$ is shown in figure 7.49a. For events

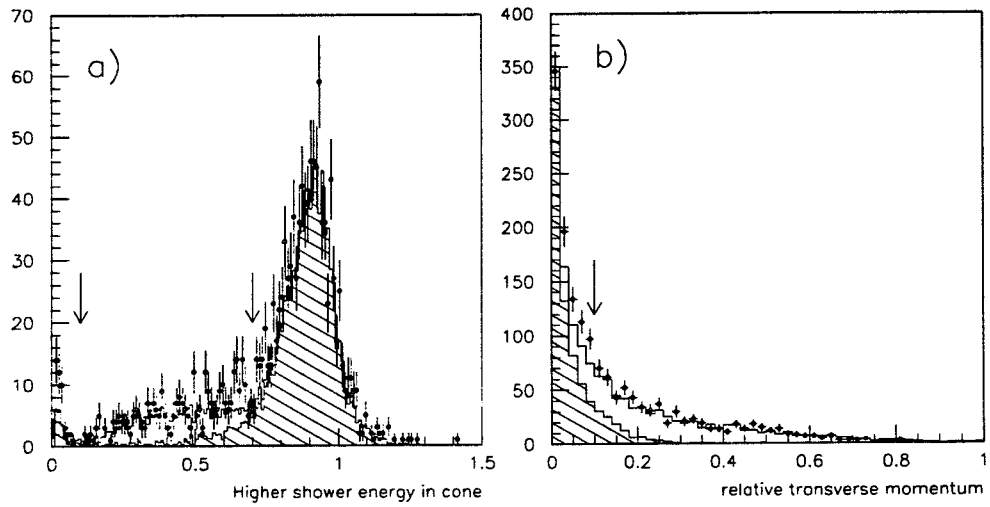

Figure 7.49: (a) The distribution of the shower energy in the cone with the higher shower energy for events from figure 7.48b in the region $R_{vis} > 0.75$. The arrows indicate the region in which the number of data and MC events was compared. (b) The relative transverse momentum for events from figure 7.48b in the region $R_{vis} \leq 0.75$ for which one no cone has a value of $|\cos\theta| > 0.9$ as described in the text. The data MC agreement in the region with a relative transverse momentum bigger than 0.1 was investigated. In both plots, the points are 1994 data, the open histograms the total 1994 MC, and the hatched histograms the background only.

with $R_{vis} \leq 0.75$ it was first required that the bigger value of $|\cos\theta|$ from the two cones fulfills $|\cos\theta| < 0.9$, where $\cos\theta$ was calculated from the information of the electromagnetic calorimeter and the tracking chamber for each cone. This cut removes most of the excess of background in the data that can be observed in figure 7.48b at $R_{vis} \approx 0.2$ while removing only about 6% of the tau pair MC. The distribution of the transverse track momentum relative to the beam energy, R_{p_t}, for the remaining events is shown in figure 7.49b. Tau pair events were then enhanced by requiring $R_{p_t} > 0.1$.

The data MC agreement was investigated for the acollinearity regions $15\,\text{deg} < \theta_{acol} < 20\,\text{deg}$, $20\,\text{deg} < \theta_{acol} < 30\,\text{deg}$, and $30\,\text{deg} < \theta_{acol} < 50\,\text{deg}$ separately. For each of those regions the data MC difference was corrected by the efficiency of the cuts derived from tau pair MC. Depending on the acollinearity region, these efficiencies vary for the peak energy points from ~ 0.65 to ~ 0.80 for the low R_{vis} region, and from ~ 0.85 to ~ 0.95 in the high visible energy region. For the peak points, the efficiency corrected data MC difference in the region $15\,\text{deg} < \theta_{acol} < 50\,\text{deg}$ was then calculated from the three acollinearity region as $127.9 \pm 43.0 \pm 22.7$ for 1994 data and MC, and $29.0 \pm 22.0 \pm 3.2$ for 1993 peak data and MC. Here the first error is statistical and the second was calculated by scaling the background MC in the region $0.1 < R^{hc}_{shw} < 0.7$, or $R_{p_t} > 0.1$, respectively, by the data MC ratio observed in the region $0.7 < R^{hc}_{shw} < 1.5$, or $R_{p_t} < 0.1$, respectively. Results were then corrected by an efficiency of about 0.84 to account for events in the region $\theta_{acol} > 50\,\text{deg}$. The resulting estimate for the data excess is 152.9 ± 58.2 for 1994 data and MC, and 34.7 ± 26.7 for 1993 peak data and MC.

The ratio of tau pair MC to background MC events in the regions where the data MC agreement was investigated gets smaller with increasing acollinearity. For the peak energy points in the three acollinearity regions from above, these

ratios are about 7, 3, and 2 in the high R_{vis} region, where the background is mainly from Bhabha events, and about 25, 6, and 1 in the low R_{vis} region, where the background is mainly from multihadronic events and two photon events. Due to the unfavorable signal to background ratio in the region $30\,\mathrm{deg} < \theta_{acol} < 50\,\mathrm{deg}$, the calculation from above was repeated by ignoring this region, and extrapolating the data excess in the region $15\,\mathrm{deg} < \theta_{acol} < 30\,\mathrm{deg}$ into the region $\theta_{acol} > 30\,\mathrm{deg}$, where the efficiency in this case is about 0.66. The results were found to be consistent with those from above. The calculation was then repeated with the cut between the low and high visible energy region moved from $R_{vis} = 0.75$ to $R_{vis} = 0.5$. No significant changes of the results were observed.

Due to the effect of radiative corrections, the fraction of tau pair events discarded by the acollinearity cut depends on the center-of-mass energy [71]. Furthermore, for the off-peak points, the background fractions of the non-resonant two photon background are much higher than for the peak points, making the separation of tau pair events from background events more difficult. In the low visible energy region where the background is mainly from multihadronic events and two photon events, the data MC ratios for off-peak data are about 15, 2, and 0.5 in the three acollinearity regions. Due to the extremely large background fraction in the region $30\,\mathrm{deg} < \theta_{acol} < 50\,\mathrm{deg}$, the data MC difference for the off-peak points was only calculated in the regions $15\,\mathrm{deg} < \theta_{acol} < 20\,\mathrm{deg}$ and $20\,\mathrm{deg} < \theta_{acol} < 30\,\mathrm{deg}$. The data excess and the corresponding errors were then calculated in the same fashion as for the peak points. The efficiency for events that fail the acollinearity cut to fall into the region $15\,\mathrm{deg} < \theta_{acol} < 30\,\mathrm{deg}$ was determined as 0.615 from 1993 p$-$2 tau pair MC, and 0.612 from 1993 p+2 tau pair MC. The resulting estimate of the data excess of events failing the acollinearity cut was calculated as 50.1 ± 18.9 for 1993 p$-$2 data and MC, and 24.7 ± 18.6 for 1994 p+2 data

and MC. Again it was checked that these results were not significantly affected when the separation between the low and high visible energy regions was moved to $R_{vis} = 0.5$. The final results for all four data samples are shown in table 7.30.

	data excess	correction factor
94	152.9 ± 58.2	1.0027 ± 0.0010
93 peak	34.7 ± 26.7	1.0022 ± 0.0017
93 p−2	50.1 ± 18.9	1.0146 ± 0.0055
93 p+2	24.7 ± 18.6	1.0052 ± 0.0039

Table 7.30: The excess of genuine tau pair data events over tau pair MC events rejected by the acollinearity cut and the resulting correction factors.

7.10 Uncertainty of the tau Branching Ratio

The tau selection as described in section 7.2.3 does not have the same efficiency for all decay channels of the τ lepton. Consequently, uncertainties in the branching ratios translate into errors of the tau pair selection efficiency. The 22 decay channels of KoralZ 4.0 $\tau^+\tau^-$ MC and their branching ratios as implemented in the 94 and 93 MC are shown in table 7.31. The most recent experimental values of the tau branching ratios shown in the table were obtained from [72]. Not in all cases were the decay modes, as implemented in KoralZ, directly measured. In table 7.31 we are using the symbol Γ_i to indicate which decay modes from [72] were used - the index i follows the numbering scheme from that reference. As can be seen, in some cases, the KoralZ branching ratios had to be composed from two or more decay modes. For the errors of the branching ratios in the table we followed the following convention: If the KoralZ branching ratio had to be composed of branching ratios from [72], the errors were added in quadrature; If an asymmetric error was given as $\Gamma_i = x^{+a}_{-b}$, we are using the value $x \pm \max(a, b)$; and

for branching ratios for which only an upper limit was given, $\Gamma_i < x$, we are using $\Gamma_i = x \pm x$. For three branching ratios, the 13th, 15th and 21st in table 7.31, no experimental value was given in reference [72]. The branching ratio for the decay $\tau^- \rightarrow \nu_\tau 2\pi^-\pi^+3\pi^0$ was obtained from [73] and for the decay $\tau^- \rightarrow \nu_\tau K^0\bar{K}^0\pi^-$ from [74]. For the decay $\tau^- \rightarrow \nu_\tau\pi^-\pi^0\gamma$ we are using the Monte Carlo results from [62] and assign a 100% error.

The following procedure was used to assess the systematic error due to the uncertainty of the tau branching ratio: First, the world averages for the tau branching ratios from table 7.31 were rescaled to add up to 1 using the formula:

$$\Gamma_i^{sc} = \Gamma_i + (1 - \sum_{j=1}^{22} \Gamma_j)\frac{\sigma_{\Gamma_i}}{\sum_{i=j}^{22}\sigma_{\Gamma_j}} ,$$

where Γ_i is the branching ratio from table 7.31, σ_{Γ_i} is its error and Γ_i^{sc} is the resulting scaled branching ratio which will be used in the following calculations. Let us denote the total number of events that are produced by a given MC run for the decay mode i by n_i and the number of events that are actually classified as a tau pair event by the cuts described in section 7.2.3 by m_i. Then the acceptance correction factor, as discussed in section 7.2.4, is simply given by $a = \sum n_i / \sum m_i$. In order to adjust this correction factor to the current world average of the tau branching ratios, we calculate

$$a_{corr} = \frac{\sum c_i n_i}{\sum c_i m_i} ,$$

where c_i is the scaling factor derived for the decay mode i from the ratio of Γ_i^{sc} and the branching ratio implemented in the MC, Γ_i^{MC}. The ratio $f = a_{corr}/a$ was calculated for the four $\tau^+\tau^-$ MC samples and will be applied as the correction factor due to discrepancies of the true tau branching ratios from the values implemented in the tau pair Monte Carlo.

Decay mode $\tau^- \rightarrow$		Current World Average		Implemented in MC 1993 MC	1994 MC
1)	$\nu_\tau \bar{\nu}_e e^-$	Γ_4	$= .17880 \pm .00180$	.17870	.17926
2)	$\nu_\tau \bar{\nu}_\mu \mu^-$	Γ_2	$= .17460 \pm .00250$	.17330	.17475
3)	$\nu_\tau \pi^-$	Γ_7	$= .11300 \pm .00400$	.11110	.11861
4)	$\nu_\tau \rho^-$	Γ_{16}	$= .25000 \pm .00400$	.25390	.24956
5)	$\nu_\tau a_1^-$	$\Gamma_{31} + \Gamma_{19} - \Gamma_{12}$	$= .17655 \pm .00461$	.17786	.16728
6)	$\nu_\tau K^-$	Γ_9	$= .00670 \pm .00050$	.00730	.00705
7)	$\nu_\tau K^{*-}$	Γ_{60}	$= .01450 \pm .00120$	.01420	.01435
8)	$\nu_\tau 2\pi^- \pi^+ \pi^0$	$\Gamma_{32} - \Gamma_{40}$	$= .05050 \pm .00304$	.04790	.05005
9)	$\nu_\tau \pi^- 3\pi^0$	$\Gamma_{21} - \Gamma_{13}$	$= .01190 \pm .00158$	.01260	.01875
10)	$\nu_\tau 2\pi^- \pi^+ 2\pi^0$	Γ_{40}	$= .00480 \pm .00050$	.00440	.00416
11)	$\nu_\tau 3\pi^- 2\pi^+$	Γ_{53}	$= .00071 \pm .00009$	.00108	.00072
12)	$\nu_\tau 3\pi^- 2\pi^+ \pi^0$	Γ_{54}	$= .00021 \pm .00008$	.00027	.00022
13)	$\nu_\tau 2\pi^- \pi^+ 3\pi^0$	–	$= .00110 \pm .00040$	.00027	.00056
14)	$\nu_\tau K^- K^+ \pi^-$	Γ_{48}	$= .00220 \pm .00170$	.00108	.00171
15)	$\nu_\tau K^0 \bar{K}^0 \pi^-$	–	$= .00300 \pm .00150$	.00108	.00125
16)	$\nu_\tau K^- K^0 \pi^0$	Γ_{29}	$= .00050 \pm .00050$	.00009	.00171
17)	$\nu_\tau K^- 2\pi^0$	Γ_{12}	$= .00045 \pm .00034$	.00107	.00050
18)	$\nu_\tau K^- \pi^- \pi^+$	Γ_{45}	$= .00380 \pm .00190$	.00570	.00203
19)	$\nu_\tau \pi^- \bar{K}^0 \pi^0$	Γ_{45}	$= .00380 \pm .00190$	.00580	.00203
20)	$\nu_\tau \eta \pi^- \pi^0$	Γ_{70}	$= .00170 \pm .00028$	.00170	.00175
21)	$\nu_\tau \pi^- \pi^0 \gamma$	–	$= .00056 \pm .00056$	.00060	.00065
22)	$\nu_\tau K^- \bar{K}^0$	Γ_{27}	$= .00290 \pm .00120$	.00000	.00308

Table 7.31: Decay channels for KoralZ 4.0 $\tau^+\tau^-$ MC and branching ratios implemented in the 93 and 94 runs. All values of the current world average for which the symbol Γ_i is shown were taken from [72] and the numbering scheme for the branching ratios corresponds to that reference.

$\tau^+\tau^-$ MC	correction
94	1.0000 ± 0.0005
93 peak	1.0004 ± 0.0005
93 p−2	1.0002 ± 0.0006
93 p+2	1.0003 ± 0.0006

Table 7.32: The contribution of the uncertainty of the tau branching ratio to the overall correction factor and systematic error.

To assess the error of the correction factor, we increase each branching ratio in turn by $2\sigma_{\Gamma_i}$, and recalculate the acceptance correction:

$$a^j_{vary} = \frac{\sum_{i\neq j} c_i n_i + c_j^{2\sigma} n_j}{\sum_{i\neq j} c_i m_i + c_j^{2\sigma} m_j} .$$

Here $c_j^{2\sigma}$ stands for the ratio $\frac{\Gamma_j^{sc}+2\sigma_{\Gamma_j^{sc}}}{\Gamma_j^{MC}}$. The absolute error on a_{corr} is then readily calculated by

$$\sigma_{a_{corr}} = \sqrt{\sum_{j=1}^{22}(a^j_{vary} - a_{corr})^2} .$$

The absolute error on the correction factor $f = a_{corr}/a$ is easily obtained by dividing $\sigma_{a_{corr}}$ by the uncorrected acceptance a. The correction factors f and their errors are shown in table 7.32 for the different $\tau^+\tau^-$ MC runs.

7.11 Four Fermion Events

This class of events arises from processes where either the initial state electron pair or the final state tau pair radiates a photon which then decays into a fermion pair. These events differ from radiative events which create a fermion pair through interaction of the radiative photon with the material of the detector only from the theoretical point of view that in the first case the photon is virtual, while in the second case it is real. From an experimental point of view, these events

are indistinguishable. Four fermion events are not included in the versions of the Monte Carlo Program KoralZ which were used in the analysis, while the cross section calculated with ZFITTER includes the contribution from only some of those final states, so that four fermion events have to be divided into a signal and a background part. All events which have no tau pair in the final final state have to be considered background. From four fermion MC created with the program FERMISV [75] it was estimated that the background contributions from the final states $\ell^+\ell^-u\bar{u}$, $\ell^+\ell^-d\bar{d}$, $\ell^+\ell^-c\bar{c}$, $\ell^+\ell^-b\bar{b}$, and $\ell^+\ell^-\ell^+\ell^-$ is about 4%, where $\ell^+\ell^-$ stands for e^+e^- or $\mu^+\mu^-$ and the final state $\ell^+\ell^-\ell^+\ell^-$ denotes any combination of these two lepton pairs. An error of 100% was assigned, such that the corresponding correction factor is 0.9996 ± 0.0004.

The remaining events with a tau pair in the final state may constitute background or signal, depending on whether the tau pair is the result of the decay of the Z^0, in which case the event has to be counted as signal, or the result of the decay of the virtual photon, in which case the event has to be counted as background. Unfortunately, it is not possible to simulate these processes separately with the existing Monte Carlo programs [76].

Clearly, the final state $\tau^+\tau^-\tau^+\tau^-$ has to be counted as signal, while for the remaining processes with a tau pair in the final state, part of the cross section has to be counted as signal while the remaining part has to be counted as background. The four fermion processes that including tau pairs in the final states and have a non-negligible cross section are shown in table 7.33. In section 7.2.4, the Monte Carlo acceptance correction a was calculated from the ratio of KoralZ $\tau^+\tau^-$ Monte Carlo events that were produced and that passed the tau pair selection cuts. This correction factor is not exact, since the efficiencies for the signal part of the four fermion events are quite different from the efficiencies of the tau pair events

final state	production cross section	accepted cross section	efficiency
$\tau^+\tau^-\tau^+\tau^-$	0.519 pb	0.038 pb	0.074
$\tau^+\tau^-e^+e^-$	1.706 pb	0.415 pb	0.243
$\tau^+\tau^-\mu^+\mu^-$	0.539 pb	0.142 pb	0.264
$\tau^+\tau^-u\bar{u}$	0.673 pb	0.176 pb	0.262
$\tau^+\tau^-d\bar{d}$	0.173 pb	0.054 pb	0.310
$\tau^+\tau^-c\bar{c}$	0.153 pb	0.003 pb	0.022

Table 7.33: Four fermion Monte Carlo predictions for the total cross section and the cross section accepted by the tau pair selection cuts for the peak energy. The last column shows the efficiency of the tau pair selection cuts for each process.

simulated with KoralZ MC. To calculate the effect of the four fermion events, the corrected acceptance correction $\tilde{a}$ was calculated from the ratio of total cross section and the accepted cross section, in each case including the contribution from the signal part of the four fermion events. As a rough estimate, half the cross section of the four fermion events with a tau pair in the final state (but excluding the final state $\tau^+\tau^-\tau^+\tau^-$) was counted as signal, the other half as background. The cross section of the final state $\tau^+\tau^-\tau^+\tau^-$ was completely counted as signal. Given a total and accepted cross section from KoralZ of 1480.5 pb and 1116.8 pb, respectively, the resulting correction is $\tilde{a}/a = 1.0010 \pm 0.0010$, where 100% of the correction was taken as the error. Counting the remaining 0.395 pb of accepted four fermion events with a tau pair in the final state as background, a correction of 0.9996 ± 0.0004 is obtained, where the error is again 100% of the correction.

Combining all three corrections and adding the errors in quadrature, the total correction factor is 1.0002 ± 0.0011 which will be applied to all four data samples.

7.12 Trigger Efficiency

If the trigger of the OPAL detector is not 100% efficient for tau pair final states, then the cross section for the process $Z^0 \rightarrow \tau^+\tau^-$ will be estimated too low and appropriate corrections have to be applied. The OPAL trigger efficiency was estimated using the trigger redundancy provided by different parts of the OPAL detector [77]. A control sample was defined for events that were triggered by a parts of the OPAL trigger which are expected to be 100% efficiency for tau pair final states (cf. section 4.2.3). For this control sample, the efficiency of the redundant triggers was checked. The corrections used in [14] to account for the inefficiency of the trigger were 1.0002 ± 0.0006 for both 1993 and 1994. These corrections are consistent with the final results derived in [77].

7.13 Combined Corrections

The acceptance correction from tau Monte Carlo from section 7.2.4 and the correction factors derived in sections 7.3 to 7.12 are summarized in table 7.34. The product of all correction factors will be applied as the correction factor $f_{\tau\tau}$ to the number of events passing the tau pair selection cuts described in subsection 7.2.3 for the corresponding data samples. The total error was calculated in quadrature from the individual errors of the correction factors. The errors between the four data samples are mostly uncorrelated, since most errors are dominated by the statistical error from the data events. A few of the errors, however, are correlated, since the corresponding correction factors were derived from the combined 1993 and 1994 data samples or since they were derived from the same Monte Carlo. These errors are those due to the cosmic ray background and inefficiency, the inefficiency and background for two photon events, the trigger efficiency and the

background from four fermion events. The combined errors from these sources are 0.16% for 1994 and 0.18%, 0.34%, and 0.31% for 1993 peak, peak−2, and peak+2, respectively. This part of the total error on $f_{\tau\tau}$ will be treated as fully correlated amongst the four data samples, while the remaining part of the error will be treated as uncorrelated. The acceptance correction factors from 1993 peak and 1994 tau pair MC in the first line of table 7.34 differ by about 0.30%. After applying all corrections, the agreement has improved to about 0.12%, which is an indication that the corrections do indeed compensate for deficiencies of the tau pair Monte Carlo simulations.

	1993						1994	
	peak−2		peak		peak+2		peak	
	f	$\Delta f/f$ [%]	f	$\Delta f/f$ [%]	f	$\Delta f/f$ [%]	f	$\Delta f/f$ [%]
Acceptance/Eff.:								
$e^+e^- \to \tau^+\tau^-$ MC	1.3364	0.18	1.3218	0.10	1.3353	0.18	1.3257	0.07
definition of $\lvert\cos\theta\rvert$	1.0000	0.41	1.0000	0.16	1.0000	0.29	1.0000	0.11
Ineff. of e^+e^- cuts	1.0008	0.58	1.0033	0.23	1.0144	0.46	1.0027	0.13
Ineff. of $\mu^+\mu^-$ cuts	0.9988	0.22	1.0019	0.13	1.0030	0.22	0.9993	0.08
Ineff. of multiplicity cuts	0.9958	0.55	1.0025	0.24	1.0032	0.45	1.0036	0.14
Ineff. of charged cones cut	1.0010	0.11	1.0016	0.07	1.0026	0.14	1.0013	0.05
Ineff. of 2γ cuts	0.9979	0.17	1.0012	0.09	1.0034	0.20	1.0004	0.05
Ineff. of cosmic ray rejection	1.0000	0.02	1.0000	0.02	1.0000	0.02	1.0000	0.02
Ineff. of acollinearity cut	1.0146	0.55	1.0022	0.17	1.0052	0.39	1.0027	0.10
Uncertainty of τ BR	1.0002	0.06	1.0004	0.05	1.0003	0.06	1.0000	0.05
Four fermion events	1.0002	0.11	1.0002	0.11	1.0002	0.11	1.0002	0.11
Trigger efficiency	1.0002	0.06	1.0002	0.06	1.0002	0.06	1.0002	0.06
Background:								
$e^+e^- \to e^+e^-$	0.9912	0.53	0.9960	0.24	0.9962	0.40	0.9940	0.12
$e^+e^- \to \mu^+\mu^-$	0.9942	0.35	0.9920	0.16	0.9917	0.29	0.9930	0.09
$e^+e^- \to$ hadrons	0.9961	0.31	0.9953	0.18	0.9963	0.34	0.9952	0.15
Two photon reactions	0.9885	0.25	0.9961	0.08	0.9915	0.18	0.9961	0.08
Cosmic rays	0.9975	0.09	0.9992	0.03	0.9982	0.07	0.9992	0.03
overall	1.3057	1.35	1.3113	0.59	1.3436	1.10	1.3097	0.38

Table 7.34: The final correction factors for all four data samples.

Chapter 8

The Lineshape Analysis

8.1 Measurement of the $\tau^+\tau^-$ Cross Section

The results from chapters 6 and 7 enable us to calculate the cross section for the production of $\tau^+\tau^-$ final states at the three energy points according to the relation

$$\sigma_{\tau\tau} = \frac{f_{\tau\tau} \cdot N_{\tau\tau}}{\mathcal{L}_{\tau l}} ,$$

where $N_{\tau\tau}$ is the number of events selected by the cuts described in section 7.2.3 and $f_{\tau\tau}$ is the overall correction factor calculated in section 7.13. The integrated luminosity for the time period over which tau pair events were recorded is denoted by $\mathcal{L}_{\tau l}$ and was calculated as described in chapter 6. Luminosity Bhabha events can only be counted when the SW detector and trigger are operational, while tau pair events can only be counted when the subdetectors, which are used to reconstruct the parameters on which the cuts are applied, are functional. In order to avoid biasing either the number of luminosity Bhabha events or tau pair events, events of either class are only counted if the SW detector and the subdetectors needed for the tau pair analysis were operational.

Events were counted separately for 1994 data and for 1993 data. For 1993 data, three energy bins were defined for center-of-mass energies with 88.5 GeV $\leq E_{cm} <$

	E_{cm}(GeV)	$N_{\tau\tau}$	$\mathcal{L}(nb^{-1})$	$f_{\tau\tau}$	$\sigma(nb)$	$\Delta\sigma(nb)$
93: p−2	89.4527	3240 ± 57	8282.4 ± 10.1	1.3057	0.5108	0.0090
peak	91.2084	8881 ± 94	7686.1 ± 9.9	1.3113	1.5152	0.0161
p+2	93.0360	4499 ± 67	8801.8 ± 10.8	1.3436	0.6868	0.0103
94:	91.1420	55674 ± 236	49465.1 ± 25.0	1.3097	1.4741	0.0063

Table 8.1: The mean center-of-mass energies for the four data samples, the number of events passing the tau pair selection cuts, and the corresponding luminosities. In the last but one column, the cross sections calculated from the luminosity, the number of events passing the tau pair selection cuts and the correction factors $f_{\tau\tau}$ are shown. All errors are purely statistical.

90.3 GeV, 90.3 GeV $\leq E_{cm} <$ 92.1 GeV, and 92.1 GeV $\leq E_{cm} <$ 93.9 GeV, respectively. For each of the energy bins, the total number of events passing the tau pair selection cuts was calculated by a running sum. To calculate the luminosity, the events passing the SWITR and SWITL selections were weighted by the theoretical cross section and the correction factors as shown in equation 6.1. The cross sections calculated for the three energy points in 1993 and for the peak energy point in 1994 are shown in table 8.1. For the lineshape analysis, tighter requirements on the status of the relevant subdetectors and triggers were applied than for the tau pair analysis in chapter 7. Hence a smaller number of tau pair events was selected in table 8.1 than in table 7.1.

8.2 Lineshape Fit for the Process $Z^0 \rightarrow \tau^+\tau^-$

In table 8.1, the average center-of-mass energies for each data sample are shown. The mean beam energies for the same nominal energies show small fluctuations between different fills. The RMS error of these fluctuations is however small compared to the systematic error of the beam energy and has been neglected.

ZFITTER was used to calculate the cross section of the process $Z^0 \rightarrow \tau^+\tau^-$ in

the Improved Born Approximation at each energy point from table 8.1 for given values of M_Z, Γ_{tot} and $\sigma^0_{\tau\tau}$. Using the minimization program MINUIT [58] those values were varied around their expected value and the corresponding theoretical cross section was calculated. For each result the χ^2 is calculated according to

$$\chi^2 = \Delta^T \nu^{-1} \Delta \ ,$$

where Δ denotes the vector of residuals between the experimental cross section measurements and the predictions by ZFITTER. The experimental result for the cross section was corrected according to equation 3.11 to obtain the cross section corresponding to the mean beam energy. The error on the beam energy spread is negligible. The covariance matrix ν is calculated from the statistical and systematic errors, taking into account the full correlations between the systematic errors for the four data sets.

The results for the mass and total decay width of the Z^0, for the peak cross section $\sigma^0_{\tau\tau}$ and for the partial width of the decay $Z^0 \rightarrow \tau^+\tau^-$ obtained from this fit were

$$\begin{aligned} M_Z &= 91.183 \pm 0.020 \text{ GeV} \\ \Gamma_{tot} &= 2.514 \pm 0.018 \text{ GeV} \\ \sigma^0_{\tau\tau} &= 2.002 \pm 0.028 \text{ nb} \\ \Gamma_{\tau\tau} &= 84.54 \pm 0.59 \text{ MeV} \ . \end{aligned}$$

In the fit, M_Z, Γ_{tot} and $(\hat{c}_a^{e\,2} + \hat{c}_v^{e\,2})(\hat{c}_a^{l\,2} + \hat{c}_v^{l\,2})$ were treated as free parameters, where $\sigma^0_{\tau\tau}$ can be directly calculated from the three fit parameters according to equations 2.31 and 2.32. To derive $\Gamma_{\tau\tau}$, lepton universality was assumed for the effective coupling constants of the tau and the electron. To calculate small effects due to the $\gamma - Z^0$ interference term in equation 2.38, and due to the mass of the

τ lepton, the actual values of the individual coupling constants were derived from the fit value of $(\hat{c}_a^{e\,2} + \hat{c}_v^{e\,2})(\hat{c}_a^{l\,2} + \hat{c}_v^{l\,2})$ by assuming the Standard Model ratios of the coupling constants.

For a second fit, the Standard Model parametrization of the lineshape was chosen in ZFITTER. Assuming a top mass of $m_t = 180$ GeV, a Higgs mass of $M_{Higgs} = 300$ Gev, using $\alpha_s(M_Z) = 0.12$ for the strong coupling constant and treating only M_Z as free parameter, the lineshape parameters were calculated as

$$\begin{aligned} M_Z^{SM} &= 91.166 \pm 0.016 \text{ GeV} \\ \Gamma_{tot}^{SM} &= 2.493^{+0.006}_{-0.007} \text{ GeV} \\ \Gamma_{\tau\tau}^{SM} &= 83.72^{+0.23}_{-0.24} \text{ MeV} . \end{aligned}$$

The error on M_Z^{SM} is the result of the fit, while the errors on Γ_{tot}^{SM} and $\Gamma_{\tau\tau}^{SM}$ are due to varying the top mass from 160 GeV to 200 GeV and the Higgs mass from 60 GeV to 1000 GeV. The results of the lineshape fits for both the Improved Born Approximation parametrization and the Standard Model parametrization are shown in figure 8.1.

The precision of the partial decay width for tau pair final states depends strongly on the precision of the mass and total decay width of the Z^0. These quantities do not depend on the final state of the Z^0 decay channel and have, due to the higher statistics, been measured most accurately from multihadronic final states. To determine the partial decay width for tau pair final states more accurately, the fit using the Improved Born Approximation parametrization was repeated, fixing the values of the mass and total width of the Z^0 to 91.1852 GeV and 2.4960 GeV, respectively, according to the results given in [14]. The resulting partial decay width is

$$\Gamma_{\tau\tau} = 84.02 \pm 0.20 \text{ MeV} .$$

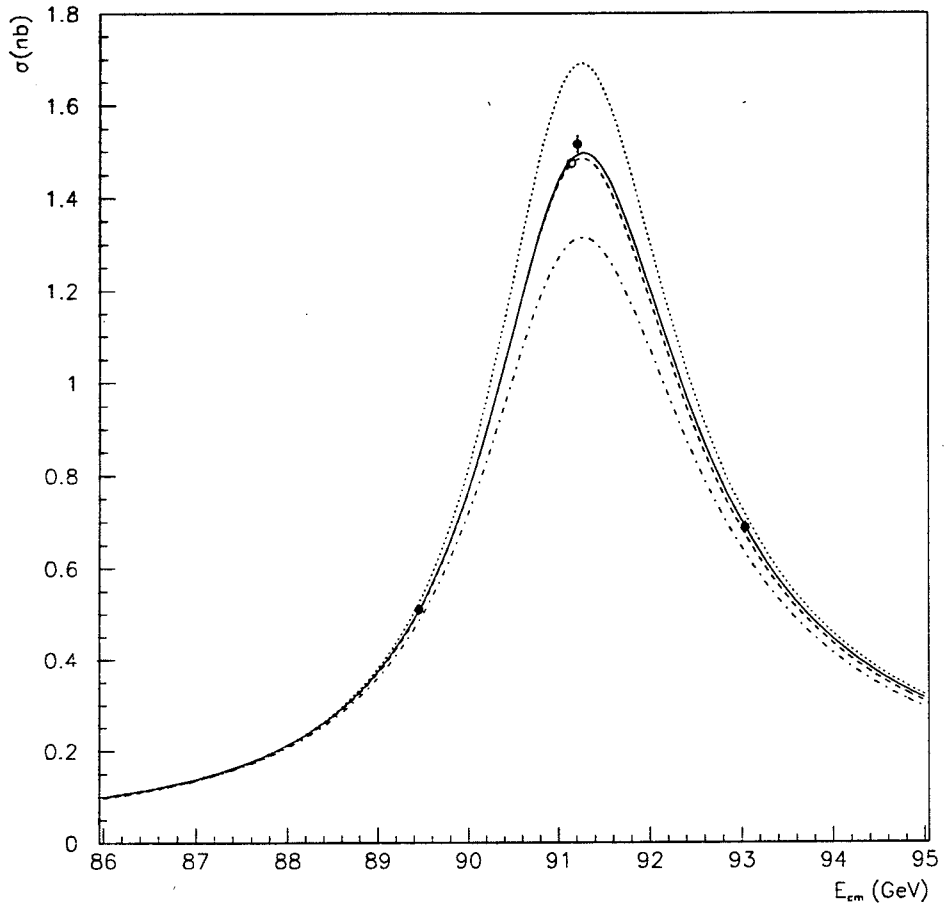

Figure 8.1: The results of a ZFITTER fit to the experimental cross sections for the process $Z^0 \rightarrow \tau^+\tau^-$. The solid circles represent the cross section measurements from 1993, while the open circle corresponds to the measurement of the peak cross section from the 1994 data. The solid line is the result of the Improved Born Approximation parametrization, and the broken line of the Standard Model parameterization as described in the text. The two fits show good agreement. In addition, the Standard Model predictions for two neutrino generations (dotted line) and for four neutrino generations (broken dotted line) are shown, where the same values for the the masses of the Z^0, the top quark, and the Higgs boson were used as for the Standard Model prediction with three neutrino generations. A fourth neutrino generation can be excluded within the Standard Model framework.

Assuming again lepton universality, the invisible width can be calculated as $\Gamma_{\rm inv} = \Gamma_{\rm tot} - \Gamma_{\rm had} - (1+\frac{2}{1+\delta_\tau})\Gamma_{\tau\tau}$, where $\delta_\tau = -0.0023$ takes into account small corrections for the mass of the tau lepton [78]. Taking $\Gamma_{\rm had} = 1746.7 \pm 5.1$ MeV from [14], one obtains

$$\Gamma_{\rm inv} = 496.9 \pm 4.1 \text{ MeV} ,$$

where the error takes into account correlations between $\Gamma_{\rm tot}$ and $\Gamma_{\rm had}$ according to reference [14]. The number of neutrino generations is obtained by dividing the invisible width by the Standard Model prediction for the neutrino decay width as

$$N_\nu = 2.974 \pm 0.025 \pm 0.007 ,$$

where the first error is experimental and the second is due to varying the top mass and Higgs mass over the ranges given above.

Chapter 9

Summary

The lineshape parameters for the decay $Z^0 \rightarrow \tau^+\tau^-$ have been measured from the data recorded during 1993 and 1994 with the OPAL detector at LEP. The cross sections needed for this measurement were determined from the ratio of the number of $Z^0 \rightarrow \tau^+\tau^-$ decays and the integrated luminosity over a given time period at three center-of-mass energies near the Z^0 resonance, namely at the nominal Z^0 peak and at about ± 2 GeV from the peak.

The integrated luminosity was measured with the Silicon Tungsten Luminometer which was installed in the OPAL detector at the beginning of 1993. The luminometer records Bhabha events within a well defined fiducial acceptance, corresponding to a Bhabha cross section which was calculated with the BHLUMI small angle Bhabha Monte Carlo program. The reconstruction of the energy and radial coordinate of a particle, their simulation in the Monte Carlo program, as well as the determination of the absolute position of the luminometer within the OPAL detector were described. The luminosity was measured with an experimental uncertainty of about 0.07%, which was combined with the preliminary error of 0.25% on the theoretically calculated small angle Bhabha cross section.

Tau pair final states were selected from the OPAL data by defining a set of

geometric and topological cuts consistent with the decay $Z^0 \to \tau^+\tau^-$. The number of events selected by these cuts was about 56 000 in 1994, and 16 000, 3 400, and 3 800 in 1993 at the peak energy, at "peak−2", and at "peak+2", respectively. All the 1994 data were collected at the peak energy. Since the τ lepton decays before detection, the cuts had to be sensitive to all leptonic and multihadronic decay channels of the τ lepton. As a result, all other visible final states of a decaying Z^0, as well as two-photon events and cosmic ray events, contribute to the background of the selected sample of events. The size of each of these backgrounds was estimated and subtracted from the data sample. From tau pair Monte Carlo, a correction factor for the overall inefficiency due to genuine tau pair events discarded by the tau pair selection cuts was calculated for each data sample. The inefficiencies for each cut were compared for tau pair data and tau pair MC, and the corresponding corrections were derived. The overall correction factors to scale the number of data events passing the tau pair selection cuts to an acceptance with no geometric or kinematic cuts, and without background contamination, were calculated as 1.3097 ± 0.0050 for 1994, 1.3113 ± 0.0077 for 1993 peak, 1.3057 ± 0.0176 for 1993 peak−2, and 1.3436 ± 0.0148 for 1993 peak+2.

Correcting the number of events passing the tau pair selection cuts by these factors and dividing the results by the corresponding integrated luminosities, the cross sections for the process $Z^0 \to \tau^+\tau^-$ for the four data samples were derived. The program ZFITTER was then used to provide the theoretical parametrization of the lineshape, and the values giving the best fit to the experimental data were obtained using the minimization program MINUIT. Using the 'Improved Born Approximation' as a Standard Model independent parametrization, the mass of the Z^0, its total decay width and the partial decay width of the process $Z^0 \to \tau^+\tau^-$ were determined as $M_Z = 91.183 \pm 0.020$ GeV, $\Gamma_{tot} = 2.514 \pm 0.018$ GeV and

$\Gamma_{\tau\tau} = 84.54 \pm 0.59$ MeV. Using published results for M_Z, and Γ_{tot} with higher accuracy, a value for the partial decay width of $\Gamma_{\tau\tau} = 84.02 \pm 0.20$ MeV was obtained. Further, using published results for the decay width of the Z^0 into quark pair final states, the invisible decay width of the Z^0 was determined as $\Gamma_{inv} = 496.9 \pm 4.1$ MeV. Dividing this result by the Standard Model prediction for the decay width of the Z^0 into neutrino pairs, the number of neutrino generations was determined as $N_\nu = 2.974 \pm 0.025 \pm 0.007$, where the first error is experimental and the second is due to the uncertainty on the masses of the top quark and the Higgs Boson.

All results were found to be in good agreement with the Standard Model predictions. The results are furthermore consistent with the assumption of lepton universality and the existence of a fourth neutrino generation can be excluded within the Standard Model framework.

Appendix A

SW Operation and Data Readout

Upon receipt of a RESET signal from the GTU in the central trigger logic, the sequencer puts the TRACK/HOLD switch of the AMPLEXes to TRACK so that the shaped signals are passed in real time to the output buffer until they peak approximately 300 ns after the electron and positron bunches collide at the interaction point [44]. Then HOLD is asserted to store the developed signal in each track/hold circuit for readout. In a normal bunch crossing cycle, the output shift register of each AMPLEX chip is first configured to select all output channels to form the sum of the energy seen in the detector for the trigger. The AMPLEX trigger sums are presented to the SW trigger system, which decides in about 7 μs whether the pattern of energy deposited in the detectors is appropriate for readout and digitizes and stores the half-tower and full-detector trigger energy sums. The GTU decides whether to send a RESET, or a TRIGGER signal, and for a RESET, the cycle is started over again by going into the tracking mode.

In case a TRIGGER signal is received, the sequencer initiates the readout of the individual pads for each detector. For readout, a single bit is shifted through the output register to select each channel in turn and pass its signal through the output buffer for individual sequential readout of each pad. The four AMPLEXes

on each ceramic are similarly multiplexed to yield a single analog output line per Silicon wafer. In trigger mode, this multiplexer delivers the sum of the four AMPLEX signals, while in readout mode it selects the individual AMPLEX chips sequentially. As soon as all the data have been digitized, even though not yet fully processed and transferred to the event builder, it is no longer necessary to hold the analog charges in the AMPLEX chips. In order to avoid pedestal drifts, the TRACK/HOLD cycle is resumed. Also, the trigger energies are read out from the SW trigger electronics – this is not done during digitization in order to avoid noise on the VME backplane bus. If the information from enough random beam crossings has been sampled, new settings for the DAC in the digitizers are calculated and downloaded into the DACs to maintain the pedestal value at 1024 digitizer counts. At this point, the LTU releases the BUSY signal and the front end electronics is ready to receive the next trigger. In the front end crates, the data is zero-suppressed, packed, and sent over VIC links to the local system crate SWLSC. There the data from the left and right detector is merged, on-line histograms are created and other monitoring is performed. Finally, the data are sent over another VIC link to the eventbuilder (EVB).

Besides the data acquisition processes, various monitoring processes are running in a designated VME crate SWCAL which is not synchronized with the LEP BX or RESET signals. The low voltage supply to the detector and the cooling water flow are controlled and constantly monitored by this crate, generating warning messages if a failure of either function causes under- or overheating of the detector. Every three hours, the z-position of the SW detector is measured with respect to flanges on the beryllium beam pipe [51]. The pressure and temperature of the central detector as well as the beam pipe temperature are obtained over the local

area network and logged together with the z-position.

A specially designed electronics module, the SW beam dump module, monitors the dark currents in the silicon wafers and, if they exceed a certain threshold, automatically dumps the LEP beam. This measure was taken to avoid radiation damage to the detector as the AMPLEX channels are easily damaged by excessive dark currents. While no data are taken, the silicon bias voltage is kept at 15 V to provide sufficient sensitivity for the beam dump system while limiting the stored energy in the detector. Prior to installation of the beam dump system, a LEP beam loss on two occasions resulted in a direct exposure of an SW calorimeter to the electron beam [79].

Bibliography

[1] S. L. Glashow, J. Iliopoulos and L. Maiani, Physical Review **D2** (1970) 1285;
S. Weinberg, Physical Review Letters **19** (1967) 1264;
A. Salam, *Elementary Particle Theory*, ed. N. Svartholm, Almquist and Wiksells, Stockholm, 1969, 367.

[2] F.J. Hasert et al., Physics Letters **B46** (1973) 138;
F.J. Hasert et al., Physics Letters **B46** (1973) 121.

[3] D Bardin, et. al, *ZFITTER, An Analytical Program for Fermion Pair Production in* e^+e^- *Annihilition*, CERN-TH 6443/92 (1992).

[4] D. Griffith, *Introduction to Elementary Particles*, Wiley, New York, 1987.

[5] F. Mandl and G. Shaw, *Quantum Field Theory*, Wiley, New York, 1984.

[6] P.W. Higgs, Physical Review Letters **12** (1964) 321; Physical Review Letters **145** (1966) 1156.

[7] D. Schaille, *Tests of the Electroweak Theory at LEP*, Fortschritte der Physik **42** (1994) 429.

[8] L. Montanent et al., *Review of Particle Properties*, Physics Reports **50** (1994) 1173.

[9] M. Caffo and E.Remiddi, *Bhabha Scattering*, CERN 89-09 (1989), p.171.

[10] D.A. Ross, J.C. Taylor, Nuclear Physics **B51** (1973) 25.

[11] M. Consoli and W. Hollik, *Electroweak Radiative Corrections for Z^0 Physics*, CERN 89-09 (September 89), p.7.

[12] W. Hollik, *Radiative Corrections and Their Role for Precision Tests of the Electroweak Theory*, Zeitschrift für Physik **C38** (1990) 165.

[13] LEP Design Report, CERN LEP/TH/83-29(1983), CERN LEP/84-1(1984).

[14] The OPAL Collaboration, *A Preliminary Update of the Z^0 Line Shape and Lepton Asymmetry Measurements with the 1993 and 1994 Data.* OPAL Physics Note PN-166 (February 1995).

[15] B.R. Martin, G. Shaw, *Particle Physics*, Wiley, New York, 1992.

[16] J. le Duff, *Beam-Beam Interactions in e^+e^- Storage Rings*, CERN 77-13 (1977), p.377.

[17] R. Assmann et al., *The Energy Calibration of LEP in the 1993 Scan*, CERN-PPE/95-10 (1995).

[18] A. Sokolev and I.M. Ternov, Sov Phys. Doklady **8** (1964) 1203.

[19] L. Arnaudon, et al., *Measurement of LEP beam energy by resonant spin depolarization*, Physics Letters **B284** (1992) 431.

[20] L. Arnaudon, et al., *Accurate Determination of the LEP Beam Energy by Resonant Depolarization*, CERN SL/94-71 (BI) (1994).

[21] D. Strom, *Determination of the LEP energy spread from the longitudinal beam size in OPAL on 1993* OPAL Technical Note TN-264 (1994).

[22] The OPAL collaboration, *The OPAL detector at LEP*, Nuclear Instruments and Methods **A305** (1991) 275.

[23] S.L. Lloyd, *The OPAL primer*, Internal OPAL note (1992).

[24] Peter Mättig, *The Photon Energy Resolution on the Lead Glass Calorimeter* OPAL Technical Note TN-324 (1995).

[25] S.R. Hou, Ph.D. Thesis, University of Maryland (1991), unpublished.

[26] J.T.M. Baines, et al., *The Data Acquisition System of the OPAL detector at LEP*, Nuclear Instruments and Methods **A325** (1993) 271.

[27] K. Riles and T.J. Smith, *The Dense Data User's Guide*, internal OPAL note (1992).

[28] M. Arignon, et al., *The Trigger System of the OPAL experiment at LEP*, Nuclear Instruments and Methods **A325** (1992) 313.

[29] M. Arignon, et al., *The Pretrigger System of the OPAL experiment at LEP*, Nuclear Instruments and Methods **A333** (1993) 330.

[30] A.K. Amundsen, et al., Nuclear Instruments and Methods **A293** (1990) 145.

[31] H.J. Klein, J. Zoll, *PATCHY Reference Manual* (1988), available from CERN Computer Center.

[32] R. Brun, J. Zoll, *ZEBRA user guide*, (1987), available from CERN Computer Center.

[33] P. Ward and D. Ward, *A GOPAL Primer*, Internal OPAL note (1993).

[34] R. Cranfield, B. Holl and R.W.L. Jones, *OPCAL user guide*, Internal OPAL note (1990).

[35] R. Brun, et al., *GEANT3 User's Guide*, DD/EE/84-1 (1994), available from CERN Computer Center.

[36] T. Sjöstrand, Comp. Phys. Commun. **39** (1986) 347;
T. Sjöstrand and M. Bengtsson, Comp. Phys. Commun. **43** (1987) 367;
T. Sjöstrand, CERN-TH/93-7112 (revised August 1995).

[37] S. Jadach et al., *The Monte Carlo Program KoralZ, Version 4.0, for the Lepton or Quark Pair Production at LEP/SLC Energies*, CERN-TH. 7075/93 (1993), submitted to Comp. Phys. Commun.;
KoralZ Version 3.8: S. Jadach et al., Comp. Phys. Commun. **66** (1991) 276.

[38] The OPAL collaboration, *Proposal for Upgrading the OPAL Luminosity Detector*, CERN/LEPC 91-8 (1991).

[39] G. Barbiellini, et al., *Energy Resolution and Longitudinal Shower Development in a Si/W Electromagnetic Calorimeter*, Nuclear Instruments and Methods **A235** (1985) 55.

[40] U. Amaldi, *Fluctuations in Calorimeter Measurements*, Physica Scripta **23** (1981) 409.

[41] L. Montanent et al., *Review of Particle Properties*, Physical Review **D50** (1994) 1173.

[42] F. Lemeilleur et al., *Longitudinal and Transverse Development of electron showers using Silicon Detectors*, Nuclear Instruments and Methods **A279** (1989) 66.

[43] A. Lee, *Analysis of Small Angle Bhabha Scattering at LEP*, Proceedings of the XXVIIth Rencontres de Moriond, March 15-22, 1992.

[44] B.E. Anderson, et al., *The OPAL silicon-tungsten calorimeter front end electronics*, IEEE Trans. Nucl. Sci. **41 (4) (6)** (1994) 845.

[45] The SW Group, *The preliminary OPAL SiW luminosity analysis: Results for the 1994 summer conferences*, OPAL Technical Note TN-142 (1994).

[46] The SW Group, *Metrology of the OPAL Silicon Tungsten Calorimeter*, OPAL Technical Note, in preparation.

[47] E. Beuville et al. *Low Noise Analog CMOS Signal Processor with a Large Dynamic Range for Silicon Calorimeters*, Nuclear Physics **B23** (1991) 198.

[48] C. Grandi, et al., *Silicon Tungsten Online System*, Internal OPAL note SW-55 (July 94).

[49] K. J. Anderson, et al., *The Chicago OPAL Si-W Readout Electronics*, Internal OPAL note SW-51 (1993).

[50] R. Kellogg, private communication.

[51] The SiW Working Group, *The Preliminary SiW Luminosity Analysis: Results for the 1994 Winter and Spring Conferences* OPAL Technical Note TN-221 (1994).

[52] S. Jadach et al., Comp. Phys. Commun. **70**, (1992) 305.

[53] The SW Group, *Testbeam Results using the OPAL Silicon-Tungsten Calorimeter Prototype* OPAL Technical Note TN-178 (1993).

[54] D. L. Wagner, *The SW ROPE Processor - SW103*, Internal OPAL note (1994).

[55] R. Kellogg *The z metrology of SiW*, Internal OPAL note (1996).

[56] R. Kellogg, private communication.

[57] The SW Group, *Metrology of the OPAL Silicon Tungsten Calorimeter*, OPAL Technical Note, in preparation.

[58] F. James, et al., *MINUIT - Function Minimization and Error Analysis, Reference Manual* (1992), CERN Program Library Entry D506.

[59] M. Caffo, H. Czyz, E.Remiddi, Il Nuovo Cimento **105 A** (1992) 277.

[60] W. Beenakker and B. Pietrzyk, Physics Letters **B304** (1993) 366.

[61] M. Foucher, private communication.

[62] S. Jadach et al., Comp. Phys. Commun. **76**, (1993) 361-380.

[63] M. Böhm, A. Denner, W. Hollik, Nuclear Physics **B304** (1988) 687;
F.A. Berends, R.Kleiss, W. Hollik, Nuclear Physics **B304** (1988) 712.

[64] T. Kawamato, *Description of the 1993 and 1994 Bhabha Event Selection*, OPAL Technical Note, in preparation.

[65] R. Battacharya, J. Smith, G. Grammer, Phys. Rev. **D15** (1977) 3267;
J. Smith, J.A.M. Vermaseren, G. Grammer, Phys. Rev. **D15** (1977) 3280.

[66] T. Smith, *Description of the 1993 and 1994 Muon Pair Selection*, OPAL Technical Note, in preparation.

[67] R. Barlow, et al. *A Detailed Description of the 1991 Muon Pair Analysis*, OPAL Technical Note TN-109 (1992).

[68] J. Kirk, R. Lahmann, *A Detailed Description of the 1993 and 1994 Tau Pair Analysis*, OPAL Technical Note, in preparation.

[69] R. Hemingway, *An OPAL tune of JETSET 7.4 using Z^0 data*, OPAL Technical Note TN-279 (1995).

[70] C. Darling, et al., *OPAL updates to JETSET 7.4 decay tables*, OPAL Technical Note TN-322 (1995).

[71] T. Tsukamoto, *tau pair analysis in 1990*, OPAL Technical Note TN-026 (1990).

[72] L. Montanent et al., *Review of Particle Properties*, Physical Review **D50**, 1173 (1994) and 1995 off-year partial update for the 1996 edition (URL: http://pdg.lbl.gov/).

[73] ALEPH Collaboration, D. Buskulic et al., *Tau hadronic branching ratios*, CERN-PPE/95-140 (1995), submitted to Zeit. für Physik.

[74] R. Decker et al., Zeit. für Physik **C58** (1993) 445.

[75] J.Hilgart, R.Kleiss, F. Le Diberder, Comp. Phys. Commun. **75** (1993) 1.

[76] M. Kobel, private communication.

[77] E. Vokurka, *Method of Calculating Muon Pair and Tau Pair Tagging Efficiencies in LA204* OPAL Technical Note, in preparation.

[78] D. Schaille, *Precision Tests of the Electroweak Interaction*, Invited Talk at the XXVII International Conference on High Energy Physics, Glasgow, 20-27 July, 1994; CERN-PPE/94-162 (1994).

[79] J.A. Lauber, *Tests of Radiation Hardness of SiW at the LP1*, OPAL TN-323, October 95